The Scientific World Journal

Structural Health Monitoring and NDE Technologies for Aerospace Applications

Lead Guest Editor: Theodore E. Matikas
Guest Editors: Mark R. Woike and Dimitris C. Lagoudas

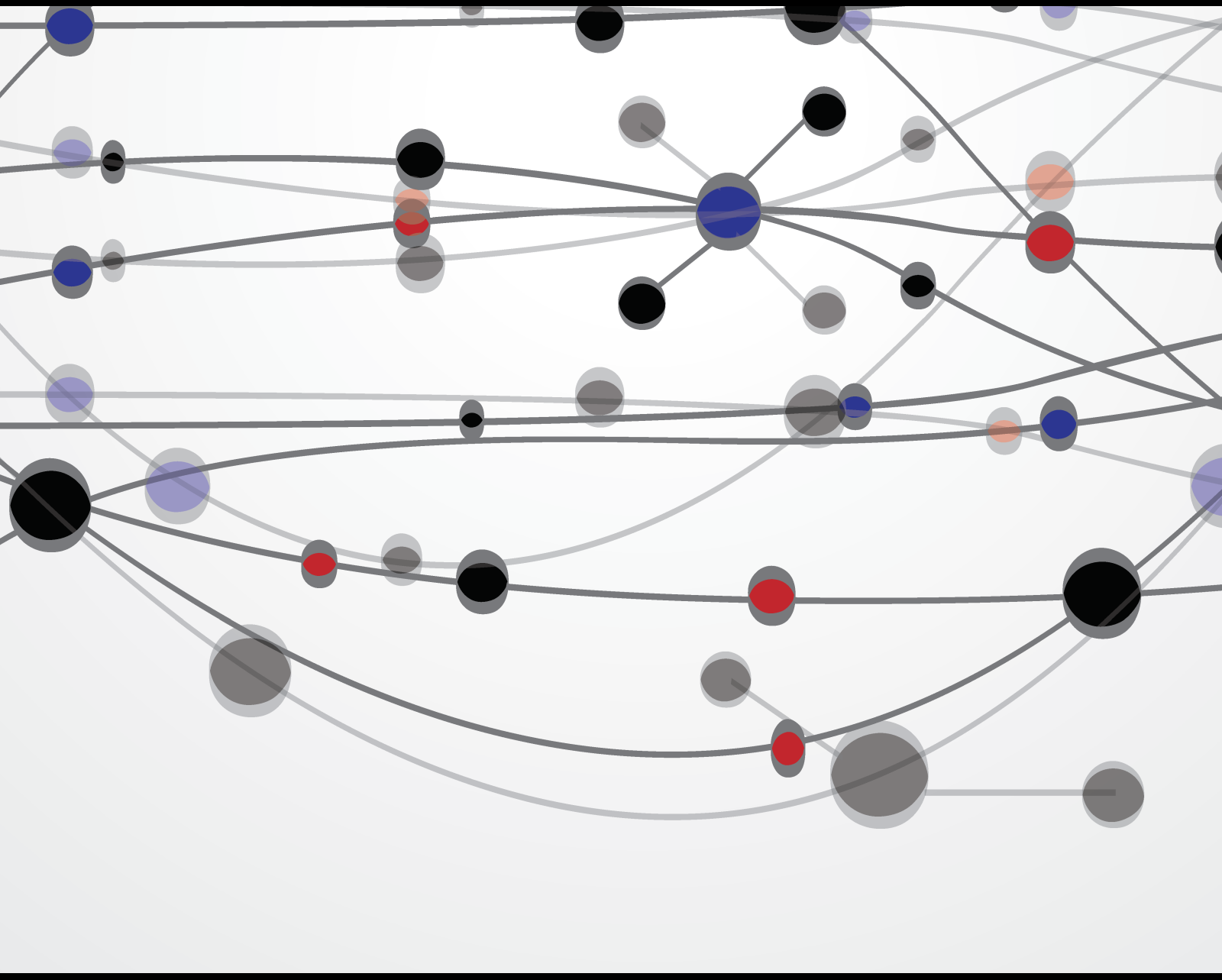

Structural Health Monitoring and NDE Technologies for Aerospace Applications

The Scientific World Journal

Structural Health Monitoring and NDE Technologies for Aerospace Applications

Lead Guest Editor: Theodore E. Matikas
Guest Editors: Mark R. Woike and Dimitris C. Lagoudas

Aerospace Engineering

Bo Cao, China

Contents

Hindawi Publishing Corporation
The Scientific World Journal
Volume 2013, Article ID 218460, 31 pages
http://dx.doi.org/10.1155/2013/218460

Research Article

High Sensitive Methods for Health Monitoring of Compressor Blades and Fatigue Detection

Mirosław Witoś

Air Force Institute of Technology (AFIT), Ks. Bolesława 6, 01-494 Warszawa, Poland

Correspondence should be addressed to Mirosław Witoś; miroslaw_witos@o2.pl

Received 15 March 2013; Accepted 29 May 2013

Academic Editors: T. E. Matikas and M. R. Woike

The diagnostic and research aspects of compressor blade fatigue detection have been elaborated in the paper. The real maintenance and overhaul problems and characteristic of different modes of metal blade fatigue (LCF, HCF, and VHCF) have been presented. The polycrystalline defects and impurities influencing the fatigue, along with their related surface finish techniques, are taken into account. The three experimental methods of structural health assessment are considered. The metal magnetic memory (MMM), experimental modal analysis (EMA) and tip timing (TTM) methods provide information on the damage of diagnosed objects, for example, compressor blades. Early damage symptoms, that is, magnetic and modal properties of material strengthening and weakening phases (change of local dislocation density and grain diameter, increase of structural and magnetic anisotropy), have been described. It has been proven that the shape of resonance characteristic gives abilities to determine if fatigue or a blade crack is concerned. The capabilities of the methods for steel and titanium alloy blades have been illustrated in examples from active and passive experiments. In the conclusion, the MMM, EMA, and TTM have been verified, and the potential for reliable diagnosis of the compressor blades using this method has been confirmed.

1. Introduction

Many different fatigue failures,

(i) low cycle fatigue (LCF)

(ii) high cycle fatigue (HCF),

(iii) very high cycle fatigue (VHCF),

(iv) thermomechanical fatigue (TMF),

could occur throughout the turbine engine's life (Figure 1). Most of them are damage to compressor blades described in the paper.

Fatigue cracks propagating in rotor blades, the incorrect control of the engine's fuel system, and the lack of knowledge on the loads affecting the bearing system generally could cause formidable hazard to flight safety (Figure 2), as well as to engine life and reliability. Therefore, the AFIT keeps looking for new methods to recognize engineering, manufacturing, overhaul and service errors as well as stochastic overloads during the engine's running. Recognition of operational and maintenance problems is the first step to actively diagnose and control fatigue progress (engine's structural durability and reliability) as well as for prolongation engine time between overhaul and TBO [1–3].

The paper presents three diagnostic methods.

(a) *A metal magnetic memory* [4–7], which has been used as a sensitive passive observer of residual and applied stresses and material damages (of ferromagnetic and some austenite parts) [8–15]. Nowadays in the world MMM method has been used only for NDT of industrial objects, for example, welding joints, gas and steam turbine parts, rope, underground pipes, supporting structures in order to increase their TBO. The method has been tested in Poland for aviation (as NDE and SHM applications) since 2008 [3, 15, 16].

(b) *An experimental modal analysis* [17–21], which has been used in Poland as a sensitive NDE method during overhaul blade tests since 2008 and the method of the high-frequency identification of blade modal properties [3, 22, 23].

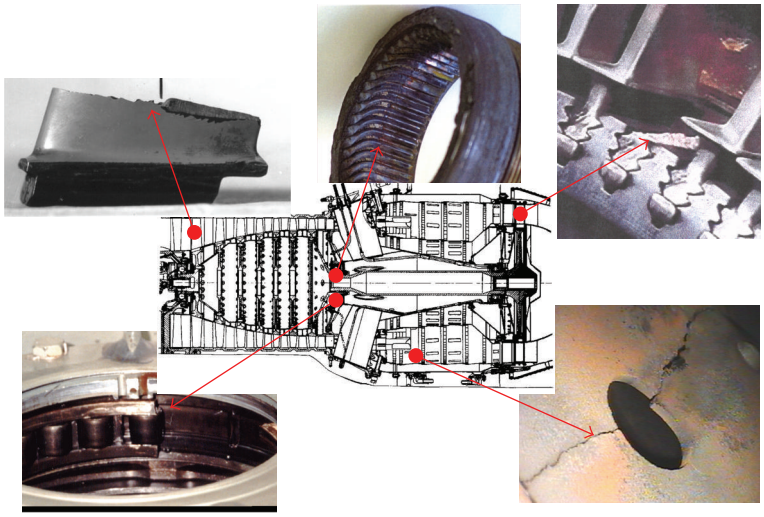

Figure 1: Problems of structural fatigue in turbine engines.

Figure 2: CF6-80 engine: fatigue destruction of III–IX stages of HP compressor [24].

(c) *A tip timing method* [25–33], which is one of the most interesting methods of complex diagnosing of jet engines and a powerful tool in order to investigate dynamic phenomena. The method has been used in the Polish Air Force since 1993 with the SNDŁ-1b/SPŁ-2b diagnosing system developed for the SO-3 jet engines. Since 1997, this method has been also used in Poland in the postrepair/postoverhaul acceptance tests. Now, the method is developed as digital board computer for structural health monitoring (SHM) in different aero-engines. Roots of the method date back to years 20 of the 20th century, when it was drawn up in the analogue version by Sir Campbell to needs of examining vibration of steam turbine blades [34]. At present the method is dynamically elaborated and used in the world, mainly in aviation, in the digital version. Standardizing works (ISA 107.1 subcommittee) are being conducted by partner of European Virtual Institute for Gas Turbine Instrumentation (EVI GTI) [35] and the Propulsion Instrumentation Working Group (PIWG) [36]. Organizations joining the largest producers of aero-engines, research and education units and companies of the metrological support. Details of the TTM application are being protected by numerous inventions, for example, [37–54].

The above described methods are sources of complex information about blade quality (of design, production, and overhaul) and real dynamics of phenomena correlated by modal properties, which have an effect on blades damage and fatigue differentiation. This information is used for holistic analysis of fatigue problems in aeroengines with influence of human and operating factors and actively control fatigue of compressor blade (Figure 3) as well as for verification of a FEM model.

2. Motivation

In the years 1975–91 as many as 25 first-stage compressor blades of ten SO-3 jet engines suffered fatigue-attributable break-offs, which caused two accidents. The metallographic examination of damaged blades made out of the 18H2N4WA alloy structural steel has proved that the crack initiation zone was located either on the leading edges (55%) or on the blade-back surfaces (45%), in the areas of nodal lines of the first mode vibration. Crack propagation occurred at low-level stresses (HCF problem) or high-level stresses (LCF problem) (Figure 4). Fatigue fracture covering as much as 95% of the blade's cross section was found in one of the blades. Furthermore, it has also been found that erosion and corrosion, both occurring on the blade's face surface, as well as fine mechanical damages on the leading edge are stress concentrators [55]. Fatigue problem was also observed in titanium blades (Ti5.8Al-3.7Mo) in the TW3-117 engines in the years 2005–2007 [3].

The gigacycle fatigue of compressor blade (VHCF problem) with "fish eye" symptoms under the blade surface has been observed at foreign users, for example, in Russia [56, 57] (Figure 4). Compressor blades run a risk of VHCF

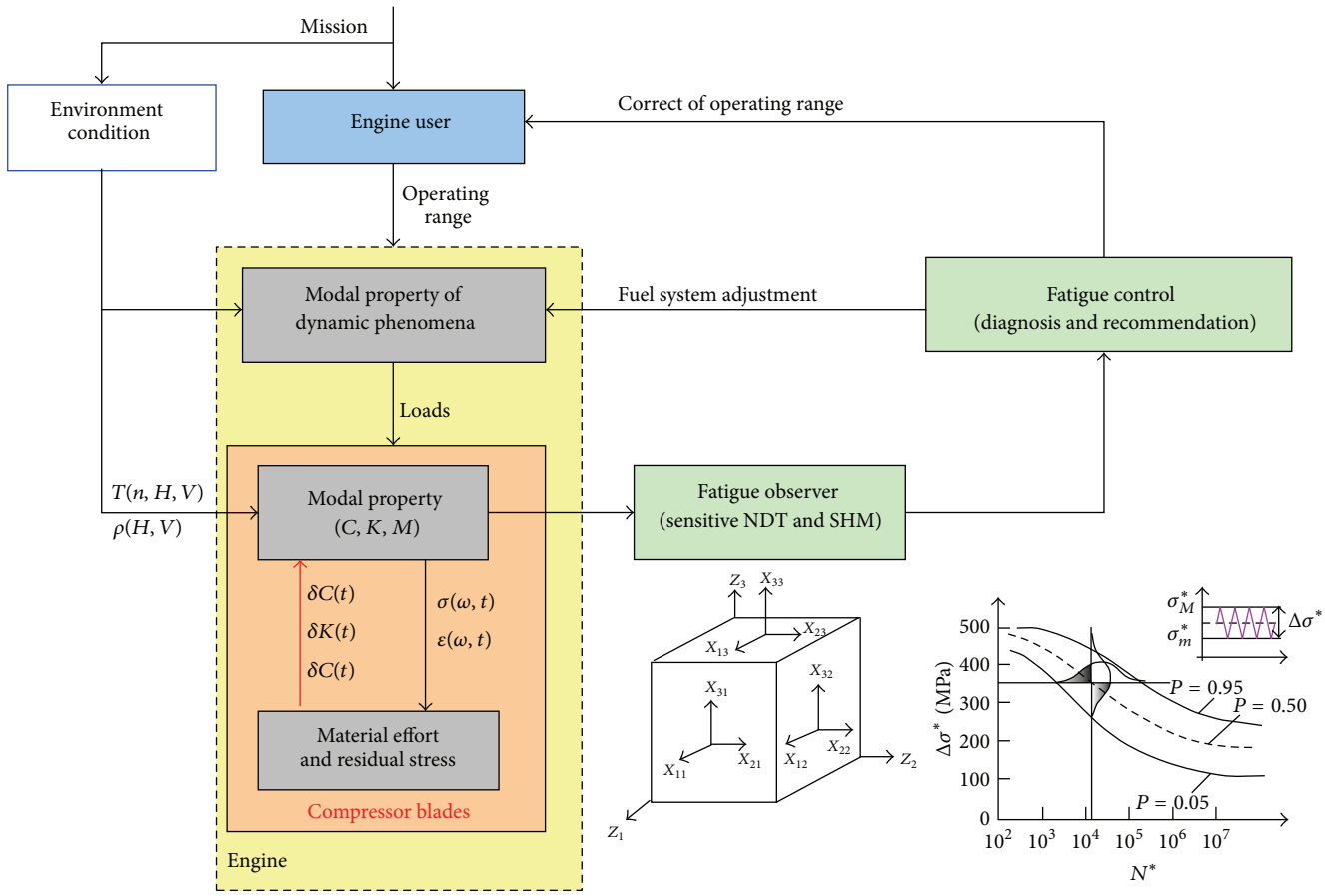

Figure 3: Idea of actively control fatigue by engine user—do not wait for blade crack [3].

problem because they count more than $3 \cdot 10^9$ cycles for 1st flexible mode and more than $1 \cdot 10^{10}$ cycles for 1st torsional mode during TBO. High risk of VHCF problem, with crack nucleation under the blade surface and stresses level below surface fatigue limits, concerns of high resistant material and blades made with surface finish techniques [58–60].

Uncontrolled blade over fatigue

(i) is a threat for service safety;

(ii) limits aeroengine life time;

(iii) increases maintenance costs.

It is also a great challenge for diagnostics engineers. Specialists, who are familiar with abilities of the NDE and SHM methods and continuum damage mechanics of material (Figure 5), are searching for answers to questions of the aero-engine user and the technologist of the renovation plant.

(a) *Level I*—before the first compressor blade crack or break-off

Which types of aero-engine are unrecognized compressor fatigue problem on?

⇓

Is it possible to assess the fatigue risk of blades through the casing of the compressor?

(b) *Level II*—technology and the quality of overhaul

What methods of the compressor blades verification should apply in the overhaul so that the blade does not break in the guarantee period?

⇓

How to recognize overload and weakened compressor blades (2nd stage of damage)?

(c) *Level III*—preventive activity in the overhaul and maintenance

If the crack of the blade was detected, what is causing for fatigue problem?

⇓

What mistakes of the engine use and repair are affecting for precipitated fatigue of compressor blades?

Classical NDE methods (X-ray, eddy current, ultrasound, magnetic particle and fluorescent) are very low effective ones for diagnosing blade crack before 3rd stage of damage because of the following.

(i) They do not answer the questions mentioned above. Finding the crack or other discontinuity of the structure, rather than its causes, is their main task.

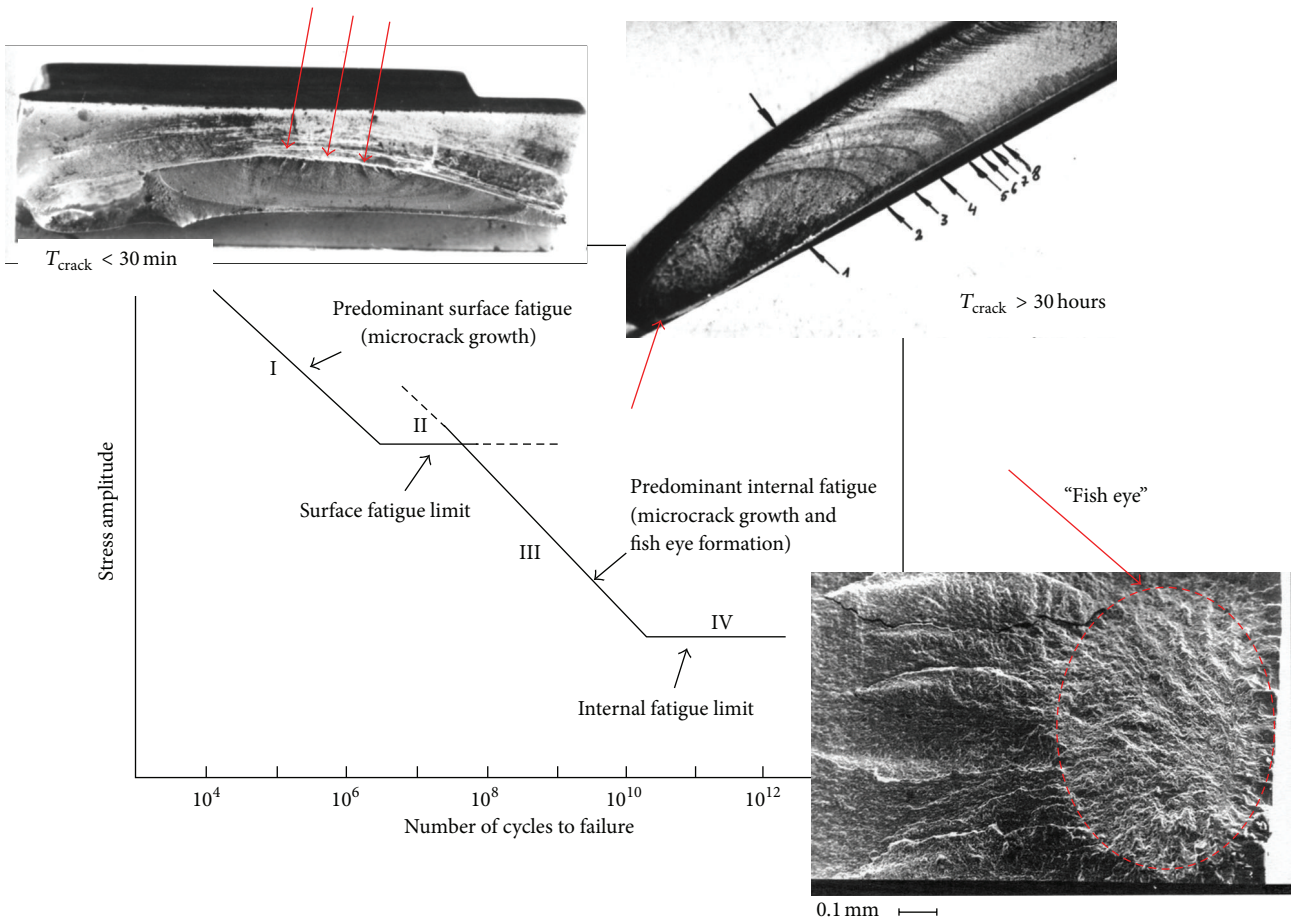

Figure 4: Fatigue problems (LCF, HCF, and VHCF) of compressor blades [3, 56].

(ii) Crack gap closing during engine standstill: Theoretical possibilities of the NDE method (detection of defects about min. size 0.3 mm) turn out to be false during examinations of the blades carried out after the longer stop of the engine, (Figure 6).

(iii) Lack of reliable information about real operating conditions.

(iv) Lack of knowledge about early cracking symptoms and mechanisms.

(v) Limited access to tested blades (because of inlet stator vane).

Other disadvantage of the NDE methods in use (during overhaul and service) is no possibility of *fatigue prognosis*.

This disadvantage is very important for blades having fatigue problems, for example, the 1st compressor blades of the SO-3 engine. These blades have design errors—too low the first-mode mistuning from the 2nd rotational harmonic excitation. Therefore, too high stress and fast fatigue crack initiation can occur during operation. These conditions take place during the take-off phase when there is a foreign object (e.g., bird) lying in the inlet or the inlet icing occurs (Figure 7). Under such conditions time between crack initiation and blade damage can be shorter than time of a single flight (LCF problem). Disturbance of the pressure and velocity in the intake are being moved by the entire length of the compressor. Hazardous blade vibrations occur only at synchronous resonance if the level of excitations is greater than acceptable. A diagram of Campbell is outlining zones of the synchronization, but it is well known only to a designer of the compressor. Flutter, surge (source of asynchronous resonances), and foreign object damage (FOD, local stress concentrator) are also source of LCF problems. Surge and FOD are easily detected by the aeroengine users.

Some errors of setting or hidden defects of the fuel control system affect the long-term working of compressor near the unstable limits (Figure 8) (stall, flutter, or surge during acceleration and deceleration, disturbance of the temperature field in compressor, combustion chamber and turbine), as well as high level of rotor unbalancing and alignment are the source of generating hidden fatigue problems of compressor blades (HCF and VHCF problems). Synchronous and asynchronous resonances are appearing in these working conditions of the compressor. The lack of distinct manifestations of the engine during disorders mentioned above causes that HCF and VHCF problems of blades, including tearing them off, are surprising for the user. Initiating the opened crack (3rd stage of damage) and its propagation are taking place at the low vibration amplitude of blades. Decreasing risk level of blades

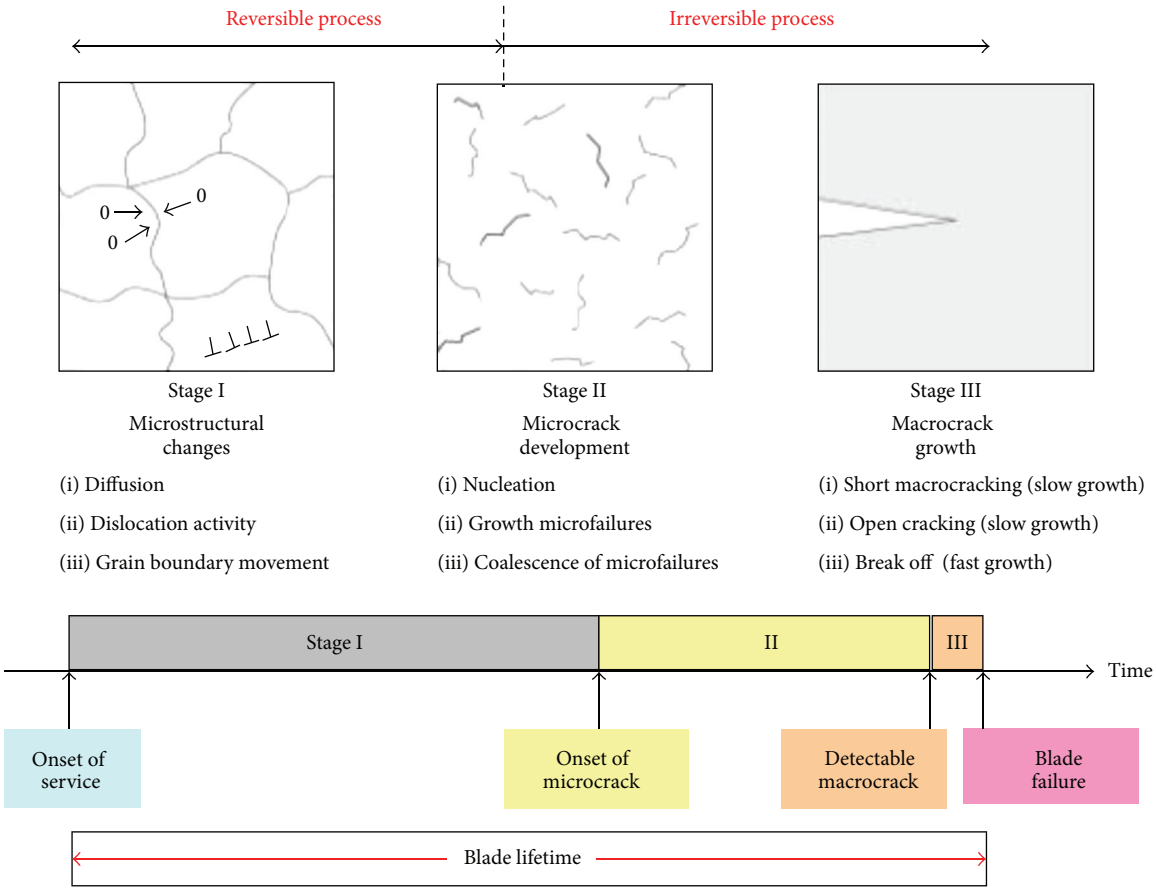

Figure 5: Continuum damage mechanics for compressor blade material. The first stage and the beginning of the second stage of damage are copying reversible changes [3].

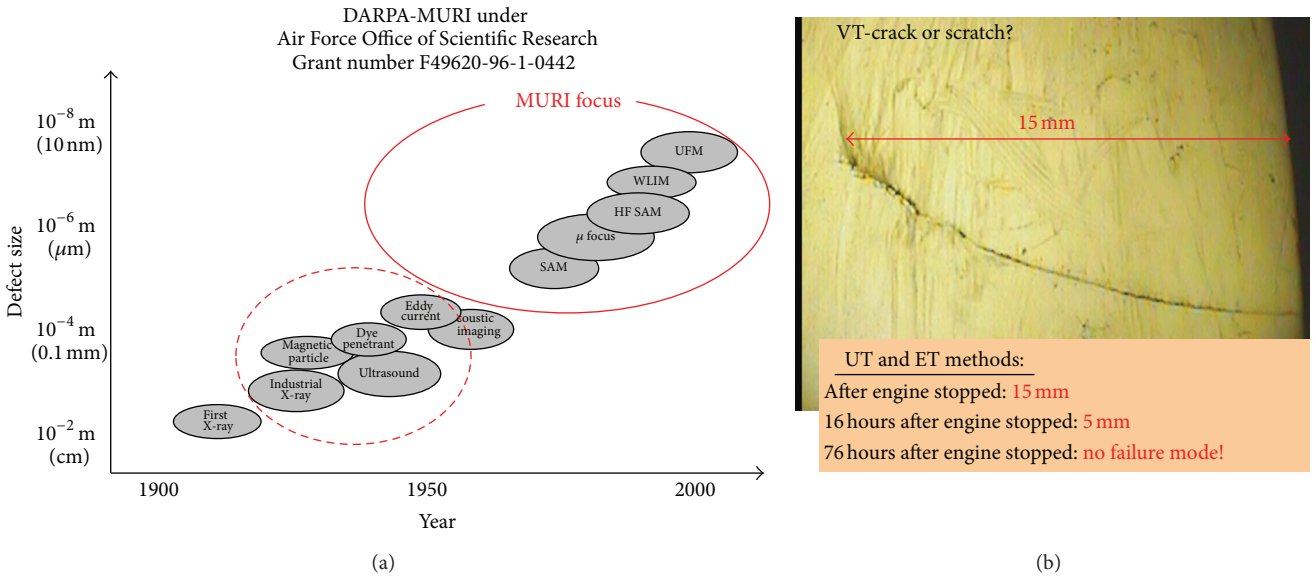

Figure 6: Showing: (a) Contemporary research capabilities of material degradation in service (the classic NDT methods) and the laboratory (MURI focus) [55]; (b) Influence residual stresses on closing the crack gap and the change of reading by ultrasound and eddy current methods after switching the engine off.

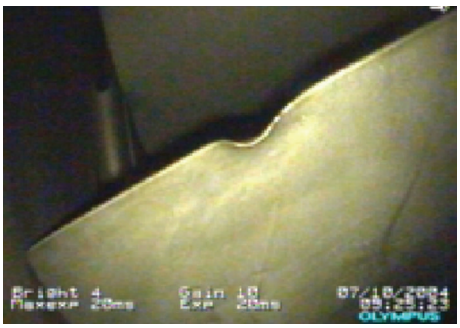

(a)

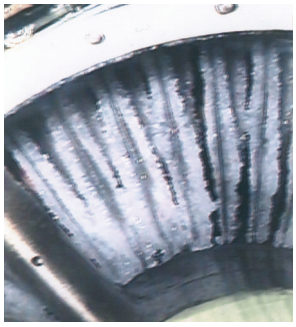

(b)

Figure 7: Showing LCF concentrations: (a) blade with FOD; (b) icing of compressor inlet.

HCF and LCF is possible by correct overhaul and operation errors, that is, shape of operating area changes [2, 3, 61–63].

Endurance problems of compressor blades can result also from new acoustic properties of a combustion chamber and the combustion process, incurred after the change of the fuel type, for example, using Jet-A1 or F-34 (NATO) in place of Jet-B or during high disturbance of temperature field in front of the turbine generated by carbon deposit of injectors [3].

Both old and new properties of disadvantageous extortions are unknown for the aero-engines user. Endurance problem of the compressor blades is noticed only after the first coincidence of cracking or breaking off the blade in service.

To sum up, fatigue problems of compressor blade are an effect rather than a cause. For the analysis of the problems, two approaches are used: classical and holistic. In *the classic approach*, the material fatigue results mainly from operating times (load cycles) and intensity of adverse phenomena (e.g., the human aspects and the specificity of aviation missions), Figure 9(a). In *the holistic approach* the material fatigue of compressor blade results from the level and the duration of disturbing the flow of the energy which aspects of the quality are affecting of the production, the repair and the use of the engine, Figure 9(b). The effective prevention requires applying the observer (the NDE and/or SHM method, methods of the signal analysis), which will be detecting not only the crack of blade, but also the cause of the hastened material fatigue (Table 1).

Table 1: Endurance threats of real blades permanence ("live") according to the theory of five elements [3].

Flow dynamics path	Kinematic loads path
Flow clocking Stall Surge Flutter Combustion instability Foreign object in inlet Flight on big angles of the attack	Centrifugal force Compressor nonaxial Rotor unbalance Compressor speed fluctuation Structure resonances Flight with big "g"

3. Concepts of Evaluating Blades

Effective and credible monitoring of the structure is possible, when technical problems are recognized, expected diagnostic symptoms are detected, and measuring and analytical methods (algorithms) could be applied.

3.1. Monitoring of the Vibration Magnitude. An intuitive diagnostic symptom of LCF problems is *blades magnitude*. Detecting the dangerous level of blade vibration during the work of an aeroengine and the change of flight conditions or the rotational speed of the engine are a base of the straightest preventive activity.

A report is describing the diagnostic rule

$$\text{if } A_{\text{blades}} < A_{\max}, \text{ then OK else LCF threat.} \quad (1)$$

This approach has advantages and disadvantages.

Advantages

(i) Practicable methods in the service and flight (for a board monitoring system);

(ii) Possible active control of blades LCF.

Disadvantages

(i) The level of the dangerous vibration amplitude is different for different mod (higher mod ⇒ smaller acceptance amplitude);

(ii) The indicator of the dangerous vibration amplitude is not detecting the HCF and VHCF threat of blades;

(iii) During the work of an engine, the vibration amplitude of the cracked blade little differs from healthy blades (influence of the centrifugal force).

3.2. Monitoring of the Mod Frequency. An intuitive diagnostic symptom of a blade crack is "a in change its modes frequency" (influence of active area change). The cracking propagation and blade break-off occur at limiting decrease in frequency [23]. The change of the blade frequency also results from erosion and the corrosion. Erosion is reducing mass of the blade and increasing the frequency. The corrosion is reducing the stiffness of the blade, and in the end the frequency of the blade is decreasing. Single compact FOD practically is not changing modal parameters of the blade, but it is a mechanical notch with concentrator of stresses.

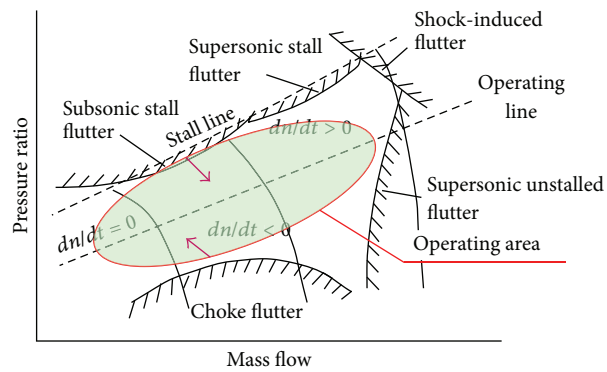

(a)

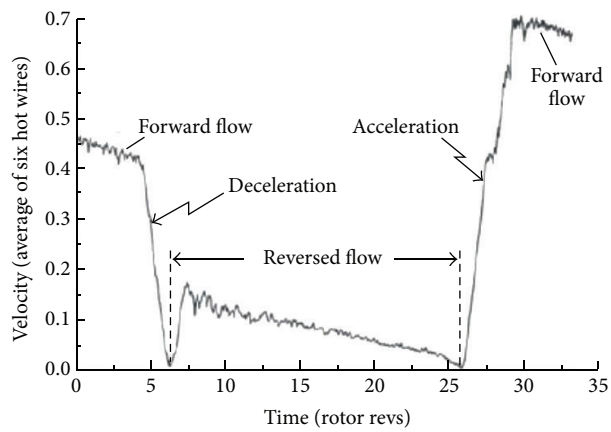

(b)

Figure 8: Showing (a) map of the compressor with information about dangerous threats [2, 3]; (b) deep surge cycle [3, 61]: the deceleration and acceleration of the flow in the compressor duct are a broadband impulse extortion for compressor blades and a bearing system (LCF concentrations) as well as with thermomechanical fatigue (TMF) for elements of a combustion chamber and the turbine.

A report is describing the diagnostic rule

$$\begin{aligned} &\text{if } f_{\text{blade}} \in \langle f_{\min}, f_{\max} \rangle, \text{ then OK} \\ &\text{else if } f_{\text{blade}} > f_{\max} \text{ then} \\ &\qquad \text{Work hardening or Erosion} \\ &\text{else if } f_{\text{blade}} \geq (f_{\min} - \Delta f_{\max}) \text{ then} \\ &\qquad \text{Softening else cracking.} \end{aligned} \tag{2}$$

This approach has advantages and disadvantages.

Advantages

(i) Practicable methods in the overhaul and service of the aero-engines;

(ii) Possible active control of blades fatigue;

(iii) Possible comprehensive diagnostics of the engine. The blades of the compressor palisade are mechanical filter about known average parameters.

Disadvantages

(i) The frequency value of cracking blades depends on the crack position, parameters at the top of the crack edge (hardening or softening), and the loading. The modal frequency of the blade can suit different sizes of cracks (Figure 10).

(ii) The blade frequency and mass distribution are tuned during assembly. Diagnostic symptom can be distorted during the manufacture and repair of compressor.

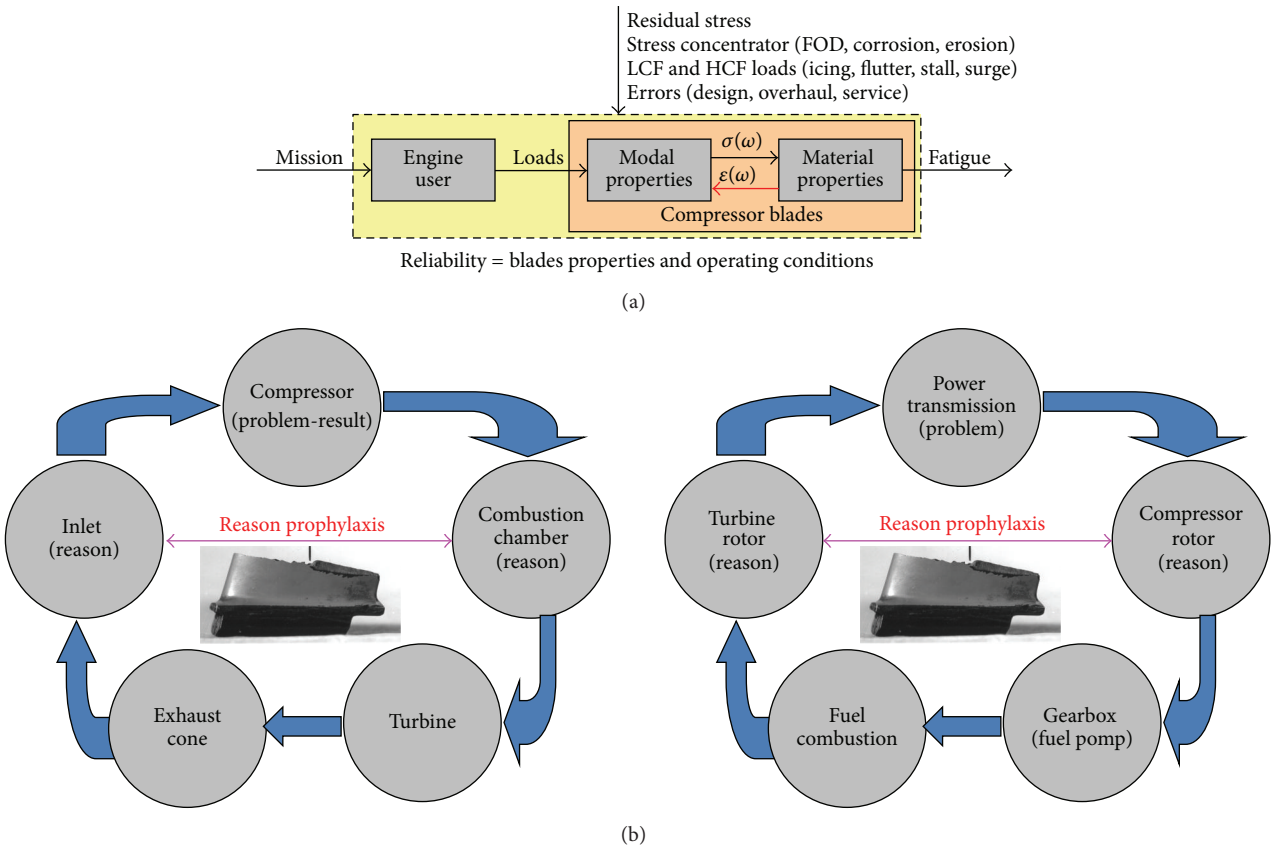

Figure 9: Analysis of cause and effect [3]: (a) classic approach with influence of human and operational factors on fatigue problems of the blades; (b) holistic approach—a compressor blade crack is a "*result*" of the wrong level of energy flow inside the engine. The "*causes*" must be sought at the inlet or the combustion chamber thermodynamic parameters (flow dynamics path) or mechanical power transmission quality and flight loads (kinematic loads path).

(iii) Blades' frequency check offers too short prognosis horizon (Figure 5). It is sufficient in the blade health monitoring only; for example, in the tip-timing method which is used to detect dangerous blades vibration and open cracks during engine operation.

3.3. Damage Monitoring of the 2nd Stage. More sensitive detection of fatigue is based on the relationship between changes in the material structure during 1st and 2nd stage of damage (before open crack), Figure 5, and subtle measurable changes of parameters (diagnostic symptoms).

Generally speaking, crystal lattice imperfections have a mechanical strengthening effect, since the lattice defects act as obstacles to the movement of dislocations when a mechanical stress is applied. Different strengthening mechanisms can be distinguished depending on the type of lattice defect contributing to the obstruction of moving dislocations [56, 64, 65]:

(i) solid-solution strengthening (interstitial/substitutional impurity atoms);

(ii) strengthening from point defects (due to vacancies);

(iii) work-hardening or strain-hardening (due to other dislocations);

(iv) grain boundary strengthening;

(v) martensite strengthening (phase transformation);

(vi) strengthening from fine particles (due to precipitates/inclusions).

Compressor blades work in temperature which is below 30% of melting temperature, that is, in *cold working regime*. Overload, stress concentration near nodal line, erosion and corrosion pitting, and fatigue, Table 2, mainly influence on the dislocation density ρ_d and the grain diameter d, defined as the average grain diameter. Cold working and fatigue change mechanical parameters of material (yield point σ_y, tensile strength σ_{utl}, hardness and microhardness, Young modulus, damping, and nonlinearity) [66–68]. In the end modal properties of the blade are changing.

The fatigue damage progression can be divided into different (partially overlapping) stages, based on studies of the basic structural changes [56, 64–71].

Fatigue Damage Initiation. Even at cyclic stress amplitudes below the macroscopic yield stress, the cyclic mechanical loading can plastically deform the material locally on a microscopically small scale: such microplastic flow first occurs in the grains that are stressed with the highest shear

Table 2: The fatigue of metal compressor blades at numbers of load cycles in the range 10^0–10^{12} [69].

Number of cycles	Description
10^0–10^3	Low cycle quasi-static or fatigue fracture (LCF problem) at availability of large "microplastic" deformation in some zones of failure. The crack nucleation below the surface.
10^3–10^5	Low cycle fatigue fracture (LCF problem) at availability rather small "macroplastic" deformation in a zone of failure (when $\sigma_e \leq \sigma_a \leq \sigma_y, \sigma_e$—a limit of elasticity). The crack nucleation from the surface.
10^5–10^8	Many classical cycles fatigue fracture (HCF problem) at availability of "microplastic" deformations in micro and macrovolumes near a zone of fatigue (when $\sigma_a \leq \sigma_e$). The crack nucleation from the surface.
10^9–10^{12}	Fatigue fracture on super high bases (VHCF problem) at availability of "microplastic" deformation in microvolumes near a zone of failure (when $\sigma_a \ll \sigma_e$). The crack nucleation on the soft inclusion below the surface.

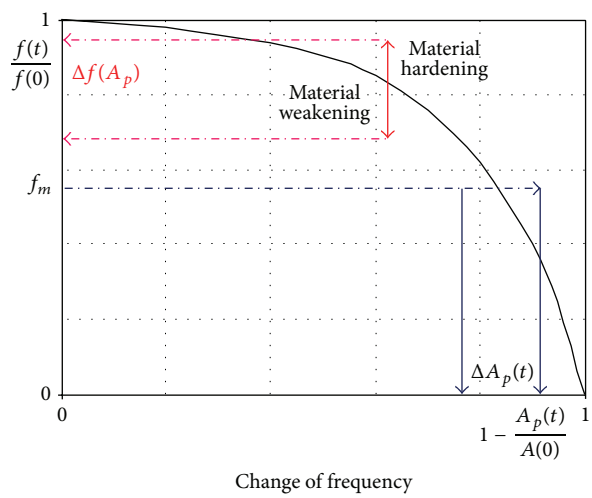

Figure 10: Lack of explicit copying of the size of the crack in the 1st modal frequency of blades [3].

stress amplitude and near inherent material imperfections (inclusions, scratches, and voids). Indeed, tensile residual stress concentrations, associated with such imperfections, lower the actual applied stress at which the material starts to plastically deform locally in some individual grains. The initiation of damage due to cyclic deformation therefore consists of microstructural changes associated with localized micro-plastic deformation in some individual grains, that is, the development of slip bands, the generation of dislocations (increase of dislocation density), and the rearrangement of dislocations into dislocation tangles, dislocation walls, and persistent slip bands. These persistent slip bands can be envisaged as embryonic fatigue cracks.

Result. Nucleation of microsized cracks along the developed slip bands in a number of grains.

Slip Band (Stage-I) Crack Growth. Consider a microcrack that is initiated inside an individual grain of a polycrystalline material. Such microcrack can grow further under sufficiently applied cyclic stress, along slip planes of high shear stress. Then, to develop further, the crack must propagate into the neighbouring grains, which have different lattice orientations and therefore different slip systems. For small microcracks to propagate, the crack needs to reorientate at the grain boundary towards a particular slip direction of the surrounding grain. Typically, the majority of lifetime corresponds with microcrack (nucleation and growth), which is moreover a regime of stable damage progression.

Result. Formation of dominant crack(s) (with dimensions of typically a few to ten grain diameters wide).

Transgranular (Stage-II) Crack Growth. As the microcrack propagates, the plastic zone around the crack tip increases and the resistance to crack growth diminishes. The crack becomes insensitive to grain boundary obstacles and to the particular slip systems of individual grains: the crack now develops in the plane normal to the tensile stress direction, and at much faster rates per loading cycle compared to stage-I crack growth.

Result. Growth of a well-defined crack, along the plane normal to the applied stress direction, and coalescence of microcracks towards a macro-crack with such critical macroscopic dimensions, that the remaining cross-sectional area of the material can no longer support the maximum applied load, and the material fails by ultimate fracture during the last stress cycle.

The material's performance concerning the fatigue damage process is typically characterized by a *S-N curve*, also known as a Wöhler curve, which gives the cyclic stress

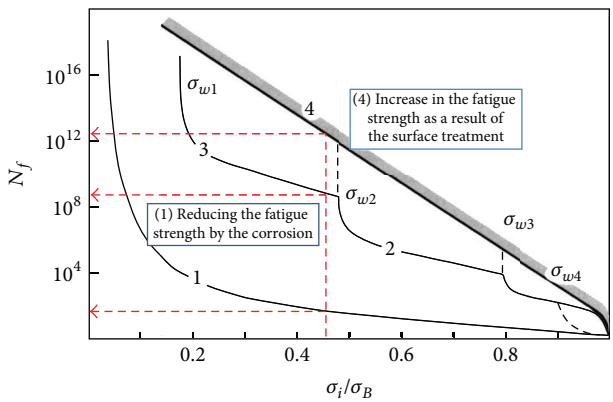

Figure 11: Influence of surface state on the number of cycles to blade failure N_f [3, 56].

amplitude σ_a as a function of the number of cycles to failure N_f, the latter in a logarithmic scale. Classically the S-N curve is not crossing $2 \cdot 10^8$ cycles what is insufficient for the compressor blades which TBO is copied through 10^{10} to 10^{14} cycles. Taking the VHCF risk into account requires using the widened S-N curve, appointed on the base of the bimodal theory of the metal fatigue (containing other bifurcations). About the real permanence of the blade (for the given level of exploitation stresses) a state of its surface (level of erosion and/or corrosion, FOD) is deciding (Figure 11). Strengthening of a metal, which represents the increase in the resistance to yielding or plastic deformation, can be obtained by changes in microstructure that impede the motion of dislocations [67, 68, 71]. Based on the type of obstacles that hinder the motion of dislocation and hence increase the strength, the yield strength σ_y of steels is usually expressed in the form of generalised equation where the contribution of all the strengthening mechanisms is added as follows [72]:

$$\sigma_y = \sigma_0 + \sigma_{SS} + \sigma_P + \sigma_{GB} + \sigma_D + \sigma_T, \tag{3}$$

where σ_0 is the lattice friction, σ_{SS} is the solid solution strengthening, σ_P is the precipitation strengthening, σ_{GB} is the grain boundary strengthening, σ_D is the dislocation strengthening, and σ_T is the texture strengthening.

In theoretical considerations, the Hall-Petch and the Bailey-Hirsch relations (4) between microstructure and mechanical parameters are given as follows:

$$\begin{gathered} \sigma_y \cong \sigma_f(T) + \frac{k_{HP}}{\sqrt{d}}, \\ \sigma_y\left(\text{after } \varepsilon_p\right) = \sigma_0 + \tau_i \cong \sigma_0 + \alpha G b \sqrt{\rho_d} \end{gathered} \tag{4}$$

with σ_f being the friction Peierls-Nabarro stress required to move a dislocation in a single crystal, T being material temperature, k_{HP} being material-dependent Hall-Petch constant which represents the difficulty required to unlock or generate dislocations in neighbouring grains, d being the grain diameter, σ_0 being the lattice friction, τ_i being the shear internal stress, α being a constant, G being the shear modulus, b being the crystal lattice parameter (base length of cubic unit cell), and ρ_d being the dislocation density.

Typical values for carbon steels are $\alpha \cong 0{,}4$, $b = 0.286$ nm, $d = 10^{-4}$–10^{-6} m, $G = 80$ GPa, $k_{HP} = 0.74\,\text{MPa}\sqrt{m}$, $\sigma_f = 70$ MPa, and $\sigma_0 = 100$ MPa.

The residual "life" of material ζ (relative residual time to blade break-off) is given by local level of dislocation density and the following relation:

$$\zeta = 1 - \frac{\sqrt{\rho_d} - \sqrt{\rho_{d0}}}{\sqrt{\rho_{d\,\max}} - \sqrt{\rho_{d0}}} \tag{5}$$

with ρ_{d0} being the dislocation density for well-annealed materials, and $\rho_{d\,\max}$ being the dislocation density for ductile strength. Typical values for carbon steels are $\rho_{d0} = 10^{-10}\ \text{m}^{-2}$, $\rho_{d\,\max} \cong 10^{-15}\ \text{m}^{-2}$.

The second stage of blade damage can be observed, for example, in "a resonance curve," (RC) measured by a laser point head during modal frequency testing [3, 23]. This approach is sufficient to solve overhaul problem (level II) with experimental modal analysis method. A report is describing the diagnostic rule (6), which will be developed at the description of method:

$$\begin{gathered} \text{if RC is for a linear object, then} \\ \text{OK or Work hardening} \\ \text{else Softening or Cracking.} \end{gathered} \tag{6}$$

This approach has advantages and disadvantages.

Advantages

(i) Simple algorithms of the data analysis and diagnostic rules.

(ii) High performance of examinations average time of objective testing (of parameters chosen mod and of the structural health condition) does not exceed 3 minutes per the blade.

(iii) Possible reliable prognosis and reduce of the risk of wrong diagnosis during engine overhaul.

(iv) The method is made available with base knowledge about relations between the material fatigue and modal properties which is being used by the tip timing method.

Disadvantages

(i) Required is direct access to the blades.

(ii) The approach requires the selection of a new sensitive observers (measurement technics and analysis methods) as well as recognition and verification of new diagnostic symptoms.

3.4. Damage Monitoring of the 1st Stage. If the blades are made of ferromagnetic material, the biggest extension of the prognosis horizon is possible. The dislocation density, the diameter of the grain, the history of mechanical load (residual stress) and applied loads change not only mechanical

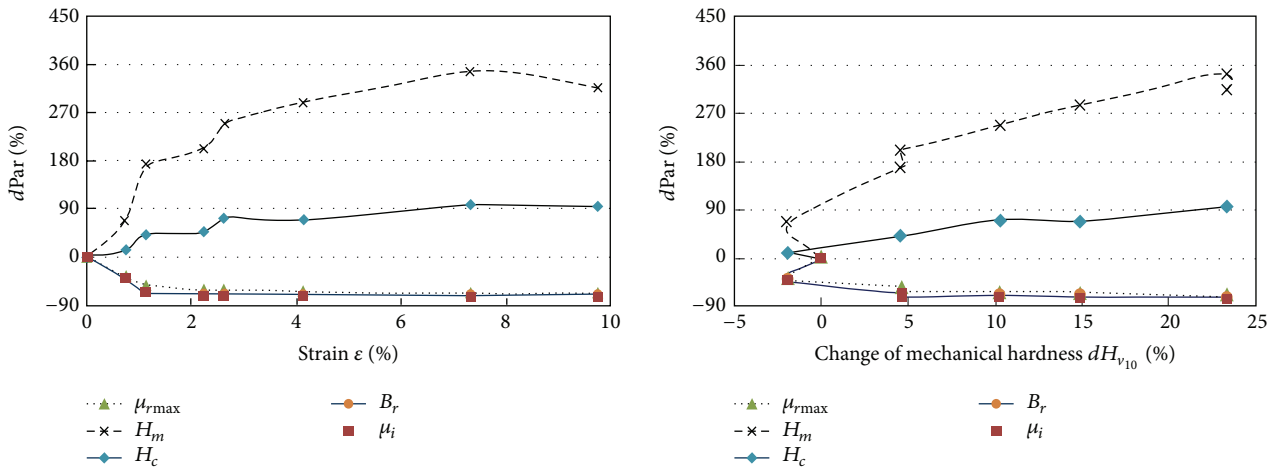

(a)

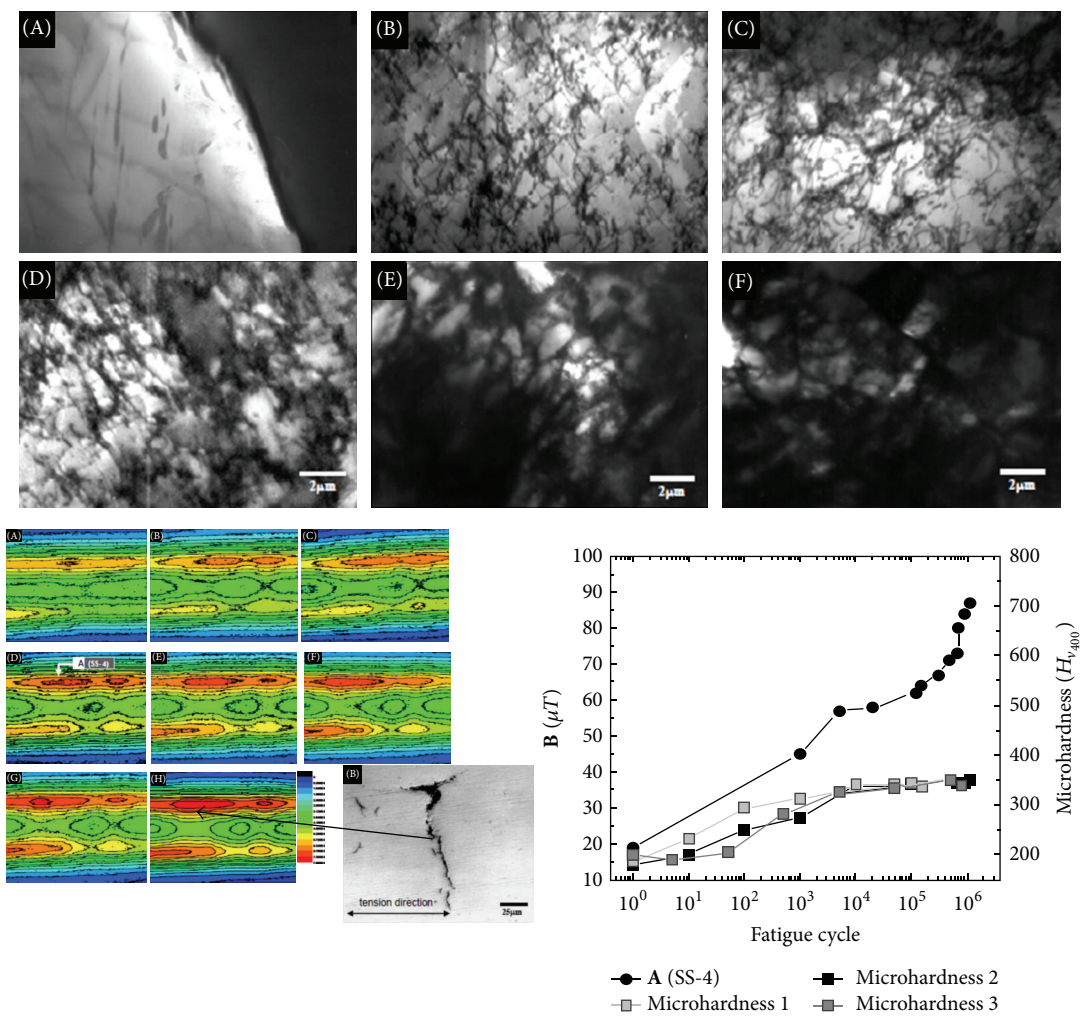

(b)

Figure 12: Showing (a) influence of static strain hardening on magnetic parameters low carbon steel with 0,17% C ($H_m = H(\mu_{r\max})$), $d\text{Par} = (\text{Par}(\varepsilon) - \text{Par}(\varepsilon = 0)/\text{Par}(\varepsilon = 0))$ [73]; (b) influence of HCF on TEM microstructure of fatigue 430 stainless steel (after 0 cycles, 1×10^3 cycles, 1×10^4 cycles, 2×10^4 cycles, 4×10^5 cycles, 5×10^5 cycles) and remanence magnetization map of the steel (after: (A) 0 cycles, (B) 1×10^3 cycles; (C) 5×10^3 cycles; (D) 2×10^4 cycles; (E) $1{,}2 \times 10^5$ cycles; (F) $1{,}45 \times 10^5$ cycles; (G) $2{,}8 \times 10^5$ cycles; (H) $9{,}2 \times 10^4$ cycles. SQUID scanning area 10×20 mm) [74].

parameters (3) but also the state of magnetizing blades, see Figure 12 and relation (7). Changes of material magnetizing, resulting from lattice-spin coupling (L-S) in the atomic scale, distribution of residual stress in the atomic micro- and macroscale, and magnetomechanical effects (reversible and irreversible) in the macroscopic scale, enable the detection of 1st phase of the damage [73–75]:

$$\begin{gathered}\mathbf{M} = \mathbf{M}_i + \mathbf{M}_r = (1 + k_H)(1 + k_\sigma)(1 + k_T)\mathbf{M}_0 \\ H_c \propto \left\{\sqrt{\rho_d}, d^{-1}\right\} \longrightarrow \left\{L_i^{-1}, \sigma_r\right\} \\ B_r, \mu_{r\,\max} \propto \left\{\rho_d^{-1}, d\right\} \\ \mu_i \propto \left\{L_i^2, \sigma_r^{-1}\right\}\end{gathered} \tag{7}$$

with $\mathbf{M}$ being magnetization; $\mathbf{M}_i$ being the induction magnetisation; $\mathbf{M}_r$ being the residual magnetisation; $\mathbf{M}_0$ being initial state of magnetizing the blade; k_H, k_σ, k_T being appropriately influence of external field, stress, and temperature; H_c being the coercive force; B_r being the remanence; $\mu_{r\,\max}$ being the maximum magnetic permeability; μ_i being the initial magnetic permeability; σ_r being the magnitude of unidirectional internal stress which represents the irregularly fluctuating magnetoelastic energy distribution; L_i being the periodic distance between internal stress centre [76].

Magnetic properties of the blades are dependent on the microstructural type, of additions alloy and residual stresses, as well as level of material damage. A report is describing the diagnostic rule (8), which will be developed at the description of method:

$$\begin{aligned}&\text{if } \mathbf{B} \in \langle \mathbf{B}_{\min}, \mathbf{B}_{\max} \rangle, \quad \left|\frac{dB}{dx}\right| < \left|\frac{dB}{dx}\right|_{\max} \\ &\text{then OK} \\ &\text{else Hardening, Erosion, Softening,} \\ &\text{Cracking, Stress Concentration Zone.}\end{aligned} \tag{8}$$

This approach has advantages and disadvantages.

Advantages

(i) Detection of reversible changes of the material fatigue (1st phase of damage).

(ii) Possible of remote observation of magnetizing blades through paramagnetic casing of compressor. It is sufficient to solve service problem—detect fatigue risk before the first blade crack (level I).

(iii) Observation of magnetizing blades during the engine stop (using irreversible magnetomechanical effects), the small rotation speed (from zero rpm), and the engine work on the operation range.

(iv) Possible reliable prognosis and reduce of the risk of wrong diagnosis during engine overhaul and service.

(v) Possible analysis postfactum of damage elements and identification of load condition prevailing during the initiation and the propagation of the crack.

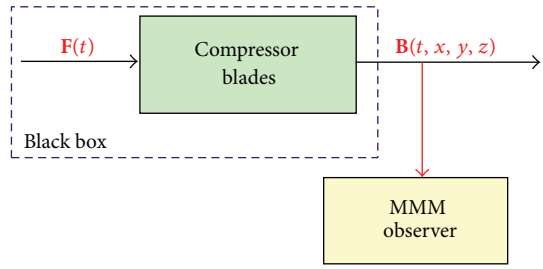

Figure 13: Signal analysis of the blade magnetizing (magnetic induction **B** in the close of the its surface) which the health monitoring and load history of the blade described.

(vi) The solution can be used for diagnosing other ferromagnetic elements of the plane, for example, of bearing, gears, shafts, pressure vessels, and landing gear.

(vii) The method is made available with base knowledge about relations between the material fatigue and stress-strain inducted magnetization and symptoms using by the experimental modal analysis and the tip timing methods.

Disadvantages

(i) Strong nonlinear rules describing the magnetization of the ferromagnetic parts, particularly in the weak magnetic field.

(ii) The approach requires the selection of a new sensitive observers (measurement technics and analysis methods) as well as recongnition and verification of new diagnostic symptoms.

(iii) Only for ferromagnetic materials and some paramagnetic steel.

4. SHM and NDE Methods

Magnetic and magnetomechanical properties of ferromagnetic blades are changing their mechanical and modal properties. The state of magnetizing blades also affects the tip timing signal (when there is an induction, vary reluctance or eddy current sensor is used to detect moving blades). The theory and experience of experimental modal analysis are an input to the tip timing method. For paramagnetic blades which material is not showing of phase transformation under the influence of stresses, the first method (Metal Magnetic Memory method) is not applicable.

4.1. The Metal Magnetic Memory Method. The MMM method (only NDE method according to ISO 24497:1-3 (2007)) is based on three pillars:

(i) magnetomechanical effects existing in ferro-magnetic material being located in a weak magnetic field of the Earth which was described by theory of the micromagnetism [76–88];

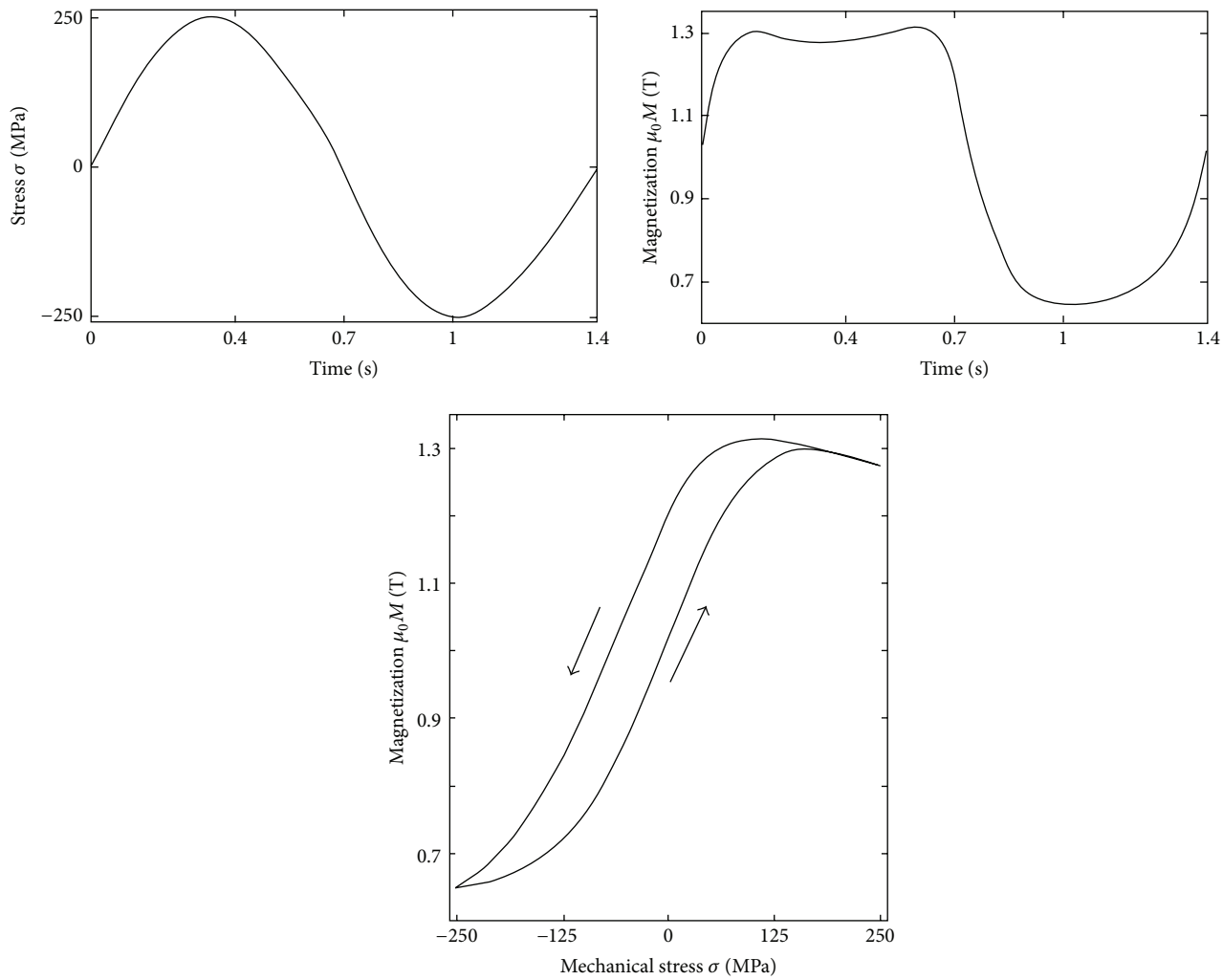

Figure 14: Stress inducted magnetization in low carbon steel ($R_e = 390$ MPa, stress level below yield strength, static magnetic field $H = 800$ A/m) [76].

(ii) magnetovision: the remote passive observation magnetic field near the testing element;

(iii) magnetostatic: solving the opposite issue of magnetostatic in the destination of the magnetizing trend from magnetic anomaly (symptom of defects, stress concentration zone, and change of element shape).

The MMM method is a typical passive observer of *the signal analysis* which is possible to apply both to NDE and SHM applications. Signal analysis is the process of determining the response of a system, due to some generally unknown excitation, and of presenting it in a manner which is easy to interpret (Figure 13).

In the macroscopic scale a constitutive law (9) is copying magnetic properties of the blade:

$$\mathbf{B} = \mu\mathbf{H} = \mu_0 (\mathbf{H} + \mathbf{M}) \tag{9}$$

with μ_0 being magnetic permeability of vacuum (in SI units system $\mu_0 = 4\pi \cdot 10^{-7}$ H/m); $\mathbf{M}$ being material magnetization [A/m], $\mathbf{H}$ being external magnetic field [A/m], and $\mathbf{B}$ being magnetic induction (magnetic flux density) [T].

4.1.1. Reversible Magnetomechanical Effects. Apart from the constitutive law $\mathbf{B}(\mathbf{H})$ or $\mathbf{M}(\mathbf{H})$, there is a second class of macroscopic observations that needs to be introduced. It is observed that when a ferromagnetic specimen is subjected to a magnetic field, its magnetization as well as its length change—Joule effect, which is described by tensor rule (10). When a ferromagnetic specimen is subjected to a mechanical stress, both it is length as well as it is magnetization change—Villari effect, which is described by tensor rule (11) and depicted in Figure 14. The actual distribution of material magnetization (molecular currents in the material) can be observed indirectly by measuring the magnetic field distribution in the nearby the object.

$$\varepsilon_{ij} = s_{ijkl}^{HT}\sigma_{kl} + d_{ijn}H_n, \tag{10}$$

$$B_m = d_{mij}^{*}\sigma_{ij} + \mu_{mn}^{T\sigma}H_n, \tag{11}$$

where $d = \partial\varepsilon/\partial H|_{\sigma}$ and $d^{*} = \partial B/\partial\sigma|_{H}$ are magnetomechanical coefficients which are appointed experimentally for

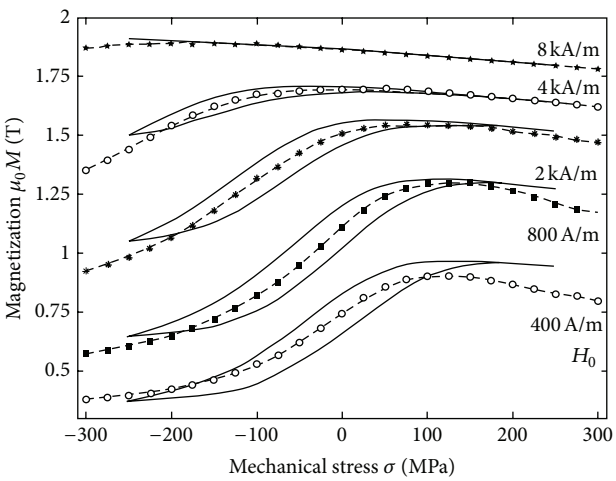

Figure 15: Experimentally obtained magnetomechanical hysteresis loop $M(\sigma(t))$ for different setting of external DC magnetic field H_0 (full lines) and compared to the reversible anhysteretic magnetomechanical behaviour at corresponding setting of H_0 (dashed line with symbols). Material: low carbon steel with 0,12% C [76].

given material at the constant tensile (stresses) σ or constant magnetic field H [75].

In (10) and (11) an influence of the change of material temperature and losses of the internal energy were omitted. Equations are describing only "reversible magnetomechanical effects."

Zones RSC of local residual stress concentration, plastic, material anisotropy (mechanical and magnetic) and dislocation concentration are potential place of cracking nucleation and local magnetic anomaly [4, 72, 76–79]. Influence of the local plastic strain of material (LCF, HCF and VHCF problems—Table 2) the best is visible in the weak magnetic field [80]. "The passive magnetic observer of the blade health monitoring (e.g., the metal magnetic memory method) is favoured."

4.1.2. Magnetomechanical Damping. Applying a stress to a ferromagnetic blade causes a variation of magnetization due to the magnetoelastic coupling, which results in the so-called "ΔE effect" and also in a related dissipation of mechanical energy during loading/unloading or in case of vibration. The latter effect can give rise to a strong magnetomechanical damping with stress-dependent and stress-independent components [81].

Experiments show that ferromagnetic materials have a higher internal friction than the paramagnetic and diamagnetic because of phenomena of an electromagnetic nature resulting from the application of elastic fields. Considering five main contributions to the total energy of a ferromagnetic material without an external field (exchange energy W_{ex}, magnetocrystalline anisotropy energy W_k, magnetoelastic (or magnetostrictive) energy W_λ, magnetostatic energy W_m, and energy of magnetic domain walls W_w), four main mechanisms of magnetomechanical damping may be defined:

(i) magnetoelastic hysteresis damping Q_h^{-1},

(ii) macroeddy-current damping Q_a^{-1},

(iii) microeddy-current damping Q_u^{-1},

(iv) damping at magnetic transformation Q_{PhT}^{-1}.

Therefore, the total magnetomechanical damping Q_m^{-1} in ferromagnetic blade can be considered as sum of these components:

$$Q_m^{-1}(\varepsilon,\omega,T) = Q_h^{-1}(\varepsilon,\omega,T) + Q_a^{-1}(\omega,T) + Q_\mu^{-1}(\omega,T) + Q_{PhT}^{-1} \quad (12)$$

contrary to Q_a^{-1} and Q_u^{-1}, the hysteretic contribution Q_h^{-1} depends on the strain amplitude. The damping Q_m^{-1} is also dependent on the load frequency ω, material temperature, and initial conditions (micro- and macrostructure, magnetization, and residual stress). "The Q_m^{-1} is nonlinear."

4.1.3. Irreversible Magnetomechanical Effects. Losses of the internal energy are being observed in the weak DC magnetic field in the form of

(i) the magnetization hysteresis loop (Figure 15);

(ii) growing magnetizing material under the influence of the cyclical load (LCF an HCF fatigue) [82]. Observed change of magnetizing material depends on the level of stresses and the number of cycles;

(iii) change of magnetizing material after unloaded ("the metal magnetic memory" or "the first loading/unloading effect") [77, 83]. The ferromagnetic blade has feature of the strain gauge with the memory of the maximum load.

4.1.4. Measuring Equipment. Potential possibilities of the MMM method were tested in active and passive experiments, which used a compass (simple magnetometer), GM-04 Magnaflux magnetometer with Hall sensor [89], 3D MEMS anisotropic magnetoresistive sensor (HMC 5843 Honeywell demo board) [90], and Energodiagnostika TSC-1 M-4 recorder with multichannel transduction sensors (scanning devices) [91]. The Earth's magnetic field ($B_E \cong 50\,\mu$T) and electromagnetic noise are natural source of the external magnetic field.

4.2. The Experimental Modal Analysis Method. Experimental modal analysis (a tool of structural analysis) is an effective aid in solving blades' fatigue problems. It allows finding an answer to the question: "Why does a blade crack?", not only: "Is it cracked?". The modal parameters of all the analysis modes (within the frequency range of interest) constitute a complete dynamic description of the blade structure [3, 17–21]:

(i) material,

(ii) geometry,

(iii) the influence of surface treatment and adding protection coating,

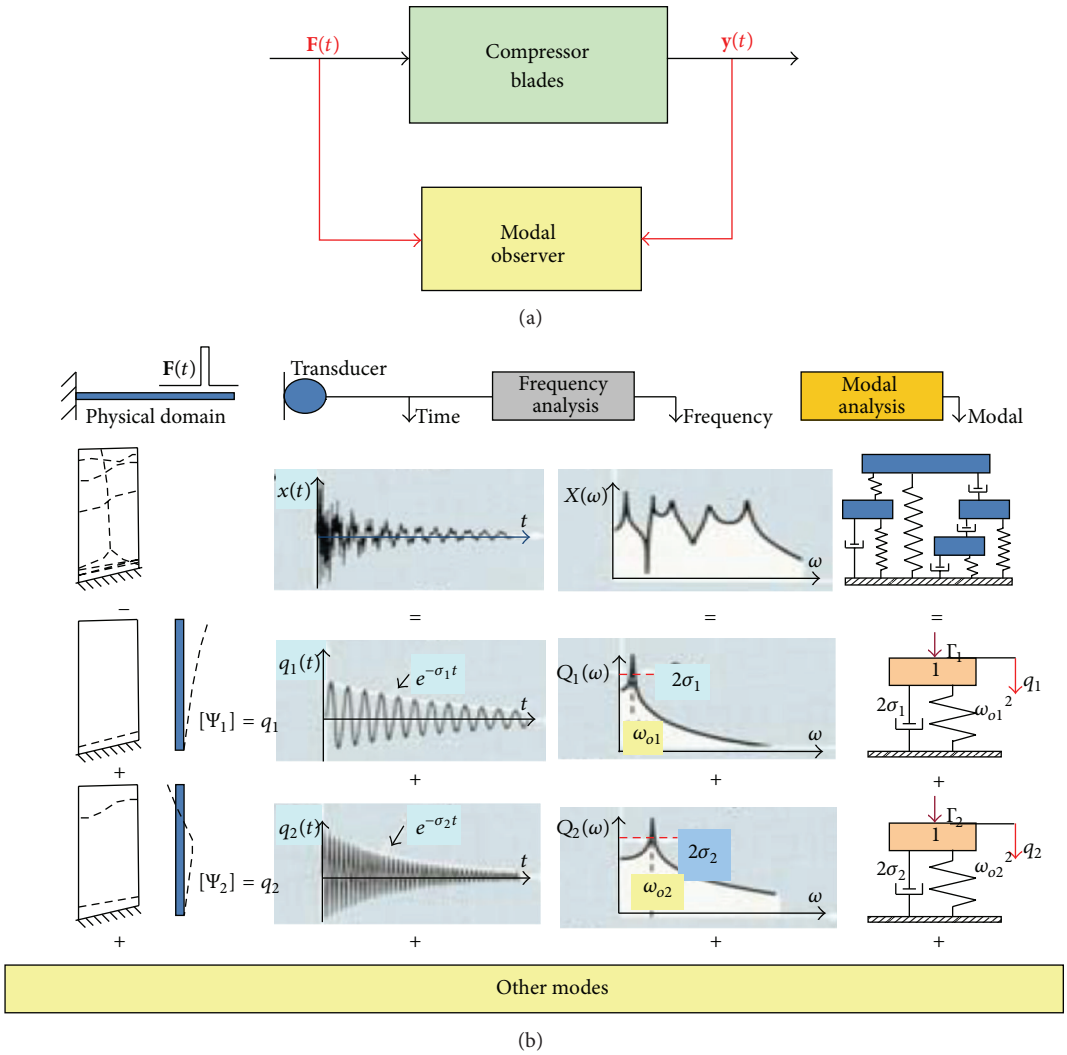

Figure 16: Blade health and mechanical properties analysis using the experimental modal analysis.

(iv) technical health (structural heterogeneity, crack, and fatigue).

The characteristic feature of blade vibration measurement on a modal excitation system is knowledge of both a force level and a blade response on it (Figure 16(a)). This can be done by stimulating the system with *measurable force* and studying *the response/force ratio*. For linear system this ratio is an independent, inherent property which remains the same whether the system is excited or at rest. That is why it is possible to identify blade modal properties for following modes.

Structural response of the compressor blade (*a lightly damped structure*) can be represented in different domains. The modal description relates to descriptions in the spatial, time, and frequency domain (Figure 16(b)).

In the illustration, each column shows the response of the blade after short struck represented in different domains.

Physical domain: the complex geometrical deflection pattern of the blade can be represented by a set of simpler, independent deflection patterns, or mode shapes.

Time domain: the vibration response of the blade is shown as a time history, which can be represented by a set of a decaying sinusoids.

Frequency domain: analysis of the time signal gives us a spectrum containing a series of peaks, shown below as a set of SDOF (single-degree-of freedom) response spectra.

Modal domain: we see the response of the blade as modal model constructed from a set of SDOF models. Since a mode shape is pattern of movement for all the points on the structure at a modal frequency, a single model coordinate q can be used to represent the entire movement contribution of each mode. The SDOF model is associated with a *frequency*, a *clamping*, and a *mode shape*. An important property of modes is that any forced or free dynamics response of structure can be reduced to a discrete set of modes. The modal parameters are as follows:

(i) modal frequency;

(ii) modal damping;

(iii) mode shape.

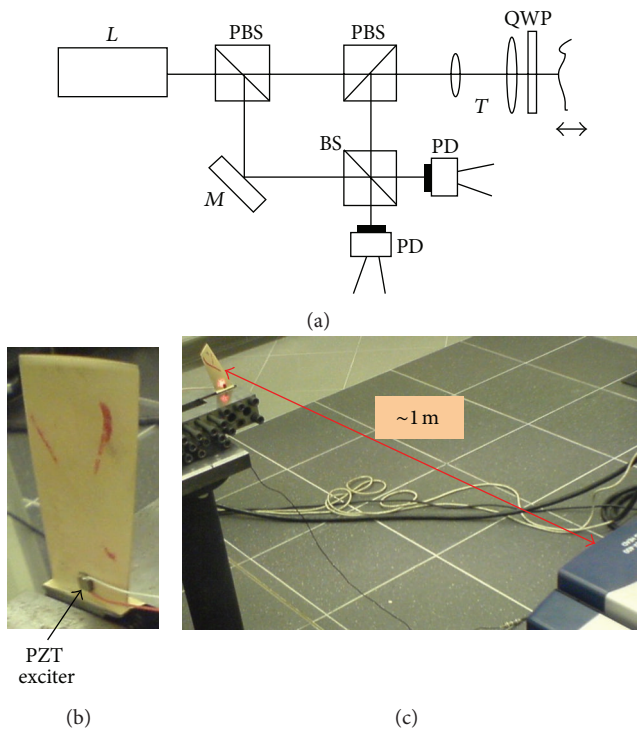

Figure 17: Experimental stand for the broadband (up to 20 kHz) modal identification of the compressor blade with the use of scanning laser vibrometer and PZT exciter.

4.2.1. Measuring Equipment. The broadband identification (up to 20 kHz) of modal properties of a compressor blade, made of 18H2N4WA steel and Ti5.8Al-3.7Mo titanium alloy, has been made on the PSV-400 Polytec scanning vibrometer [92] and low power PZT exciter (Figure 17).

This approach has advantages and disadvantages.

Advantages

(i) Automation of the measurement;

(ii) Mode frequency and node lines are very precisely identified;

(iii) Weak clamping of blade is possible;

(iv) Input data to numerical modeling of modal and fatigue properties;

(v) Vibration frequency up to 20 MHz and vibration velocities up to 20 m/s;

(vi) Scan area (±20° about X, Y) and grid definition;

(vii) High speed (>50 points/s) and resolution (<nm, 0.002°);

(viii) High angular stability (<0.01°/h).

Disadvantages

(i) High cost and weight measurement equipment (7,5 kg);

(ii) The small vibration amplitude is not opening the crack.

Table 3: Potential field of tip timing method use.

Object	Transmitter of putting the angle turnover
Wind turbine	Blade
Helicopter	Main rotor blade Tail rotor blade
Propeller aircraft	Propeller blade
Power turbine	Turbine blade
Jet engine	Compressor blade Turbine blade
Turboprop	Compressor blade Turbine blade
ABS systems, gearbox	Gear wheel
engine control unit	Gear wheel
bearings	Rolling element

The identification of early fatigue and cracking symptoms of these blades has been made on the Brül & Kjær electrodynamic exciter 4802T [93]. The experimental stand (Figure 18), used during the SO-3 and TW3-117 engine overhauls, included the following:

(i) the MTI Instrument laser measurement system MicroTrack II with CMOS measurement head LTC-120-40 [94];

(ii) the Vibration Research Corporation VR-8500 controller that includes 24 bit A/D and D/A converters, and RISC processor [95];

(iii) the Vibration Research Corporation Vibration View software to control the exciter, data acquisition, and analysis [96].

The sensitivity of measurement system is 100 mV/mm.

This approach has advantages and disadvantages.

Advantages

(i) Load up to 60 g (a = 588 m/s^2)—LCF & HCF test is possible;

(ii) Low cost of laser head;

(iii) Frequency response: 20 kHz max (laser) and 4 kHz max (exciter);

(iv) Resolution at 20 kHz filter: ±5 μm;

(v) Filter setting: 20 kHz–0.1 Hz;

(vi) High temperature stability (0.005%/K) and linearity (0.05% FSR or better).

Disadvantages

(i) Single point measurement;

(ii) Great demand of the electric power.

4.3. The Tip Timing Method. The tip timing idea consists in observing displacement of loaded component part, Table 3, with "irregular sampling" (one time to the turnover of the rotor). In our case, it will be a rotating and vibrating compressor blades. Blade vibration and deflection are a source of a time-interval change between flexible key phases.

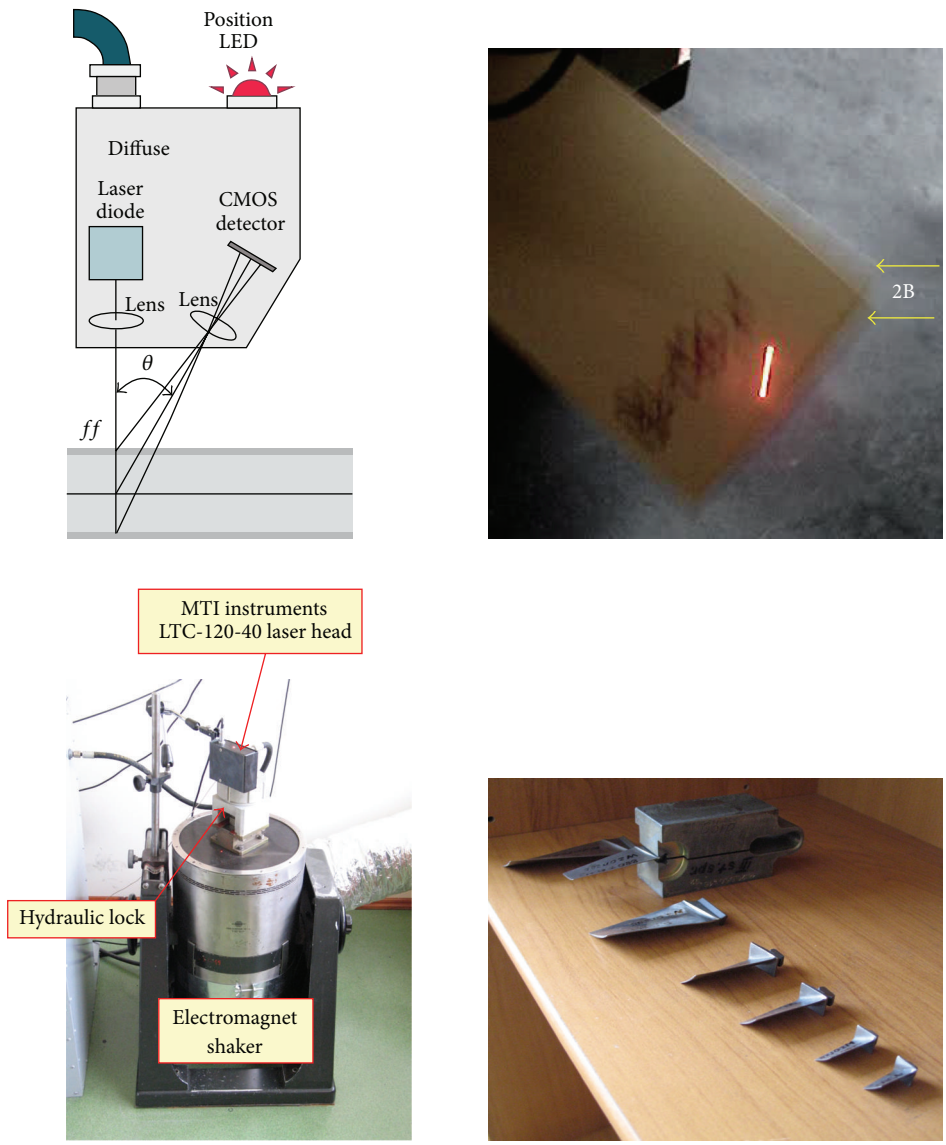

Figure 18: Workstation for the low-frequency (up to 4 kHz) modal identification of the compressor blades.

The tip timing observer (sensor) is built onto a fixed part of compressor. Its analog signal depends on the sensor type (Figure 19). Time period signal (time of blade arrival, TOA) would be measured with a frequency method or delay line (time-to digital converter) [3, 25, 96, 97].

Measured signal TOA(k) is discreet representatives of the continuous signal $S(t)$ which contains the following:

(i) aperiodic part $A(t)$—average instantaneous rotational speed of perfect stiff rotor;

(ii) oscillating part $P(t)$—resultant from pitch errors, blade, rotor and disk vibration, and instantaneous rotational speed perturbations (from the engine control system, flow, g-force, clearance in a kinematic system, and torsional vibration);

(iii) noise and weak oscillating components $I(t)$.

Signal S is described by the following relation:

$$S(t) = A(t) + P(t) + I(t) \tag{13}$$

so it is possible to design a general-purpose observer for *real operating conditions* of rotating parts and have a complex view on the following:

(i) disadvantageous dynamic phenomena (flutter, stall, surge, resonance, and load coupling);

(ii) the influence of production, overhaul, and maintenance real conditions on the level of malfunctioning and fatigue prognosis.

Every component of $S(t)$ is used to diagnose. An oscillating part $P(t)$ is a main carrier of diagnostic information about blades damage and danger dynamics phenomena. Aperiodic part $A(t)$ and part $I(t)$ give the capability to compare new diagnostic symptoms to the health of machinery.

Signal TOA(k)—a number of pulses Code$_i$ with clock frequency counting between key phases (blades)—includes

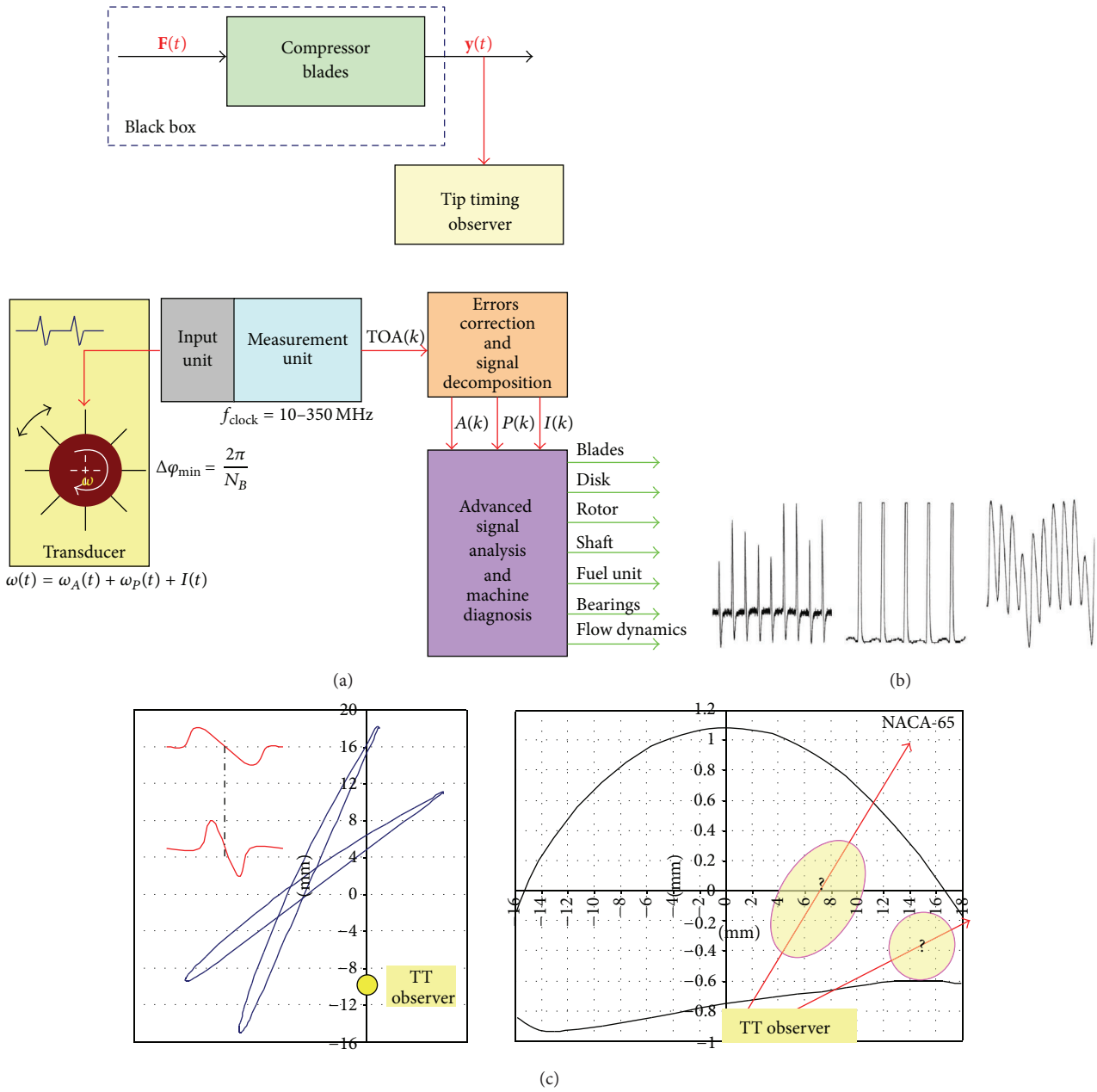

Figure 19: Showing (a) an idea and a block structure of the tip timing method; (b) a shape of analog signal for vary reluctance (VR), optical and eddy current (EC) sensor. Signal with VR and EC sensors also contains information about magnetizing blades; (c) main problem of VR and EC sensors—precise relation of the analog signal with putting the top of the blade with regard to the sensor (Where is the blade? Which point of the blade top is in the relation with the characteristic point of the analog signal?) [25].

"three groups of variables" (14) to be identified in effect of further numerical signal analysis

$$\begin{aligned} \mathrm{TOA}(k) &= \mathrm{Code}_i = K_{i,i+1}\mathrm{Trunc}\left(\frac{t_{i,i+1}}{t_{\mathrm{clock}}}\right) \\ &= \left(\frac{1+\zeta_B}{1+\zeta_\omega}\mathrm{TOA}_{\mathrm{avg}}\right)_{i,i+1}, \quad i \in \langle 1, 2, \ldots, N_B \rangle, \\ \mathrm{TOA}_{\mathrm{avg}} &= \frac{2\pi/N_B}{\omega} \end{aligned} \tag{14}$$

with k being discrete time, $K_{i,i+1}$ the error and disturbance factor ($K_{i,i+1} = 1$ for data without error), N_B the number of blades, $t_{i,i+1}$ the time interval between two blade passes (with momentary pitch), t_{clock} the time period of generator pulses (with model of the time), $\mathrm{TOA}_{\mathrm{avg}}$ the average momentary time of arrival of the perfect rotor and the blade palisade (without influence of rotor unbalance and vibration and blade pitch errors), ζ_B the jitter of blades group components, ζ_ω the jitter of rotor group components, and ω the angular velocity of ideal rotor.

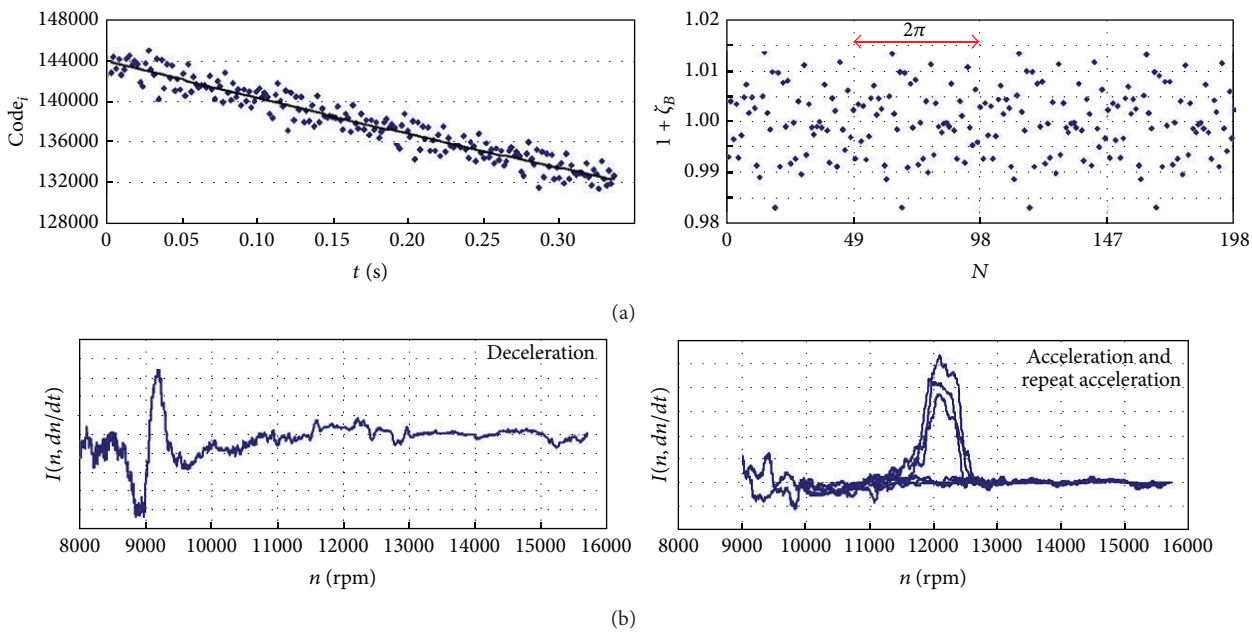

Figure 20: Result of the DETREND procedure for TOA(k) signal measured for (a) the last stage of SO-3 engine compressor (49 blades in the palisade)—the pitch errors are dominating in the jitter ζ_B; (b) the first stage of SO-3 engine compressor—the component $I(k) = I(n, dn/dt)$ is revealing the influence of some asynchronous parts of jitter ζ_ω on the component $A(k)$ (e.g., rotor vibration, fluctuation in the rotational speed on the compressor limits) [3].

The jitter of blade group components includes

ζ_P: pitch errors (N_B of aperiodic variables);

ζ_{Bi}: vibration of i the blade (N_B of independent multimodal generators);

ζ_C: compressor case vibration;

ζ_{DP}: dynamic phenomena of TTM sensor

so it is described by the following relation:

$$\zeta_B(k) = \zeta_P(k) + \zeta_{Bi}(k) + \zeta_K(k) + \zeta_{\mathrm{DP}}(k). \quad (15)$$

The jitter of rotor group components includes

ζ_F: influence of control unit and changes of the momentary rotation speed;

ζ_R: transverse and torsional vibration of rotor;

ζ_E: alignment error (eccentricity)

ζ_A: alignment error (misalignment),

so it is described by the following relation:

$$\zeta_\omega(k) = \zeta_F(k) + \zeta_R(k) + \zeta_E(k) + \zeta_A(k). \quad (16)$$

The jitter ζ_ω is a source of FM modulation which is mainly problem of TOA(k) signal disintegration (to components A, P, and I after signal verification and numerical correction) and analysis of the blades health and vibration. Signal components of TOA(k) are obtained with the DETREND procedure (Figure 20).

The scope of interest of numerical data processing includes [3, 25–33]

(i) vibration level of all blades at the same time,

(ii) disadvantageous dynamic phenomena,

(iii) blade stress and health,

(iv) disk health,

(v) engine health (the engine fuel system and the bearing system).

Signal subcomponents are obtained with the narrow-band filtering, AM/FM demodulation and spectrum analysis (e.g., CORDIC, DFT and DASP algorithms are used). Blade vibrations are shown in the form of phase distributions as points of phase trajectory crossing the phase plane [25, 55] (Figure 21).

A main characteristic feature of the tip timing method is information that lasts about a total number of modal frequency periods between two subsequent points of phase trajectory crossing the phase plane, with basic modal parameters of the blades preserved. This phenomenon enables detection of the LCF and HCF crack initiation and propagation in the blade during the engine operation. Other characteristic features of the TTM are the following.

(i) Irregular signal sampling rate: the Nyquist-Landau law describes discrete-time information.

(ii) Periodic measurement data structure: data can be illustrated with matrix with N_B columns (number of blades) and rows that represent each full 360 degrees cycle of a rotor.

(iii) The inherent in a signal oscillating parts that are not connected with blade vibration: there are two groups of oscillating parts of a signal: synchronized and nonsynchronized with rotor rotational frequency.

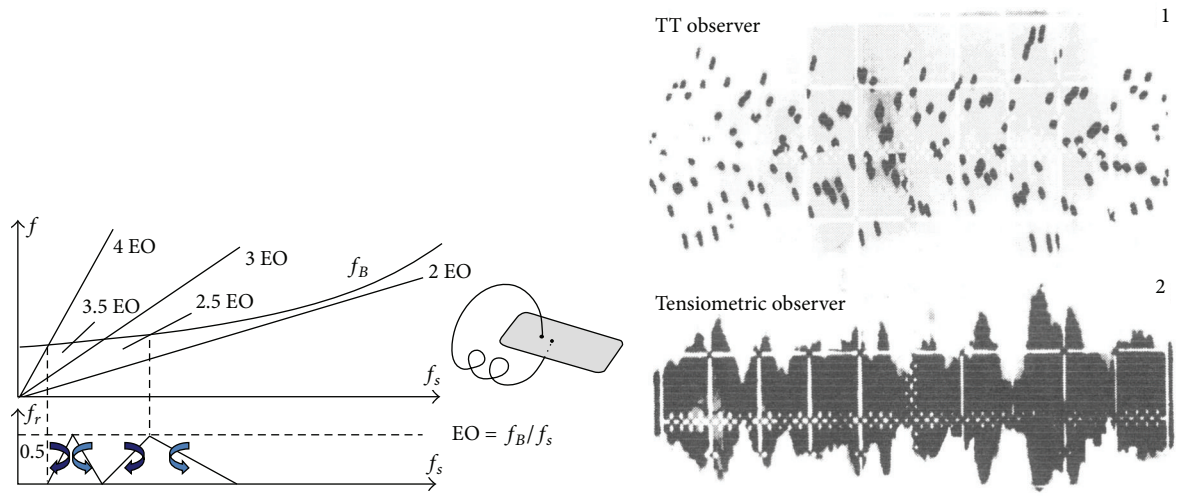

(a) (b)

Figure 21: Relation between vibration of the blade top (the TT observer, $f_{\text{sampling}} \cong f_{\text{rotor}} \pm \Delta f_{\text{jitter}}$) and stresses at the base of the one (the strain gauge observer, f_{sampling}=4 kHz). Three first modal frequencies of the blade: 350 Hz, 1380 Hz, and 1890 Hz, max. rotational frequency of the rotor $f_{\text{rotor,max}}$ = 260 Hz [55].

4.3.1. The SNDŁ-1b/SPŁ-2b System. In 1993, a diagnostic system was developed and introduced into the service on the TS-11 "Iskra" trainer. The system is based on results of the active and passive tests. It consists of [62] the following.

(i) *The blade excessive vibration warning device SNDŁ-1b*: a two-channel analogue phase detector that warns a pilot of conditions that can induce accelerated HCF of blades, for example, deposition of foreign matter such as ice, bird, or other resonance-based phenomena.

(ii) *The ground-based inspection instrument SPŁ-2b (digital phase detector, f_{clock} = 10 MHz) for*

(a) periodic recording of blade vibration,

(b) inspections of the SNDŁ-1b health, with no need to have it disassembled,

(c) detection of errors of the engine rotational-speed indicators (in cabins I and II), with no need to disassemble them.

(iii) *The SPŁ-2b software*: a set of programs that form the nucleus of the advisory/expert system used to diagnose the SO-3 engine. The software comprises

(a) *the database with text data*: that is, a verified set of information on the object under examination and technical specifications of operating/monitoring it;

(b) *the database containing measuring data*: more than 7000 records on the Polish population of the SO-3 engines, collected during more than 20 years, taken at OAT = 248 to 308 K (−25 to +35°C), p_A = 959,9 to 1026,6 hPa (720 to 770 mm Hg), and humidity of 20 to 100%; also, the SO-3 overhaul-delivered data (collected during 15 years), including, among other things, information on frequency spacing of blades in the blade ring. The base also includes hidden software usage files (*logs*). They are made automatically without user knowledge. They are the base to valuate diagnostics system usage correctness;

(c) *the database containing numerical models*: compressor blades, the fuel system, and the rotor bearing system. The models are also used to identify how errors made during manufacturing, operation, and repairs/overhauls can affect the engine operational safety. Another application can be the postfactum analyses of air accidents;

(d) *the database with diagnostic rules*: contains the algorithms used to interpret measuring results and bringing diagnosis of the first-stage compressor blades and the transmission, as well as the expert diagnostic of a fuel system. The diagnostic rules also facilitate automatic identification and verification of the source of measurement data (the engine type and the serial number thereof) and software-based synchronisation of taking subsequent records. The database comprises also procedures of identification and correction of measurement errors and procedures of identification of errors in the operational use of the diagnostic system.

5. Research Results

Chosen findings were obtained during active and passive experiments.

5.1. The Metal Magnetic Memory Method. Very good relation has been observed between the MMM results and blade

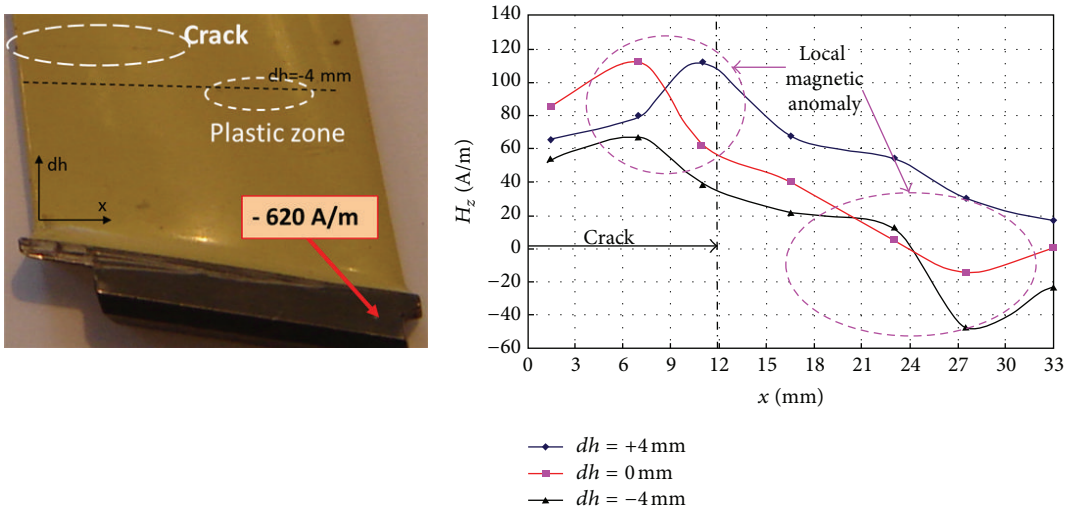

(a) (b)

Figure 22: MMM symptoms of cracked blade after HCF test [3, 22].

node lines after LCF tests [3]. Local magnetic anomaly has been also observed near the close crack gap after HCF tests (Figure 22). The MMM method is widening the possibility of the blade verification by the RSC detection before the appearance of the endurance fracture (Figure 23). Nevertheless, the most interesting phenomenon is nondestructive detect of blade erosion and stress prehistory (a change of residual magnetization) after the engine stopped (Figure 24). Based on previous research and theoretical evidence does not rule out the possibility of diagnosing VHCF problems by MMM method. During measurements of the state of blades magnetizing through the compressor casing new symptoms was demonstrated for the tip timing method (Figure 25).

5.2. The Experimental Modal Analysis Method. Experiments have been performed in five stages in which

(i) the measurement method has been verified,

(ii) blade modal properties have been identified,

(iii) blade cracking symptoms have been identified,

(iv) early symptoms of fatigue have been identified,

(v) new diagnostic symptoms have been verified for titanium blade.

5.2.1. Identification of the Modal Properties. It was proven that PZT exciter and Polytec scanning vibrometer could be used for the modal identification of compressor blades. Measuring collected data is a verified knowledge used for tuning the FEM model up (Figure 26).

It has been also proven that used simple measurement technique (MTI laser head and sine test) guarantees reliable modal results when vibration amplitude is higher than 2 μm. Reliable resonance curve shape during sine test has been obtained for force frequency: 2.5 Hz/min for 1st flexible mode (1F, $Q_s > 350$) and 1.0 Hz/min for 1st torsion mode (1T, $Q_s > 1000$). Such a stand gives an ability to make precise measurements with an exact test profile and frequency step. The measurement system gives almost laboratory accuracy. That's why it let [23]:

(i) precise identification of blade modal properties in measured frequency range;

(ii) metrological factors influence analysis on recorded resonance characteristics;

(iii) modal parameters trends analysis be observed during fatigue tests.

Hereinafter of point 5, results will be presented from sine test. To analyze data we can use operator transmittance described by the following relation

$$G(\omega) = \frac{Y(\omega)}{X(\omega)} \left[\frac{m}{m}\right] \tag{17}$$

with $X(\omega)$ being the magnitude of the exciter head displacement; $Y(\omega)$ being the magnitude of the blade point displacement; ω being angular frequency of cyclic load.

5.2.2. Modal Properties of a Defect-Free Blade (Noncracked). In the case of a defect-free blade (health) resonance characteristics of particular modes were gained, ones that could be well described with a model of a single-degree-of-freedom linear system (SDOF)—of mass m suspended on a spring with spring rate K and viscous damping C [17–19, 23]. For sine test SDOF model describes the following relation:

$$\begin{gathered} m\frac{d^2 y(t)}{dt^2} + C\frac{dy(t)}{dt} + Ky(t) = F(t), \\ F(t) = A(\omega)\sin(\omega t), \\ y(t) = B(\omega)\sin(\omega t + \varphi(\omega)). \end{gathered} \tag{18}$$

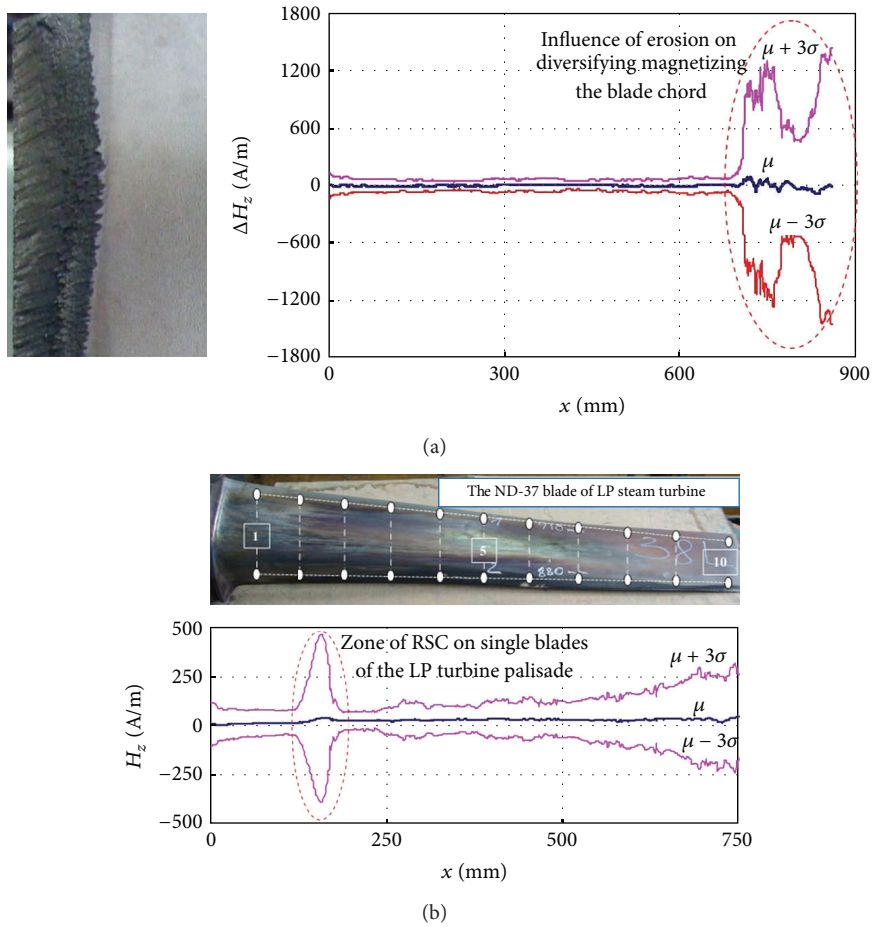

Figure 23: Early detection of the hidden fatigue risk (blade overload and diversifying the income of erosion) on the example of the ND37 blades of the steam turbine [3].

Characteristics of subsequent modes remain continuous under resonance conditions and exhibit good symmetry around the resonance frequency (within the bandwidth of 3 dB) (Figure 27) (left side). The blade displacement at the measuring point can be described as follows

(i) vibration amplitude

$$b(\omega) = \frac{y_{st}}{\sqrt{\left[1-(\omega/\omega_o)^2\right]^2 + \left((\delta/\pi)(\omega/\omega_o)\right)^2}}, \quad (19)$$

(ii) vibration phase angle

$$\varphi(\omega) = \arctan\left(\frac{(\delta/\pi)(\omega/\omega_o)}{1-(\omega/\omega_o)^2}\right), \quad (20)$$

where ω_0 is a free vibration frequency, δ is a logarithmic damping decrement.

5.2.3. Diagnostic Symptoms of a Cracked Blade. When analyzing resonance curve shape we can observe how different it is for cracked blade. The blade has all nonlinear properties [17, 21, 23] which describe a nonlinear 2DOF model (Figure 27) (right side).

Close to the resonance frequency it is possible to observe two branches of characteristics: resonance attractor, S_r (red line) and nonresonance attractor, S_n (blue line) and jumps between them. The shape of a crackedblade's resonant curve is affected by the blade's material and conditions existing on the edge of the crack gap (weakening or hardening, friction). The characteristic curve is sloped to the left (towards lower frequencies) for the crack with material weakening. On the other hand, for the gap with material hardening, the curve is sloped to the right (towards higher frequencies) (Figure 28). The knowledge of resonant curve inclination is essential for correct interpretation of measurements, including correct identification of the resonant and nonresonant branches. During one-sided test we observe "asymmetry" resonance curve with seeming quality factor being decreased. Resonance frequency and characteristics are functions of a blade amplitude. They were not asymmetry symptom for the following.

(i) Small loads that do not develop an open crack: asymmetry is growing with a load increase.

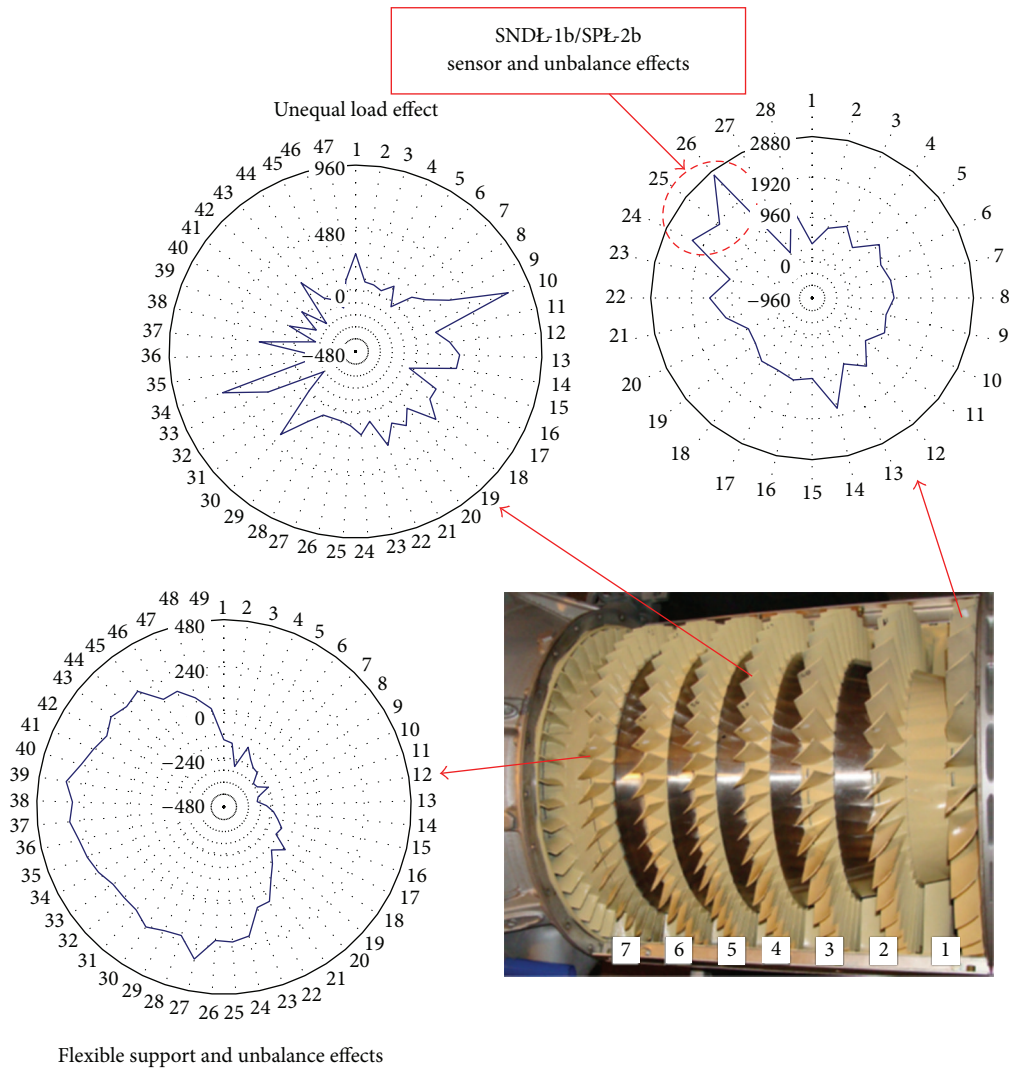

Figure 24: Detection of stress prehistory (irreversible process of stress magnetization) and identification of blade fatigue risk [3, 22].

Table 4: Blade with 11 mm length damage (starting from TE) placed 20 mm from lock [23, 25].

Blade	Frequency change (Hz)		
	1st mode	2nd mode	3rd mode
Cracked	−12	+7	−27
Notched (no friction)	−13	−5	−80
Difference (%)	**−0.28**	**−0.86**	**−2.73**

(ii) A notch on a blade, which was used as a simplified crack model (no friction at a notch hole): no friction in notch modeled blade is a source of other differences in modal properties, Table 4, and fatigue (JCF phenomena).

The obtained characteristics of the cracked blade cannot be described with an SDOF linear model. The blade crack forms a two-degrees-of-freedom (2DOF) nonlinear system for any form of blade vibration. The equivalent linear equation that satisfies the nonlinear equation with accuracy ε takes the following form:

$$\frac{d^2 y}{dt^2} + 2h_\varepsilon(b)\frac{dy}{dt} + \alpha_\varepsilon^2(b)\, y = \varepsilon p \cos(\omega t), \tag{21}$$

where ε is small parameter, p is amplitude of the exciting force, b the steady-state vibration amplitude, $\alpha_\varepsilon(b)$ the equivalent natural (free-vibration) frequency, and $h_\varepsilon(b)$ the equivalent elementary damping coefficient.

The measured and analyzed parameters of the blade are described with the following relationships:

(i) vibration amplitude

$$b(\omega) = \frac{\varepsilon p}{\sqrt{\left(\alpha_\varepsilon^2(b) - \omega^2\right)^2 + 4h_\varepsilon^2(b)\,\omega^2}}, \tag{22}$$

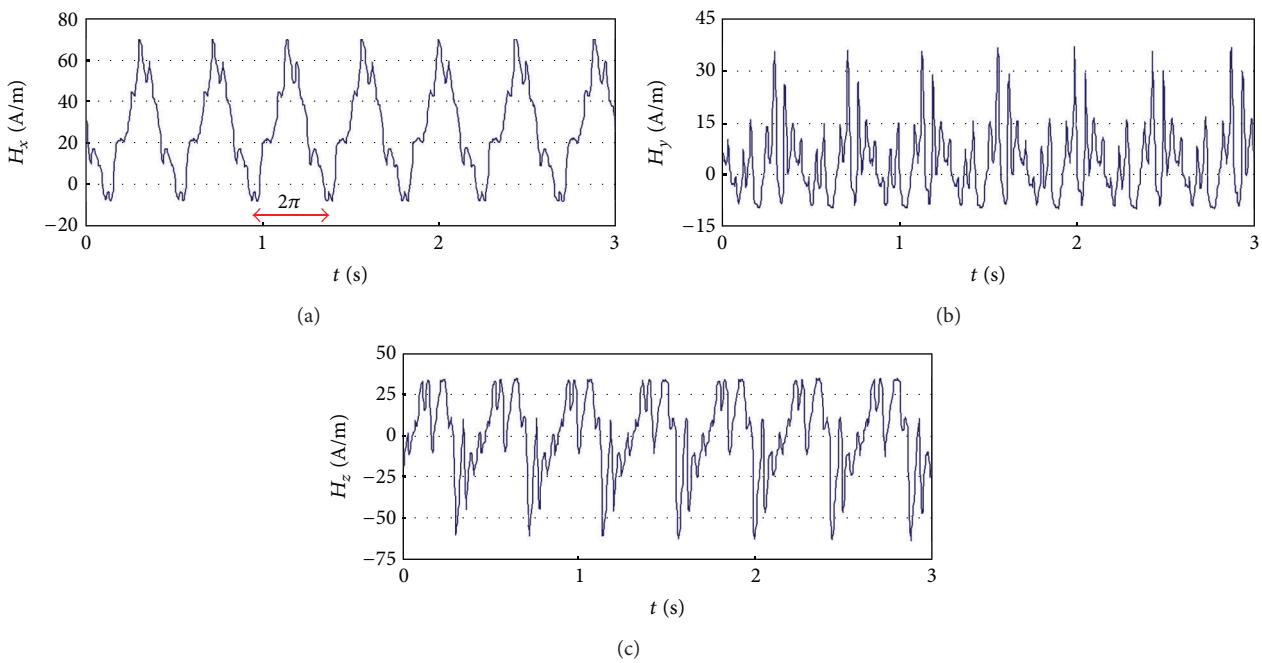

Figure 25: Components of the magnetic field measured on the suface of compressor casing (H_x: along the pivot of the engine, H_y: tangensial to the casing, and H_z: normal to the surface) [3].

(ii) resonance frequency

$$\omega = \sqrt{\left(\alpha_\varepsilon^2(b) - 2h_\varepsilon^2(b)\right) \pm d},$$
$$d = \sqrt{4h_\varepsilon^2(b)\left(h_\varepsilon^2(b) - \alpha_\varepsilon^2(b)\right) + \left(\frac{\varepsilon p}{b}\right)^2}, \tag{23}$$

(iii) vibration phase angle

$$\varphi(\omega) = \arctan\left[\frac{-2h_\varepsilon(b)\,\omega}{\alpha_\varepsilon^2(b) - \omega^2}\right]. \tag{24}$$

5.2.4. Early Fatigue Identification. The LCF and HCF data analysis showed that blade modal properties could be used to observe the material strengthening phase [23]. Increase in the 1st mode resonance frequency of approximately 0.4% and reducing material damping are symptoms of the initial resonance system quality factor growth (correlation with structural and magnetic anisotropy) (Figure 29). This phase can be described with linear SDOF model.

The growing asymmetry of the resonance curve was observed only in the final fatigue phase (Figure 30); it preceded the 1st mode frequency decrease.

5.2.5. JCF Phenomena. Influence of the cracked blade's resonant curve discontinuity on the propagation rate was tested for blades made from titanium alloy. It was found that in the case of constant frequency input (HCF tests without fine tuning to current resonant frequency), characteristic curve sloping to right and resonant curve discontinuity helps stopping the crack propagation.

The speed rate of its development was conditioned by the load history of a blade. The asymmetry is a symptom of the material weakening phase [3, 23]. The speed rate of the resonance curve asymmetry development, from the very first symptom of an open crack, is determined by the blade loading history.

Discontinuity of the resonant curve (blade pulse input discharge and load even for constant external load) is a source of very fast crack propagation during frequency transient phase—the phenomenon is called Jump Cycle Fatigue (JCF) (Figure 31).

The JCF is a reason for the serial material tearing during the decrease in excitations frequency, observed in the unstable phase of cracking. Those observations are fundamental for the prognosis of crack propagation velocity and determination safe prognosis horizon for blade operation and fatigue reverse engineering—correct interpretation of fracture structure (answer on the question "How many load cycles took place during crack propagation?"). Arrest lines of fatigue strap map only a number of cycles for internal loads. Their values could be bigger several times than a number of cycles for external loads, which result from a flight mission profile.

5.3. The Tip Timing Method. The object under scrutiny has been the 1st stage compressor blade (28 blades made out of the 18H2N4WA steel, each 100 mm long, chord 37 mm, twisted by the angle of 38°). Frequencies of three subsequent modes of blade vibration were as follows (average values): 350 Hz and 1380 Hz (bending vibration), 1890 Hz (torsional vibration).

5.3.1. Synchronous Resonance. During examination with a strain gauge no evident symptoms of interrelationships between the disk and blade vibrations were observed—compressor stages are of compact design. However, it was

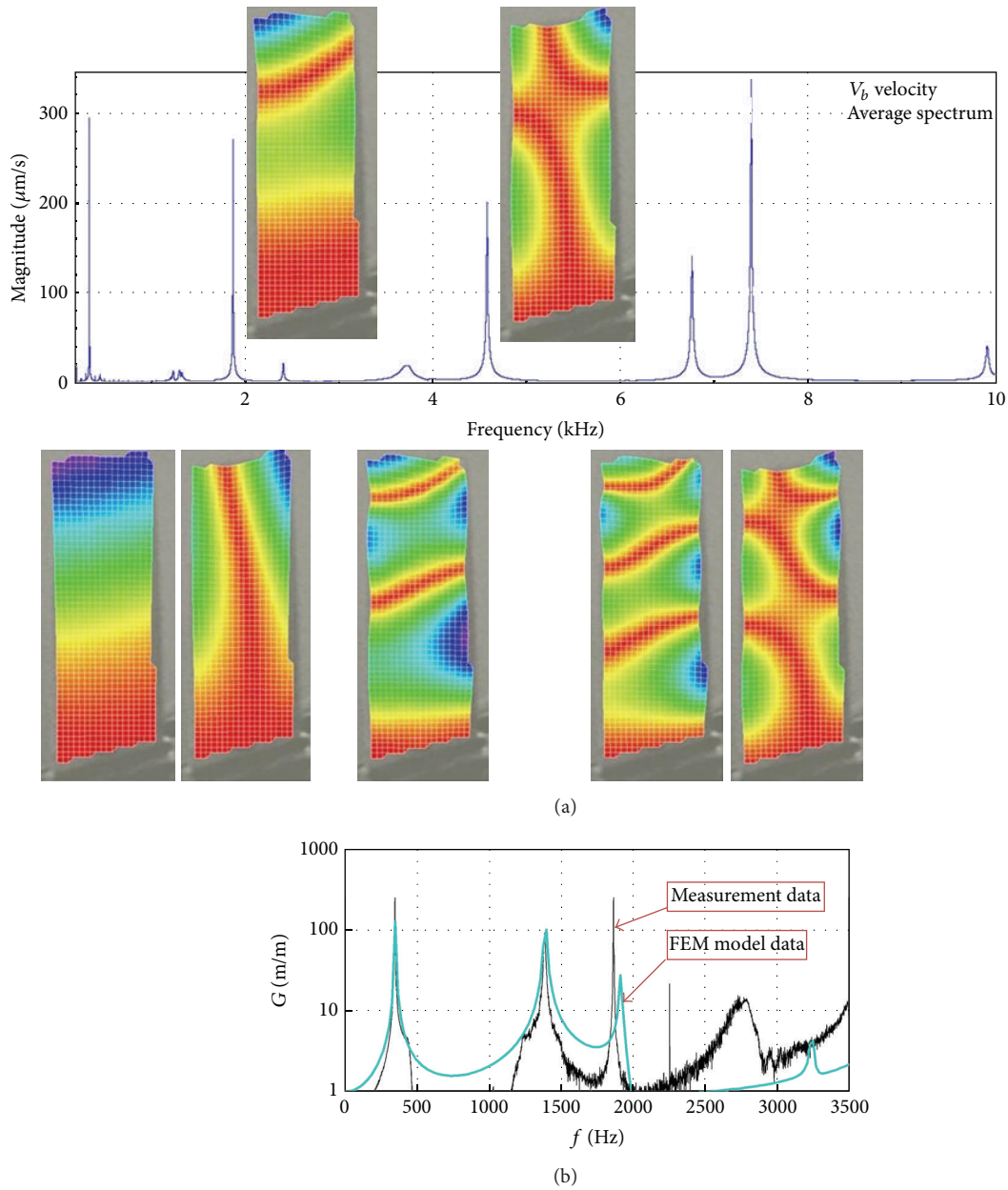

Figure 26: Identification of blade modal properties using (a) PZT exciter and laser scanning vibrometer (906 test points); (b) experimental data and FEM model of the steel blade (before the FEM model is tuning) [3, 22].

observed that, within the take-off range of the SO-3 engine operation (n = 15600 rpm), synchronisation of blade vibration with forces from the 2nd harmonic of the rotational speed ($f_{1\text{mode}}$ = 520 Hz) may occur (Figure 32(a)). Such phenomena observed, for example, after some foreign object (bird, ice) has been deposited on the stator blade-ring, induce blade vibration up to some dangerous level where the material yield point is reached and exceeded, and quick initiation and propagation of the LCF and HCF cracks occur. Under such conditions of blade operation, time of safe operation of any turbojet engine may be much shorter than one flight/mission of an aircraft.

5.3.2. Asynchronous Resonance. The work of an engine in the compressor limits (during acceleration and deceleration of the rotation speed) exaggerated shading in the intake whether exaggerated mistakes of the rotor alignment are creating condition for the asynchronous resonance of compressor blades and HCF problems (Figure 33). They are not only endangered blades of the compressor but also other sub-assemblies of the engine, for example, bearing, gears, and shafts. The endurance risk of subassemblies mentioned above can be reduced through the engine user. For that purpose an aperiodic component TOA(k) is being used (phase portrait of the rotation speed) [61–63].

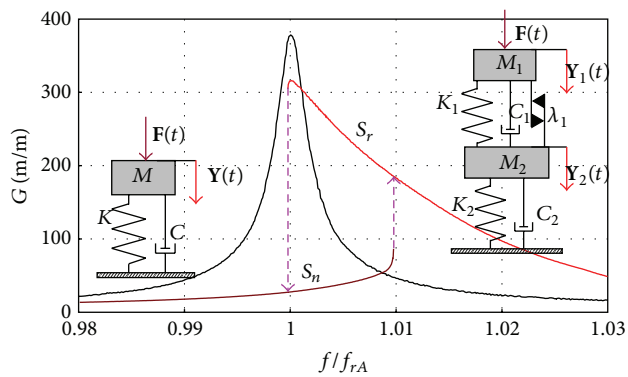

FIGURE 27: The effect of a crack on the 1st mode characteristics shape (steel blade, $a = 19.62\ \mathrm{m/s^2}$, f_{rA}: frequency of amplitude resonance) [23].

5.3.3. The Blade Cracking. After an analysis of destructive testing results (controlled propagation of blade cracking under normal conditions of operating the SO-3 engine) it was found that [55]

(i) during the blade cracking initiation (no open crack visible on the blade surface) only change in the B factor of dynamic increment of blade vibration frequency is seen (Figure 34(a)); frequency of the blade's free vibration $f_B(0)$ is constant

$$f_B(n) \cong \sqrt{f_B(n=0)^2 + Bn^2}, \tag{25}$$

(ii) the occurrence of a blade crack decreases in the range of excitations from the rotational-speed II harmonic by 1000 rpm ($\Delta f = 16.6$ Hz) (Figure 34(b)). At the moment, frequency (the 1st mode) of the blade's free vibration changed by less than 3 Hz;

(iii) when the crack reaches about 30% of the blade profile, evident reduction in frequency of free vibration and decrease in the range of excitations from the rotational-speed III harmonic ($n \cong 8000$ rpm) were observed;

(iv) just before the blade break-off (about 65% of profile for the crack from the leading edge, 95% of profile for the crack from the back of the blade), an evident effect of stiffening due to centrifugal forces was observed (Figure 34(c)). Changes in the dynamic scale inflicted by the broken blade are comparable with those in other dynamic scales (the influence of the engine's rotational speed).

It has been proven that the TTM gives credible prognosis for 50 engine work hours—"over $9 \cdot 10^7$ HCF and 100 LCF cycles, 1/8 TBO [3, 23, 62]." It has been also proven that TTM symptoms of the cracking are closely related to

(i) *the strengthening phase*: the quality factor of the resonance system increases together with the friction mode frequency;

(ii) *the weakening phase*: growth in the resonance curve asymmetry and growth in nonlinearity.

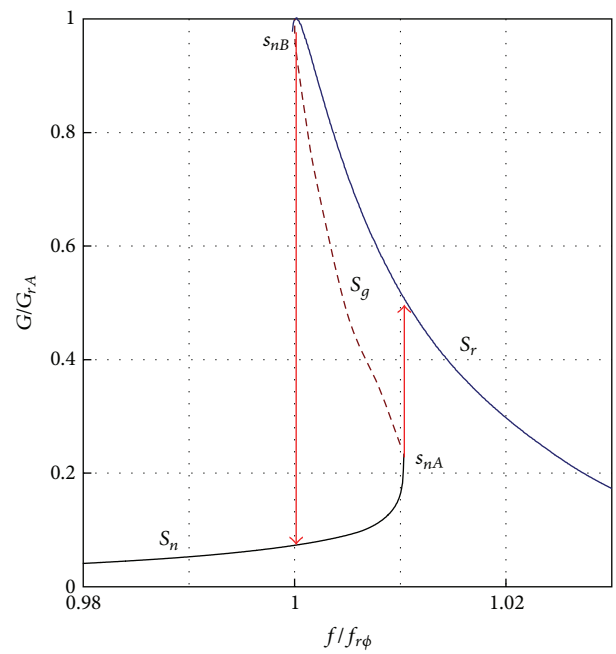

(a)

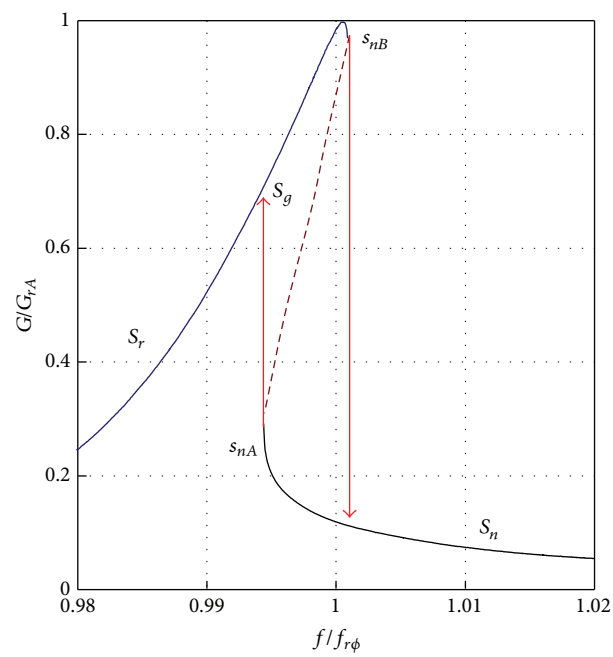

(b)

FIGURE 28: Shape of resonance characteristic for cracked blade with: (a) material weakening on the crack tip; (b) material hardening on the crack tip [3, 23].

6. Conclusion

(1) Described methods are mutually supplementing, which results in the synergy effect. The verified knowledge enables better modeling of continuum damage mechanisms and improving research method.

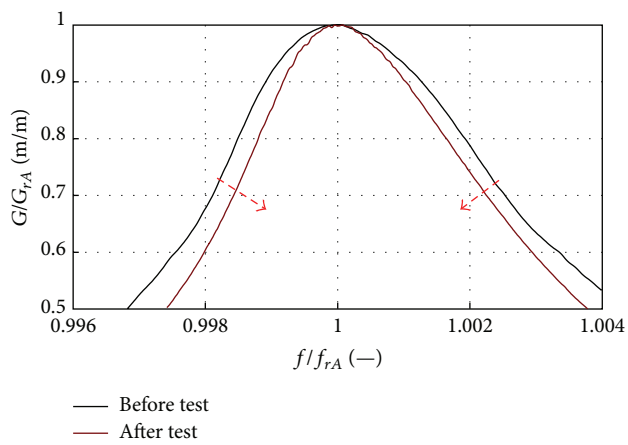

Figure 29: Changes in modal parameters during material strengthening phase [3, 23].

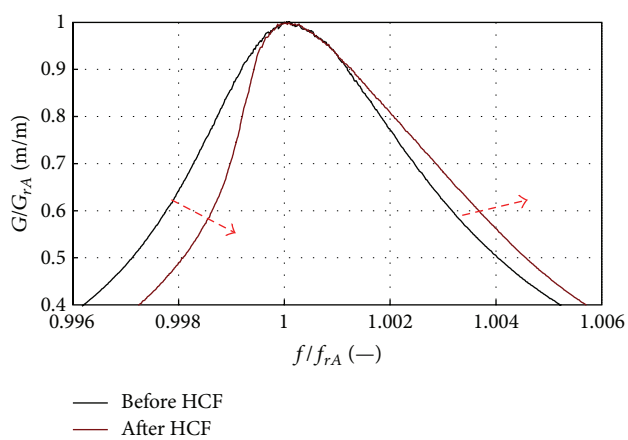

Figure 30: Changes in modal parameters during material weakening phase ($\delta f_{rA} = -0.5$ Hz) [3, 23].

(2) New opportunities of the metal magnetic memory method, including diagnosing and identification of hidden risk of material fatigue (before the opened crack, measurements through the casing, and SHM application), have been proven.

(3) The high effectiveness of the experimental modal analysis method has been demonstrated on the basis of tests of more than 3000 compressor blades. A possibility of the automatic detection of the crack, the weakness (fatigue softening) and strengthening (strain hardening) of the blade, has been presented. The shape of resonance curve is diagnostic symptom.

(4) Active control of blade fatigue by the aeroengine user is possible. During 20 years of using the tip timing method in the Armed Forces of Poland, the following things have occurred.

(a) The statistical mean time between fatigue break-offs of blades has been increased (eleven times for calendar-based data and seven times on the hourly basis). Since 1991 the fatigue crack of any compressor blade in the SO-3 engines has not been registered in spite of the existing fault in design.

(b) The surge as a result of maladjustment of the fuel system and latent defects of subsystems has been eliminated (mainly fatigue problems results from maintenance).

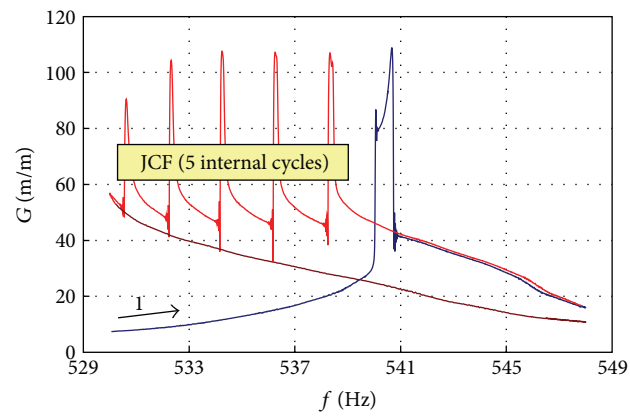

Figure 31: The JCF phenomenon for a cracking blade with Ti5.8Al-3.7Mo (sine sweep 4 Hz/min with constant external load) [3, 23].

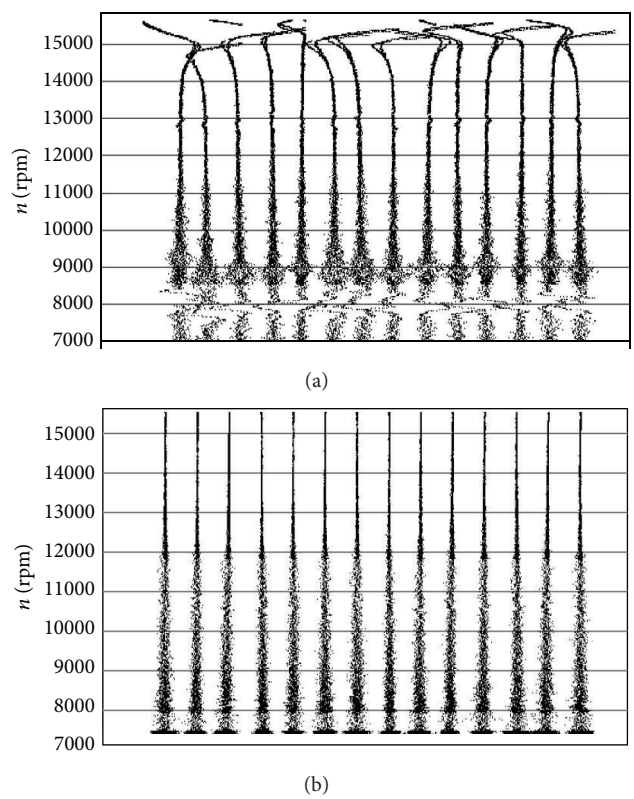

Figure 32: How foreign-matter depositions may affect the level of stress in the SO-3's 1st stage compressor blades [55]: (a) effect of foreign matter in compressor inlet; (b) model amplitude-phase spectra of the 1st compressor blade.

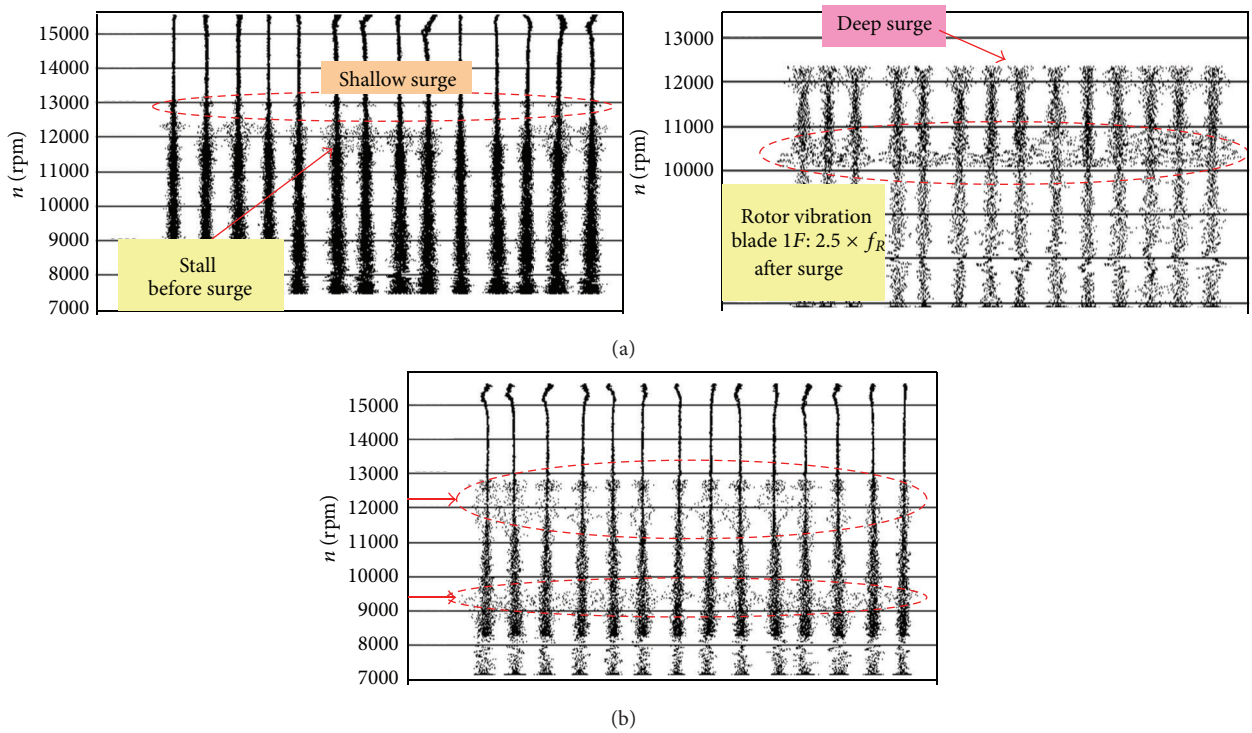

FIGURE 33: The asynchronous resonance of the compressor blades [55, 61, 63]: (a) before, during, and after the surge; (b) during identification of the surge limit (p_3 signal disconnected from FCU).

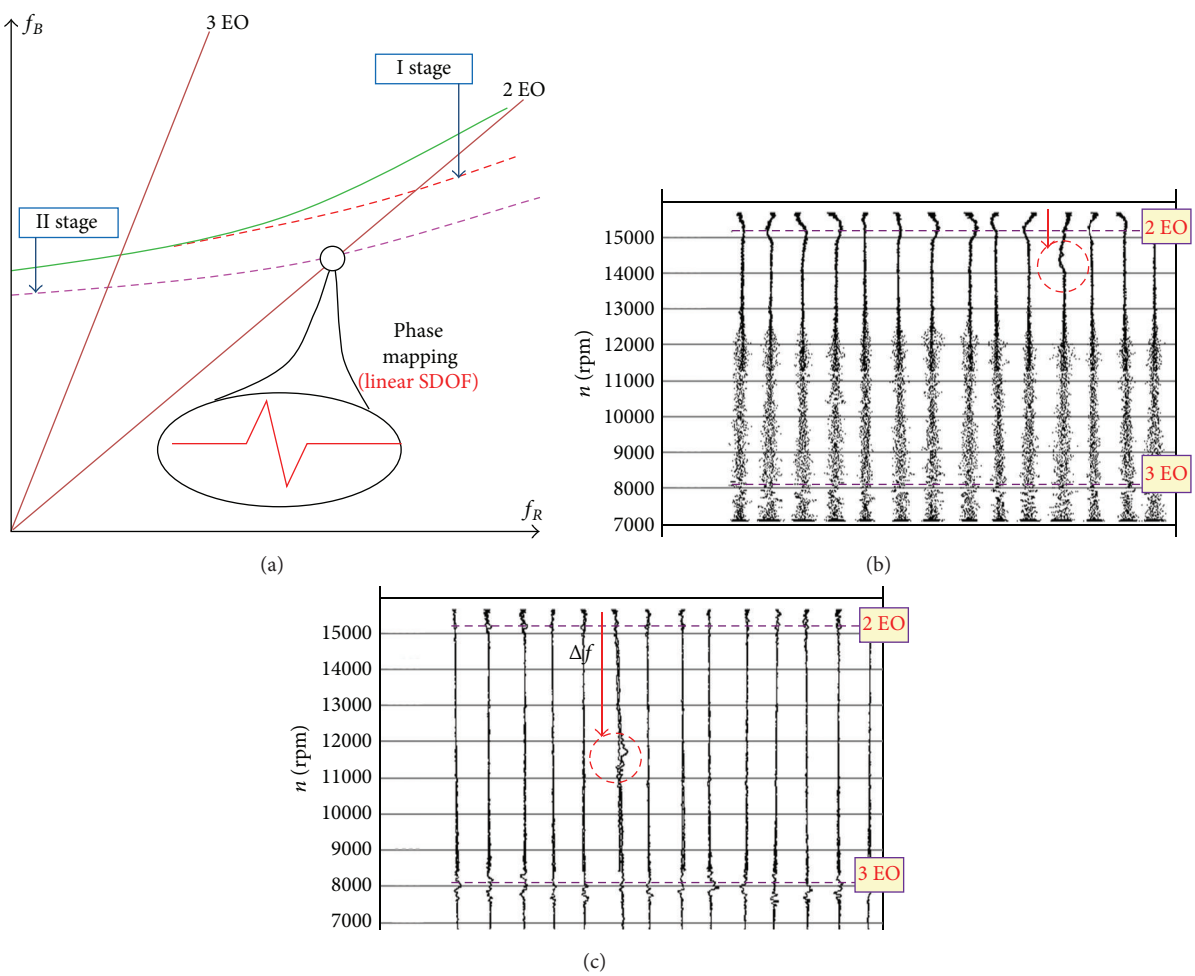

FIGURE 34: The effect of blade cracking [55]: (a) blade frequency plotted in the Campbell diagram; (b) the first stage of blade cracking, changes only B; (c) final stage of blade cracking, 5 minutes before break (signal after low-pass filtering).

(c) Five SO-3 engines have been taken out of service due to excessive errors in shapes of the blades.

(5) Nonlinear properties of a crack blade are fundamental for the prognosis of the crack propagation rate and for the determining safe prognosis horizon. The modal symptoms of material damage are correlated with magnetic symptoms. Asymmetry of resonant curve has not been found on the blade with notched-a simple crack simulation model, often found in the literature.

Acknowledgments

The study has been prepared under some research projects financially supported by the National Centre for Research and Development of Poland, the Ministry of Science and Higher Education of Poland, and the Ministry of National Defence of Poland. In examinations of compressor blades a staff of Institute of Fluid Flow Machinery Polish Academy of Science, aviation units, and the Military Aviation Works No. 1 gave the technical assistance.

References

[1] "More intelligent gas turbine engines," RTO-TR-AVT-128, NATO, 2009, http://www.cso.nato.int/pubs/rdp.asp?RDP=RTO-TR-AVT-128.

[2] "Active control of engine dynamics," RTO-EN-020, AVT-083, NATO, November 2002, RTO AVT/VKI Special Course, 2001, Rhode-Saint-Genese, Belgium, http://www.cso.nato.int/Pubs/rdp.asp?RDP=RTO-EN-020.

[3] M. Witoś, "Increasing the durability of turbine engines through active diagnostics and control," *Research Works of AFIT*, no. 29, 324 pages, 2011.

[4] V. T. Vlasov and A. A. Dubov, *Physical Bases of the Metal Magnetic Memory Method*, ZAO "Tisso" Publishing House, Moscow, Russia, 2004.

[5] ISO-24497-1. Non-destructive testing-Metal magnetic memory. Part 1: Vocabulary, 2007.

[6] ISO-24497-2. Non-destructive testing-Metal magnetic memory. Part 2: General requirements, 2007.

[7] ISO-24497-3. Non-destructive testing-Metal magnetic memory. Part 3: Inspection of welded joints, 2007.

[8] A. Dubov and S. Kolokolnikov, "The metal magnetic memory method application for online monitoring of damage development in the steel pipes and welded joints specimens," *Welding in the World*, vol. 57, no. 1, pp. 123–136, 2013.

[9] K. Yan, Z. D. Wang, B. Deng, and K. Shen, "Experimental research on metal magnetic memory method," *Experimental Mechanics*, vol. 52, no. 3, pp. 305–314, 2012.

[10] M. Roskosz, "Metal magnetic memory testing of welding joints of ferritic and austenitic steels," in *proceedings of the 40th International Conference and Exhibition*, pp. 219–228, Pilsen, Czech, NDT for Safety/Defektoskopie, 2010.

[11] X. Ding, J. Li, F. Li, and X. Pang, "Magnetic memory inspection of high pressure manifoolds," in *Proceedings of the 17th World Conference on Non-Destructive Testing*, Shanghai, China, October 2008.

[12] Q. Liu, J. Lin, M. Chen et al., "A study of inspecting the stress on downhole metal casing in oilfields with magnetic memory method," in *Proceedings of the 17th World Conference on Nondestructive Testing*, Shanghai, China, October 2008.

[13] X. Hai Yan, X. M. Qiang, Y. Zhijun, and Z. Lihong, "Stress state Analysis of failure blade with MMM method," http://www.paper.edu.cn/.

[14] M. Iwaniec, M. Witoś, M. Roskosz, and S. Gontarz, "Diagnosis of bearer structures of high voltage lines using magneto-mechanical effects," in *Proceedings of the 4th Scientific and Technological Conference Diagnostics of Material and Industrial Components DMiUT*, Gdansk, Poland, May 2012.

[15] M. Witoś, "The reference signal of geomagnetic field for MMM expert systems," *Key Engineering Materials*, vol. 518, pp. 384–395, 2012.

[16] M. Witoś and M. Zieja, "High sensitive methods for fatigue detection," *Diagnostyka*, vol. 3, no. 59, pp. 25–34, 2011, *Journal of KONBiN*, 2011, vol. 1, no. 17, pp. 307–326.

[17] N. M. M. Maia and J. M. M. Silva, *Theoretical and Experimental Modal Analysis*, Research Studies Press LTD, Taunton, Mass, USA, 1997.

[18] D. J. Ewins, *Modal Testing: Theory, Practice and Application*, Research Studies Press LTD, Baldock, UK, 2nd edition, 2000.

[19] W. Heylen, S. Lammens, and P. Sas, *Modal Analysis Theory and Testing*, KUL Press, Leuven, Belgium, 1997.

[20] B. J. Schwarz and M. H. Richardson, *Experimental Modal Analysis*, CSI Reliability Week, Orlando, Fla, USA, 1999.

[21] L. A. Ostrovsky and P. A. Johnson, "Dynamic nonlinear elasticity in geomaterials," *Revista Del Nuovo Cimento*, vol. 24, no. 7, pp. 1–46, 2001.

[22] M. Witoś and M. Stefaniuk, "Compressor blade fatigue diagnostic and modeling with the use of modal analysis," *Fatigue of Aircraft Structure*, vol. 1, no. 3, pp. 112–133, 2010.

[23] M. Witoś, "On the modal analysis of a cracking compressor blade," *Research Works of AFIT*, no. 23, pp. 21–36, 2008.

[24] "Report on aircraft PP-VNN," engine failure, 2000, http://aviation-safety.net/database/.

[25] J. F. Brouckaert, *Tip Timing and Tip Clearance Problems in Turbomachinary*, Lecture Series 3-2007, VKI Belgium, 2007.

[26] Agilis Non-Intrusive Stress Measurement System, Fundamentals, http://www.agilismeasurementsystems.com/.

[27] B. W. Ayes, S. Arnold, C. Vining, and R. Howard, "Application of generation 4 non-contact stress measurement system on HCF demonstrator engines," in *Proceedings of the 10th National Turbine Engine High Cycle Fatigue (HCF) Conference*, Dayton, Ohio, USA, 2005.

[28] F.-J. Duan, Z.-Q. Fang, Y.-Y. Sun, and S.-H. Ye, "Real-time vibration measurement based on tip-timing for rotating blades," *Opto-Electronic Engineering*, vol. 30, no. 1, pp. 29–31, 2005.

[29] A. von Flotow and M. J. Drumm, *Engine Sensing Technology Hardware and Software to Monitor Engine Rotor Dynamics Using Blade Time-of-Arrival and Tip Clearance*, Hood River, Ore, USA, 2002.

[30] R. Przysowa and J. Spychala, "Health monitoring of turbomachinery based on blade tip-timing and tip-clearence," RTO-MP-AVT-157 Paper 14, NATO, 2008.

[31] R. Washburn, "Amplitude and phase variations associated with low order resonance responses subjected to time varying excitation sources," in *Proceedings of the 9th National Turbine Engine High Cycle Fatigue Conference*, Dayton, Ohio, USA, 2004.

[32] M. Witoś, "Turbine engine health/maintenance status monitoring with use of tip timing method," in *Proceedings of the 4th Workshop on Structural Health Monitoring*, T. Uhl, W. Ostachowicz, and J. Holnicki-Szulc, Eds., pp. 157–164, DEStech Publication, 2008.

[33] M. Zielinski and G. Ziller, "Noncontact crack detection on compressor rotor blades to prevent further damage after HC-failure," RTO MP-AVT-121 paper 19, NATO, 2005.

[34] W. Campbell, "Elastic-fluid turbine rotor and method of avoiding tangential bucket vibration therein," Patent US 1, 502, 904, 1924.

[35] http://www.evi-gti.com/.

[36] http://www.piwg.org/.

[37] G. H. Hardigg and P. A. Swarthmore, "Apparatus for measuring rotor blade vibration," Patent US 2, 575, 710, Westinghouse Electric Corporation, 1951.

[38] H. Shapiro, "Vibration detector and measuring instrument," Patent US 3058339, Curtiss-Wright Corporation, Propulsion Products Division, 1962.

[39] I. E. Zablotsky, J. A. Korostelev, A. Y. Lebedev, L. B. Sviblov, and E. M. Tolchinsky, "Vibrator indicator for turboengine rotor blading," Patent US 3, 467, 358, 1969.

[40] J. Smejkal, M. Jindra, and Z. Brezina, "Apparatus for switching pulses in measuring the vibration of rotating parts during operation of a machine," Patent US 3, 597, 963, Skoda Czechoslovakia, 1971.

[41] J. Naegeli and A. Maurer, "Method and apparatus for monitoring the state of oscillation of the blades of a rotor," Patent US 4, 153, 388, Sulzer Brothers Ltd, 1979.

[42] V. E. H. Ellis, "Vibration monitoring in rotary machines," Patent US 4, 593, 566, Rolls Royce Ltd, 1986.

[43] G. I. Marron and W. B. Rethage, "Blade pitch measurement apparatus and method," Patent US 4, 827, 435, Westinghouse Electric Corporation, 1989.

[44] F. S. McKendree and P. F. Rozelle, "Nonsynchronous turbine blade vibration monitoring system," Patent US 4, 887, 468, Westinghouse Electric Corporation, 1989.

[45] R. P. Kending, R. A. Lucheta, and F. S. McKendree, "Turbine blade fatigue monitor," Patent US 4, 955, 269, Westinghouse Electric Corporation, 1990.

[46] R. Kudelski and R. Szczepanik, "System for signalling the fact of exceeding admissible amplitude of vibrations by vanes of a fluid-flow machine," Patent 184530 (PL), Air Force Institute of Technology, 1991.

[47] M. Twerdochlib, P. F. Rozelle, and S. Sarasas, "Apparatus and method for removing common mode vibration data from digital turbine blade vibration data," Patent US 5, 148, 711, Westinghouse Power Corporation, 1992.

[48] M. Witoś, A. Gawin, and A. Szczepankowski, "Sposob diagnozowania technicznego wirujacych lopatek maszyny wirnikowej oraz uklad do diagnozowania technicznego wirujacych lopatek maszyny wirnikowej," Patent PL 169219 (B1), Instytut Techniczny Wojsk Lotniczych, 1996.

[49] R. P. Kendig, R. A. Lucheta, and F. S. McKendree, "Turbine blade fatigue monitor," Patent KR960014013 (B1), Westinghouse Electric Corporation, 1996.

[50] M. Yukio and E. Masanori, "Vibration measuring apparatus for rotor blade," Patent JP3038382 (B2), NATL Aerospace Lab, 2000.

[51] V. A. Mednikov and V. V. Shchegolev, "Method for determining amplitude of oscillations of turbomachine blade," Patent RU2207524 (C1), 2003.

[52] I. Hideyasu, N. Kenichi, and M. Shinya, "Moving blade failure diagnosing method of gas turbine and device therefor," Patent JP3663609 (B2), Ishikawajima Harima Heavy Ind, 2005.

[53] V. V. Shchegolev, "Method for metering vibration amplitudes of turbomachine blades," Patent RU2244272 (C1), 2005.

[54] M. Zielinski and G. Ziller, "Method and device for detecting cracks in compressor blades," Patent WO2010054644 (A2), MTU Aero Engines Gmbh, 2010.

[55] M. Witoś, *Diagnosing of technical condition of turbine engine compressor blades using non-contact vibration measuring method [Ph.D. thesis]*, ITWL, Warszawa, Poland, 1994.

[56] A. A. Shaniavski, *Modeling of Fatigue Cracking of Metals. Synergetics For Aviation*, Publishing House of Scientific and Technical Literature 'Monography', Ufa, Russia, 2007.

[57] A. A. Shaniavski, *Tolerance Fatigue of Aircraft Components. Synergetics in Engineering Applications*, Publishing House of Scientific and Technical Literature 'Monography', Ufa, Russia, 2003.

[58] Y. Murakami, T. Nomoto, and T. Ueda, "Factors influencing the mechanism of superlong fatigue failure in steels," *Fatigue and Fracture of Engineering Materials and Structures*, vol. 22, no. 7, pp. 581–590, 1999.

[59] Y. Murakami, M. Takada, and T. Toriyama, "Super-long life tension-compression fatigue properties of quenched and tempered 0.46% carbon steel," *International Journal of Fatigue*, vol. 20, no. 9, pp. 661–667, 1998.

[60] T. Sakai, "Review and prospects for current studies on very high cycle fatigue of metal materials for machine structural use," *Journal of Solid Mechanics and Materials Engineering*, vol. 3, no. 3, pp. 425–439, 2009.

[61] A. Szczepankowski, *Diagnosing of Technical Condition of Turbine Engine Using Rotational Speed Phase-Mapping Method [Ph.D. thesis]*, ITWL, Warszawa, Poland, 1999.

[62] R. Szczepanik and M. Witoś, "Aeroengine condition monitoring system based on non-interference discrete-phase compressor blade vibration measuring method," RTO-MP-051, NATO, 2001, http://ftp.rta.nato.int/public//PubFullText/RTO/MP/MP-051///MP-051-PSP-13.pdf.

[63] M. Kowalski, "Phase mapping in the diagnosing of a turbojet engine," *Journal of Theoretical and Applied Mechanics*, vol. 50, no. 4, pp. 913–921, 2012.

[64] S. Kocanda, *Zmeczeniowe Pekanie Metali*, WNT , Warszawa, Poland, 1985.

[65] M. A. Almojil, *Deformation and recrystal-lisation in low carbon steels [Ph.D. thesis]*, Manchester Materials Science Centre, 2010.

[66] V. Novikov, *Grain Growth and Control of Microstructure and Texture in Polycrystalline Materials*, CRC Press, Boca Raton, Fla, USA, 1996.

[67] A. H. Cottrell, *The Mechanical Properties of Matter*, John Wiley and Sons, New York, NY, USA, 1964.

[68] F. R. N. Nabarro, "Dislocations in a simple cubic lattice," *Proceedings of the Physical Society*, vol. 59, no. 2, article 309, pp. 256–272, 1947.

[69] N. A. Makhutov and M. M. Gadenin, "Nonlinear deformation and fracture mechanics for engineering approaches in design of structure," *Mechanical Engineering, Energy Systems and Sustainable Development*, vol. 1, http://www.eolss.net/.

[70] W. Cui, "A state-of-the-art review on fatigue life prediction methods for metal structures," *Journal of Marine Science and Technology*, vol. 7, no. 1, pp. 43–56, 2002.

[71] G. Socha, "Experimental investigations of fatigue cracks nucleation, growth and coalescence in structural steel," *International Journal of Fatigue*, vol. 25, no. 2, pp. 139–147, 2003.

[72] F. B. Pickering, *Physical Metallurgy and the Design of the Steels*, Applied Science Publishers, London, UK, 1978.

[73] S. M. Thompson, *The magnetic properties of plastically deformed steels [Durham theses]*, Durham University, 1991, http://etheses.dur.ac.uk/3600/.

[74] T.-K. Lee, J. W. Morris Jr., S. Lee, and J. Clarke, "Detection of fatigue damage prior crack initiation with scanning SQUID microscopy," in *Review of Progress in Quantitative Nondestructive*, vol. 25, pp. 1378–1385, August 2005.

[75] R. Newnham, *Properties of Materials. Anisotropy, Symmetry, Structure*, Oxford University Press, Oxford, UK, 2005.

[76] L. Vandenbossche, *Magnetic Hysteretic Characterization of Ferromagnetic Materials with Objectives towards Non-Destructive Evaluation of Material Degradation [Ph.D. thesis]*, Universiteit Gent, 2009.

[77] J. A. Ewing, *Magnetic Induction in Iron and Other Metals*, "THE ELECTRICIAN" Printing and Publishing, London, UK, 1900.

[78] K. Yaegashi, "Dependence of magnetic susceptibility on dislocation density in tensile deformed iron and Mn-steel," *ISIJ International*, vol. 47, no. 2, pp. 327–332, 2007.

[79] W. Liang, D. Fang, Y. Shen, and A. K. Soh, "Nonlinear magnetoelastic coupling effects in a soft ferromagnetic material with a crack," *International Journal of Solids and Structures*, vol. 39, no. 15, pp. 3997–4011, 2002.

[80] C. W. Burrows, "Correlation of the magnetic and mechanical properties of steel," Scientific Papers of the Bureau of Standards, no. 272, 1916, http://www.archive.org/.

[81] M. S. Blanter, I. S. Golovin, H. Neuhäuser, and H. R. Sinning, *Internal Friction in Metallic Materials. A Handbook*, Springer, Berlin, Germany, 2007.

[82] M. F. Fischer, "Note on the effect of repeated stresses on the magnetic properties of steel," *Bureau of Standards Journal of Research*, vol. 1, no. 5, pp. 721–732, 1928.

[83] I. M. Robertson, "Magneto-elastic behaviour of steels for naval applications," MRL Technical Report MRL-TR-90-27, DSTO Materials Research Laboratory, 1991.

[84] T. Yamasaki, S. Yamamoto, and M. Hirao, "Effect of applied stresses on magnetostriction of low carbon steel," *NDT and E International*, vol. 29, no. 5, pp. 263–268, 1996.

[85] D. L. Atherton and D. C. Jiles, "Effects of stress on magnetization," *NDT International*, vol. 19, no. 1, pp. 15–19, 1986.

[86] R. R. Birss and C. A. Faunce, "Stress-induced magnetization in small magnetic fields," *Journal de Physique*, vol. 32, supplement, no. 2-3, pp. 686–688, 1971.

[87] E. W. Lee, "Magnetostriction and magneto-mechanical effects," *Reports on Progress in Physics*, vol. 18, pp. 184–229, 1955.

[88] C. M. Smith and G. W. Sherman Jr., "A study of the magnetic qualities of stressed iron and steel," *Physical Review*, vol. 4, pp. 267–273, 1914.

[89] http://www.magnaflux.com/.

[90] http://www.magneticsensors.com/.

[91] http://www.energodiagnostika.ru/.

[92] http://polytec.com/.

[93] http://www.bksv.com/.

[94] http://www.mtiinstruments.com/.

[95] http://www.vibrationresearch.com/.

[96] http://www.acam-usa.com/.

[97] http://highlandtechnology.com/.

Hindawi Publishing Corporation
The Scientific World Journal
Volume 2013, Article ID 823603, 13 pages
http://dx.doi.org/10.1155/2013/823603

Research Article

Crack Propagation Analysis Using Acoustic Emission Sensors for Structural Health Monitoring Systems

Zachary Kral,[1,2] Walter Horn,[1,2] and James Steck[1,2]

[1] *Wichita State University, Wichita, KS 67260, USA*
[2] *Department of Aerospace Engineering, 1845 Fairmount, Wichita, KS 67226, USA*

Correspondence should be addressed to Zachary Kral; ztkral@wichita.edu

Received 14 March 2013; Accepted 19 June 2013

Academic Editors: T. E. Matikas and M. R. Woike

Aerospace systems are expected to remain in service well beyond their designed life. Consequently, maintenance is an important issue. A novel method of implementing artificial neural networks and acoustic emission sensors to form a structural health monitoring (SHM) system for aerospace inspection routines was the focus of this research. Simple structural elements, consisting of flat aluminum plates of AL 2024-T3, were subjected to increasing static tensile loading. As the loading increased, designed cracks extended in length, releasing strain waves in the process. Strain wave signals, measured by acoustic emission sensors, were further analyzed in post-processing by artificial neural networks (ANN). Several experiments were performed to determine the severity and location of the crack extensions in the structure. ANNs were trained on a portion of the data acquired by the sensors and the ANNs were then validated with the remaining data. The combination of a system of acoustic emission sensors, and an ANN could determine crack extension accurately. The difference between predicted and actual crack extensions was determined to be between 0.004 in. and 0.015 in. with 95% confidence. These ANNs, coupled with acoustic emission sensors, showed promise for the creation of an SHM system for aerospace systems.

1. Introduction

Even though the current method of inspecting aircraft, consisting of ground inspections for damage after a set number of flight hours, works well from an aircraft safety point of view, it can be improved upon for greater productivity. An in-flight structural health monitoring (SHM) system would allow for better use of components, as specific lifetimes could be determined. Maintenance cost might be reduced since an SHM system could be embedded into the aircraft structure, thereby reducing or eliminating the need to remove the aircraft from service to scan for damage during the ground inspection. Ground inspections of aircraft, even using simple nondestructive testing techniques, generally require the aircraft be pulled from service so that its components can be inspected for damage. Structural components are replaced if sufficient damage is found. Research is underway to develop a structural health monitoring (SHM) system as a means to improve current maintenance procedures. This system would consist of an array of sensors and associated analysis which would scan for damage in-flight and perform real-time damage analysis of an aircraft's structure. If damage is recognized long before failure occurs, then a damage tolerance and prognostic assessment could be implemented, allowing for a determination of the remaining life of components.

This paper contains the results of an investigation of the abilities of a passive ultrasonic scanning system, called an acoustic emission system. The focus of this research effort was on the development of a quick, accurate and precise method of automating a structural health monitoring (SHM) system to optimize the analysis capabilities of an acoustic emission system in order to locate and assess damage in a structural component. The basic acoustic emission system was augmented with an artificial neural network analysis to provide near real-time analysis of acoustic emission data measured from aircraft structural components, during routine service operations.

1.1. Acoustic Emission. As a crack propagates in a material, molecular bonds are broken, releasing small amounts of energy. The energy released spreads throughout the surrounding material in the form of strain waves. These waves are minute deformations in the material with wave frequencies in the ultrasonic range from 500 kHz to 3 MHz. Generally all structural deformations transmit some form of energy into the material, resulting in waves similar to those of crack growth. The acoustic emission system of the study consisted of piezoelectric sensors, which were configured to receive waves, generated by other sources, such as crack extensions or impact events, within the structural component under investigation. However, the detected waves can be quite complex due to how strain waves travel in solid structures, based on wave dispersion and effects of geometry boundaries [1–3]. The recorded voltage time histories were broken down into characteristics of the waves, such as amplitude, rise time, and duration, using software provided by Physical Acoustics Corporation [4]. These characteristics of the waves were recorded with a network of sensors and analyzed via different software methods through MATLAB [5] and NeuralWorks [6] to determine if cracks were present and growing and whether the structural component should be replaced. A custom designed artificial neural network was used for the post-processing analysis of the detected waves.

The energy released during the deformation of a material occurs at two stages of the deformation. One is at the onset of plastic deformation, and the other when fracture occurs. This can be illustrated using the results of a simple test, performed at the National Institute for Aviation Research (NIAR) at Wichita State University. A metallic coupon was subjected to a monotonically, increasing pseudo-static tensile load, with one acoustic emission sensor attached. The results of the test to failure are presented in Figure 1. The load-displacement curve, illustrated as the solid line in the figure, follows the normal convention of being linear to the yield point and nonlinear thereafter. Each of the discrete points on the plot is a measurement of the hit count of each strain wave detected during the test. The strain wave was detected if the voltage received by the sensors was above 0.0178 V. The hit count is the number of signal excursions over this defined threshold. Other waveform characteristics can be obtained and used as a description of a strain wave. Other researchers have used the rise time [7] or energy of a wave to describe a signal obtained. The hit count property has a linear correlation with the energy of the signal as well. Although more signal properties could aid in a better damage detection system, these initial experiments focused on the hit count as the sole wave property. At the yield strength of around 1700 lb. and displacement of 0.133 in., some strain waves were detected and recorded. At the point of fracture, more strain waves were detected with similar levels of energy. At the instant of final fracture two strain waves with large energy were measured. Thus the two main states associated with released strain waves detectable by an acoustic emission system are at the onset of plastic deformation and at the point of fracture. The research reported in this paper involved an examination of the energy of strain waves produced at a crack tip at the instant of extension to determine the severity of the fracture. A second theory was proposed and observed that might provide a method to better locate growing cracks in structures by accounting for the presence of the plastic zone in the vicinity of the crack tip.

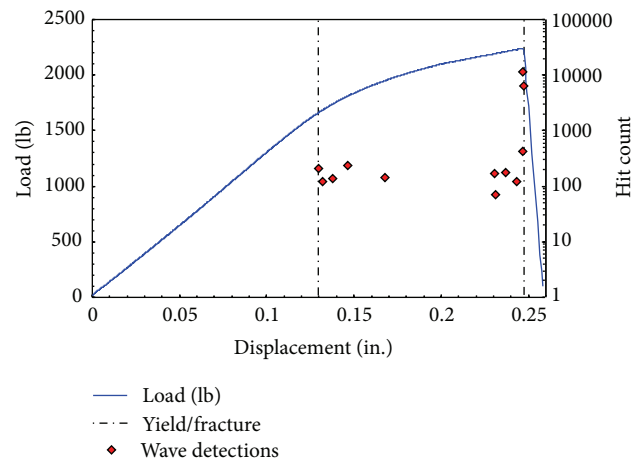

Figure 1: Correlation of the detected strain waves and the load-displacement curve of a uniaxially loaded metal sample with single acoustic emission sensor. Individual points are the energies associated with individual strain waves detected by sensor.

Energy is released within a material for two different transition events when the deformation of the material changes from pure elastic deformation to a combination of elastic and plastic deformation and at the point of crack extension associated with fracture. This energy is detectable by the piezoelectric sensors of the acoustic emission system. The amount of energy released by a fracture is generally far greater than the amount accompanying plastic deformation. However, both instances occur for growing cracks. The tip of a crack is the site for very large stresses. Before the crack extends, a region or zone of plastic deformation is achieved in the vicinity of the crack tip. This plastic region can be approximated, using Von Mises criterion, to determine the boundaries of the plastic zone. For the thin-walled structures of this research, the plastic zone covered a very small region near the crack tip, while the major portion of the structure underwent purely elastic deformation.

As a crack is initiated in the material, the plastic zone at the tip is quickly formed. As loading to the structure is increased, the crack will increase in size as illustrated in Figure 2(a). Thus at any increment of crack propagation a crescent-shaped region of new plastic deformation is created as illustrated in Figure 2(b). This shape may vary for fatigue loading, but for simplicity a basic shape can be examined.

Borrowing an idea from the distributed point source method [8] for approximating wave sources in a material, consider that each molecular change is a point source of infinitesimally small diameter, which releases a strain wave into the surrounding area. These point sources could be placed close together, forming a wave front with a specific geometric shape. By the superposition principle overlapping waves will start to cancel one another as the distance between the point sources becomes smaller. As the number of point

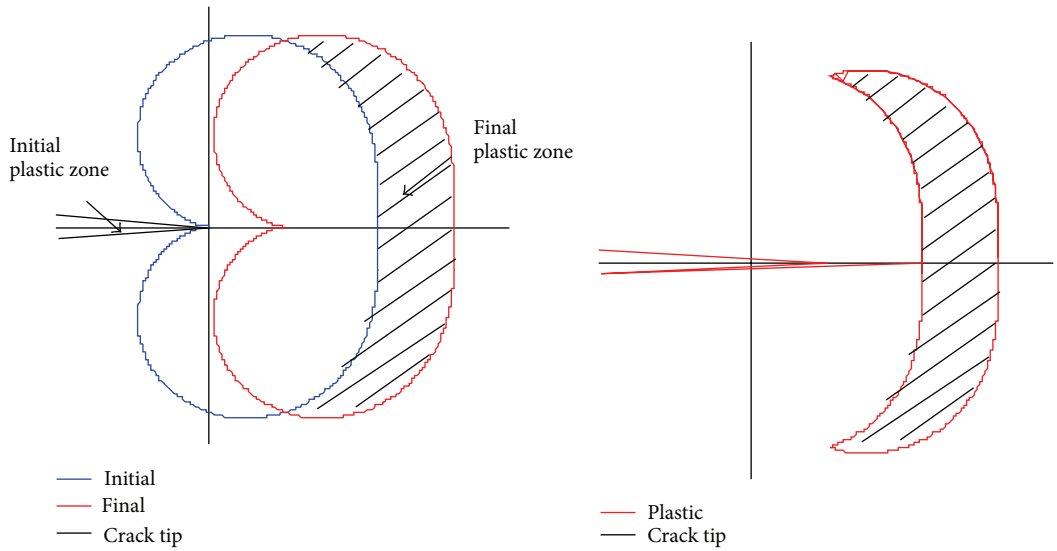

(a) Crack and plastic zone growth (b) Region of new plastic deformation

Figure 2: Crack tip and plastic zone for a thin plate.

sources increases to infinity and the distance between points approaches zero, the geometric shape of the wave becomes continuous and smooth. Waves will travel outward with this smooth shape in a direction normal to the boundary of the shape. This idea is illustrated in Figure 3, using a straight line as an example. This idea was originally used for generating wave shapes by piezoelectric actuators. However, this idea may also be applied to a collection of point sources generated by the crescent shape of the new plastic region formed during crack growth rather than a series of actuators. The wider region of the crescent shape, near the horizontal axis in Figure 2(b), contains more energy than at the sharp, pointed tips of the new plastic zone. Thus acoustic emission sensors ahead of the tip of the growing crack will detect strain waves of higher magnitude of energy when compared to sensors detecting the same wave above or behind the direction of a growing crack (see Figure 4). For example, in the figure, energy from a strain wave received by sensor (b) would be greater than the energy of the same wave received by sensor (a). Based on the direction of the growing crack, a wedge shape of intensity or magnitude of energy can be drawn, protruding outward from the crack tip. In other words, the detected wave energy increases as θ approaches 0. This allows for a line-of-sight principle to be applied to triangulation methods to compare detections at multiple sensors resulting from the same wave. This effect is observed in a following experiment using aluminum material to confirm the notion of directional strain waves propagating from a crack tip during crack extension.

1.2. Artificial Neural Network. The nervous system of humans consists of a network of passive sensors capable of detecting changes within the body. If a change is detected, the system reacts by sending a signal to the brain for further analysis of

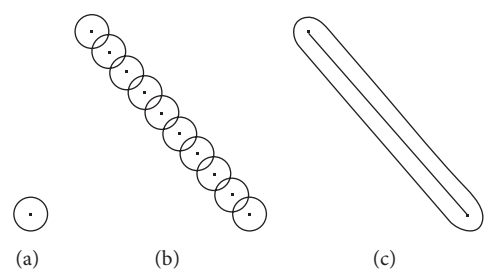

Figure 3: Distributed point source method idea illustrated. (a) Single source, (b) multiple sources, and (c) infinite sources.

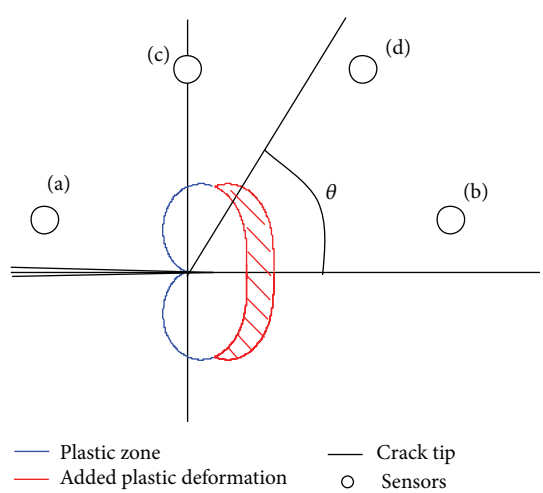

Figure 4: Sensor placement regions around a crack tip (a) receives lowest energy waves, (b) receives highest energy waves, and (c) receives lower energy waves compared to (d).

the situation. More intense signals are generated for larger anomalies that identify the specific location of the anomaly. A similar idea for a passively scanning SHM system for an aircraft has been studied for this paper. That is, as a crack grows in a structural component, the amount of energy released as strain waves is linked to the size of the crack propagation. For large crack growth, more energy is released, and thus more intense strain waves are detected by an acoustic emission system.

An artificial neural network (ANN) is an analysis system that emulates the process of the brain of humans in that a set of inputs is analyzed to obtain a desired output set. This process allows for approximate, but quick, analysis of complex problems and systems. An ANN utilizes pattern recognition and rapid analysis for approximations of varying datasets. It is fault and noise tolerant and can account for some unknown variables and errors in the data and still achieve a desired output. The ANN was an attractive candidate system to analyze the complex ultrasonic waves, traveling through the material, due to the presence of nonrelated noise and other unaccounted or unknown variables [1]. An ANN was sought to mimic the ability of the human nervous system to determine the location and extent of damage. Previous research has found damage detection to be a suitable application for ANN as well [8].

Artificial neural networks were first created around the same time as serial computers were introduced. These networks were composed of algorithms to mimic the thought processes of an organic brain to analyze a set of inputs in order to obtain a desired output set. Through a fuzzy logic system, the human thought process was emulated mathematically with a network of connected nodes and adjustable weighted values on the paths connecting the nodes, which can establish a relationship of a set of input variables to a set of output variables. Similar to a human brain, this network can be "taught" the relationship of inputs to outputs using example sets of inputs and outputs. After a sufficient number of examples have been introduced, the network can then be used to determine a trained approximation for the output associated with a new input set within the range of the examples used for training. This process approximates the output set, using "fuzzy" logic. The true power of a neural network is demonstrated when used to evaluate complex problems. Because of the training process of neural networks, a complex relationship of inputs to outputs can be found quickly, accurately, and precisely if taught well. The advantages offered by the neural network when applied to a structural health monitoring system of ultrasonic sensors allow for quick assessment of the complex strain wave signals generated by the piezoelectric signals. This could result in an accurate, almost real-time damage assessment of structural components, which may occur while the aircraft is in-service. Due to the constraints of strain waves travelling through the material, received by the acoustic emission sensor, travel by wire to a computer, and finally analyzed to obtain usable results, no SHM system will be truly instantaneous in real time. The efforts of the research presented in this paper were to develop a system, which will be as fast as possible, allowing for almost real-time sensing and analyzing.

Other researchers have investigated the integration of artificial neural networks in structural health monitoring systems. Lee et al. have developed a structural neural system, which utilizes acoustic emissions and a specialized data collection process to determine damage location in a flat structure [9]. A similar research investigated the potential of artificial neural networks as a means to postprocess complicated ultrasonic signals. Strain waves from a point source were detected by a series of piezoelectric strips. The signals from these strips were used in a feed-forward artificial neural network to determine location. The system was proven to locate point sources within the area of interest on the structure. This research demonstrated that there is a possible use of artificial neural networks coupled with nondestructive evaluation techniques to identify damage within the structure [10]. Another example is the research work performed by Crupi et al. An artificial neural network was trained to know what the normal operating conditions were. Any deviation to this would be from the result of damage. The outlier in data would be a signal that damage was present within the system, and further investigation would be required [11]. Artificial neural networks have also been employed to building structures. By analyzing the natural frequencies of a building's frame, an artificial neural network had learned to estimate damage severity on a scale from 0 to 1. The network was proven to predict the presence with low error [12]. Previous research studies have demonstrated that artificial neural networks are applicable in the field of nondestructive testing.

The concept of an artificial neural network was introduced by McCulloch and Pitts in the 1940s. Rumelhart, Hinton, and Williams provided significant improvements of the procedure by including increased learning and solving abilities for complex problems, during their work in the 1980s [13]. Through these studies, a neural network process was developed that was suitable for application in the ultrasonic testing addressed in this research.

An ANN is a system of connected nodes, activated when sufficient incoming signals are received. Each node has a binary activation of active or not, that is, 1 or 0, along with partial activations between 0 and 1 to account for approximations, or "fuzzy logic." If a node is activated, it sends a signal to the next set of nodes. Each connection between a node and the next layer of nodes has a weighted value as well, affecting how the outputs of each node affect the next receiving node. The system then "learns" from training examples by optimizing these internodal weights to obtain an ideal input-to-output operation. The architecture of the networks used in this investigation was a simple one-way network, consisting of layers of nodes, which affect the next layer. Similar to control theory, the network created was called a feed-forward network, where all connections between nodes are one directional, as illustrated in Figure 5. No signals were sent backward through the network, so that the process is not time dependant and thus most suitable for this problem. The input variables form their own, first set or layer of nodes in the network, and then several sets of nodes, called hidden layers, follow. The network illustrated in Figure 5 is a feed-forward network with only one hidden

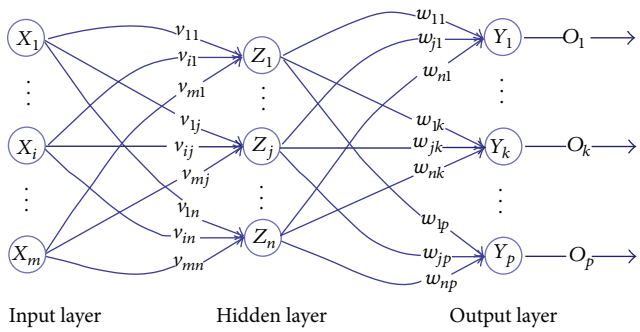

Figure 5: Feed-forward artificial neural network adapted from [9].

layer; however, multiple hidden layers may be added as well. The final layer of nodes is the output set, representing the output of the entire network.

ANNs optimize these internodal weights by "learning" a dataset of inputs to outputs, using a training dataset. This is usually a general sweep of combinations of inputs to outputs that the network would encounter in operation. Once taught a set of inputs to outputs, the neural network can be used to analyze new spontaneous datasets which fall within the range of the data contained in the learning dataset. The advantage of the neural network lies in its ability to use this learning procedure to approximate outputs associated with approximate inputs, which would otherwise require strenuous, time-consuming methods to determine the appropriate input/output relationship. Crack detection in an aircraft SHM system requires fast, accurate detection and analysis of the condition of structural components in flight to assure that damage is recognized before structural failure occurs.

Each node of the network follows a mathematical model represented by (1), where function f is a sigmoid function and the notation is taken from that of Figure 5:

$$O_k = f\left(\sum_{j=1}^{n} w_{jk} \cdot Z_j\right). \tag{1}$$

Here, the sum of the weighted outputs of the hidden layer, Z_j, which are connected to node k in the output layer, goes into an activation function, which then becomes the output for node k in the output layer, O_k. This equation is the mathematical model for a node in the output layer, but it also applies to all other nodes in previous layers as well. Unlike serial or digital computers, where the activation function is limited to a hard threshold of on or off (1 or 0 resp.), neural networks allow for smooth transitions, resulting in better approximations of similar functions.

Adjustment of the weights between the nodes comes about through a method presented by Rumelhart, Hinton, and Williams [13], which involves using the error between the desired outputs, t_k, and the output obtained by the network, O_k, to adjust the weights, w_{jk}, of Figure 5 and (1), using (2) below

$$\Delta w_{jk} = \alpha \cdot Z_j \left[(t_k - O_k) \cdot f'\left(\sum_{j=1}^{n} w_{jk} \cdot Z_j\right)\right],$$
$$w_{jk}^{\text{new}} = w_{jk}^{\text{old}} + \Delta w_{jk}. \tag{2}$$

This process, based upon an optimization method of adjustment by way of greatest descent, uses a learning curve rate, designated as α in (2), to adjust the weights slowly. The error values for the output layer, shown in the brackets in (2), are transmitted backwards through the network in a similar way as described in (1) to determine the error values for the hidden layer. Once the error values have been determined, the weight adjustments can be obtained for other connections within the network. Through many iterations of the training dataset, the weights within the neural network can be optimized.

For the purposes of this study, the training was conducted by repeatedly introducing a training set of input-to-output data to the neural network, until an RMS error, E, reached a minimum value. Using q datasets within the training routine, the error was found using the following equation:

$$E = \sqrt{\frac{1}{q}\sum_{i=1}^{q}\sum_{k=1}^{p}(t_k - O_k)_i^2}. \tag{3}$$

After the entire collection of training sets was used in adjusting the weights once, called an epoch, an RMS error was computed. The network was then constrained to learn for a specific number of epochs before ending the training process. The number of epochs required was large enough to find a minimum RMS error point for the training sets.

2. Experiment

Several experiments were performed on flat aluminum panels (Al 2024-T3) to determine the ability of an artificial neural network to analyze damage within a structural element. Two different panels were designed and used: one with a width of 6 in. and a thickness of 0.032 in. and another with dimensions of 4 in. wide and 0.05 in. thickness. Detailed dimensions of the panels are illustrated in Figure 6. Flat, thin panels were used to simplify the experiments. Two different methods were investigated to utilize a neural network to determine the severity, or extension length, of the crack growth and the position of a crack tip. These experiments are reported on in Sections 2.1 and 2.2, respectively.

2.1. Magnitude of Crack Extension. The first series of experiments focused on determining the extension of a crack over a short period of time using an acoustic emission system. In the case of stable crack growth, further extension will cease after a specific crack length is obtained. The crack will not extend further until a certain load condition is applied. These small crack extensions consist of rapid increasing bursts that

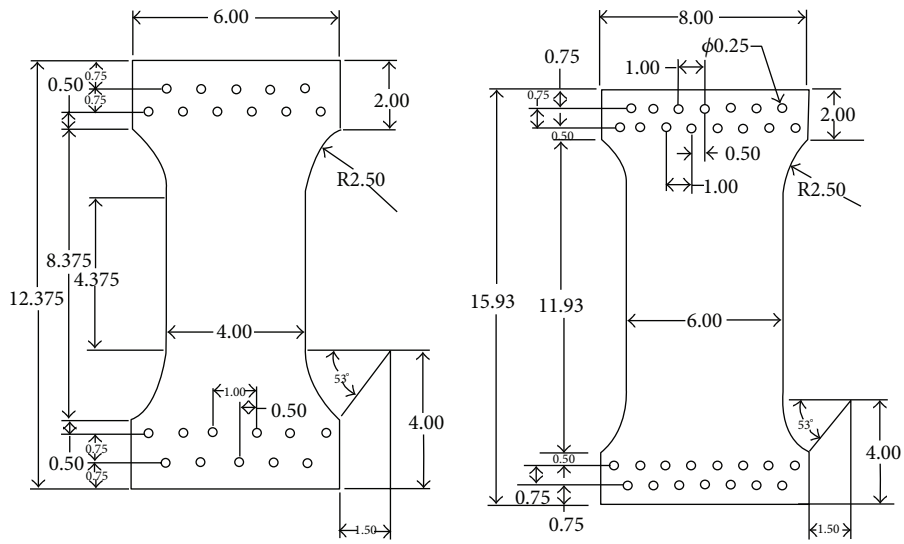

(a) Panel used for severity analysis thickness of 0.050 in.

(b) Panel used for location analysis thickness of 0.032 in.

Figure 6: Dimensions of test panels used for experiment. Panels consisted of Al 2024-T3.

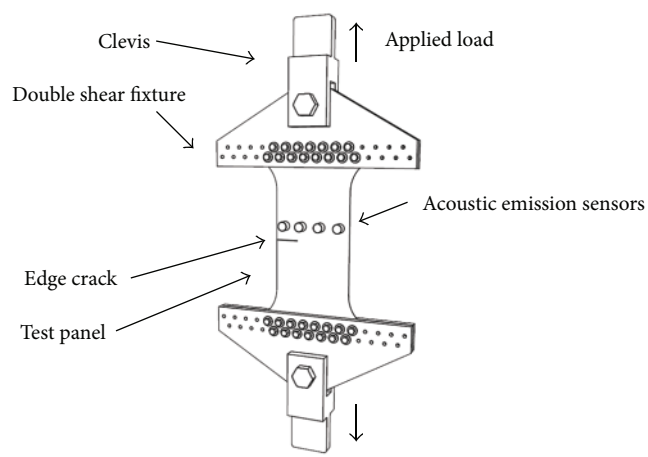

(a) Setup for test panel. Panel is seen in pin, clevis setup to be mounted into MTS Sintech 5/G machine

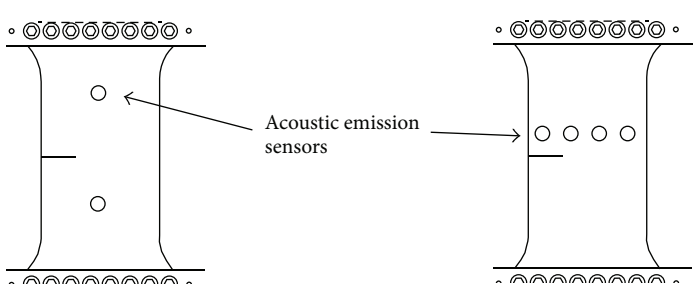

(b) Sensor placement for crack severity. Acoustic emission sensors mounted in a line perpendicular to crack plane of the edge crack

(c) Sensor placement for plastic zone location trends. Acoustic emission sensors mounted in a line parallel to the crack plane of the edge crack

Figure 7: Test panel setup for detecting strain waves from crack propagation. Setup for test panel in pin, clevis setup to be mounted into MTS Sintech 5/G machine.

are close to instantaneous. The purpose of these experiments was to use the detections of an acoustic emission system for a known crack extension to train an artificial neural network to link certain detections to specific crack length growths. The trained ANN could later be used to determine the length of a crack from acoustic emission measurements.

Figure 6 contains drawings that detail the dimensions of the two different test panels used in the experiments. The panel, shown in Figure 6(a), was subjected to a uniaxial tensile load to initiate crack extension in order to measure the magnitude of an increment of crack growth. An initial crack was cut into the panel from one of the side edges in the test region, and then the panel was statically loaded with an MTS Sintech 5/G machine through a pin and clevis setup as illustrated in Figure 7. The loading was gradually increased, until crack extension occurred. The crack length was measured at specific load intervals by an observer, using digital calipers. These measured crack lengths were used to create a learning dataset for an artificial neural network. Likewise, they were used to compare the crack extension calculated with a neural network relative to the actual measured values. The acoustic emission sensors, located as shown in Figure 7, continuously monitored for any crack growth during the increasing-load process. The recorded acoustic emission signals were later used for analysis with an artificial neural network. Only two sensors were used for this test since crack growth size was desired and not the position of the crack (see Figure 7(b)). The sensors were placed at similar positions away from the crack tip to avoid any effects of plastic zone deformation as well as confirm that the sensors were functioning properly.

A neural network analysis program could not be added to the Physical Acoustics software [4] used to measure the strain waves in the test samples. Therefore, the measured strain wave data were exported and post-processed. A dataset was created with the acoustic emission software, the measured elapsed time, and the wave characteristics for analysis, described in the following paragraph. The commercial software, NeuralWorks [6], was used to create the neural network to generate the datasets. A MATLAB [5] program was created to simulate receiving the strain waves over time. This was performed to recreate the experiment in a controlled program, allowing ease of data manipulation. During the performance of the actual experiment software constraints did not allow the ability to link a neural network analysis feature to the acoustic emission software. Thus, MATLAB programming was used to post-process the experimental data using ANNs.

The strain wave data were received continuously over time. For an artificial neural network input dataset, a small time interval was used for determining the increment of crack growth associated with the large number of strain waves detected over the short period of time of the crack extension. The energy values from each detected wave were placed into a 10 bin histogram. The output consisted of the change in crack growth or difference from initial size to final size over that time step. These input and output datasets were used in the network architecture, illustrated in Figure 8. Experimenting with different network architectures, two hidden layers were found to increase precision and accuracy of the output values, while minimizing the processing time of the network. This neural network system proved to work well for predicting the magnitude of crack growth for a flat panel.

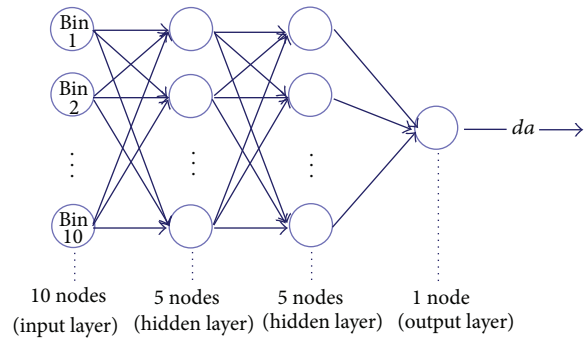

Figure 8: Artificial neural network created to determine the extent of crack growth for a small time interval.

2.2. Crack Positioning. The next series of experiments focused on crack location and the effects of sensor placement, relative to a crack tip position. The purpose of the experiment was to develop an artificial neural network system, which could relate to the detections acquired from nearby acoustic emission sensors and determine the location of the crack tip from which the strain waves originated. Although more research will be required to develop an artificial neural network capable of this process, the research described in this paper concerns the theoretical aspects. Through a simple experiment the relative detections of neighboring acoustic emission sensors were compared by an observer. Based upon existing trends a neural network could be developed and trained to find similar trends. The inputs consisted of the same detected wave over several acoustic emission sensors; in this case, the maximum amplitude of each detected wave was the characteristic used. The output of the artificial neural network was the position of the crack tip from which the wave originated.

Four acoustic emission sensors were used for the crack positioning experiment. These were placed in a line parallel to the plane of the edge crack (see Figure 7(c)). This positioning allowed for sensors to lie ahead of the crack front and other sensors to be behind the crack front. The purpose of this experiment was to determine the validity of the theory described earlier relative to the influence of the plastic zone on the characteristics of the strain waves in the structure.

3. Results and Discussion

The crack extension calculated by an artificial neural network (ANN), using the measured acoustic emission strain wave data, was compared with the actual measured crack extension for both training and testing datasets. The abilities of the ANN were assessed using an RMS error in comparison to the actual and values predicted by the ANNs. The concept of plastic zone interference on the release of strain waves in the material was examined as well, leading to possible future

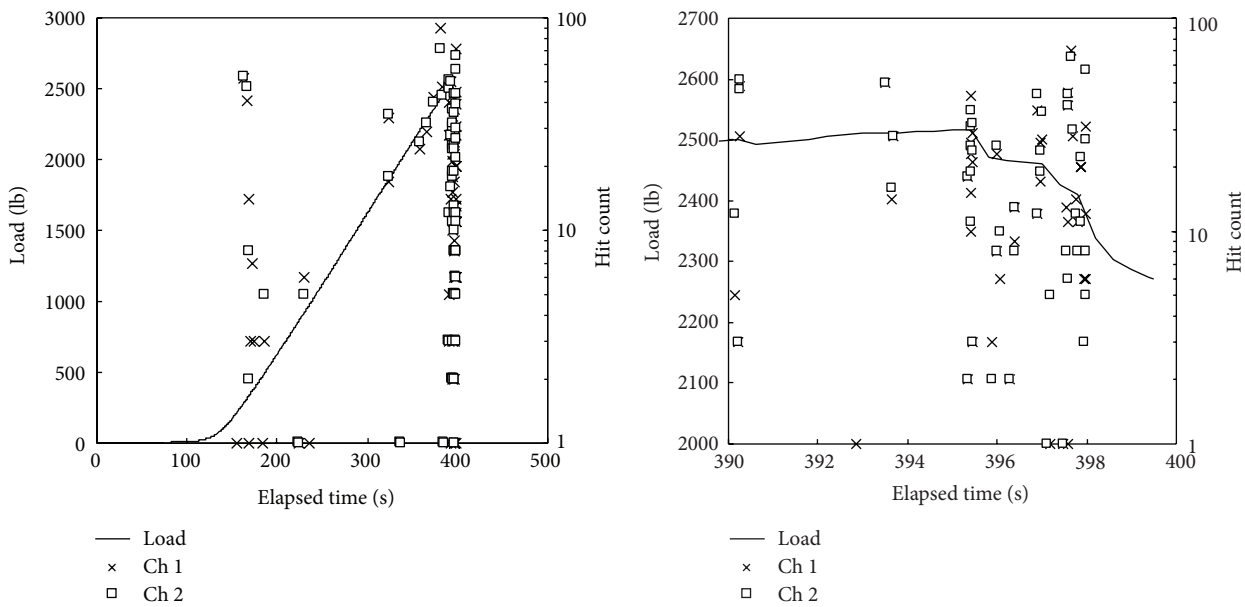

(a) Acoustic emission detections from the entire experiment

(b) Acoustic emission data during the crack extension

Figure 9: Example of test results for panel load to onset of crack extension. Each point on the plot is a single strain wave detected by either sensor 1 or 2. Although some measurements appear simultaneous in recording, there are microseconds between recordings.

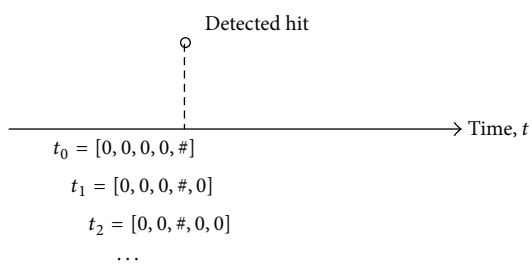

Figure 10: Example of the sliding time window used for experiment.

research. The neural networks created for this research were capable of detecting the actual crack extension of the test set.

3.1. Magnitude of Crack Extension

3.1.1. Training Datasets. The MTS machine was configured to increase the tensile load necessary to produce a displacement in the test section at a rate of 0.01 in./min. The instrumentation of the MTS machine tracked the loading force applied to the test specimen, as well as the applied displacement of one end of the specimen with respect to the other as a function of time. At a specific applied load the crack increased in size as evidenced by a sudden drop in the force applied and a corresponding sudden increase in the number of strain waves detected by the acoustic emission system. In addition any crack extension greater than 0.05 in. was audible to the observers of the experiment. As soon as these phenomena were detected, the MTS machine was manually turned off, so that the displacement did not increase further and the applied load went to zero. The crack length was measured, using a digital calipers, and the displacement of the load heads was reset to the original position. This process allowed for acoustic emission detections for a series of finite increments of crack growth, which could then be used for a training set for an artificial neural network to identify a crack extension event.

The data contained in Figure 9 illustrate the results for one of the experiments using the method described above. For this case, crack growth began around 396 sec after the initiation of the applied load. Sudden decreases in load indicate instances of crack extension. As shown in Figure 9(b), a plot zoomed into the crack growth time period; there were five different instances where increments of crack growth occurred (390 sec, 393 sec, 395.2 sec, 397 sec, and 398 sec). An accurate measurement of crack length growth was only possible to be taken before and after applying load to the panel. The percentage of the total crack growth at each instance was estimated, such that the cumulative crack growth equaled the measured change of the crack length.

Once increments of crack growth were estimated for each intermediate time step, the entire elapsed time from the beginning of loading was broken down into eight second intervals of time or time windows. A sliding time window for real-time monitoring was created that stepped through time at a step of 1.6 seconds. This procedure allowed for multiple readings from the same detection (see Figure 10). Within each time window, multiple detections could be observed. These were normalized into a histogram of the data within the time window, thus removing any time dependence. A histogram was made of 10 bins, grouping the values of the energy value of each strain wave between zero and a normalized maximum value of 100. The energy value had exponential

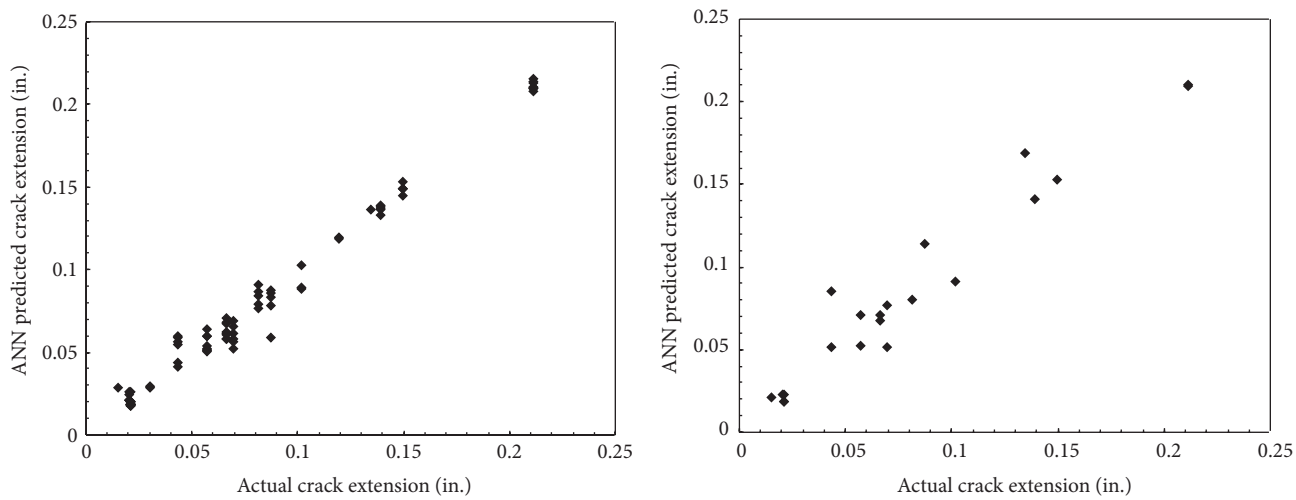

(a) Training dataset

(b) Testing dataset

Figure 11: Results of training an artificial neural network to determine the magnitude of crack growth. These plots relate the target, or measured, size of crack growth in inches to the estimated ANN results. The correlation between the target values and ANN results was 0.9872 for the training dataset and 0.9453 for the testing dataset.

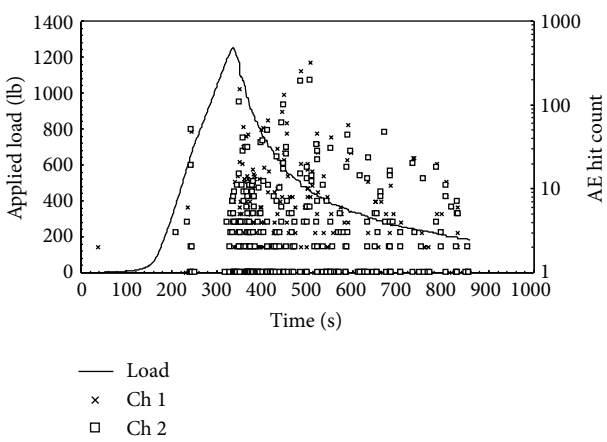

Figure 12: Strain wave detections of acoustic emission sensors from a panel under tensile loading. Initial crack extension occurred around 360 seconds and continued under displacement control.

Table 1: Example data sets of histogram values and respective crack growth sizes. Time listed is for the start of the time window.

Time (sec)	Histogram values	Crack growth present ("yes," "no")	Crack growth size (in.)
381.80	0 0 0 1 0 0 1 0 0 0	0 1	0
383.40	0 0 1 2 1 0 0 0 0 0	0 1	0
391.40	16 7 4 7 0 1 0 0 0 0	1 0	0.1495
396.20	9 4 1 3 1 2 0 0 0 0	1 0	0.0299

characteristics, so a logarithmic scale was used. Some strain waves had an energy value of zero. Thus the logarithmic value was not taken from these values. Finally each time value was provided a crack growth amount and a grouping of either crack growth present or not. Four examples of the final datasets are provided in Table 1.

Two artificial neural networks were created for two separate purposes. Both neural networks used the ten histogram bin values as input sets. The first network, named the "yes-no network," was a self-organizing map. This network was used to classify each time window into two groups; "yes" crack growth was present or "no" crack growth present. This was accomplished with a network with a Kohonen layer of 20 nodes × 20 nodes. The neighborhood started at 15 nodes and was decreased with each epoch until grouping was complete. These nine experiments were used to train this network into the two groups. The Kohonen layer was then connected to two output nodes, each representing either "yes" or "no" to crack growth. The connections between the Kohonen layer and the output nodes were trained with the backpropagation, using the NeuralWorks software Delta rule, and used hyperbolic tangent activation functions. The purpose of this network was to filter out noise from the strain waves corresponding to actual crack growth.

With this first network being completely trained a second neural network, called the "severity network," was constructed. This severity network used the histogram values to determine the crack growth extension in inches. The network was trained with the measured data of the nine experiments, using only the time windows where crack growth was present. It consisted of a backpropagation network with two hidden layers of five nodes each. Again, Delta rule training was used along with hyperbolic tangent activation functions. The results of the training process are presented in Figure 11. From the nine experiments, 106 datasets contained one of the defined crack growth times. From this, 85 were used to train the neural network and the remaining 21 were used to initially test the abilities of the neural network. The network was trained for 50,000 epochs or iterations through the datasets.

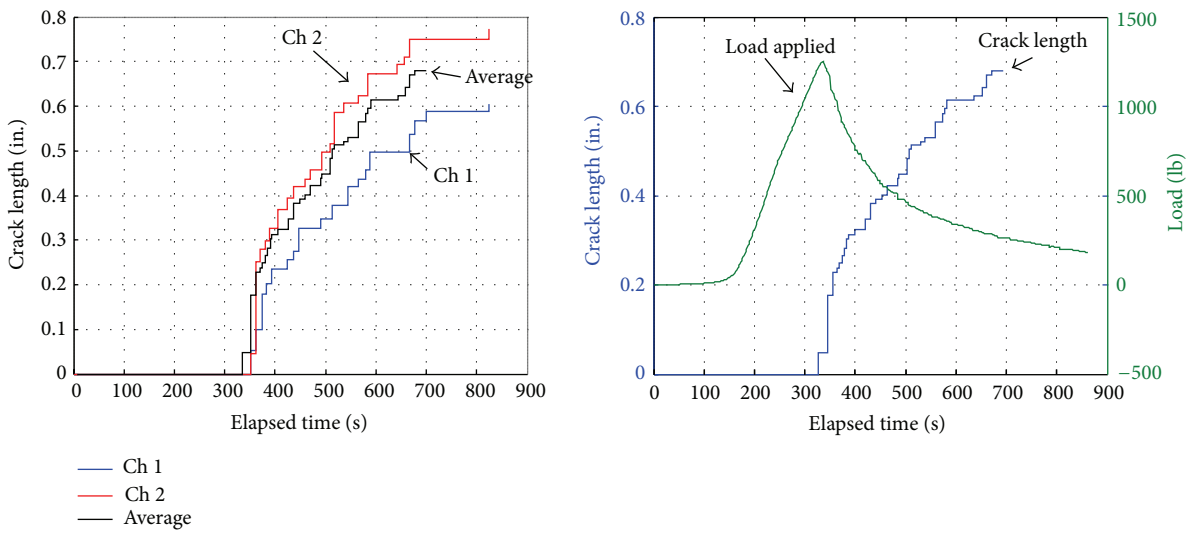

(a) Individual sensor predictions

(b) Average crack length from both sensors. Loading curve displayed as well

Figure 13: Crack growth length over time, approximated by neural networks.

This number of iterations through the training data allowed for the RMS error of the network to be minimized. Figure 11 shows the results for the trained and testing datasets used in the neural network. The graph on the left contains a display of the output relationship between the crack lengths measured values and the length of the crack, estimated by the artificial neural network. The graph on the right shows the results from the testing datasets. This figure shows the relation between the measured size of the crack extension for each dataset in inches and the output of the trained severity network. The ideal case for the graphs shown in the figure would be a straight line, representing a 1-to-1 ratio between actual measurements and the ANN estimations. Due to complexities, these plots vary slightly but are close to the desired values with a resulting correlation of the plots of 0.9872 for the training dataset and 0.9453 for the testing dataset, which are both close to a value of 1. The predicted values of the ANN differed from the actual crack extensions by 0.003 in. and 0.005 in. with a 95% confidence level. For the testing set with the same confidence level, the ANN differed the predictions from the actual crack extensions from 0.004 in. to 0.015 in. This showed promise for the ability of a neural network to be a useful analysis tool of a structural health monitoring system due to the very small differences between the neural network estimated values of crack growth and the measured crack growth values.

3.1.2. Testing Datasets. Once the two artificial neural networks were created and fully trained, the next step was to use these in a situation, where datasets not previously presented to the networks were used. To accomplish this task, a tenth experiment was conducted. However, for this experiment, the MTS machine was not stopped at the initiation of crack growth but instead allowed to continue increasing displacement over an extended time. The experiment was finally stopped around the 850 second mark. The detections of strain waves for this experiment are reported in Figure 12. Only the initial and final crack lengths were measured for this experiment, but some conclusions could be drawn from the data. The initial crack began to extend at around 360 sec. The crack then slowly increased in size while the panel was loaded in displacement control, until the loading was halted at about 850 sec. The total increase in crack size was measured to be 0.972 in.

The measured AE data shown in Figure 12 indicate that there was a great deal of noise and many strain waves detected after the crack extension was initiated. This dataset was evaluated using the neural networks, using the same time windows as those of the training sets. Histograms were made of ten bins each with the same range as before. This new dataset was first used in the yes-no network. Here the outputs of the network categorized each histogram into either crack growth or noise present. The datasets determined to be crack growth and not noise were then used in the severity network. This network then determined the size of the increment of crack growth over the time window.

This experiment used two separate sensors. The data from each sensor were separated and run through the two neural networks. Figure 13(a) contains graphs of the results of the networks in terms of crack length. As time increased in the experiment, the total crack length increased. Finally an average of the two signals was taken to determine a net crack length value. This average crack growth length is illustrated again in Figure 13(b) along with the load history. The crack length followed the trend predicted by the shape of the loading curve. A sudden increase in the length of the crack occurred at the time crack extension began, and the crack slowly increased in size as the controlled displacement of the MTS machine continued. The final length of the cumulative crack extension length computed using the results of the neural network predictions shown in Figure 13(b) was

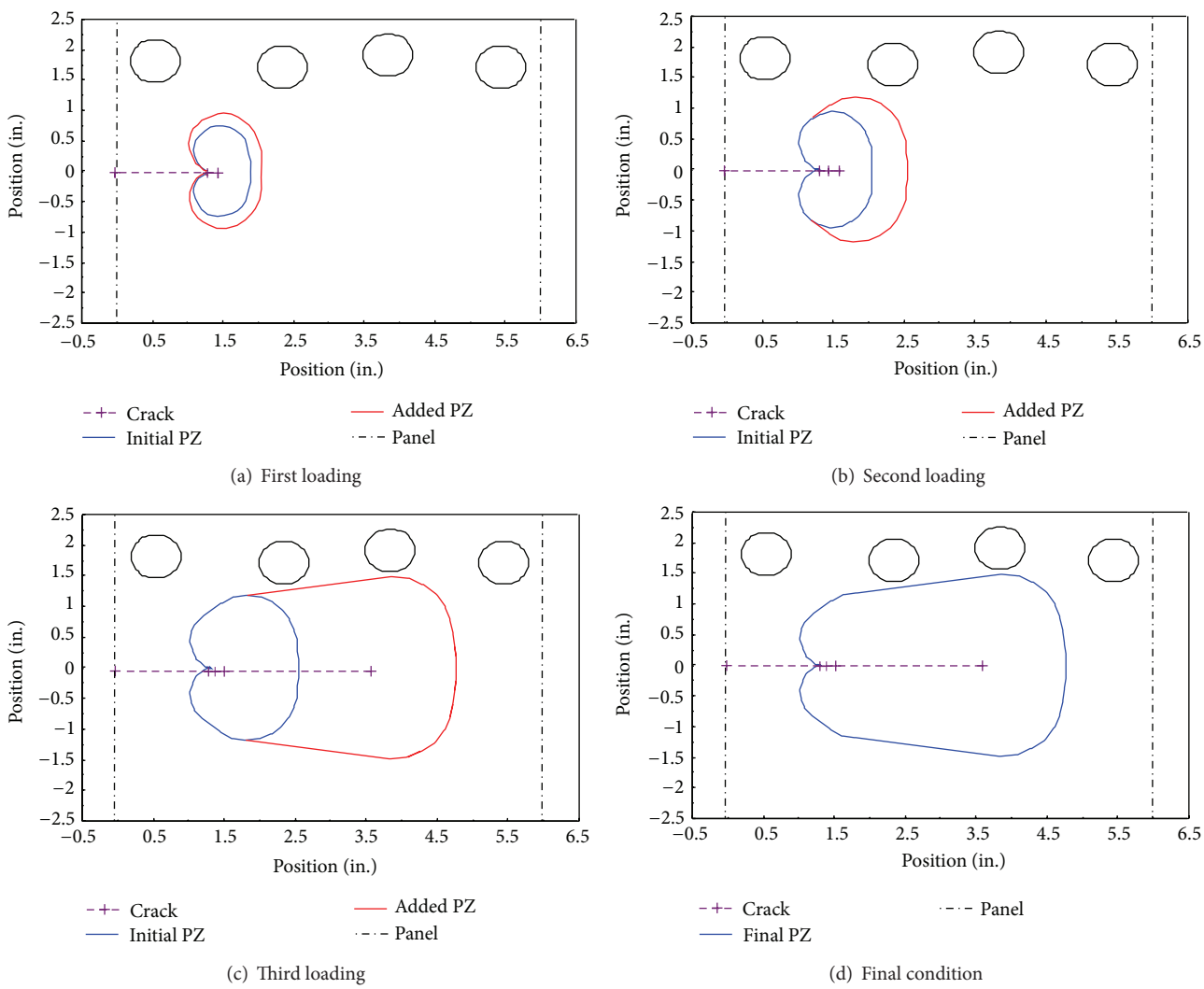

Figure 14: Crack location and sensor placement. Plastic zone is shown around the propagating crack tip. Sensors are labeled Channels 1 to 4 from right to left.

0.6805 in. This measured value of the total crack extension was of 0.810 in. or a difference of 0.13 in. Sensor 2 received more acoustic emission signal detections than sensor 1. Thus, sensor 2 reflected more reliable events and was a more reliable sensor. A weighted average with more emphasis on sensor 2 resulted in an approximation of 0.700 in or a difference of 0.09 in. This difference was considered to be an acceptable approximation for the purposes of this experiment.

3.2. Crack Location and Plastic Phenomenon. Figure 14 illustrates the location of four sensors relative to a crack during crack extension. The plastic zone at the crack tip has been shown to increase in size until the final crack length of 1.98 in. For each increment of crack growth, a single detectable strain wave was produced and is shown in Figure 15. For this experiment, the amplitude of the strain wave was the characteristic of the wave used for comparison. As the crack grew, the single strain wave was detected by each of the four sensors. For crack growths before the final increment the detected amplitudes of the strain waves at each sensor remained close to one another. However, for the large extension of the crack tip the detected amplitudes of the strain wave became skewed. As shown in Figure 15(c) the sensors closest to the crack tip, sensors 2 and 3, received the highest amplitude waves with sensor 1 detecting the third largest amount. The waves detected by sensor 4 had smaller amplitudes compared to the other three sensors. These measured observations support the theory presented earlier regarding the effects of location of the crack tip and growth direction relative to the position of the sensor.

Further, if this trend is recognizable to an observer of the experiment, then an artificial neural network should be able to deduce a similar trend and be able to predict location of a crack by the amplitude of the detected wave. With multiple sensors of known positions detecting the same waves, a comparison between amplitudes of different sensors with known locations might be used to determine the location of the crack tip in a structure.

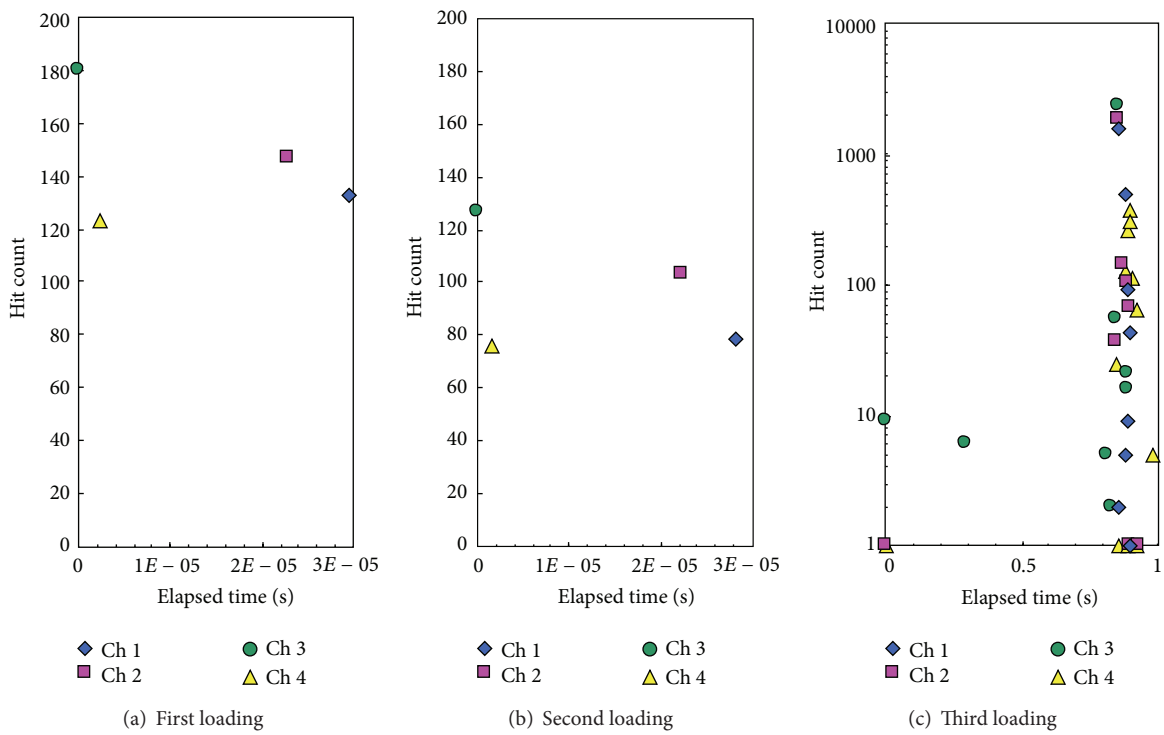

Figure 15: Strain wave detections from crack propagation. The panel was loaded and then unloaded after crack initiation. Each crack "growth" shown is the result of the crack becoming unstable and then stabilizing at a new length.

The proof of concept was examined in this experiment. Due to limited data and knowledge of the wave properties, this process will need to be explored in future studies. Further testing and research will be performed by locating the position of actual crack propagation. Since energy is released at the crack tips, these will be the positions located by the neural network, allowing the entire crack to be determined as the distance between the two close crack tips. This network will then be coupled with a crack severity neural network to determine the ability of neural networks to assess damage detected by an acoustic emission system. Future study will involve combining the severity artificial neural network and a new neural network to determine the location of the crack tip.

4. Conclusion

A novel method of implementing artificial neural networks and acoustic emission sensors to form a structural health monitoring system for metallic structures was presented. Flat aluminum panels, similar in thickness to those found in many aerospace structures, were subjected to increasing static loading during laboratory tests. As the load increased, a crack in the panel increased in size, releasing strain waves into the material. These waves were then detected by acoustic emission sensors, and artificial neural networks were implemented to analyze the strain waves. From a feed-forward neural network, the crack length could be approximated with reasonable precision. Plastic zone influence on strain waves released was also observed during the analysis of the experimental data. Through a second experiment, sensors placed behind the crack front were found to detect waves with smaller amplitudes than the sensors placed in other locations. Future study will involve using this knowledge to train, or teach, an artificial neural network to determine the location of a growing crack based on this difference in amplitude. These two artificial neural networks, coupled with acoustic emission sensors, form the initial stages of the development of a structural health monitoring system for aerospace systems with the capability of determining damage severity and locations within structures.

Nomenclature

ANN:	Artificial neural network
NIAR:	National Institute for Aviation Research
SHM:	Structural health monitoring
E:	Root mean square error
O_j:	Output from node j in an artificial neural network
t_k:	Desired or target values for an output dataset
w_{ij}, v_{ij}:	Weight for path from node i to node j of an artificial neural network
X_i, Y_i, Z_i:	Node i in row of input, hidden, or output layers of an artificial neural network, respectively
α:	Learning coefficient
θ:	Angle of deviation from the plane of a crack.

Acknowledgment

The authors thank the Department of Energy for its support (DOE DE-FG36-08GO88149).

References

[1] J. L. Rose, "Dispersion curves in guided wave testing," *Materials Evaluation*, vol. 61, no. 1, pp. 20–22, 2003.

[2] D. Mateescu, H. Yong, and A. K. Misra, "Analysis of smart structures with piezoelectric strips subjected to unsteady aerodynamic loads," in *Proceedings of the 48th AIAA/ASME/ASCE/AHS/ASC Structures, Structural Dynamics, and Materials Conference*, pp. 3662–3680, Honolulu, Hawaii, USA, April 2007.

[3] T. Kundu, *Ultrasonic Nondestructive Evaluation: Engineering and Biological Material Characterization*, CRC Press, Boca Raton, Fla, USA, 2004.

[4] Physical Acoustics Corporation, *PCI-2 BaSed AE SyStem USer'S Manual, Rev. 3*, Princeton, NJ, USA, 2007.

[5] The MathWorks, Inc., "MATLAB v6. 5. 0. 180913a Release 13 Manual," Software Package, 2002.

[6] NeuralWare, Inc., "NeuralWorks Professional II/PLUS User's Manual," Software Package, 1997.

[7] D. G. Aggelis, E. Z. Kordatos, and T. E. Matikas, "Acoustic emission for fatigue damage characterization in metal plates," *Mechanics Research Communications*, vol. 38, no. 2, pp. 106–110, 2011.

[8] D. Placko and T. Kundu, *DPSM For Modeling Engineering Problems*, Wiley-Interscience, Hoboken, NJ, USA, 2007.

[9] J. Lee, G. Kirikera, I. Kang, and M. Schulz, *Structural Health Monitoring Using Continuous Sensors and Neural Network Analysis*, Institute of Physics Publishing, Smart Material Structures 15, University of Cincinnati, Cincinnati, Ohio, USA, 2006.

[10] G. R. Kirikera, J. W. Lee, M. J. Schulz et al., "Initial evaluation of an active/passive structural neural system for health monitoring of composite materials," *Smart Materials and Structures*, vol. 15, no. 5, p. 1275, 2006.

[11] J. W. Lee, G. R. Kirikera, I. Kang, M. J. Schulz, and V. N. Shanov, "Structural health monitoring using continuous sensors and neural network analysis," *Smart Materials and Structures*, vol. 15, no. 5, p. 1266, 2006.

[12] V. Crupi, E. Guglielmino, and G. Milazzo, "Neural-network-based system for novel fault detection in rotating machinery," *JVC/Journal of Vibration and Control*, vol. 10, no. 8, pp. 1137–1150, 2004.

[13] L. Fausett, *Fundamentals of Neural Networks: Architectures, Algorithms, and Applications*, Prentice Hall, Upper Saddle River, NJ, USA, 1994.

Hindawi Publishing Corporation
The Scientific World Journal
Volume 2013, Article ID 185769, 12 pages
http://dx.doi.org/10.1155/2013/185769

Research Article

CIB: An Improved Communication Architecture for Real-Time Monitoring of Aerospace Materials, Instruments, and Sensors on the ISS

Michael J. Krasowski,[1] Norman F. Prokop,[1] Joseph M. Flatico,[2] Lawrence C. Greer,[1] Phillip P. Jenkins,[3] Philip G. Neudeck,[1] Liangyu Chen,[2] and Danny C. Spina[4]

[1] *NASA Glenn Research Center, 21000 Brookpark Road, Cleveland, OH 44135, USA*
[2] *Ohio Aerospace Institute, NASA Glenn Research Center, 21000 Brookpark Road, Cleveland, OH 44135, USA*
[3] *U. S. Naval Research Laboratory, 4555 Overlook Avenue SW, Washington, DC 20375, USA*
[4] *Jacobs Technology, NASA Glenn Research Center, 21000 Brookpark Road, Cleveland, OH 44135, USA*

Correspondence should be addressed to Norman F. Prokop; norman.f.prokop@nasa.gov

Received 12 April 2013; Accepted 4 June 2013

Academic Editors: T. E. Matikas and M. R. Woike

The Communications Interface Board (CIB) is an improved communications architecture that was demonstrated on the International Space Station (ISS). ISS communication interfaces allowing for real-time telemetry and health monitoring require a significant amount of development. The CIB simplifies the communications interface to the ISS for real-time health monitoring, telemetry, and control of resident sensors or experiments. With a simpler interface available to the telemetry bus, more sensors or experiments may be flown. The CIB accomplishes this by acting as a bridge between the ISS MIL-STD-1553 low-rate telemetry (LRT) bus and the sensors allowing for two-way command and telemetry data transfer. The CIB was designed to be highly reliable and radiation hard for an extended flight in low Earth orbit (LEO) and has been proven with over 40 months of flight operation on the outside of ISS supporting two sets of flight experiments. Since the CIB is currently operating in flight on the ISS, recent results of operations will be provided. Additionally, as a vehicle health monitoring enabling technology, an overview and results from two experiments enabled by the CIB will be provided. Future applications for vehicle health monitoring utilizing the CIB architecture will also be discussed.

1. Introduction

The International Space Station is a unique space vehicle in that it is currently the largest artificial satellite in orbit around the Earth. The U S portion of the ISS has been designated as a national laboratory by the Congress. The ISS provides a unique environment of extreme hot-cold thermal cycling, cosmic radiation exposure [1], atomic oxygen presence, vacuum, and microgravity. This allows for long duration experiments and space testing of devices and structures. While testing and experiments take advantage of this unique environment, facility equipment must operate reliably in it. Electronic components and integrated circuits (IC) are especially susceptible to radiation effects from the environment in LEO. These effects can present themselves in two ways: long-term dose damage associated with total ionizing dose (TID) or through single event effects (SEE). Long-term or TID results in permanently damaging an IC by altering the crystal lattice of the semiconductor, which can result in changing bias voltages and currents which affect circuit operation. Where single event upsets (SEU) are transient, energy is transferred from ionizing particles to the IC. This energy transfer is localized, so individual transistors on an IC are affected. Single events caused by radiation may only result in the flip of a single bit or the corruption of an analog signal. If an affected bit is part of an instruction for microcontroller or processor, the result could result in operational failure. Further, an SEE-induced phenomenon known as a single event latchup (SEL) could also result in a loss of data but, in extreme cases, may cause a hard destructive failure which could result in the

permanent loss of a circuit component. With this in mind, care must be taken in the design of any electronic system expected to operate reliably on the ISS for extended period of time and be tolerant of the expected radiation environment.

To support science payloads, the ISS as a facility provides three telemetry communications interfaces [2] for resident experiments with its associated physical layer/protocol: low rate data link: MIL-STD-1553; medium rate data link: Ethernet; and high rate data link: fiber optic. Each interface can provide telemetry to the ground. Increased bandwidth comes with increased cost in development to meet the physical interface requirements. The only interface available throughout the ISS is the MIL-STD-1553 bus. In addition to telemetry data, the Mil-STD-1553 bus performs the command, health, and status data transfer. This is done for safety reasons, so that health and status data are transmitted on the most reliable communication bus.

The MIL-STD-1553 [3] "Aircraft Internal Time Division Command/Response Multiplex Data Bus" defines a physical layer as well as a bus protocol. The MIL-STD-1553 bus is highly reliable and robust in that it is a deterministic command and response protocol. The ISS adds additional layers to those of the MIL-STD-1553 standard, in effect making the ISS MIL-STD-1553 implementation a superset of the military standard. Which allows ISS MIL-STD-1553 hardware to interface with other space and aircraft platforms, but not necessarily the converse. The MIL-STD-1553 bus is deployed on numerous U S military aircrafts including the F-16 Falcon, F/A-18 Hornet, AH-64 Apache, and P-3C Orion and has also been adopted by North Atlantic Treaty Organization (NATO). The MIL-STD-1553 bus transmits data at 1 Mbit/second. The command and response protocol of the bus adds overhead, reducing the effective bit rate for data transfer. In addition, the ISS adds overhead to the bus transfers. One layer added by ISS to the MIL-STD-1553 telemetry is the Consultative Committee for Space Data Systems (CCSDS) headers, which allow for data telemetry routing in space. Each node in the telemetry system is provided with a unique application identifier (APID), which is part of the CCSDS header, to enable routing. These APIDs allow a user on the ground to receive telemetry and command their node from anywhere with internet connectivity. The ISS allots 12.8 kBytes of telemetry data per second, some of which is used for overhead. The ISS allows commands from the ground to be routed to APIDs residing on the MIL-STD-1553 bus.

Onboard the ISS, there is an Express Logistics Carrier (ELC) facility which is primarily designed to store ISS replacement parts but also has two science payload slots per platform [4]. Each science payload site has 28 V and 120 V power available. A MIL-STD-1553 communications repeater (bus controller) link to the ISS is also provided by the ELC, allowing telemetry data to pass through.

The CIB was needed to be the communications backbone for a permanent testbed on the ELC of the ISS which would utilize the ISS telemetry of the MIL-STD-1553 bus. The CIB needed to provide simpler communication interface to experimenters while maintaining the reliability expected of a space flight system on the ISS. The CIB needed to be designed with radiation tolerance and reliability as primary considerations. The CIB was designed by the NASA Glenn Research Center (GRC) Mobile and Remote Sensing (MaRS) Laboratory. The first experiment set to utilize the testbed was the Materials on the International Space Station Seven (MISSE7) [5]. MISSE7 was comprised of numerous passive experiments and over 21 active experiments using the command and telemetry capabilities provided by the CIB. MISSE7 used two Extra-Vehicle Activity (EVA) deployable suitcase-like containers called a Passive Experiment Container (PEC) in which numerous experiments are contained. These PECs are carried by astronauts, opened, and mounted on the ELC. When the experiment was completed, an additional EVA was used to retrieve the PECs and install a new one for the follow-on experiment set, MISSE8. This exchange required a physical communications link which was swappable. The need for on-orbit exchange of PECs required a physical communications link robust enough to withstand potential damage encountered during the swap.

The CIB was installed during Space Transportation System-129 (STS-129) and is currently flying on the exterior of the International Space Station mounted on the Express Logistics Carrier 2 (ELC-2). The CIB provides a simple, RS-485-based communications interface between experiments, instruments, or sensor systems and the ELC's MIL-STD-1553 bus. This allows developers to design on simple platforms without having to confront the difficulty of integrating their experiments directly into the ELC or the ISS. The CIB currently provides serial communication supporting twenty active systems. Figure 1 shows the CIB within the MISSE7 communication architecture including the interface to the ISS telemetry through the ELC. Follow-on experiments (MISSE8) leave the CIB in place and swap out one or both of the allowed PECs.

This paper will discuss in detail the technical development and design of the CIB hardware and architecture. Recent results from current operations aboard the ISS will be provided. Specific experiments supported by the CIB like a Silicon Carbide Junction Field Effect Transistor (SiC JFET) health monitoring and a solar cell health monitoring will be discussed. Future health monitoring applications to include node to node schemes will also be briefly discussed.

2. CIB Design

The CIB is designed to be a highly reliable and radiation hard communications bridge from the ISS/ELC MIL-STD-1553 to onboard experiments, sensors, and health monitoring systems. The CIB is constructed from components designed or known to be radiation tolerant of LEO conditions for over 20 years of operation. Further, the CIB is designed to be tolerant of the electrostatic discharge (ESD) anticipated to occur during removal and insertion of new payload systems over multiple missions.

Communications over each RS-485 bus was limited to 9600 baud, which is 9600 bits of data per second for eight bit words. Though theoretically capable of at least ten times this bandwidth, the CIB was designed for 9600 baud as a consequence of some experiments in MISSE7 being only capable of that rate due to hardware or software constraints. Thus,

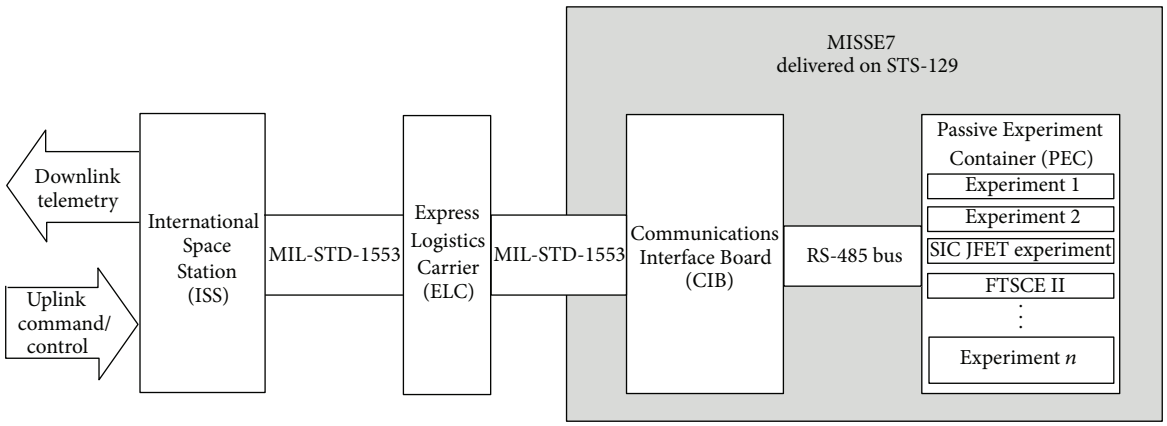

Figure 1: Diagram of the MISSE7 communication architecture and interface to the International Space Station telemetry through the Express Logistics Carrier.

the lowest common denominator dictated bus speed. A reprogrammed CIB could support higher baud rates and could dynamically change baud rate to accommodate each experiment. A block diagram of the CIB interfaced to a string of experiment systems is given below in Figure 2. Note that all systems interface to the CIB via a full duplex RS-485 bus system and each system has associated with it a unique hardware enable line.

3. Hardware Interface

The RS-485 standard specifies a multidrop serial bus which can be full or half-duplex. The CIB implements a full duplex multidrop bus, where each experiment or sensor is a stub or drop on the bus, and reception and transmission happen on separate lines. Since MISSE7 was to support two physically separate experiment containers, the designers provided two RS-485 buses from the CIB, one for each container. The multidrop bus provides a concern for reliability as one errant transceiver can corrupt the bus. To mitigate against this risk, the CIB implements a hardware transmission enable, as well as requiring a software enable function on the experiment side.

Experimenters must provide a hardware handshaking interface as shown in Figure 3, wherein the enable line from the CIB is shown schematically to provide one half of a signal set necessary to enable a system's transmit hardware. The second half of the signal set is provided by the system through response to an initiating packet transfer from the CIB on the RS-485 bus containing the system's APID. This interface prevents experiments from transmitting without being selected and communicated to by the CIB. The interface must be implemented in hardware so that the experiment cannot interfere with the RS-485 bus during communications slots not associated with it. The cause of this out of order bus use could be the result of a software failure, for example. The CIB maintains a permission bitmap that can be overwritten by a command from the ground. If a given experiment is locked out via the bitmap (for any number of scheduling reasons or after detection of system failure), its enable is never asserted and is prevented from communicating.

This transmission scheme allows for the full duplex hardware Universal Asynchronous Receiver Transmitter (UART) common to most microcontrollers/microcomputers/computers or which can be easily configured into programmable logic or as a software UART routine on microcontrollers which allow for interrupt on transition. Thus, systems may be easily configured using simple and available hardware and design tools.

The byte format is 8 bit, one start bit, stop bit, and no parity. The baud rate is 9600 which simplifies requirements for the simpler hardware and offer forgiveness in timing and deskew.

The CIB rotates around through its list of 20 APIDS, polling each experiment one at a time, in order, as long as power is applied. This method is chosen as the desired way to maximize bandwidth for the experiments. If a system needs to pass more than one packet set of data, it merely waits until the CIB returns to it at a later time.

In addition to the transmission lines (TX), receive lines (RX), +5 Volt power, and ground are the enable lines for the experiments. Within the example experiment hardware is the logic to enable failsafe transmission on the shared RS-485 bus as required by the CIB Interface Control Document [6]. The separate enable wire provided to each experiment is detailed in the following illustration in Figure 4.

An enable line is pulled low for a particular system prior to the CIB transmitting to that system. A 10 Volt transient absorber (dual redundant 5 volt transient absorbers) and a 1 kΩ resistor occupy the output of each enable line as shown in Figure 4 and are present to mitigate against electrostatic discharge and also to a short to +28 condition should it occur at an experiment. As noted earlier, the enable wire is used by the system to enable its transmitter hardware if it has also received a valid packet from the CIB. Commencement of the packet transfer from CIB occurs no less than 250 ms from the assertion of enable. This enable signal removes the obligation of the systems from having to monitor all the traffic on the TX line while listening for transmissions dedicated to themselves.

Also, this active low enable signal can be used to locally enable a pass element to provide the system power. Thus, an experiment may come alive upon a powerup initiated by this

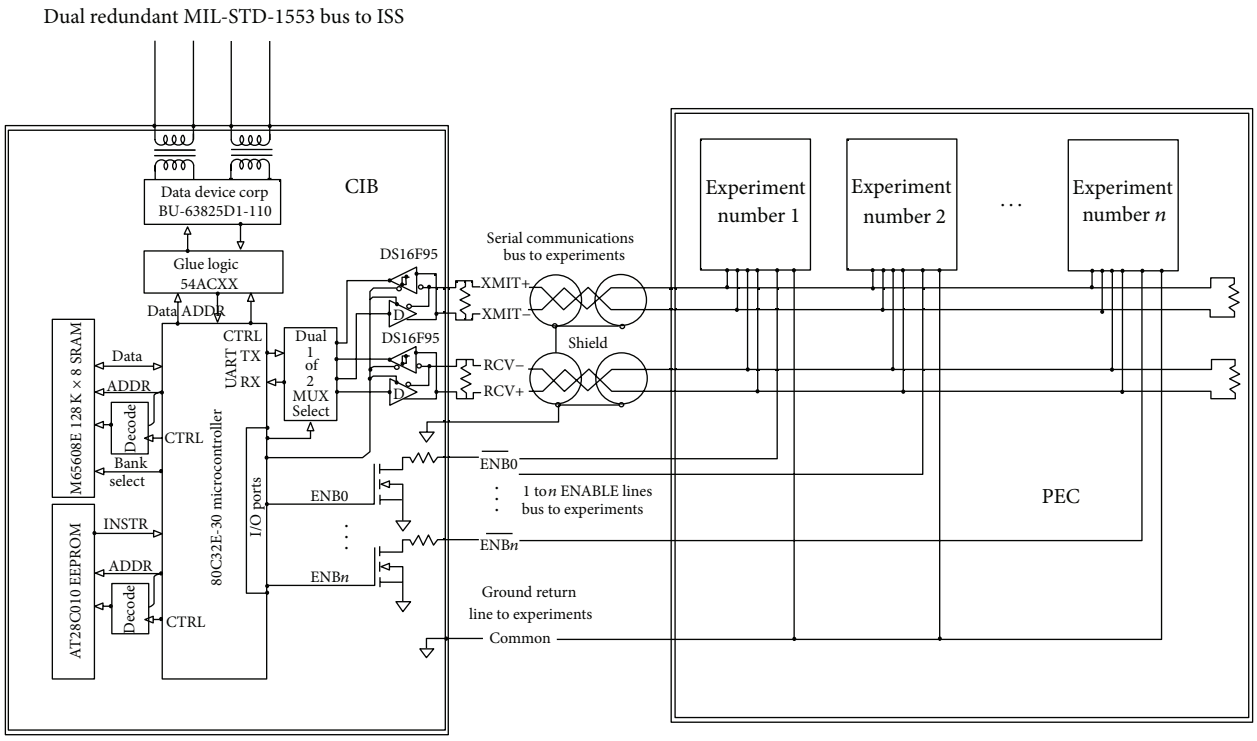

Figure 2: A block diagram of the Communications Interface Board (CIB) interfacing between the International Space Station (ISS) MIL-STD-1553 bus and the experiments residing on the Passive Experiment Container (PEC) (image courtesy of NASA).

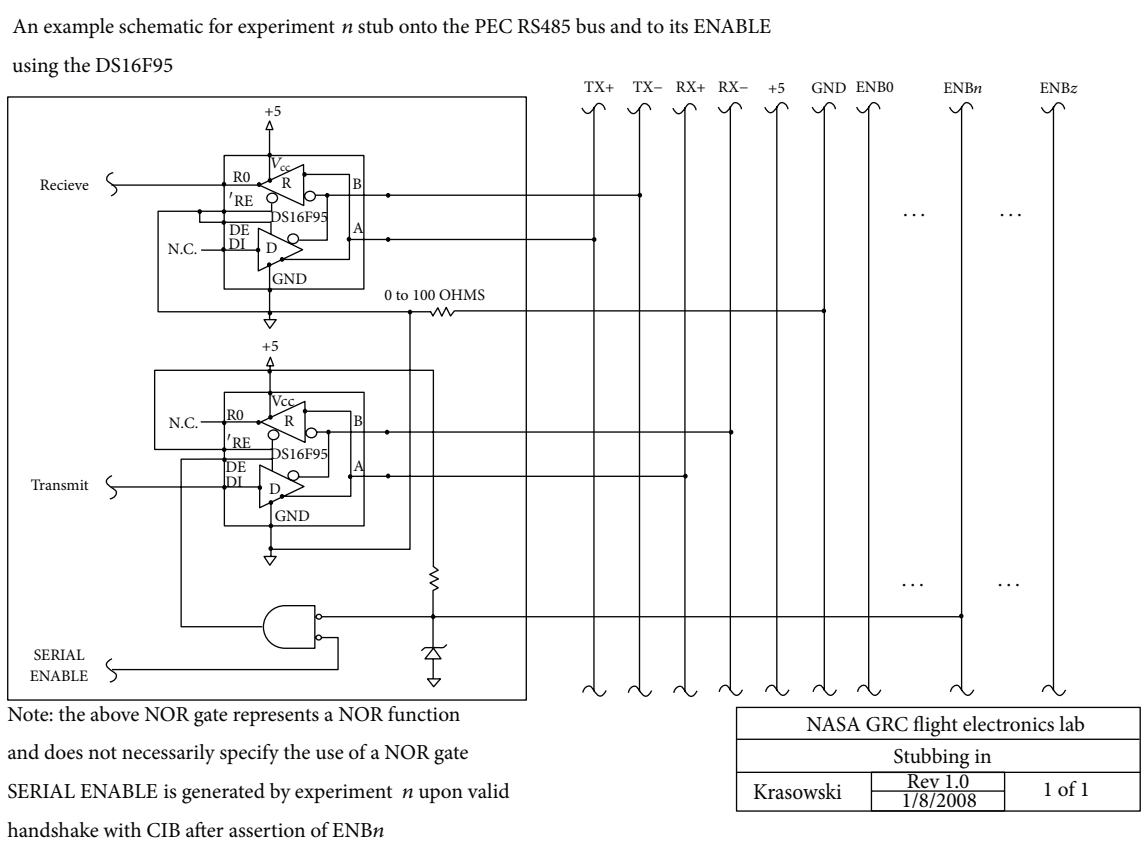

Figure 3: Schematic diagram of the RS-485 bus interface provided to experiments by Communications Interface Board (CIB) (image courtesy of NASA).

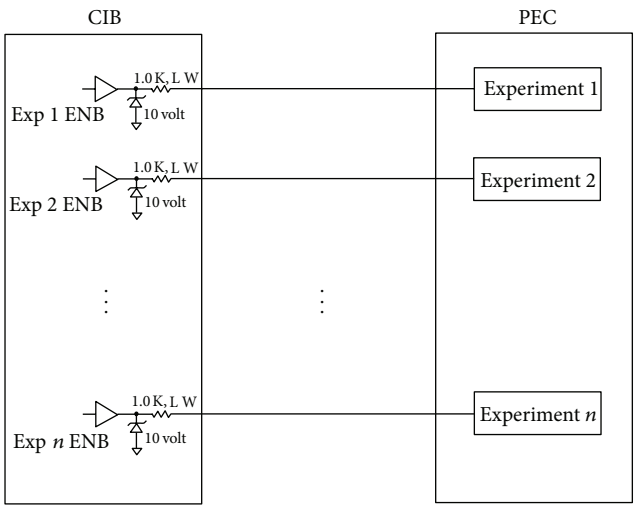

Figure 4: Schematic of the CIB enable lines for experiments onboard the Passive Experiment Containers (PECs). Current limiting resistors as well as voltage limiting Zender diodes to protect CIB enable circuitry from experimental failure are shown within the CIB (image courtesy of NASA).

signal. The systems are expected to be capable of accepting a packet from the CIB 250 milliseconds from the assertion of the enable, and so boot-up must occur consistent with this delay. Failure to receive this command and reply after 250 ms results in the CIB disasserting the enable line and moving on to the next experiment. This is of consequence to a system which uses the time between sequential acquisitions of itself by the CIB to perform its tasks. After completion of task and data transfer with the CIB, a system may turn itself off. Removal of power when not operating reduces some radiation total dose effects and can also remove the conditions for and thus clear a nondestructive latchup.

Each transfer starts with a packet from the CIB containing the experiments APID, and so theoretically experiments do not need to consider the state of an enable line but merely listen for their APID. Given this fact and since the two communications busses are RS-485 links, with proper wiring considerations, over thirty experiments per RS-485 bus are possible with a reprogrammed CIB.

4. Software Description

The CIB firmware is built on a commercially available real-time kernel. The firmware consists of serial input/output, CCSDS packet building, time keeping, and MIL-STD-1553 support modules in addition to top-level modules that manage data handling and poll experiments.

Data handling is straightforward. Experimenters have only to implement a very simple protocol to enable communication. All packets have a fixed length. Command packets are 116 bytes long, data packets are 1274 bytes long, and acknowledgment packets are 10 bytes long [6]. The CIB will query experiments one at a time. Each query has the form in Box 1.

The firmware packs experiment data into CCSDS packets for transmission and unpacks commands received from the ground. This relieves developers from the task of implementing CCSDS packet handling.

Experiments can be controlled through commands of up to 104 bytes in length. No processing is done on commands by the CIB; they are simply passed to the experiment. Commands may contain any kind of data including firmware updates. Experiments are polled in round-robin fashion, each transaction requiring roughly 2.5 seconds. Experiments can transmit up to 2 MB/day. An experiment may receive a command from the ground or transmit data during a single transaction. Data from the experiment is wrapped in a CCSDS packet and buffered in the MIL-STD-1553 transceiver.

MIL-STD-1553 transactions occur in frames. The minor frames contain different transactions. A major frame consists of minor frames. The major frames are repeated. The ELC uses ten 100 ms minor frames for each major frame. The result is that data packets received from experiments are buffered a maximum of one second before being transmitted on the MIL-STD-1553 bus. In addition to passing data, the MIL-STD-1553module initializes the transceiver, updates the time, and transmits the health and status packets of Table 1 once per major frame.

5. CIB Hardware

The core of the CIB is the 80C32E-5962-0051801QQC radiation tolerant 8 Bit ROMless microcontroller. This performs all processing functions within the system. The 80C32E has the following environmental operating specifications [7]: temperature range is military (−55°C to 125°C), no single event latch-up (SEL) below a linear energy transfer (LET) threshold of 80 MeV/mg/cm^2, and is tested up to a total dose of 30 krads (Si) according to MIL-STD-883 method 1019.

Program memory for the CIB is stored in the AT28C010-12DK-MQ-128Kx8 parallel EEPROM which is reprogrammable in circuit at the bench but which is not reprogrammable on-orbit. The AT28C010 has the following environmental operating specifications [8]: temperature range is military (−55°C to 125°C), no SEL below an LET threshold of 80 MeV/mg/cm^2, and is tested up to a total cose of (according to MIL-STD-883 method 1019): 10 krad (Si) read-only mode when biased and 30 krad (Si) read-only mode when unbiased.

Dynamic memory for the CIB is embodied in an M65608E-5962-8959818MZC radiation tolerant 128Kx8 very low-power Complementary Metal Oxide Semiconductor Static Random Access Memory (CMOS SRAM). The M65608M has the following environmental operating specifications [9]: military temperature range is (−55°C to +125°C), no SEL below a LET threshold of 80 MeV/mg/cm^2 @ 125°C, and is tested up to a total dose of 30 krad (Si) according to MIL-STD-883 method 1019.

MIL-STD-1553 communications are effected through the BU-63825D1-300 Space Advanced Communication Engine (Sp'ACE II) BC/RT/MT interface module. The Sp'ACE II has the following environmental operating specifications [10]: total gamma dose immunity of 1×10^6 Rad, LET threshold of 63 MeV/mg/cm^2, and a soft error rate of 2.56×10^{-5} errors/device-day.

/ENBn for experiment *n* is asserted

After 250 milliseconds the CIB will transmit:
SOP CRC Address Timestamp Packet Type Command or Padding

If the above packet is valid the experiment will transmit:
SOP CRC Address Timestamp Packet Type Data and/or Padding

If the CIB receives a valid packet from the experiment the CIB will acknowledge the packet:
SOP CRC Address Timestamp Packet Type = ACK

Box 1

Table 1: Health and status packet format transmitted once per major frame (once per second).

Type	Variable	Description
Unsigned char	opto[2]	State of optoisolators that determine whether the AO and FTSCE experiments are enabled
Unsigned long	last_poll_time	Beginning of the current polling cycle
Unsigned short	poll_cycles	Number of completed polling cycles
Unsigned char	poll_map[20]	Determines which experiments are to be polled
Unsigned short	sequence[20]	Packet sequence number of each of the experiments
Unsigned char	valid_crc[20]	0×FF = valid
Unsigned long	last_cmd_time[20]	Time last experiment command received
Unsigned long	last_cib_cmd_time	Time last CIB command received
Unsigned char	valid_ack[20]	0×FF = valid
Unsigned short	cmd_cnt[20]	Count of commands sent to experiments
Unsigned short	cib_cmd_cnt	Count of commands sent to CIB
Unsigned short	err_cmd	Command for nonpolled APID. Error = APID. 0×FFFF = no error
Unsigned short	err_poll	Invalid polling table received. Unused
Unsigned char	last_cmd[106]	Last command transmitted to experiments
Unsigned char	last_cib_cmd[106]	Last command transmitted to the CIB
Unsigned char	last_ftsce_cmd[100]	Last command sent to FTSCE
Unsigned char	ftsce_data[124]	Data transmitted by FTSCE
Unsigned char	reserved[64]	

The core components of the CIB hardware are listed in Table 2 along with their relevant environmental specifications.

MIL-STD-1553 coupling transformers and the two clock crystals are screened for space applications. All other active components are deemed radiation hard to this mission through consultation with the customer. A photograph of the CIB is given in Figure 5. The radiation environment in LEO consists primarily of trapped protons with some galactic cosmic rays and solar particles. The expected and agreed to limit for total ionizing dose for the CIB was less than 300 rad(si) per year (behind shielding). The CIB componentry is accepted to be SEU tolerant and SEL hard to the ISS LEO radiation environment. As such, the CIB was designed for long duration survival to the LEO radiation environment.

6. Results

The Communications Interface Board, or CIB, embodies the first demonstration of a permanent communications and control interface for deployable experiments to characterize materials, systems, and components exposed to LEO. The CIB was and is the core of two of the earliest science payloads on the ELC affixed to the external structure of the ISS as part of an Express Payload Adapter (ExPA). These two experiments, deployed by astronauts during EVA, are MISSE7 and -8. MISSE7 was deployed, had a successful mission, and was subsequently returned to Earth. MISSE8 remains on orbit at the time of this writing. The CIB was delivered to the ISS on STS-129 in November 2009 along with MISSE7. Table 3 lists experiments which use command and telemetry data provided by the CIB. MISSE7 then returned when MISSE8 was delivered in May 2011, with the CIB remaining aboard to provide the simplified telemetry interface for MISSE8. Table 4 lists MISSE8 experiments utilizing command and telemetry data enabled by the CIB. MISSE8 is scheduled for return in March 2014.

The original intent for the CIB was to embody the communications component of a MISSE-specific infrastructure capable of supporting two PECs with up to 20 separate experiments with power, uplink, and downlink capabilities. A PEC is a suitcase-like metal container which, when opened

Table 2: CIB core system components and respective environmental operating specifications.

Function	Part number	Temperature range	Single event latchup (SEL) threshold	Total radiation dose
Microcontroller	80C32E	−55°C to 125°C	>80 MeV/mg/cm^2	30 krad (Si)
Program memory	AT28C010	−55°C to 125°C	>80 MeV/mg/cm^2	10 krad (Si) under bias 30 krad (Si) when unbiased
Dynamic memory	M65608E	−55°C to 125°C	>80 MeV/mg/cm^2	30 krad (Si)
MIL-STD-1553 interface module	BU-63825		Immune	1 Mrad

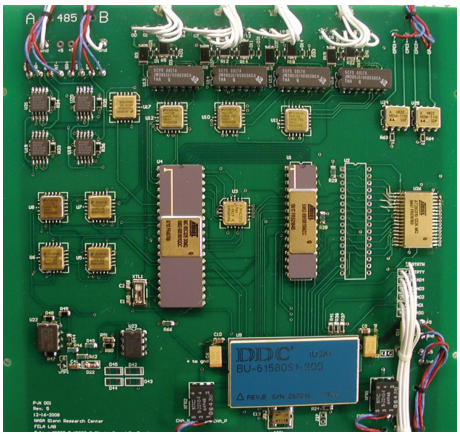

Figure 5: Photograph of the flight Communications Interface Board (CIB) circuit board. This image was taken prior to delivery, during functional testing of the circuit board, and prior to the insertion of the flight MIL-STD-1553 transceiver (image courtesy of NASA).

and deployed, presents two opposing experiment surfaces. Two PECs can thus provide zenith and nadir along with ram and wake presentations. This infrastructure greatly reduces the ISS interface complexity for future MISSE experiments. Experimenters would thus have a well-defined power and communication interface to the ISS to build to as well as an EVA compatible mechanical structure for deploying two MISSE style PECs. Further, continuous monitoring of components and samples while on orbit removes the requirement of an experiment returning to Earth for postmission analysis. As such, at end of mission, experiments may be disposed of via deorbiting as will be the case for part of MISSE8.

The decommissioning of the space shuttle brought with it a loss of EVA deployable experiments, and as such the PEC structure is inconsistent with new requirements for robotic deployment of science payloads and environmental sensors for insertion onto the ELCs. However, the CIB arguably represents a communication and control interface for a system consistent with current specifications.

While the CIB hardware currently residing on ELC2 onboard the ISS may not be utilized after the completion of MISSE8, it should be recognized that the architecture is suitable for future use in vehicle health monitoring applications. The current hardware design has been proven to be highly reliable in the demanding space flight environment. The simple telemetry interface provided by the CIB enabled the experiments listed in Table 3 on MISSE7 and Table 4 on MISSE8, respectively. Broad applications enabled by the CIB should be noted, from processor testing to solar cell health monitoring and from CMOS image sensor testing to a variety of materials testing. Two individual experiments specifically related to vehicle health monitoring will be discussed in the next section.

7. Health Monitoring Enabled by the CIB

7.1. SiC JFET Health Monitoring Experiment. An example of a health monitoring circuit flown on MISSE7 was the silicon carbide (SiC) Junction Field Effect Transistor (JFET) Experiment designed by the NASA GRC mobile and remote sensing laboratory and SiC development group. NASA GRC has a long history in extreme temperature range silicon carbide electronics and packaging development having demonstrated SiC logic circuits operating over a temperature range of −125°C to 500°C [11]. Current long duration extreme temperature testing is performed in laboratory ovens and cold chambers, but future use is anticipated on flight vehicles. In an effort to demonstrate the technology in a flight environment, a health monitoring experiment was designed for SiC JFETs in high temperature packaging which was the first space flight of this technology. The experiment consisted of two SiC JFETs, one in room temperature commercial packaging, the other in high temperature packaging developed by the Ohio Aerospace Institute and NASA GRC [12].

The experiment monitors the current versus voltage transfer characteristics or a curve trace of both transistors during the flight. The transfer characteristics of the transistors show any electrical or physical degradation of the transistors, which is the primary concern of this experiment demonstration. This transfer characteristics are generated with a microcontroller-based curve tracing circuit. The CIB RS-485 protocol includes a timestamp in each transaction, which the SiC JFET uses to determine when to initiate a curve trace. To minimize bandwidth used, the SiC JFET experiment will only run once every hour. When the CIB queries this experiment, if the timestamp does not lie in the first ten minutes of the hour, the experiment will power itself down to wait for the next query. In addition to using the CIB enable line as a safety to lockout transmission on the RS-485 bus, this experiment uses the enable line as a signal to a latch to enable powering up. The CIB assertion of the enable line powers the experiment up, after which the experiment listens for the CIB command packet. The experiment receives the timestamp,

Table 3: Materials on the International Space Station Experiment Seven (MISSE7) flown on ISS from November 2009 to May 2011.

Short experiment name	APID	Experiment description	Provider
MCPE	1300	Multicore processor single event upset testing	Naval Research Laboratory
GRC experiment set	1301	SiC transistor health testing [12], H2 sensor, and zenith/nadir AO monitor	NASA GRC
SEUXSE	1302	Xilinx FPGA SEU Testing	Sandia National Laboratory
Not used	1303		
Not used	1304		
CIE	1305	CMOS imager experiment	Assurance technology
FTSCE II	1306	Solar cell health monitoring [14–18]	NRL, NASA GRC, and AFRL
Boeing ram side experiment	1307	Materials testing	Boeing
HyperX	1308	High performance low-power processor, SEU testing [19]	NASA GSFC
SpaceCube "A"	1309	Advanced processor design SEU testing [20, 21]	NASA GSFC
SpaceCube "B"	1310	Advanced processor design SEU testing [20, 21]	NASA GSFC
Wake AO fluence monitor	1311	Wake atomic oxygen fluence monitor/thermal control paints Experiment	NASA GRC
Boeing wake side experiment	1312	Materials testing	Boeing
AFRL wake 1	1313	Tribology measurements	AFRL Dayton, U of Florida
AFRL wake 2	1314	Tribology measurements	AFRL Dayton, U of Florida
AFRL ram 1	1315	Tribology measurements	AFRL Dayton, U of Florida
AFRL ram 2	1316	Tribology measurements	AFRL Dayton, U of Florida
iMESA	1317	Miniaturized electrostatic analyzer [22]	U.S. Air Force Academy
LTESE	1318	Lead-free technology experiment in space environment	MSFC
Ames	1319	Thermal protection systems sensors	NASA ARC, NASA LaRC, NASA JSC, and Boeing
Boeing PICA	1320	Materials testing	Boeing
Ram atomic oxygen fluence monitor/thermal control paints experiment	1321		NASA GRC

determines if the time is within the ten-minute window, and then either proceeds with curve tracing or goes to sleep.

Figure 6 shows experiment data in the form of curve traces from midflight monitoring of the SiC transistor health. Both the room (Figure 6(a)) and high temperature (Figure 6(b)) packaged transistor test data are shown. The graph overlays preflight curves with those 6 months into the flight. These midflight results show no degradation of transistor performance during the 6-month period [12].

The experiment board shown in Figure 7 resided at APID 1301 as shown in Table 3. In addition to the SiC JFET experiment, the circuit board and electronics set also supported two additional experiments the Makel Gas Sensor and the atomic oxygen fluence monitor, neither of these will be discussed. The design of the CIB enables many types of health monitoring to be performed, with the sample rate being the limiting factor.

7.2. Forward Technology Solar Cell Experiment II. Another experiment toward vehicle health monitoring enabled by the CIB is the Forward Technology Solar Cell Experiment II (FTSCE II). The experiment was designed by the U. S. Naval Research Laboratory with instrumentation development by the NASA GRC MaRS Lab. This experiment monitored solar cell health by measuring current versus voltage (I-V) curve characteristics. Space vehicles in Earth orbit rely on

Table 4: Materials on the International Space Station Experiment Eight (MISSE8) flown on ISS from May 2011 to present (April 2013).

Short experiment name	APID	Experiment description	Provider
None	1300		
Reflectarray	1301	Characterize performance of components of a flexible, phased array antenna	NASA GRC
SEUXSE	1302	Xilinx FPGA SEU testing	Sandia National Lab
Not used	1303		
Not used	1304		
PASCAL	1305	Primary arcing effects on solar cells at LEO	Lockheed Martin, JAXA, Kyushu Institute of Technology
FTSCE III	1306	Solar cell health monitoring [23–25]	NRL, NASA GRC, and AFRL
Not used	1307		
HyperX	1308	High performance low-power processor, SEU testing [19]	NASA GSFC
SpaceCube "A"	1309	Advanced processor design SEU testing	NASA GSFC
SpaceCube "B"	1310	Advanced processor design SEU testing	NASA GSFC

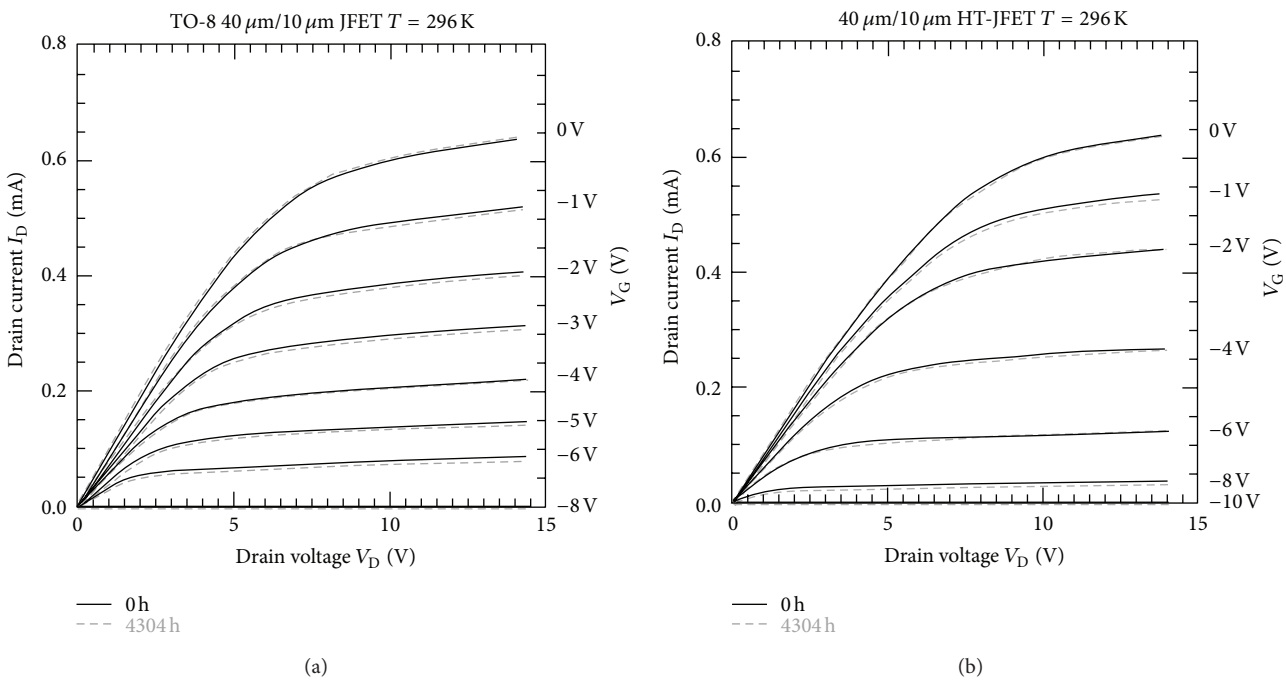

Figure 6: Current versus voltage transfer curves for given gate voltages of the two flight silicon carbide (SiC) Junction Field Effect Transistors (JFETs). (a) shows characteristics for room temperature packaged JFETs, for preflight, and after over six months of flight. (b) shows the characteristics for the high temperature packaged SiC JFET (image courtesy of NASA).

photovoltaic or solar cells as their power source. Space environment effects can degrade photovoltaic cell performance providing less power to the vehicle, and thus affecting the health and operating envelope of the space vehicle. While technology can be used to mitigate the degradation, the space vehicle designer and operator should know how the system will degrade and respond to the changing power system output.

Photovoltaic cells have current versus voltage characteristic which can provide insight into the health of the cell. Figure 8 shows an example of a solar cell I-V curve from initial FTSCE II on-orbit data. Performance degradation of the cell will show up as less current output, shifting the curve in Figure 8 downward along the vertical axis as the cell degrades. FTSCE II is comprised of 36 experimental solar cells as shown in Figure 9 along with measurement circuitry

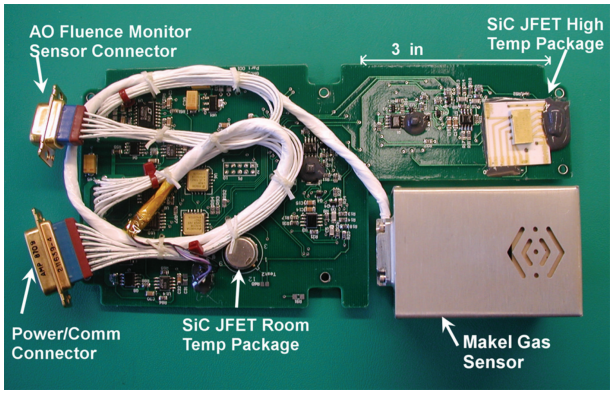

Figure 7: Silicon carbide junction field effect transistor (SiC JFET) health monitoring flight experiment circuit board (image courtesy of NASA).

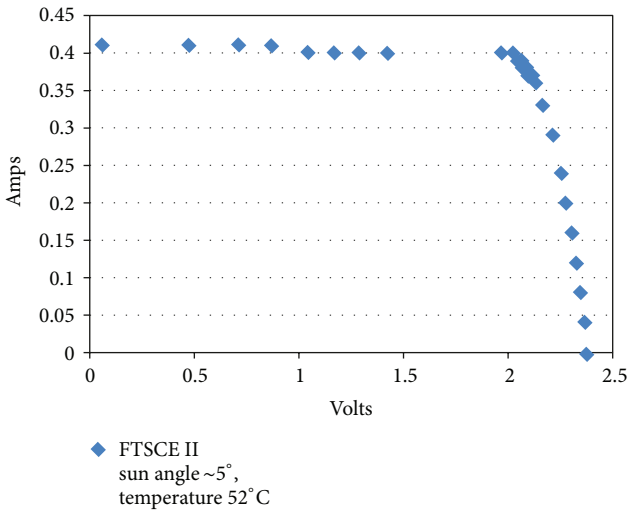

Figure 8: Typical I-V (current versus voltage) curve for a solar cell as measured by the Forward Technology Solar Cell Experiment II (FTSCE II).

to provide I-V curve data along with environment parameters of temperature and sun position in relation to the solar cells. The measurement hardware of FTSCE II flown on MISSE7 is actually a reflight of the same hardware originally designed for and flown as FTSCE I on MISSE 5 [13]. FTSCE II resided at the APID 1306 and would transmit data packets consisting of I-V curve data along with relevant environmental parameters. Future results covering the complete FTSCE II experiment are expected, while selected results from in flight data are presented in [14–17].

8. Future Health Monitoring Applications

The CIB design discussed in this paper is one possible hardware implementation of the architecture. This design was focused on providing reliable operation within a radiation environment. So, the hardware implementation described represents a design to achieve this goal. The architecture of

Figure 9: Sun looking face of the Passive Experiment Container (PEC) containing passive material samples and cells as flown on Materials International Space Station Experiment 7 (MISSE7). Solar cells can be denoted by the wires to attach to the measurement circuitry of the Forward Technology Solar Cell Experiment II (FTSCE II) (image courtesy of NASA).

the CIB may also be realized with a different hardware set to suit other needs. For instance, in a more benign environment, the choices for suitable hardware increase significantly and the design could also be shrunk physically. The hardware could be implemented in a variety of processing platforms which might even include the MIL-STD-1553 interface onboard. One likely hardware target for the CIB architecture is a field programmable gate array (FPGA). This reconfigurable platform would allow the processing unit and communication to exist in single IC, greatly shrinking the physical footprint of the circuitry. A smaller CIB would provide greater access to additional flight platforms.

Another consideration for future use is the reliability of the sensors and instruments which utilize the RS-485 bus. As the sensors mature and are demonstrated to be more reliable in operation, the enable lines provided by the CIB might not be needed. This elimination would reduce the wiring needed as well as the physical size of the CIB.

Hardware changes are not the only possible architecture modifications which would lead to expanded use. Software alterations may also be applied to allow increased use of the architecture. For instance, current CIB protocol might be expanded. The CIB operated with a command/response protocol, where the CIB controlled the RS-485 bus in much the same way as the bus controller in the MIL-STD-1553 bus. One feature possible on a command/response bus is node to node communication. Because the CIB uses packet-based transfers, the software protocol could be expanded to include these node to node transfers, whereby a request for node to node transfer is communicated to the bus controller, which is then granted by the CIB through an additional message. Even in the current configuration, node to node transfer is possible, since a node needs only to actively listen to the bus, for messages encoded in its packet.

Future use of this architecture may be a vehicle health monitoring bus included in aircraft/spacecraft electronic systems. The CIB or future hardware could be the interface between all health monitoring sensors and the crafts central control unit. Used in this manner, the CIB could provide the craft with vehicle health information through a single interface such as the MIL-STD-1553 bus.

9. Conclusion

This paper demonstrates that the CIB is an improved architecture enabling simple vehicle health monitoring on the ISS. While the ISS has in place a communications architecture which enables health monitoring, telemetry, and control, the CIB improves and adds to this infrastructure by providing a simpler interface. This is accomplished by interfacing with the ISS MIL-STD-1553 bus and providing two multidrop RS-485 busses for experiments, sensors, and health monitoring systems to communicate on. The RS-485 busses make available the MIL-STD-1553 telemetry, command, and control services without the complex development required for MIL-STD-1553. This simpler interface enables sensor and instrumentation development for vehicle health monitoring applications.

The CIB provides this simpler communication interface while maintaining the reliability expected of a space flight system on the ISS. The CIB was developed with radiation tolerance and reliability as the primary design considerations. With over three years of successful operation on the ISS over two missions, the CIB has proven to be highly reliable and tolerant to the LEO radiation environment while providing simpler vehicle health monitoring communication support.

The CIB also enabled future materials and device development which lead to further use in health monitoring systems. This paper gave two examples of a health monitoring experiment flown on the external of the ISS for over a year. The SiC JFET is a high temperature component which has uses throughout a vehicle to include health monitoring in extremely hot environments. The flight on MISSE7 was the first space flight of this technology and was only possible with the simple telemetry interface provided by the CIB. FTSCE II demonstrated solar cell health monitoring on the ISS with real-time telemetry enabled by the CIB.

The CIB design discussed is one implementation of the architecture. This architecture might be expanded on or implemented differently for a different platform. Another processing technology might be utilized in the architecture in a more benign environment such as an aircraft. Future software development may use the CIB protocol to support node to node transfer, allowing sensor fusion techniques for vehicle health monitoring.

Acknowledgments

The authors would like to acknowledge George Y. Baaklini, branch chief of the Optical Instrumentation and NDE Branch at the NASA Glenn Research Center, and Robert Walters of the Naval Research Laboratory for support of this work. This work was funded by the U. S. Naval Research Laboratory.

References

[1] "Space station ionizing radiation design environment," Tech. Rep. NASA SSP-30512 Revision C, June 1994.

[2] "International standard payload rack to international space station, software interface control document part 1," Tech. Rep. NASA SSP, 52050 Revision G, 2007.

[3] "Aircraft internal time division command/response multiplex data bus," Tech. Rep. U.S. Department of Defense MIL-STD-1553B, 1996.

[4] "EXPRESS Logistics Carrier (ELC) development specification," Tech. Rep. NASA SSP-52055 Revision C, 2006.

[5] P. P. Jenkins, R. J. Walters, M. J. Krasowski et al., "MISSE7: Building a permanent environmental testbed for the international space station," in *Proceedings of the 9th International Conference on Protection of Materials and Structures From Space Environment (ICPMSE '08)*, vol. 1087, pp. 273–276, May 2008.

[6] "Communications interface board serial interface specification," Tech. Rep. NASA/NRL ICD Document, Revision 9, 2009.

[7] Atmel Corporation, "Rad. Tolerant 8-bit ROMless Microcontroller 80C32E Datasheet," 2007.

[8] Atmel Corporation, "Space 1-MBit (128K x 8) Paged Parallel EEPROMs AT28C010-12DK Datasheet," 2011.

[9] Atmel Corporation, "Rad. Tolerant 128K x 8, 5-Volt Very Low Power CMOS SRAM M65608E Datasheet," 2008.

[10] Data Device Corporation, "BU-63285 Space Level MIL-STD-1553 BC/RT/MT Advanced Communication Engine (SP'ACE II) Terminal Datasheet," 2005.

[11] P. G. Neudeck, M. J. Krasowski, L.-Y. Chen, and N. F. Prokop, "Characterization of 6H-SiC JFET integrated circuits over a broad temperature range from −150°C to +500°C," *Materials Science Forum*, vol. 645–648, pp. 1135–1138, 2010.

[12] P. G. Neudeck, N. F. Prokop, L. C. Greer III, L.-Y. Chen, and M. J. Krasowski, "Low earth orbit space environment testing of extreme temperature 6H-SiC JFETs on the international space station," *Materials Science Forum*, vol. 679-680, pp. 579–582, 2011.

[13] M. J. Krasowski, L. C. Greer, J. M. Flatico, P. P. Jenkins, and D. C. Spina, "Big science, small-budget space experiment package aka MISSE-5: a hardware and software perspective," in *Proceedings of the 19th Space Photovoltaic Research and Technology Conference*, September 2005.

[14] P. P. Jenkins, R. J. Walters, M. Gonzalez et al., "Initial results from the second forward technology solar cell experiment," in *Proceedings of the 35th IEEE Photovoltaic Specialists Conference (PVSC '10)*, pp. 1124–1127, June 2010.

[15] K. M. Edmondson, A. Howard, P. Hausgen et al., "Initial on-orbit performance analysis of Inverted Metamorphic (IMM3J) solar cells on MISSE-7," in *Proceedings of the 37th IEEE Photovoltaic Specialists Conference (PVSC '11)*, pp. 3719–3723, June 2011.

[16] T. Stern and A. Reid, "Modular solar panels using components engineered for producibility," in *Proceedings of the 37th IEEE Photovoltaic Specialists Conference (PVSC '11)*, pp. 1626–1629, June 2011.

[17] A. D. Howard, D. M. Wilt, P. P. Jenkins, K. M. Trautz, P. Hausgen, and J. M. Merrill, "Selected on-orbit data from the FTSCE II aboard the MISSE 7 testbed," in *Proceedings of the 38th IEEE Photovoltaic Specialists Conference (PVSC '12)*, pp. 3275–3280, June 2012.

[18] T. D. Sahlstrom, P. E. Hausgen, J. Guerrero, A. D. Howard, and N. A. Snyder, "Ultraviolet degradation testing of space protective coatings for photovoltaic cells," in *Proceedings of the 33rd IEEE Photovoltaic Specialists Conference*, pp. 1–5, May 2008.

[19] A. S. Keys, J. H. Adams, R. E. Ray, M. A. Johnson, and J. D. Cressler, "Advanced avionics and processor systems for space and lunar exploration," in *AIAA Space 2009 Conference and Exposition*, Anaheim, Calif, USA, September 2009, AIAA 2010-8783.

[20] D. Petrick, "SpaceCube: current missions and ongoing platform advancements," The MAPLD Workshop, 2009, https://nepp.nasa.gov/mapld_2009/.

[21] K. M. Zick, C.-C. Yu, J. P. Walters, and M. French, "Silent data corruption and embedded processing with NASA's spacecube," *IEEE Embedded Systems Letters*, vol. 4, no. 2, pp. 33–36, 2012.

[22] R. Balthazor, M. G. McHarg, C. L. Enloe et al., "Sensitivity of ionospheric specifications to in situ plasma density observations obtained from electrostatic analyzers onboard of a constellation of small satellites," in *Proceedings of the AIAA/USU Conference on Small Satellites, SSC12-IV-1*, Logan, Utah, USA, 2012.

[23] B. Cho, R. Lutz, J. Pappan et al., "IMM experimentation in the next frontier: Emcore's participation in the MISSE-8 program," in *Proceedings of the 35th IEEE Photovoltaic Specialists Conference (PVSC '10)*, pp. 110–112, June 2010.

[24] T. D. Sahlstrom, P. E. Hausgen, D. M. Wilt, A. D. Howard, M. D. Anderson Jr., and N. A. Snyder, "Space flight experiment: advanced solar cells and protective materials on the ISS exterior," in *Proceedings of the 35th IEEE Photovoltaic Specialists Conference (PVSC '10)*, pp. 2610–2615, June 2010.

[25] S. Gasner, M. Tresemer, S. Billets, D. Bhatt, and P. Wallis, "Design & fabrication of the lockheed martin solar cell demonstration experiment for the ISS Forward Technology Solar Cell Experiment II," in *Proceedings of the 34th IEEE Photovoltaic Specialists Conference (PVSC '09)*, pp. 791–793, June 2009.

Hindawi Publishing Corporation
The Scientific World Journal
Volume 2013, Article ID 715945, 12 pages
http://dx.doi.org/10.1155/2013/715945

Research Article

Nondestructive Damage Evaluation in Ceramic Matrix Composites for Aerospace Applications

Konstantinos G. Dassios,[1] Evangelos Z. Kordatos,[1] Dimitrios G. Aggelis,[2] and Theodore E. Matikas[1]

[1] *Department of Materials Science & Engineering, University of Ioannina, 45110 Ioannina, Greece*
[2] *Department of Mechanics of Materials and Constructions, Vrije Universiteit Brussel, Pleinlaan 2, 1050 Brussels, Belgium*

Correspondence should be addressed to Theodore E. Matikas; matikas@cc.uoi.gr

Received 20 April 2013; Accepted 6 June 2013

Academic Editors: D. Ouinas and K. N. Shivakumar

Infrared thermography (IRT) and acoustic emission (AE) are the two major nondestructive methodologies for evaluating damage in ceramic matrix composites (CMCs) for aerospace applications. The two techniques are applied herein to assess and monitor damage formation and evolution in a SiC-fiber reinforced CMC loaded under cyclic and fatigue loading. The paper explains how IRT and AE can be used for the assessment of the material's performance under fatigue. IRT and AE parameters are specifically used for the characterization of the complex damage mechanisms that occur during CMC fracture, and they enable the identification of the micromechanical processes that control material failure, mainly crack formation and propagation. Additionally, these nondestructive parameters help in early prediction of the residual life of the material and in establishing the fatigue limit of materials rapidly and accurately.

1. Introduction

Owing to their unique properties such as damage tolerance, fracture toughness, wear and corrosion resistance with respect to monolithic ceramics, and crack growth resistance, CMCs can withstand severe thermomechanical loading conditions [1] and are used today in many aerospace applications as braking systems, structural components, nozzles, and thermal barriers. SiC fibres are the number one candidate reinforcement for such composites as they offer high strength and modulus, thermal stability, and good mechanical performance under high temperatures [2].

The importance of monitoring the structural safety of aerospace structures is imperative. Prevention of catastrophic failure as well as safe and economical management of the structures can be achieved by early assessment of material conditions before the appearance of large-scale fracture. Regular observation of the structures for signs of damage or deterioration will enable the realization of proper repair actions which, in turn, will help extend the useful life span of the component. Among the highly sought-after nondestructive methods capable of monitoring the structural integrity of aerospace structures in an efficient and economical manner, infrared thermography and acoustic emission stand out for being fast, straightforward, and highly reliable. Today both the National Aeronautics and Space Administration (NASA) and Astrium, the European space company, use IRT and AE to detect defects in shuttle wings, rudders and tails, thruster chamber assemblies, and other composite components [3–8]. While IRT captures the thermal energy emissivity of the specimen which is directly related to the damage mechanisms that form and develop during material fracture, the idea behind AE monitoring is that any fracture incident inside a material releases energy which propagates in the form of elastic waves and can be captured at the surface of the material by appropriate sensors.

While IRT and AE have been successfully applied to detect flaws in CMCs, little information is available on their potential to capture and follow the formation of subsurface cracks. Moreover, it is extremely interesting to investigate the advantages of combined application IRT and AE and to

evaluate complementary input that these two techniques can give about CMC damage.

In the present work, IRT and AE are combined to monitor the formation and development of damage during cyclic and fatigue loading of SiC-fiber reinforced barium osumilite (barium, magnesium, aluminium, and silicate (BMAS)) glass-ceramic matrix composites. IRT was used to identify the most critical, with respect to fracture, damage mechanisms as well as to monitor crack propagation under cyclic and dynamic loads and to predict the composite's residual life. State-of-the-art IR lock-in thermography was used in a unique manner to rapidly and precisely assess the fatigue limit of the CMC, using data from a single specimen test. AE parameters were very powerful in identifying and quantifying real time damage in the CMC. The significance of a large number of IRT and AE indices with respect to mechanical performance and damage evaluation is discussed and explained in the text.

2. Experimental

2.1. Materials and Mechanical Testing. SiC/BMAS laminates were provided as 3 mm thick plates. The BMAS glass matrix consisted of 50 wt% SiO_2, 28 wt% Al_2O_3, 7 wt% MgO, and 15 wt% BaO and was reinforced by SiC Tyranno fibers stacked and hot-pressed at 1200°C for 10 min in a symmetric $(0/90)_{4s}$ orientation. During hot-pressing, a chemical reaction between the fiber and the oxides of the matrix is known to result in the formation of a weak carbon-rich interphase [9] responsible for large-scale bridging and pull-out phenomena during composite fracture [10]. Rectangular specimens of dimensions $105 \times 12 \times 3\ mm^3$ were prepared in a vertical CNC with fiber orientation in the external plies set to 0° with respect to the specimen's longitudinal axis. Double-edge notch (DEN) specimens of initial notch-to-width ratios of 0, 0.2, and 0.35 were prepared using a diamond wafering blade intended for cyclic tension testing as shown in Figure 1. Dogbone specimens were prepared for monotonic tensile testing as well as for fatigue loading (Figure 1).

All mechanical testing was performed at ambient temperature on an Instron 8800 servohydraulic frame equipped with a ±100 kN load cell. Specimens were gripped with a pressure of 4 MPa and were tested without end tabs at a nominal gauge length of 50 mm. Static tensile testing, both monotonic and cyclic, was performed under crosshead displacement control with a rate of 0.2 mm/min corresponding to an initial strain rate of $4.0 \times 10^{-3}\ min^{-1}$ within the 25 mm gauge length of the external, knife-edge-mounted axial extensometer. In cyclic tension experiments with unloading/reloading loops, unloading commenced at 10^{-3} strain and repetitions occurred with a step of 1.5×10^{-3} strain. The composites were unloaded to full relaxation before reloading.

Fatigue step loading until fracture was conducted on dogbone specimens. The first loading step was set to 10% σ_{ULT} and endured for 6000 cycles. The commencing load level was chosen to be low in order to capture the whole mechanical response of the material. The subsequent four loadings, up to 60% σ_{ULT}, occurred with a step of 10% σ_{ULT}. At 60% σ_{ULT} the fatigue loading step was decreased to 5% σ_{ULT} and remained such until specimen fracture. The frequency of the sinusoidal fatigue load was 10 Hz and R was 0.1. The fatigue loading protocol is represented schematically in Figure 2.

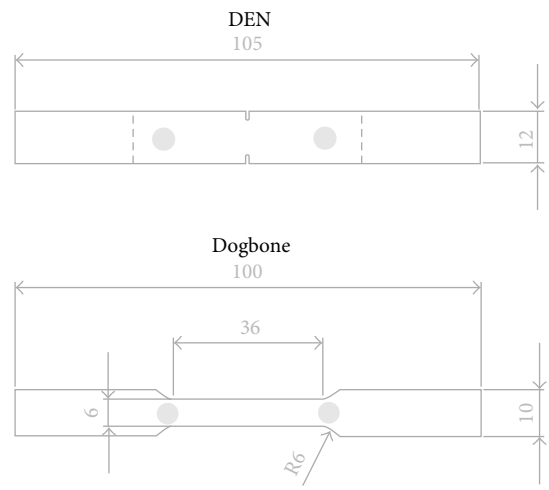

Figure 1: Double-edge-notch and dogbone specimen configurations with marked AE monitoring locations (grey circles).

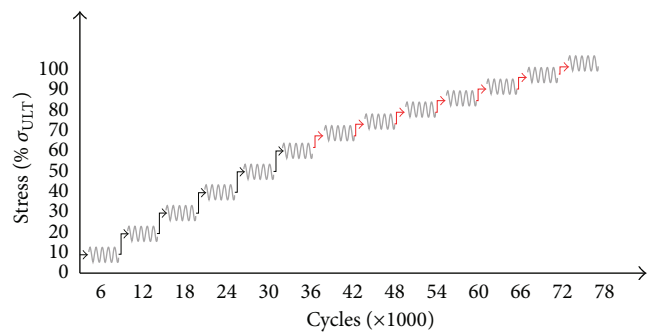

Figure 2: Schematic of fatigue loading protocol.

2.2. Acoustic Emission Monitoring. Acoustic emission activity was monitored throughout mechanical testing on all specimens using two "Pico" microminiature AE sensors tape-mounted at a separation of 40 mm on the central part of the specimen (Figure 1). In static tests (monotonic and cyclic tension) the sensors were mounted on the same side of the specimen as the extensometer. This manner of mounting always provided an instrument-free face on the specimen that could be monitored by IRT in real time. Acoustic coupling between the sensors and the specimen was provided by application of silicon grease. The broadband frequency response of the sensors, 50–800 kHz, enabled signal acquisition from a wide range of damage mechanisms. On the other hand, their small size facilitated geometric location of event sources along the specimen. AE sampling was conducted on a PCI-2 board (Physical Acoustics Corporation, Princeton, NJ, USA) with a sampling rate of 5 MHz, an amplification of 40 dB, and a threshold of 45 dB that enabled exclusion of ambient noise from the recorded signal.

2.3. Thermography. Throughout testing, temperature variations due to the applied loading, on the AE/extensometer-free face of the specimen, were monitored by an infrared thermography camera (CEDIP, MIW). The camera featured a cooled indium antimonide (InSb) detector (3–5 μm), a focal plane array (FPA) with pixel format of 320 (H) × 240 (V), and a temperature sensitivity of 20 mK. Temperature was recorded with a sampling rate of 100 Hz. Aliasing was avoided by recording the baseline emissivity of the material prior to load application by capturing the IR fingerprint of the surface with the thermal camera.

Throughout cyclic loading of DEN specimens of the SiC/BMAS composite, thermographs were recorded from the high-stress concentration area between the notches. For lock-in thermography measurements during fatigue loading, specimens were spray-coated with a matte black varnish in order to achieve uniform high-level surface emissivity. Optimal field of view (FOV) conditions were achieved by positioning the camera at approximately 40 cm in front of the gripped specimen. The IR camera was connected to the lock-in amplifier which, in turn, was connected to the servohydraulic controller. This enabled the synchronization of the lock-in amplifier and the testing machine frequencies and capturing of lock-in images and data during fatigue loading. The IR camera was used to measure the amount of energy emitted as infrared radiation, which is a function of the temperature and emissivity of the specimen. According to a previous study, the measured energy corresponds to the intrinsically dissipated energy while the fatigue limit is located at the break of the intrinsic dissipation regime of the loaded specimen [11].

3. Results and Discussion

3.1. Mechanical Response under Static Tension. The stress-strain response of notched and dogbone SiC/BMAS specimens under cyclic and monotonic tension, respectively, is presented in Figure 3. Unnotched specimens exhibited a triple regime behavior consisting of a linear initial part followed by a regime of gradually decreasing tangent modulus and a final regime of apparent stiffening. The second regime (regime "II") is associated mainly with interfacial damage, most importantly interfacial debonding but also with progressive matrix cracking evidenced as decreasing material stiffness (average slope of unloading/reloading loops). In the third regime (regime "III") an increase in material stiffness and tangent modulus coupled with an almost linear stress-strain relationship are apparent. In this ultimate regime, the mechanisms of interfacial debonding and matrix cracking have reached a saturated state; hence, material damage is not governed by the interface or matrix anymore; but by a mechanism of superior strength, essentially load bearing by intact fibers [12]. Similar triple regime phenomena with prefailure macroscopic stiffening and linear stress-strain relationships have been encountered before [13]. As observed in the curves of Figure 3(b), Regime III is absent from the mechanical behaviors of notched specimens. This is probably due to premature fiber—hence also composite—stemming from stress concentration in the vicinity of the notch roots.

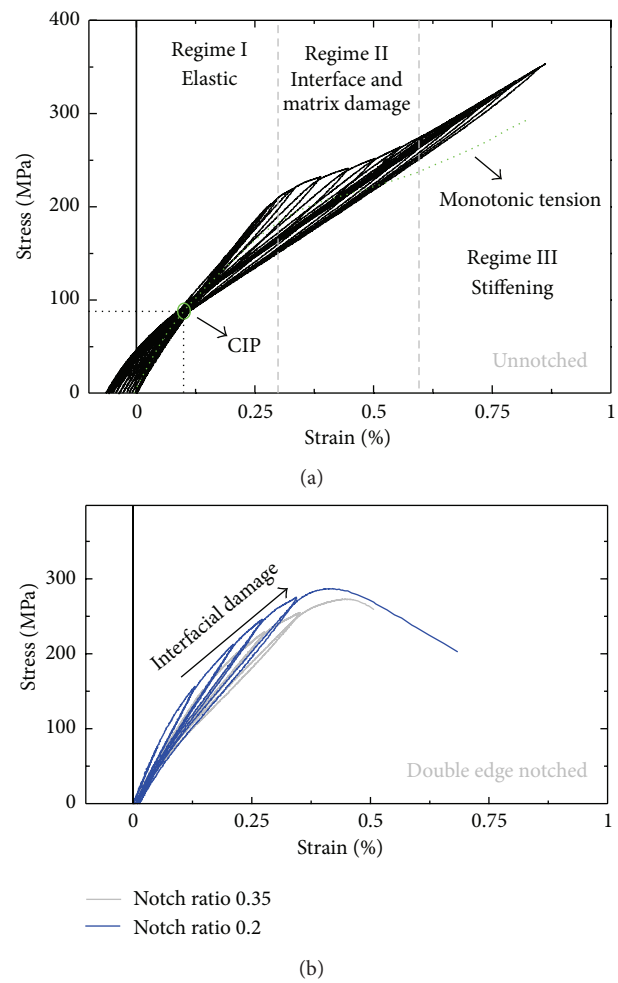

Figure 3: Stress-strain response of SiC/BMAS under monotonic loading (dotted line in (a)) and cyclic tension with unloading/reloading loops for (a) un-notched specimens and (b) notched specimens with various notch lengths.

In notched specimens instead, the material failed soon after the maximum load was attained, giving minimal "tail" effects.

Most importantly, the stress-strain curves of unnotched specimens are defined with unique precision, a common intersection point (CIP) of unloading-reloading curves in the first quadrant of the stress-strain curve in the tension domain. The coordinates of the CIP, 0.001 strain and 90 MPa stress, are directly related to the axial residual stress state of the composite [14, 15]. While a thorough analysis of the CIP feature for the particular composite has been the subject of a previous work [16], it is interesting to repeat here that a self-assembled CIP had never before been encountered experimentally.

Comparing the monotonic and cyclic tension curves for the SiC/BMAS composite (Figure 3(a)), it can be concluded that cyclic loading results in an increase by 20% in attainable material stress, calculated at fracture. If this increase is due to higher amounts of energy dissipated at damage mechanisms such as interfacial debonding, matrix cracking, and load bearing by intact fibers [10], it is then suggested that cyclic

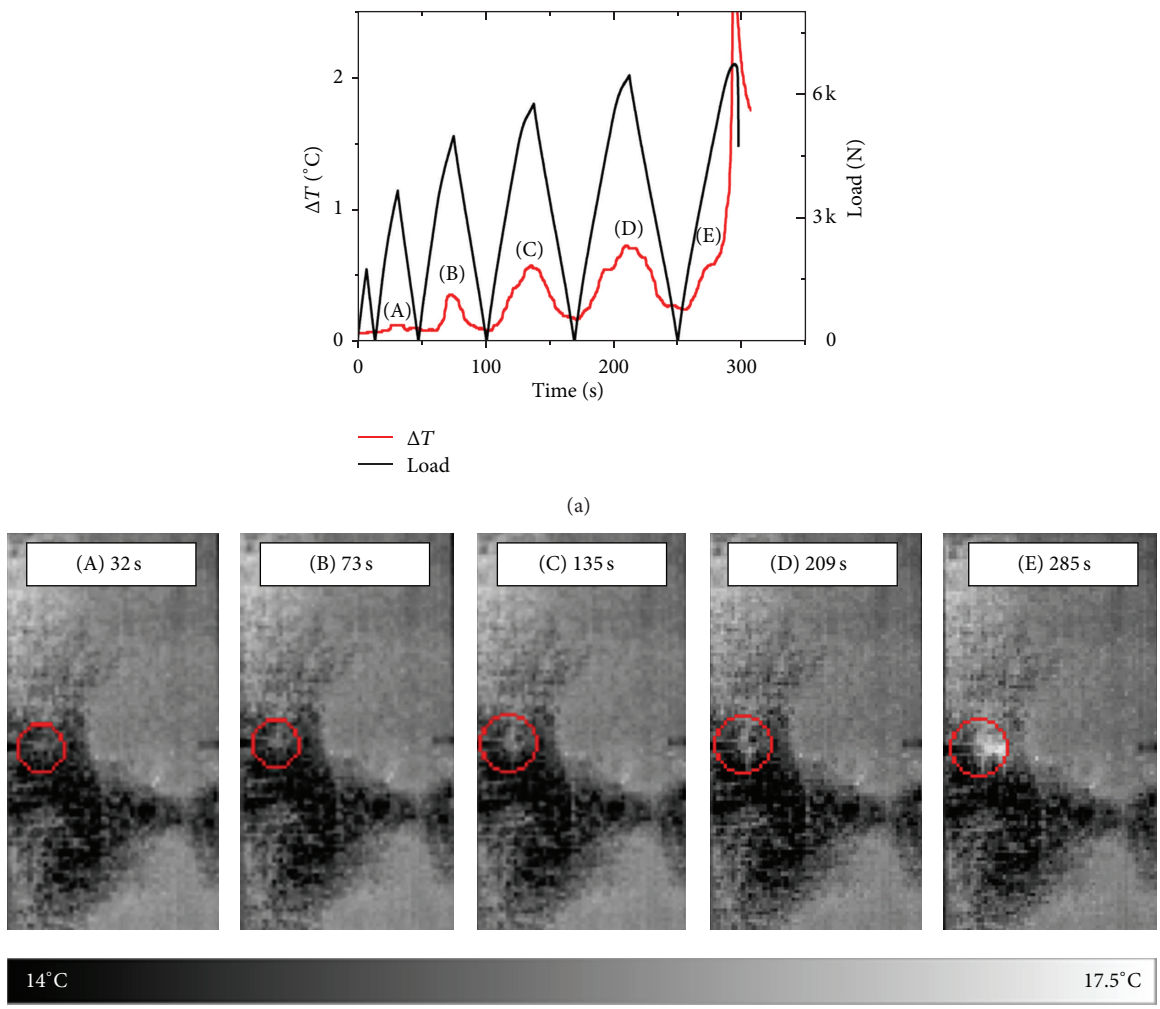

Figure 4: (a) ΔT and load versus time for a 0.35 notch-to-width ratio specimen loaded in cyclic tension. Sequential alphabet letters indicate instance of thermographs presented in (b).

loading by itself improves the energy dissipation capacity of the material. The existence of another energy dissipation mechanism, pull out, anticipated by the weak interfacial bond discussed in the experimental section, was verified after the end of the tests: failed specimens had not separated in two pieces after removal from the grips, with the frame still indicating small load values of the order of a few Newtons. This meant that fibers had failed within the matrix environment and had pulled out noncompletely before removal of the specimens from the grips [17].

Composite strength and modulus appeared to increase with decreasing notch length. Unnotched specimens enjoyed average strengths and moduli of 355 MPa and 151 GPa, respectively. The corresponding values for the 0.2 and 0.35 notched-to-width length were 280 MPa/119 GPa and 270 MPa/108 GPa, respectively.

3.2. Thermography

3.2.1. Static/Cyclic Loading. Temperature variation as measured by IRT, ΔT, and load is shown in Figure 4(a) as a function of time for a DEN specimen with a 0.35 notch-to-width ratio. Indices "A" to "E" denote the instances of the thermographs shown in Figure 4(b), collected at the notched ligaments of the composites. It is observed that peak ΔT location coincides with the location of maximum load for every cycle, whereas peak ΔT magnitude increases with progressing loading, hence also material damage. At the ultimate cycle, the ΔT trace appears to follow a completely different pattern than those in previous cycles, wherein temperature appears to drastically increase, indicating that the specimen is heading for catastrophic fracture.

In Figure 4(b), the locations of crack initiation, as identified by IRT, are indicated by a red circle mark. The apparent high-temperature area located outside and to the right of the circle mark is a baseline pattern that exists even before load application and remains constant until catastrophic failure. It is associated with the specimen's surface emissivity, not with material damage. It should not be ignored that IRT is concerned with temperature *variations* as a result of progressive damage, not with *absolute* values. Under this rationale,

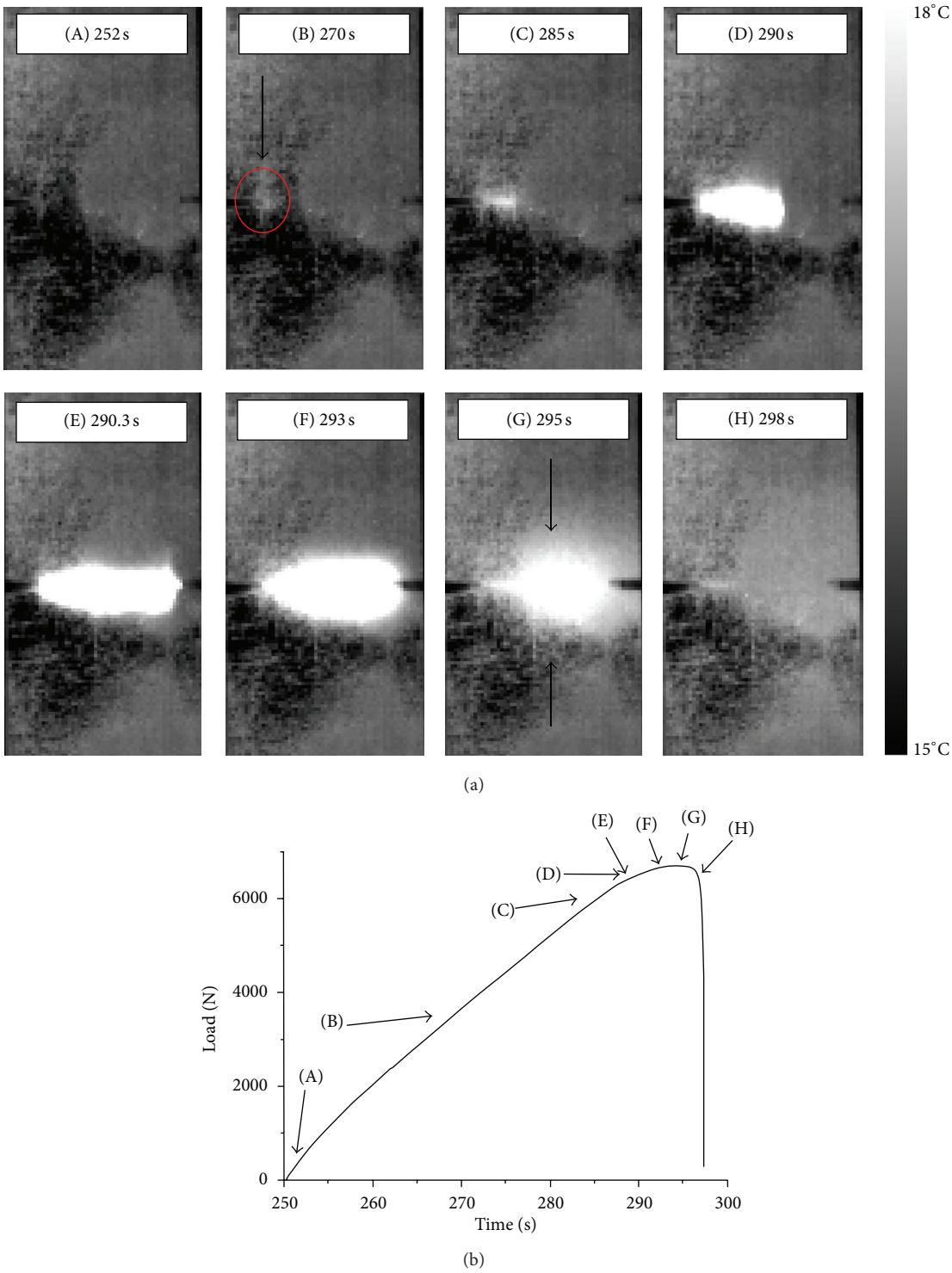

Figure 5: Final loading cycle of 0.35 notch-to-width ratio DEN specimen. (a) Thermographs showing crack propagation and (b) load versus time curve.

no noticeable change in temperature is seen up to 32 sec experimental time (thermograph (A) of Figure 4(b)). 73 sec within testing (thermograph (B) of Figure 4(b)), very small temperature variations can be observed within the marked (circle) area. Temperature increases become more obvious in thermographs (C) and (D) of Figure 4(b), 135 and 209 into loading, respectively. It is indicated that the damage is extending in area and magnitude. In the last loading cycle, 285 sec

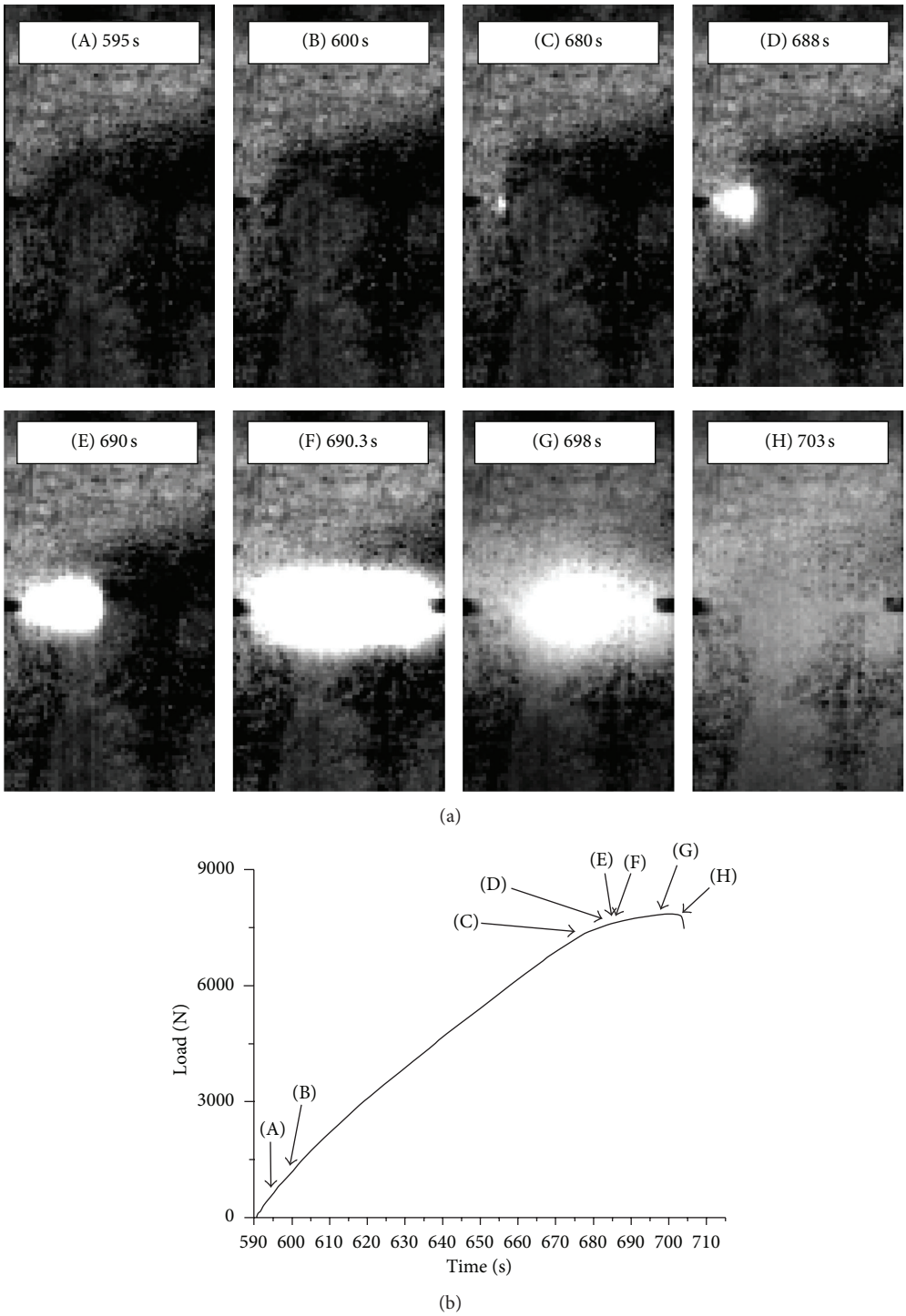

Figure 6: ((a), (b)) Thermographs of crack propagation and diagram of load versus time of final loading cycle (0.2 notch-to-width ratio specimen).

in the test, a dramatic increase in temperature throughout the whole notched ligament signifies that material failure is imminent.

The thermographic behaviour within the ultimate loading cycle, of the same 0.35 notch-to-width ratio specimen, is demonstrated in Figure 5 and analyzed in the following. Indices "A" to "H" presented in Figure 5(b) define the instances of the thermographs in Figure 5(a) (note the notch roots). In thermograph (A) of Figure 5(a), no hot appears exist within the notched ligament. In the next instance, thermograph (B) of Figure 5(a), a red arrow indicated what appears to be crack initiation. At 285 sec, thermograph

(C) of Figure 5(a), a significant temperature difference is observed, which coincides with the change in the slope of the mechanical response curve. It is believed that from this instance on, subsurface crack starts propagating from the left notch root with direction to the right. It is important to establish this instance as precisely as possible, as this will facilitate early prediction of the final fracture. It is noted that the associated time (285 sec) corresponds to 73% of the total duration of this ultimate loading cycle. 5 sec later (thermograph (D) of Figure 5(a) at 290 sec) the subsurface crack appears to span half of the notched ligament while only another 300 msec later (thermograph (E) of Figure 5(a)) it propagates abruptly and unstably towards the right notch. The maximum temperature is attained (thermograph (F) of Figure 5(a)) at an instance that coincides with the maximum load of the final loading cycle. This temperature is associated with the matrix cracking saturation and the load bearing completely by the reinforcing fibers. Temperature starts decreasing at the left notch in the next thermograph, (G) of Figure 5(a), while it increases above and under the subsurface crack, as indicated by black arrows. This increase is due to the fiber failure under the critical level of applied load. Failed fibers pull out giving rise to the frictional thermal energy evidenced in thermograph (H) of Figure 5(a).

Similar trends were observed for DEN composites with smaller notches, as in specimens with 0.2 notch-to-width ratios; the thermographic behaviour within the ultimate loading cycle of such a specimen is demonstrated in Figure 6 and analyzed in the following. Again, indices "A" to "H" presented in Figure 6(b) define the instances of the thermographs in Figure 6(a). After 600 sec of testing time, Figure 6(a)(B), no "warm" damage areas are seen in the thermographs. Crack initiation appears at 680 sec, Figure 6(a)(C), which compares favorably with the instance of slope change in mechanical behavior of the material. It is hence possible to foresee early fracture still at 80% of the final cycle duration. In the subsequent thermographs Figure 6(a)(D) and (E), the subsurface crack propagates from the left notch towards the middle of the notched ligament. The crack then propagates abruptly and unstably towards the right notch. A temperature variation profile compatible with pull out is seen again in the last thermograph, Figure 6(a)(H), where the specimen has failed completely.

Peak ΔT is shown in Figure 7 for the two notch lengths used in the current study. It is observed that specimens with shorter notches exhibit ΔT of 15°C at fracture while the ones with longer notches exhibit ΔT values around 10°C. It is believed that in specimens with larger notched ligaments (smaller notches), damage evolves over a wider material region throughout testing; hence peak temperature at the critical load is not high. On the other hand, damage is accumulated and relieved not so drastically in a specimen with less material available within the notched region.

3.2.2. Fatigue. Lock-in thermography was applied during fatigue loading of SiC/BMAS dogbone specimen. The intrinsically dissipated energy as monitored by the IR camera for 10 different stress levels ranging from 30% to 90% σ_{ULT} is plotted as a function of % σ_{ULT} in Figure 8.

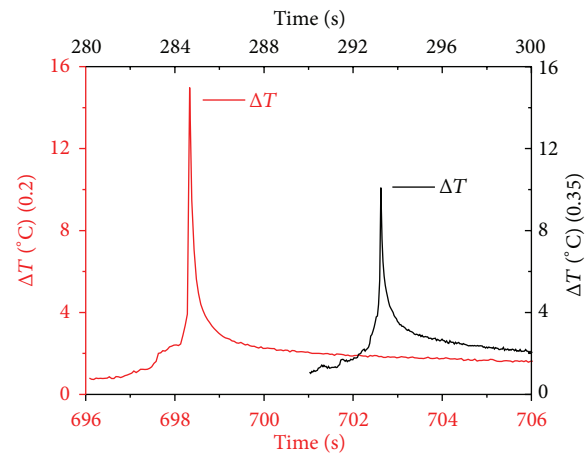

Figure 7: Peak ΔT for the two notch lengths used in the DEN specimens.

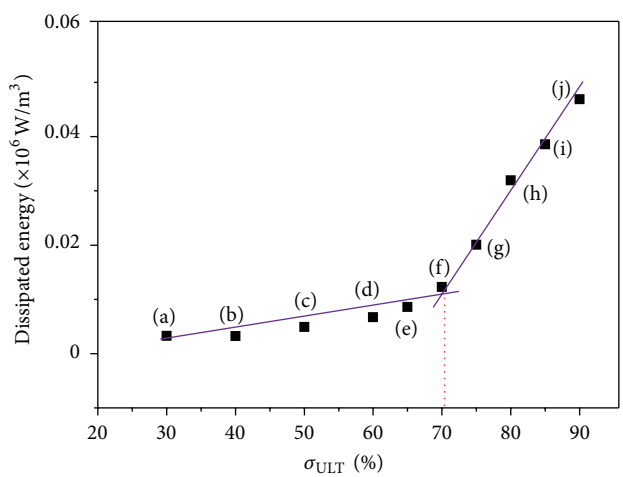

Figure 8: Dissipated energy versus % σ_{ULT} for fatigue-loaded SiC/BMAS.

The curve exhibits two distinct slopes, visualized by the two linear regressions seen in Figure 8. At low stress levels, 30% to 60% σ_{ULT}, the dissipated energy increases with a low rate, while from 70% σ_{ULT} and upwards it rises considerably more rapidly. The intersection point of the two lines defines the fatigue limit of the material. The value of fatigue limit calculated for the cross-ply SiC/BMAS through the thermographic approach of this study is 70% σ_{ULT} or 205 MPa.

An examination of the thermographic pattern of cross-ply SiC/BMAS at different stress levels is of particular interest in view of the established fatigue limit value. This information is presented in Figures 9(a)–9(j), wherein the 70% σ_{ULT} fatigue level which corresponds to thermograph Figure 9(f). Two distinct cases are made obvious by examination of this figure: (i) thermographs Figures 9(a)–9(d) depict low energies in cold (blue) color coding in the initial loading stages associated with minimal material damage and (ii) thermographs Figures 9(e)–9(j) capture progressive damage accumulation which is captured by increasingly warmer colors (high energy). In the first four thermographs, up to

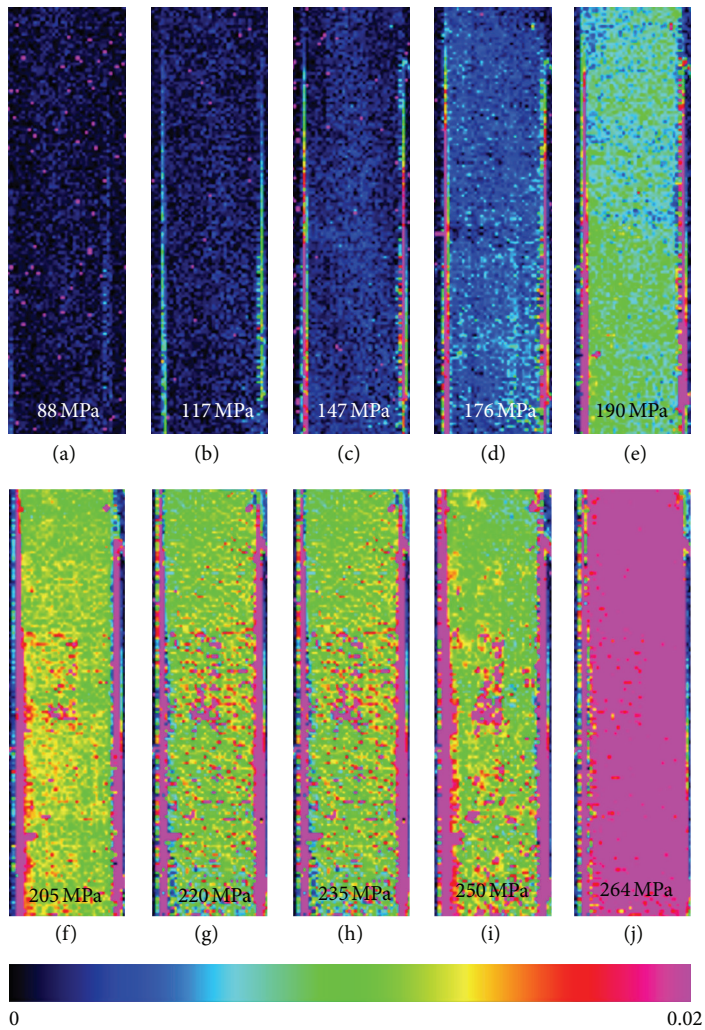

Figure 9: Thermographic pattern during fatigue loading of a SiC/BMAS composite.

176 MPa applied stress, there is practically no appreciable change in the dissipated energy. In the fourth thermograph, Figure 9(e), a slight change in color can be attributed to the saturation of elastic energy accumulation on the onset of appearance of fatigue. A totally dissimilar energy distribution pattern appears in thermograph Figure 9(f) due to the unfolding of internal energy dissipation phenomena such as interfacial damage, delamination, and fiber sliding across the debonded interface [18]. At thermographs Figures 9(g)–9(j) (75%–90% of σ_{ULT}), a raise in energy can be noticed indicated by the increment of the magenta spots until fracture. At the particular loading level, this energy can be attributed to fiber bridging, fiber failure, and pull out.

3.3. Acoustic Emission

3.3.1. Static/Cyclic Loading. Cumulative AE signal history collected during cyclic loading of a DEN specimen with 0.35 notch-to-width ratio is shown in Figure 10 alongside with strain. The rate of AE acquisition exhibits fluctuations according to the cyclic loading protocol. Specifically, AE rate increases as the load increases to the maximum within each cycle. After these maxima points, the AE rate decreases without however being completely eliminated, at the cycle's minimum load. The total activity was of the order of 4000 signals.

Apart from the cumulative activity, which counts the separate acquisitions of the sensors, different AE descriptors help to distinguish the severity of the condition according to loading level. Two of them are the ASL and RMS. ASL is the average signal level defined as the average amplitude of samples of the rectified waveform while RMS is the square root of the average of the squares of all points of a waveform (root mean square) [19].

They are given by

$$\text{ASL (Average Signal Level): ASL} = \frac{1}{n}\left(x_1 + x_2 + \cdots + x_n\right)$$

$$\text{RMS (root mean square, } X_{\mathrm{rms}}\text{): } X_{\mathrm{rms}} = \sqrt{\frac{1}{n}\left(x_1^2 + x_2^2 + \cdots + x_n^2\right)}, \tag{1}$$

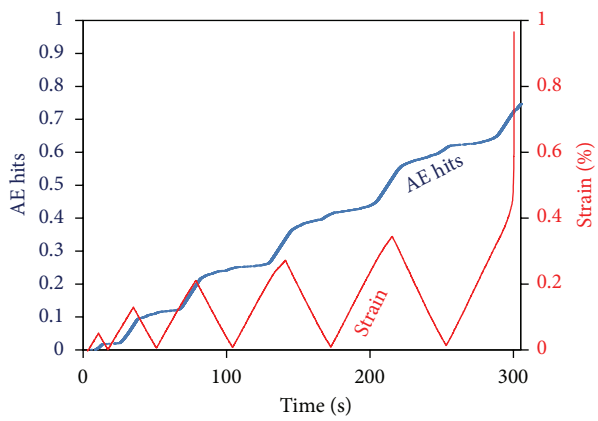

Figure 10: Strain and AE cumulative history for specimen B.

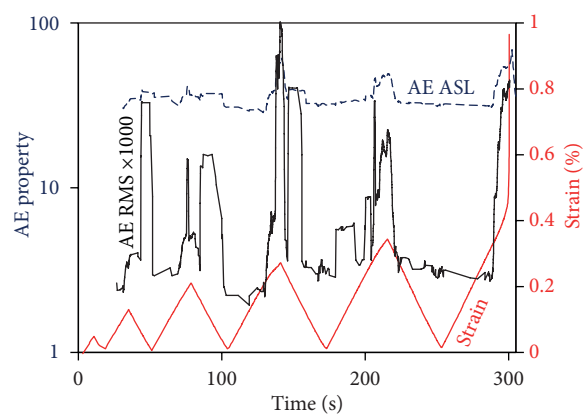

Figure 11: Strain history and AE amplitude parameters for a double-edge notched specimen with notch-to-width ratio of 0.35.

where n is the number of samples (waveform points) and x_i stands for the rectified amplitude of the waveform samples.

Therefore, both of them are indicative of the AE signal emitted by the fracture. Figure 11 shows the sliding average (window of 20 points) for both AE parameters. Focusing on the ASL first, local peaks are indicated at the moments of local maxima of strain, especially for the last three cycles. This means that at those periods of high strain, stronger fracture incidents take place which are recorded as waveforms with different intensity characteristics. The same holds for the RMS which again gives a measure of the elastic energy recorded by the sensor being proportional of the pressure wave that impinged on the sensor's surface. The values of RMS were multiplied by a thousand for visibility reasons in the graph. These parameters show that monitoring of AE and specific qualitative AE features allows the recording of the high stressing moments and the whole loading history until the material is brought to failure.

Apart from the amplitude or energy-related parameters, significant information can be derived by the frequency content of the emitted waves. In mechanical materials it has been shown that a drop of frequency indicates increase of

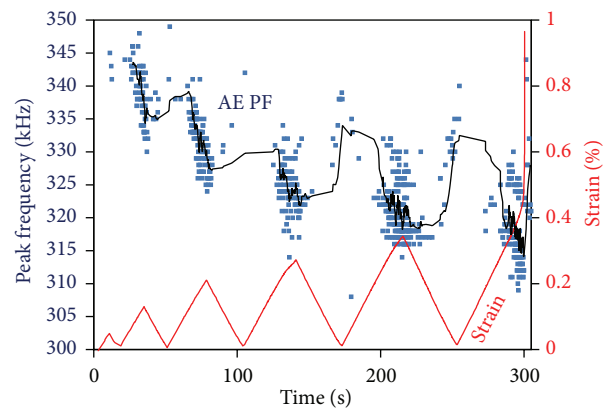

Figure 12: Strain history and AE peak frequency for a double-edge notched specimen with notch-to-width ratio of 0.35. The solid line is the sliding average of recent 20 points.

damage accumulation and is linked with the shift between fracture modes (e.g., initial tensile matrix cracking to ultimate shearing) [20, 21]. The index that is displayed here is peak frequency (PF) and is the frequency of the highest peak of the FFT of the AE waveforms. Using the specific AE sensors typical peak frequencies average around 450 kHz which is the maximum sensitivity of the sensors, while different bands from 100 kHz up to approximately 800 kHz can also be recorded. Figure 12 focuses on a specific family of emissions which initially exhibit frequencies between 330 and 350 kHz. It can be easily seen that this group of emissions are registered near the maxima of the strain cycles. However, one certain trend is that the main frequency of this family steadily drops in frequency after each cycle. This drops is of the order of 5 to 10 kHz in each cycle resulting in an average of 315 kHz at the last cycle just before failure. This drop of frequency is a result of the shifting between fracture mechanisms within the material since the monitoring conditions (sensors, separation distance) were constant throughout the experiment duration.

The observed behavior can be due to the increasing number of interfacial F that is expected to happen at the higher strain levels of the cycles. This allegation is supported by visual evidence of fiber bundle sliding and existence of off-axis layers seen in the postmortem side view of a specimen's notched ligament, microphotograph in Figure 13. It is observed that crack opening is approximately 500 μm. It is also observed that fibers are bridging the crack sides being pulled out of the matrix. While rupture of a large number of individual fibers is evident, fiber bundles have not failed completely since the specimen was removed in one piece after the test.

3.3.2. Fatigue Loading. During fatigue loading continuous monitoring by AE was applied, as mentioned earlier. Apart from the activity (number of emissions) all different AE parameters were recorded. As the fatigue life proceeds and damage is being accumulated, apart from the larger number of signals which are emitted, the nature (waveform shape) of the AE incidents starts to change. One of the indicative AE

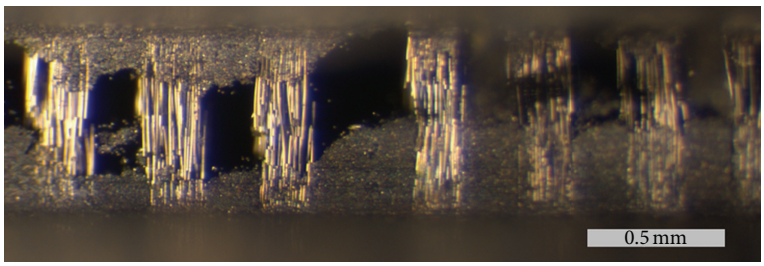

Figure 13: Stereoscope image of the side of a fractured specimen.

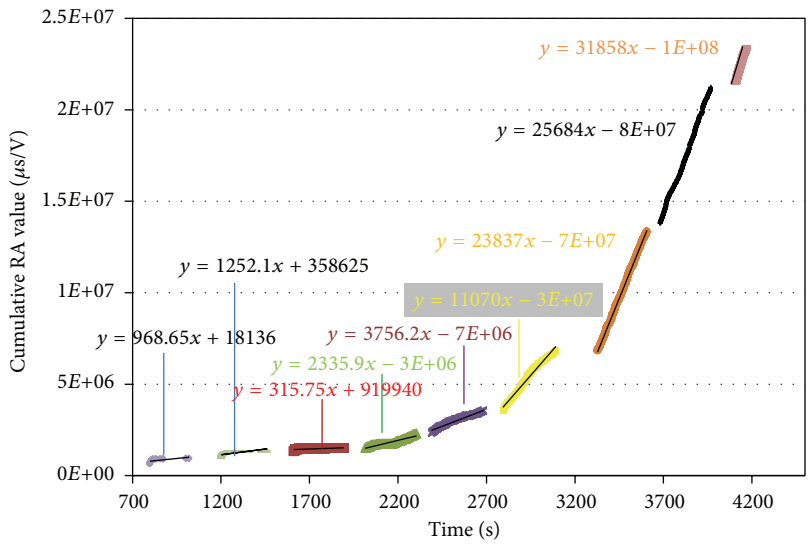

Figure 14: Cumulative RA value for the different fatigue loading stages.

descriptors is the RA value which is the inverse of the rising angle of the waveform and is given by

$$\mathrm{RA} = \frac{\mathrm{RT}}{A}, \tag{2}$$

where RT is the rise time of the waveform (or delay between the onset and the highest peak in μs) and A is the amplitude of the highest peak in V. In general this feature increases as damage develops along with the shift of the failure mechanisms from matrix cracking to shearing phenomena like interfacial sliding and debonding [18, 19]. Therefore, RA values are progressively increasing until the final failure of the specimen. Figure 14 shows the cumulative RA value for the different stages of fatigue loading. As mentioned above, at the early stages, RA values accumulation is low. At the block of loading starting at approximately 2000 s (70% of UTS) the RA values seem to accumulate at a higher rate, which is increasing for each successive step.

The rate of RA accumulation is shown in Figure 15. This allows a more clear visualization of the trends between the AE and RA at different stages. It is concluded that the curve can be fitted by two straight lines. The change of slope between the two lines occurs below 75% load which is a certain indication that significant changes take place after that load level. At lower loads, the events emit notably lower RA values showing less intensity compared to levels higher than 75%. The intersection of the two lines is between 70% and 75% and coincides well with the change of slope in the corresponding thermal dissipation curve presented earlier. This shows that both techniques can register small but delicate changes of the failure processes, depending on the fatigue loading. It seems that although incidents that, emit acoustic emission and heat are

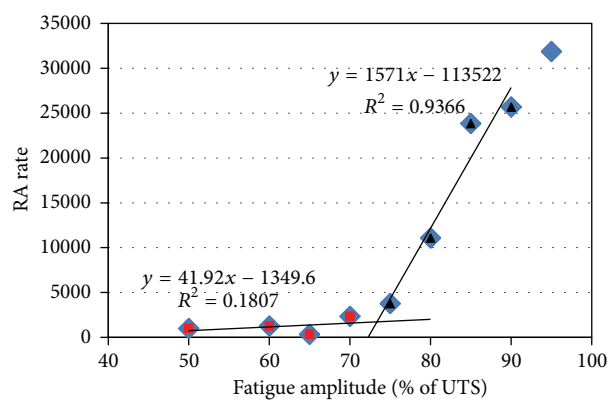

Figure 15: RA increasing rate for different fatigue loading amplitudes.

induced by low loading, these exhibit distinct values from corresponding events at loads higher than the fatigue limit which eventually will lead to the failure of the specimen.

4. Conclusions

Thermography and acoustic emission were used to capture the initiation and evolution of damage in SiC-fiber reinforced glass-ceramic matrix composites under static and fatigue loading. Infrared thermography results helped identify the intact fiber population as the mechanism that control ultimate material failure and that under the presence of notches the composite fails shortly after the attainment of a saturated matrix cracking state. Infrared thermography (IRT) was also used to monitor, both in location and in time, the crack propagation path during mechanical testing in cyclic tension and fatigue. The technique also enabled early prediction of the residual life of the material, as early as at 73% of the duration of the final loading cycle. Successful application of the technique under such dynamic conditions where the surface changes with usage is close to real-life scenarios found in aerospace applications.

A novel infrared lock-in thermographic methodology was used for the determination of the fatigue limit of the ceramic matrix composites (CMCs). The limit was unconventionally rapidly assessed by the thermographic technique at 70% σ_{ULT} (i.e., 205 MPa). The outcome makes lock-in IRT a new, versatile, and accurate method that overcomes the limitations of Wöhler's curve approach, as it significantly reduces experimental time and requires testing of a single sample only for obtaining the fatigue limit of the material.

Furthermore, acoustic emission (AE) monitoring enables monitoring fracture behavior in real time. Apart from the increase of AE acquisition for higher load and damage accumulation, energy- and frequency-related parameters help discern the moments higher stress. Descriptors like the root mean square (RMS) and average signal level (ASL) increase their values at high stresses, while peak frequency shows the inverse trend, being continuously downgraded for the successive loading steps. Concerning fatigue, AE showed the capability of detecting the different intensity of the fracture incidents. Waveform shape parameters like the RA exhibit changes as the load increases above the fatigue level of the material. The results are benchmarked by the heat dissipation curves offered by thermography and allow the determination of the fatigue limit of the material by using only one specimen.

References

[1] A. G. Evans, "The mechanical performance of fiber-reinforced ceramic matrix composites," *Materials Science and Engineering A*, vol. 107, pp. 227–239, 1989.

[2] J. J. Brennan and K. M. Prewo, "Silicon carbide fibre reinforced glass-ceramic matrix composites exhibiting high strength and toughness," *Journal of Materials Science*, vol. 17, no. 8, pp. 2371–2383, 1982.

[3] J. G. Sun, M. J. Verrilli, R. Stephan, T. R. Barnett, and G. Ojard, "Nondestructive Evaluation of Ceramic Matrix Composite Combustor Components," NASA/TM-2003-212014, April 2003.

[4] E. I. Madaras, W. P. Winfree, W. H. Prosser, R. A. Wincheski, and K. E. Cramer, "Nondestructive evaluation for the space shuttle's wing leading edge," in *Proceedings of the 41st AIAA/ASME/SAE/ASEE Joint Propulsion Conference and Exhibit*, July 2005, AIAA 2005-3630.

[5] W. P. Winfree, E. I. Madaras, K. E. Cramer et al., "NASA langley inspection of rudder and composite tail of American Airlines Flight 587," in *Proceedings of the 46th AIAA/ASME/ASCE/AHS/ASC Structures, Structural Dynamics and Materials Conference*, pp. 5636–5644, April 2005, AIAA 2005-2253.

[6] H. Mei, Y. Xu, L. Cheng, and L. Zhang, "Nondestructive evaluation and mechanical characterization of a defect-embedded ceramic matrix composite laminate," *International Journal of Applied Ceramic Technology*, vol. 4, no. 4, pp. 378–386, 2007.

[7] J. G. Sun, C. M. Deemer, W. A. Ellingson, and J. Wheeler, "NDT technologies for ceramic matrix composites: oxide and nonoxide," *Materials Evaluation*, vol. 64, no. 1, pp. 52–60, 2006.

[8] F. Levallois, A. Sobeczko, A. Proust, D. Marlot, and J.-C. Lenain, "Non-destructive testing of GAIA frame by means of acoustic emission monitoring during launch simulation tests," in *Proceedings of the 30th European Conference on Acoustic Emission Testing & 7th International Conference on Acoustic Emission*, University of Granada, Granada, Spain, 2012.

[9] P. M. Benson, K. E. Spear, and G. C. Pantano, "Interfacial characterisation of glass matrix/Nicalon SiC fiber composites: a thermodynamic approach," *Ceramic Engineering and Science Proceedings*, vol. 9, pp. 663–670, 1988.

[10] K. G. Dassios, "A review of the pull-out mechanism in the fracture of brittle-matrix fibre-reinforced composites," *Advanced Composites Letters*, vol. 16, no. 1, pp. 17–24, 2007.

[11] M. P. Luong, "Fatigue limit evaluation of metals using an infrared thermographic technique," *Mechanics of Materials*, vol. 28, no. 1–4, pp. 155–163, 1998.

[12] K. G. Dassios, D. G. Aggelis, E. Z. Kordatos, and T. E. Matikas, "Cyclic loading of a SiC-fiber reinforced ceramic matrix composite reveals damage mechanisms and thermal residual stress state," *Composites Part A*, vol. 44, pp. 105–113, 2013.

[13] C. Cady, F. E. Heredia, and A. G. Evans, "In-plane mechanical properties of several ceramic-matrix composites," *Journal of the American Ceramic Society*, vol. 78, no. 8, pp. 2065–2078, 1995.

[14] G. Camus, L. Guillaumat, and S. Baste, "Development of damage in a 2D woven C/SiC composite under mechanical loading: I. Mechanical characterization," *Composites Science and Technology*, vol. 56, no. 12, pp. 1363–1372, 1996.

[15] M. Steen, "Tensile mastercurve of ceramic matrix composites: significance and implications for modelling," *Materials Science and Engineering A*, vol. 250, no. 2, pp. 241–248, 1998.

[16] K. G. M. Dassios and T. E. Matikas, "Residual stress-related common intersection points in the mechanical behavior of ceramic matrix composites undergoing cyclic loading," *Experimental Mechanics*, vol. 53, no. 6, pp. 1033–1038, 2013.

[17] K. G. Dassios and T. E. Matikas, "Large-scale interfacial damage and residual stresses in a glass-ceramic matrix composite," *Composite Interfaces*, vol. 19, no. 8, pp. 523–531, 2012.

[18] C. Koimtzoglou, K. G. Dassios, and C. Galiotis, "Effect of fatigue on the interface integrity of unidirectional Cf-reinforced epoxy resin composites," *Acta Materialia*, vol. 57, no. 9, pp. 2800–2811, 2009.

[19] W. Kaewwaewnoi, A. Prateepasen, and P. Kaewtrakulpong, "Measurement of valve leakage rate using acoustic emission," in

Proceedings of the International Conference on Electrical Engineering/Electronics, Computer, Telecommunications, and Information Technology (ECTI '05), pp. 597–600, Pattaya, Thailand, May 2005.

[20] M. Ohtsu, "Recommendation of RILEM TC 212-ACD: acoustic emission and related NDE techniques for crack detection and damage evaluation in concrete: test method for classification of active cracks in concrete structures by acoustic emission," *Materials and Structures*, vol. 43, no. 9, pp. 1187–1189, 2010.

[21] D. G. Aggelis, S. Verbruggen, E. Tsangouri, T. Tysmans, and D. van Hemelrijck, "Characterization of mechanical performance of concrete beams with external reinforcement by acoustic emission and digital image correlation," *Construction and Building Materials*, vol. 47, pp. 1037–1045, 2013.

Hindawi Publishing Corporation
The Scientific World Journal
Volume 2013, Article ID 596506, 10 pages
http://dx.doi.org/10.1155/2013/596506

Research Article

New Sensors and Techniques for the Structural Health Monitoring of Propulsion Systems

Mark Woike,[1] Ali Abdul-Aziz,[1] Nikunj Oza,[2] and Bryan Matthews[2]

[1] *National Aeronautics and Space Administration, Glenn Research Center, Cleveland, OH 44135, USA*
[2] *National Aeronautics and Space Administration, Ames Research Center, Moffett Field, CA 94035, USA*

Correspondence should be addressed to Mark Woike; mark.r.woike@nasa.gov

Received 15 April 2013; Accepted 6 June 2013

Academic Editors: D. Greatrix, C. Hajiyev, A. Kalfas, Y.-H. Li, and L. Massotti

The ability to monitor the structural health of the rotating components, especially in the hot sections of turbine engines, is of major interest to aero community in improving engine safety and reliability. The use of instrumentation for these applications remains very challenging. It requires sensors and techniques that are highly accurate, are able to operate in a high temperature environment, and can detect minute changes and hidden flaws before catastrophic events occur. The National Aeronautics and Space Administration (NASA), through the Aviation Safety Program (AVSP), has taken a lead role in the development of new sensor technologies and techniques for the in situ structural health monitoring of gas turbine engines. This paper presents a summary of key results and findings obtained from three different structural health monitoring approaches that have been investigated. This includes evaluating the performance of a novel microwave blade tip clearance sensor; a vibration based crack detection technique using an externally mounted capacitive blade tip clearance sensor; and lastly the results of using data driven anomaly detection algorithms for detecting cracks in a rotating disk.

1. Introduction

The development of in situ measurement technologies and fault-detection techniques for the structural health monitoring of gas turbine engines is of major interest to NASA's Aviation Safety Program and the aeronautical community. The rotating components of modern gas turbine engines operate in severe environmental conditions and are exposed to high thermal and mechanical loads. The cumulative effects of these loads often lead to high stresses, structural deformities, cracks, and eventual component failure. Current structural health monitoring practices involve periodic inspections and schedule-based maintenance of engine components to ensure their integrity over the lifetime of the engine. However, these methods have their limitations, and failures are experienced leading to unscheduled maintenance and unplanned engine shutdowns. To prevent these failures and enhance aviation safety, the NASA Glenn Research Center has investigated new sensor technologies and techniques for the in situ structural health monitoring and detection of defects in gas turbine engines.

Much of the research effort to date has dealt with the development of low technology readiness level (TRL) structural health concepts with the intent of validating these concepts and transitioning them to higher TRLs for usage on actual aero engine hardware. In this study, microwave blade tip clearance and blade tip timing sensor technology is being investigated as a means of making high temperature noncontact structural health measurements in the hot sections of gas turbine engines. It is specifically being targeted for use in the high pressure turbine (HPT) and high pressure compressor (HPC) sections to directly monitor the structural health of the rotating components. The capability to make in situ health measurements is a need that has been identified by the aero engine community as blade damage in the HPT and HPC sections account for 12 percent of the inflight engine shutdown events and 32 percent of the damage events that caused engine removal for unscheduled maintenance [1].

Currently there are no off-the-shelf blade tip clearance sensors that are used in commercial turbine engines for in-situ structural health monitoring, as there are challenges with

the sensors being able to operate in and survive the harsh high temperature environment. Microwave sensor technology is appealing in that it is accurate, it has the ability to operate at extremely high temperatures, and is unaffected by contaminants that are present in turbine engines. In addition to its use for structural health monitoring, this type of sensor also has parallel usage in improving engine performance through its use in active turbine tip clearance control schemes. As a means of better understanding the issues associated with the microwave sensors, a series of evaluation experiments were conducted to evaluate their performance on aero turbine engine like hardware.

Along with the development and evaluation of new types of blade tip clearance sensors, efforts have been placed into developing techniques that utilize these sensors for the structural health monitoring of engine components. The vibration based crack detection experiment that will be discussed involved introducing a notch to simulate a crack on a subscale turbine engine disk and monitoring its vibration response as the disk was rotated at speeds up to 12 000 rpm. The vibration response was characterized by using externally mounted capacitive blade tip clearance sensors to measure the combined disk-rotor system's whirl amplitude and phase during operation. Testing was performed on a clean undamaged baseline disk and a disk with a 50.8 mm long notch machined into the disk to simulate a crack. The responses were compared and evaluated against the theoretical models to investigate the applicability and success of detecting the notch.

And finally, in parallel with the vibration based crack detection investigation an experiment using data driven anomaly detection algorithms was undertaken as a means of evaluating whether these data mining techniques could be used to detect a fault or an anomaly in a rotating engine disk. In this experiment blade tip clearance data sets were acquired on an undamaged subscale engine rotor disk as it was operated at speeds up to 10 000 rpm. This baseline data was used to train three different data mining algorithms. Data was then acquired from a damaged disk with a known crack and the data mining algorithms were used to detect the presence of the crack.

This paper presents a summary of key results and findings obtained from three different structural health monitoring approaches that have been investigated. This includes evaluating the performance of a novel microwave blade tip clearance sensor; a crack detection technique using externally mounted blade tip clearance sensors; and lastly discussing the results of a data driven anomaly detection technique for sensing cracks in a rotating rotor disk.

2. Microwave Blade Tip Clearance/Blade Tip Timing Sensors

The ability to monitor the structural health of the rotating components, especially in the hot sections of turbine engines, is of major interest to aero community in improving engine safety and reliability [2]. In addition, the active control and minimization of the gap between the rotating turbine blades and the stationary case of gas turbine engines is being sought as a means of increasing engine efficiency, reducing fuel consumption, reducing emissions, and increasing engine service life [3]. The use of instrumentation for these applications in gas turbine engines requires sensors that are highly accurate and can operate in a high temperature environment. To address this need, microwave sensor technology is being investigated as a means of making high temperature noncontact blade tip clearance and tip timing measurements for use in structural health monitoring and active clearance control applications in turbine engines. This technology is appealing due to its high accuracy and its potential to operate at extremely high temperatures that are present in turbine engines. It is intended to use blade tip clearance to monitor blade growth and wear and blade tip timing to monitor blade vibration and deflection.

2.1. Sensor Background and Theory. NASA has worked with Radatec (now Meggitt Inc.) through the Small Business Innovation Research (SBIR) program for the development of microwave sensor technology for high temperature noncontact blade tip clearance and blade tip timing measurements. The initial development of the technology was accomplished through a phase II SBIR contract awarded in 2002. Further development of the technology was accomplished in 2004 through 2005 as part of NASA's Ultra Efficient Engine Technology (UEET) Program. A prototype first generation 5.8 GHZ system was delivered as part of a phase III SBIR commercialization contract in 2007 and a second generation 24 GHZ system along with upgraded electronics was delivered as part of subsequent follow-on contracts in 2009 and 2010, respectively.

The microwave blade tip clearance sensor operates essentially as a field disturbance device. The tip clearance probe contains both a transmitting and receiving antenna. The sensor emits a continuous microwave signal and measures the signal that is reflected off a rotating blade. The sensor measures the changes in the microwave field due to the blade passing through the field. The motion of the blade phase modulates the reflected signal and this reflected signal is compared to an internal reference. Changes in amplitude and phase directly correspond to the distance to the blade. The time interval of when the blade passes through the field is measured to provide blade tip timing. More detailed information on the sensor's theory of operation can be found in [4–6]. The microwave blade tip clearance probes are made of high temperature material and are designed to operate in temperatures up to 900°C. The first generation probes (Figure 1(a)) operate at 5.8 GHz and can measure clearance distances up to one-half the radiating wavelength which is 25 mm. The second generation probes (Figure 1(b)) operate at 24 GHz and can measure clearance distances up to 6 mm. The 5.8 GHz sensor is targeted for use on large rotating machinery such as land based power turbines or in the fan sections of aero gas turbine engines. The 24 GHz sensor is being targeted for use in smaller rotating machinery applications such as the turbine and compressor sections of aero engines. This technology has an ultimate goal of obtaining

(a) (b)

Figure 1: Microwave blade tip clearance probe (Meggitt). (a) 5.8 GHz probe. (b) 24 GHz probe.

Figure 2: Axial vane fan located at the 10 × 10 SWT.

Figure 3: NASA Turbofan.

clearance measurement accuracies approaching +/−25 μm. A frequency response of up to 5 MHz is typical, with up to 25 MHz being possible with this technology which lends itself for use in structural health monitoring applications for the measurement of blade deflection and vibration.

2.2. Experimental Results. NASA's primary goal is to demonstrate this microwave blade tip clearance sensor technology on an actual gas turbine engine in a relevant high temperature environment. However, the use of microwave sensors for this application is an emerging concept. Techniques on their use and calibration needed to be understood and developed. In addition, the microwave sensor's accuracy and ability to make blade tip clearance and deflection measurements had to be assessed prior to use on actual engine hardware. As a means of better understanding the issues associated with the microwave sensors, a series of experiments were conducted to evaluate the sensor's performance on aero engine type applications. A summary of these experiments and their results are as follows.

The first generation 5.8 GHz microwave sensors were used to a make blade tip clearance measurements on a large axial vane fan and a subscale NASA Turbofan. The purpose of the test on the large Axial Vane Fan (Figure 2) was to develop the infrastructure required for the calibration of the sensors and the techniques for their use in the field to make clearance measurements on large rotating machinery. The motivation behind their use on the NASA Turbofan (Figure 3) was to evaluate the first generation sensor's ability to acquire blade tip clearance data on an aero engine size test article and blades. Blade tip clearance data sets were acquired for several test runs of the NASA Turbofan. Data was acquired at a variable sampling rate that was synchronized to the fan's speed. Each measurement consisted of two revolutions of data with 10 000 samples taken per revolution. Figure 4 shows the individual blade clearances measured for several fan speeds. It is clearly noted from the polar plot that the tip clearances decreased as the fan speed is increased.

This result is expected and is due to the growth and expansion of the turbofan's composite blades as the fan operates at higher speeds. An average decrease of 0.22 mm was observed as the rig speed was increased to 8 875 rpm. The change in clearance detected in this experiment was within the range predicted for these blades. In addition, the change in tip clearances measured by the microwave sensors was nearly identical to previously recorded values obtained with capacitive clearance sensors. In previous test entries, changes in tip clearances of up to 0.22 mm were also noted when the turbofan was operated over the same speed range. These two initial experiments served as test beds for the development of techniques and infrastructure required for the calibration of the sensors and successfully demonstrated the microwave clearance sensor's ability to make measurements on aero engine size hardware.

The second generation 24 GHz sensors were used to make measurements on a 32 blade subscale turbine engine like

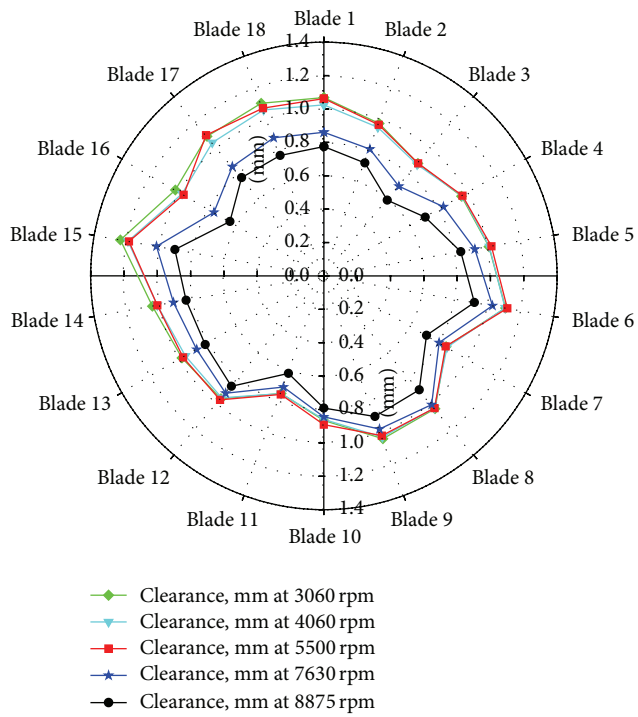

Figure 4: Blade tip clearance polar plot for probe #1, 90° location—NASA Turbofan experiment.

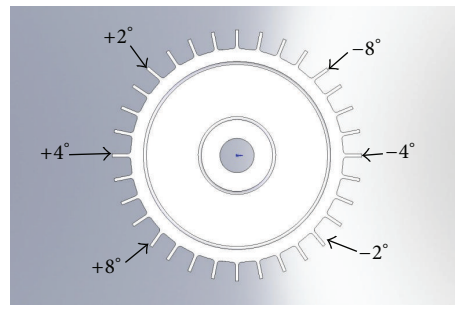

Figure 5: Simulated turbine disk with prebent blades for blade tip deflection testing.

disk and on an actual compressor stage from a small aero engine. These experiments were conducted in a laboratory environment using a calibration spin rig, a High Precision Spin Rig, and a High Temperature Spin Rig for the purposes of evaluating the second generation sensor's capability of making both clearance and timing measurements on small aero engine hardware. The 32 blade subscale engine disk (Figure 5) was manufactured to have 6 equally spaced blades that were bent at predefined angles or deflection distances. The purpose of this experiment was to evaluate the sensors ability to generate blade tip clearance and blade tip timing measurements simultaneously. During this experiment it was successfully demonstrated that the sensors were able to reliably make absolute measurements down to a clearance level of 100 μm. This was an improvement over the previously demonstrated minimum measurement of 500 μm made with the first generation sensors. This ability to measure very low clearance ranges is critical for use in closed loop clearance control applications. In addition, the sensor was able to simultaneously detect the minimum deflection of 0.70 mm (2 degrees) that was machined onto the disk. It is planned to further explore this capability by fabricating a disk that has smaller deflections in order to see the minimum deflection that can be reliably measured.

The investigation using a compressor stage from a small aero engine was conducted for the purposes of calibrating the sensors for future use on a small compressor and evaluating their ability to measure blade tip clearances on actual engine hardware over the very low clearance ranges typically associated with aero engines. For this experiment clearances were successfully measured over a range from 0.10 to 1.50 mm with a maximum observed error of +/− 0.021 mm. These results were encouraging in that the sensor was able to make measurements on actual aero engine hardware over a relatively low clearance range within the desired accuracy of +/− 0.025 mm. However, it is acknowledged that these results were achieved in the ideal set-up of a laboratory and that the results may differ in an actual engine due to noise and other environmental effects.

In summary, the evaluation testing that was accomplished on the microwave blade tip clearance technology has shown that sensors are a viable option for propulsion health monitoring and clearance control applications. Techniques for the calibration, integration, and use of the sensors to make measurements on aero engine hardware were successfully developed and both the first and second generation sensors have been successfully demonstrated on rotating machinery and aero engine hardware. A demonstration test of these sensors along with other advanced technologies on an engine ground test is being planned to occur in the 2013-2014 timeframe.

3. Vibration Based Crack Detection Technique

This crack-detection methodology involved introducing a notch on a simulated turbine engine disk and monitoring its vibration response as the disk was rotated at speeds up to 12 000 rpm. The vibration response was characterized by monitoring the disk-rotor system's whirl amplitude and phase during operation. The whirl amplitude and phase were derived from the blade tip clearance profile that was measured using externally mounted blade tip clearance sensors. This type of sensor was chosen as it represents the type of sensor that is most likely to be installed on a commercial engine due to its minimal installation impact, low overhead, and parallel benefits that it can bring to improve engine performance through its use in active turbine tip clearance control. The testing was performed on a clean undamaged baseline disk and on a damaged disk with a 50.8 mm long notch machined into the disk to simulate a crack. The experiment was conducted at the NASA Glenn Research Center's High Precision Spin Rig, a rig which is ideally suited for the development and validation of low technology readiness level (TRL) concepts before implementation on more

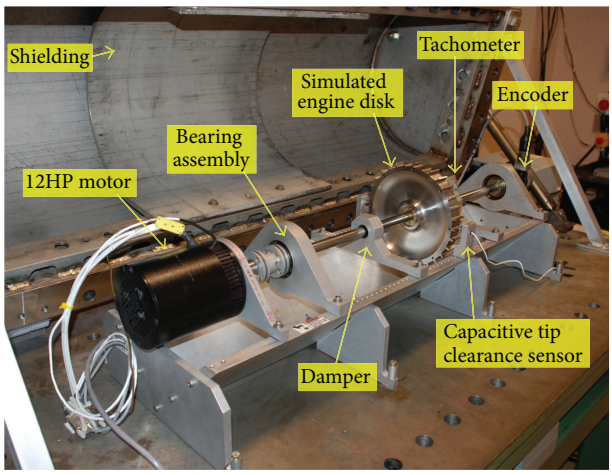

Figure 6: High Precision Spin Rig.

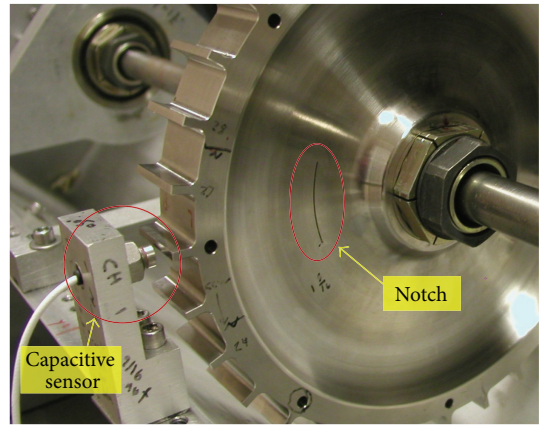

Figure 7: Capacitive blade tip clearance sensor and subscale turbine engine disk with notch.

expensive and complicated rotating machinery. A description of the High Precision Spin Rig, the baseline theory behind this technique, the experimental setup, and the results are discussed.

3.1. High Precision Spin Rig Description. Figure 6 shows the Rotordynamics Laboratory's High Precision Spin Rig, which can accommodate simulated engine rotor disks of up to 235 mm in diameter. It has a stainless steel shaft with a length of 781 mm and diameter of 20 mm. The shaft is supported by precision contact ball bearings on each end and has adjustable dampers that were positioned along the length of the shaft for these experiments. An encoder mounted on the end of the shaft was used by the control system to provide closed-loop control of rig speed. A secondary optical tachometer was used to record the speed into the data system and to synchronize the data to the rig's rotation. A 12-hp custom-built, brushless direct-current (dc) motor was used to rotate the spin rig and the subscale engine disks at speeds up to 12 000 rpm.

The rig was set up to acquire two channels of radial blade tip clearance data from the simulated engine disk using capacitive displacement sensors (Figure 7). These sensors were developed as part of a NASA Small Business Innovation Research (SBIR) contract and were different from traditional capacitive sensors in that their operation was based on a dc offset technique instead of the typical modulation technique. A National Instruments System was used to acquire data from the capacitive displacement probes at a fixed sampling rate of 1 MHz. This system and its application software were delivered as part of the SBIR contract for the capacitive blade tip clearance sensors. The system used custom data acquisition and processing applications that were tailored for acquiring and processing data from the blade tip clearance sensors.

3.2. Experimental Theory and Setup. The theory behind the crack-detection methodology that was investigated was based on previous theoretical and experimental work performed by Abdul-Aziz et al. [7, 8], Gyekenyesi et al. [9, 10], and Haase and Drumm [11]. The goal of this experiment was to determine if the crack-detection methodology investigated in these earlier studies could be validated by using the spin rig to conduct tests on simulated engine rotor disks with a notch introduced to replicate a crack.

The detection methodology is based on monitoring the vibration response of rotating disks to determine if a crack has developed. The theory implies that a defect, such as a crack, creates minute deformations in the disk as it is rotated. The deformation, in turn, creates a speed-dependent shift in the disk's center of mass. It was theorized that this shift could be detected by analyzing the vibration whirl amplitude and phase as measured by the blade tip clearance profile. The system's behavior was modeled after a 2-degree-of-freedom Jeffcott rotor. The model predicts that the vibration amplitude peaks when a clean, undamaged disk goes through the first critical speed but heads to a lower steady-state value as the speed is increased above the critical speed. Correspondingly, the phase shifts 180° when going through the first critical speed and then stabilizes to a steady-state value as the speed is increased past critical. At this point, the rotor is rotating about the combined system's center of mass and has stabilized. However, as the speed of a cracked disk is increased, centrifugal forces open the crack. This, in turn, deforms the disk and shifts its center of mass. At speeds above critical, the crack-induced shift in the disk's center of mass starts to grow and dominate the overall system's vibration response. The modeling predicts that, instead of heading toward a steady-state value, the vibration amplitude will change as a second-order function of rotational speed as it is increased beyond the first critical speed. This can be detected by analyzing the vibration response of the disk-rotor system, particularly the amplitude and phase of the first harmonic, as the system is operated over a range of speeds.

The testing approach used in this experiment was to spin a subscale engine disk over a speed range from 0 to 12 000 rpm and simultaneously record its vibration response. The vibration response was acquired as previously described using capacitive displacement probes to measure the blade

tip clearance profile. Two subscale simulated engine turbine disks were tested. The first disk was undamaged and was used to acquire the baseline vibration response data. The disk had an outside diameter of 235 mm, a bore thickness of 25.4 mm, and an outside rim thickness of 31.75 mm. The thinnest portion of the disk's web was 2.54 mm. Thirty-two teeth to simulate blades were evenly spaced around the circumference of the disk. Each simulated blade had a cross section of 31.75 mm by 3.30 mm and a height of 8.38 mm. The disk was made of a nickel base alloy, Haynes X-750 (Haynes International, Inc.) and had a weight of 4.88 kg.

The damaged disk is shown in Figure 7. It was identical to the baseline disk with the exception that a 50.8 mm long notch had been introduced in its mid-span region to imitate a crack in the disk. The mid-span region was selected since prior finite-element analysis had shown that this area experienced high stress levels during operation. The data acquired from this disk were compared with the data from the undamaged baseline disk to determine if the simulated crack could be detected by analyzing the vibration response. Supportive analytical calculations were made using finite-element analysis to complement the experimental work and determine the expected radial growth of the disk. The finite-element analysis predicted a radial growth on the order of ~0.075 mm at the highest operating speed, 12 000 rpm. This was within the detection limit of the blade-tip-clearance instrumentation. However, it should be noted that the major effect that was to be monitored was how the notch changed the combined center of mass of the disk-rotor system and its vibration amplitude and phase, not the radial blade tip growth of the disk.

3.3. Experimental Results. The experimentation consisted of operating the baseline and notched disks at several speed profiles and recording their vibration responses using the capacitive blade tip clearance sensors. The first harmonic component of the tip-clearance profile for each revolution was then analyzed to determine if the amplitude and phase exhibited the expected characteristics associated with a crack in the disk. Approximately 15 test runs were conducted for each disk. A typical test run or cycle consisted of ramping up the disk's speed from 0 rpm to a predefined maximum speed, remaining on condition for 0 to 60 s, then ramping back down to 0 rpm. Blade tip clearance data were acquired over the entire cycle. Data sets were acquired at ramp rates of 60 and 100 rpm/s for peak operating speeds of 5 000, 10 000, and 12 000 rpm. In addition, complex mission profiles were conducted where the speed was ramped to various power levels in an attempt to simulate the rigorous loading conditions that an engine would experience during a typical mission.

The run profile presented in this paper is shown in Figure 8. It is typical of the profiles that were used in the investigation. For this test case, the speed of the disk was increased from 0 to 10 000 rpm at a ramp rate of 100 rpm/s, cycled between 10 000 and 5 000 rpm for three cycles, then ramped down from 10 000 to 0 rpm. This was done to simulate a mission profile from start-up to full power and

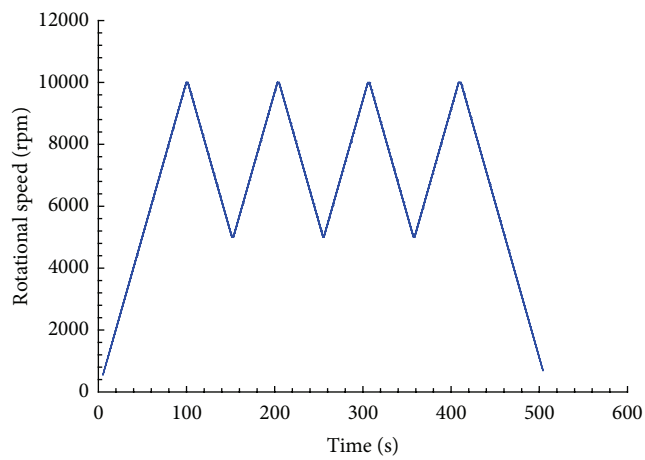

Figure 8: Simulated mission profile.

to observe the effects of cyclical loading on the disks. This ramping up and down also maximized the amount of data that could be acquired over a wide range of speeds, which was critical for the validation of this concept.

Figure 9 shows the results from this multiple-cycle test run for both the baseline and notched disks. The figure shows the analysis for the last cycle, starting at 10 000 rpm and ending at 0 rpm. As previously discussed, the presence of a crack is indicated if a second-order speed-dependent variation can be observed in the vibration amplitude as it is operated in the postcritical speed regime. In this test case, a speed-dependent rise was observed in the amplitude data for the notched disk. The area of interest showing the speed-dependent rise is highlighted within the circle of Figure 9(b). A curve-fit analysis, shown in Figure 10, was conducted on the vibration data in this region and it was found to closely follow a second-order polynomial fit, thus following the predicted behavior and potentially indicating the presence of the simulated crack.

Although the vibration data looked promising in this region, it was also observed that the second-order speed-dependent variation was not consistent over the entire range and that it appeared to reset itself at a speed of ~9500 rpm. Moreover, this relatively large amplitude variation was not consistently observed in other test runs, which cast some doubt on whether the effect was entirely due to the notch or to some other factor that is yet to be determined. However, this case yielded the best data so far and showed positive indications of being able to detect a defect such as a crack by analyzing the disk's vibration response as it is operated over a range of speeds. It is theorized that what made this case different, and more promising than other test runs, is that this test was conducted towards the end of the test series and many cycles had been placed on the disk prior to this test run. In addition, the disk experienced more loading because of the cyclical nature of the test profile. Overall, the results were promising and plans are in place to further investigate and refine this crack-detection technique as part of future studies.

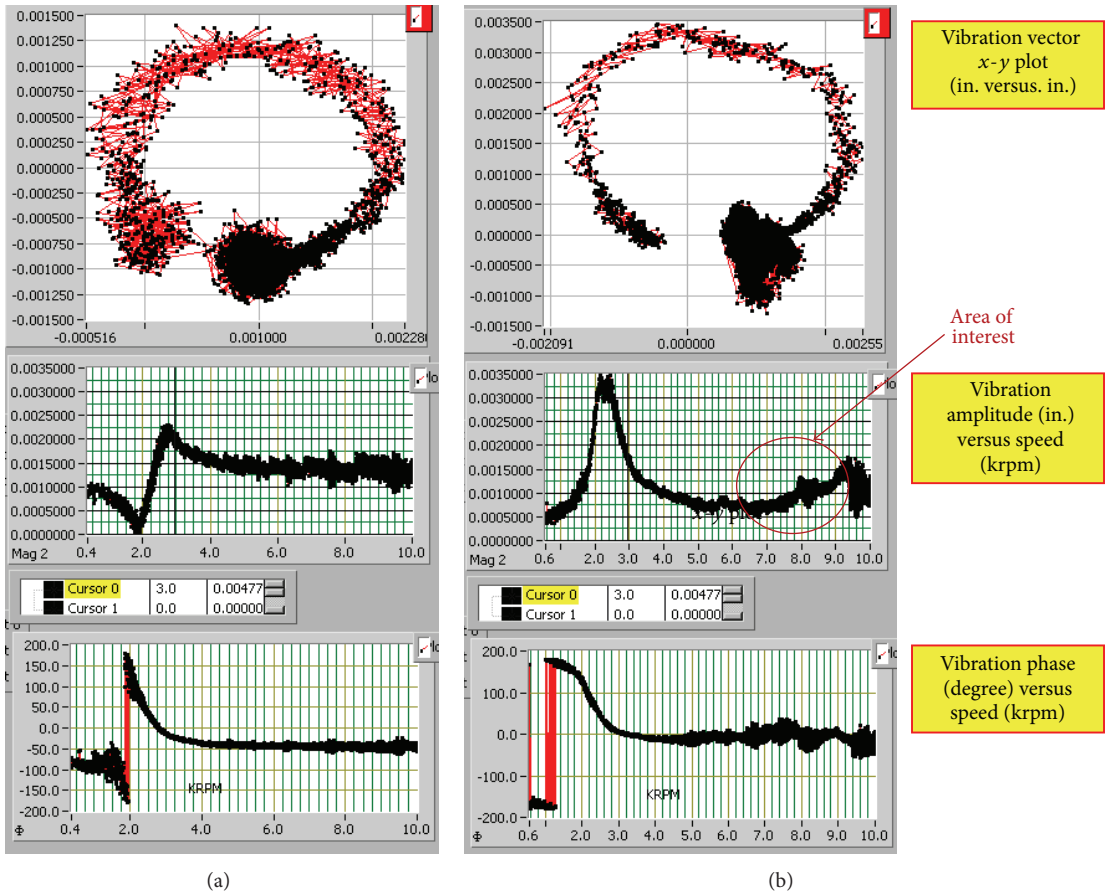

Figure 9: 10 000 rpm multiple-cycle run comparison. (a) Baseline disk. (b) Notched disk.

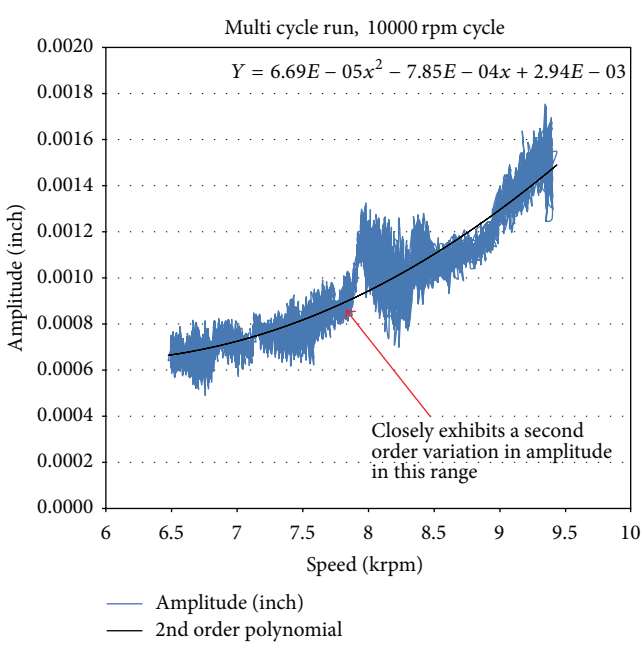

Figure 10: Detailed vibration amplitude plot for 10 000 rpm multiple-cycle run.

4. Data Driven Anomaly Detection Technique

In addition to the experimental work previously described, parallel health monitoring assessments have been conducted using data mining algorithms in order to detect flaws, such as cracks, in a rotating engine disk. In this technique blade tip clearance data were acquired on an undamaged subscale engine disk using the same 10 000 rpm multi-cycle run profile that was used for the previously described vibration based technique. These baseline data were used to train three different data mining algorithms: Orca, Inductive Monitoring System (IMS), and One-Class Support Vector Machine (OCSVM) [12–15]. These algorithms were then used to analyze the blade tip clearance data that was acquired from a damaged disk which had a notch machined into it to simulate a crack in order to evaluate their performance and determine if the algorithms could detect the presence of the notch due to changes in the disks operating characteristics as measured by the blade tip clearance sensors.

As stated previously, three different techniques were investigated: Orca, Inductive Monitoring System (IMS), and One-Class Support Vector Machine (OCSVM). These methodologies provide a technique that can monitor the health of

Table 1: Multiple 10 000 rpm cycle test results.

	Algorithm	Correct detection rate	False alarm rate	Accuracy	Area under ROC
5% false alarm rate	Orca	100%	5%	97.55%	1.00
	IMS	93%	5%	94.02%	0.93
	OCSVM	100%	5%	97.55%	0.99
90% correct detection	Orca	90%	0.58%	94.62%	1.00
	IMS	90%	0.36%	94.73%	0.93
	OCSVM	90%	1.26%	94.28%	0.99

a system with fidelity by training the model to identify normal system parameters from abnormal ones. This is implemented by defining groups of consistent system parameter data using nominal system data. These training data are then used to model the system. Upon learning how the system should behave under nominal operating conditions, these models are then used to identify abnormal behavior, such as a crack or flaw in the disk which causes a change in the known operation of the system.

4.1. Detection Algorithms

4.1.1. Orca. Orca is an outlier detection algorithm which uses a Euclidean distance nearest neighbor based approach to determine outliers. For computational efficiency, it employs a modified pruning technique which allows it to perform in near linear time. For each point in the test data set, where a point is a row in the data set consisting of measurements taken at a single point in time, Orca calculates the nearest neighbor points from the reference data set. The output from Orca is a distance score which represents the average distance to its k-nearest neighbors; the more anomalous the point is the higher the score, since the nearest neighbors are farther away. More information about this algorithm can be found in [13].

4.1.2. Inductive Monitoring System (IMS). IMS is a cluster based modeling method. The algorithm is given a set of nominal data points and builds a model by agglomerative clustering of the data points. The resulting model is used to generate anomaly scores for new data. For each test data point, IMS finds its distance to the nearest cluster's boundary. The score that is reported is the sum of the squares of the distances from the test data point to the dimensional bounds of the closest cluster. If a data point falls entirely within the cluster bounds, the point is expected to represent normal behavior and it is assigned a score of zero. More information about IMS can be found in [12].

4.1.3. One-Class Support Vector Machine (OCSVM). OCSVM is a one-class nonlinear kernel based algorithm that maps the training data to a higher-dimensional feature space and then linearly separates nominal data from anomalies in that feature space. The idea is that such a model corresponds to a nonlinear model in the original data space but still maintains the benefit of a linear model in that it is guaranteed to return the model with the lowest error over the training set. The algorithm identifies a subset of the training data, called the "support vectors," which is used to generate a hyperplane model. The anomaly score that is reported is the distance from the test data point to the hyperplane as measured in the feature space. More information on OCSVM can be found in [14, 15].

4.2. Analysis-Results. For the multiple-cycle test run previously shown in Figure 8 blade tip clearance data were recorded for both the undamaged and damaged, notched, disk. For the analysis, the 32 individual blade tip clearance measurements acquired for each revolution were utilized in training and evaluating the three anomaly detection algorithms. The undamaged disk's data was randomly divided in half. The first half was used for training of the algorithm and second half was used for validation. The means and standard deviations for all 32 channels were calculated for the training data and used to normalize both the training and testing data sets.

The plots of Figure 11 are the global anomaly scores for each of the algorithms for both the validation undamaged data set and the damaged data set over time. The anomaly scores are portrayed as positive values and any nominal points are represented as zero. This was done to allow for similar comparison across the algorithms. It is important to note that OCSVM allows some nominal sample points in the training set to be classified as anomalous. This percentage is governed by the Nu parameter, which is set by the user, but for which we set currently at the default value of 10%. Due to this characteristic of the algorithm 10% of all nominal data tested may result in anomalous classification. In analyzing the effectiveness of the three techniques in Table 1 the threshold for correct detection was set to 90% to make the comparisons fair between all three algorithms, since OCSVM, in this case, was optimized for a correct detection of 90%.

Figure 11 shows all three algorithms and they appear to have performed quite well in differentiating between the nominal undamaged disk and the damaged, notched disk test runs. Orca and OCSVM seem to show slightly better performance across a few of the metrics. In Table 1 the metrics used for comparison are correct detection, false alarm rate, accuracy, and area under the Receiver Operating Characteristic (ROC) curve. The ROC curve is a plot of false positives versus true positives. The ideal curve is one that has a 90° bend in it shooting straight up with the false positive = 0 and holding the true positive = 1 across resulting in an area of 1.00. When fixing the false alarm rate at 5%, Orca and

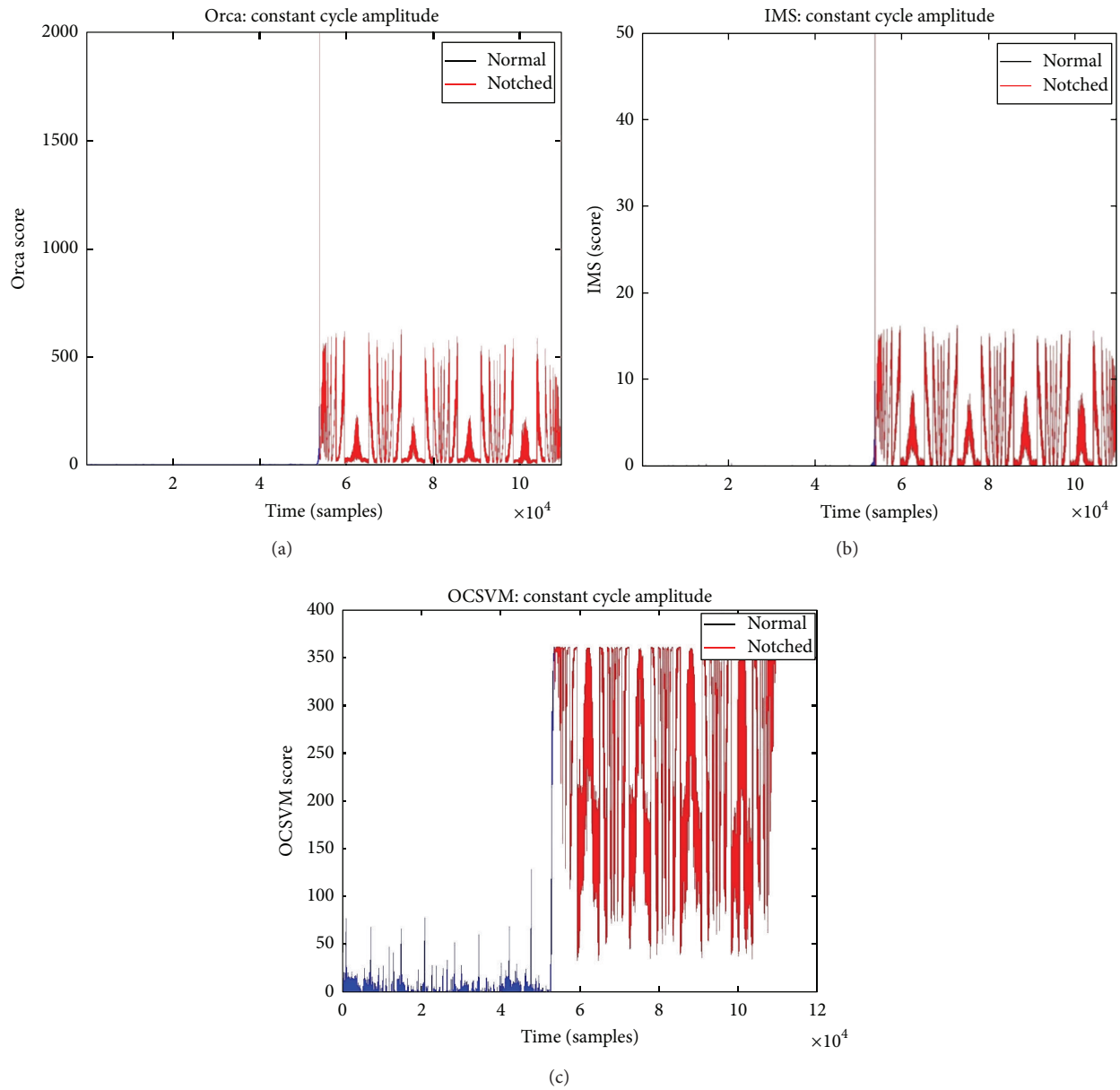

Figure 11: Results of the data driven anomaly detection techniques. (a) Orca. (b) IMS. (c) OCSVM.

OCSVM both have 100% correct detection rate of the notched anomalous data, where IMS's correct detection rate is at 93%. When fixing a threshold so that the correct detection rate is 90%, all three show very good false alarm rates. An additional metric, that is independent of choosing a threshold, is measuring the area under the ROC curve. When comparing this metric across the three algorithms, all three methods are reporting very good areas with Orca and OCSVM doing slightly better than IMS. The results obtained showed that the detection algorithms are capable of predicting anomalies in the rotor disk with very good accuracy. Each detection scheme performed differently under the same experimental conditions and each delivered a different level of precision in terms of detecting a fault in the rotor.

5. Conclusion and Future Plans

The work presented in this paper represents a summary overview of the on-going research activities that are being conducted at the NASA Glenn Research Center for the development of new sensors and fault detection techniques for the structural health monitoring of rotating turbine engine components. The main focus of these efforts is to first develop and validate low technology readiness level (TRL) structural health monitoring concepts and then mature them for further use on more complicated aero engine hardware.

The microwave blade tip clearance sensor technology was found to be a promising option for use in structural health monitoring applications for gas turbine engines. The sensors

have been successfully demonstrated on aero engine like hardware. The first generation 5.8 GHz sensors were used on a large axial vane fan and on a NASA Turbofan for the purposes of evaluating the sensor's ability to acquire blade tip clearance data on an aero engine size test article and blades. The second generation 24 GHz sensors were used to make basic blade tip deflection and low range clearance measurements on a simulated engine and on a small aero engine's compressor disk in order to evaluate the sensor's capability of making both clearance and timing measurements on small aero engine hardware. A ground test with these sensors installed on a full scale engine is being planned for the 2013-2014 timeframe.

The vibration based crack detection experimental results showed that this technique has the potential and merit to be used for detecting cracks on a rotating disk. The data acquired from the 10 000 rpm multiple-cycle test run showed a speed-dependent rise in the vibration amplitude, indicating that a crack-induced shift in the disk's center of mass was present. Other test cases equally showed that the system was on the verge of being able to detect the simulated crack using this technique, but not all of the expected trends were consistently observed. Nevertheless, this technique looks very promising and appears to have the sensitivity to detect faults in the rotor disk system. However, additional work remains warranted to further validate and refine this crack detection concept.

Additional health monitoring was performed through combined experimental and data-driven anomaly detection techniques. Three different automatic data-driven detection algorithms, Orca, OCSVM, and IMS, were used. These techniques were utilized to analyze blade tip clearance data acquired from the rotor operating under undamaged and damaged conditions to check the viability of the detection methodology and to evaluate the performance of each approach. The results obtained showed that the detection algorithms are capable of predicting anomalies in the rotor disk with very good accuracy. Each detection scheme performed differently under the same experimental conditions and each delivered a different level of precision in terms of detecting a fault in the rotor. Overall rating showed that both the Orca and OCVSM performed better than the IMS technique, but in the end all of the algorithms showed promise and will be further refined for eventual use in detecting flaws in rotating components of an engine.

References

[1] U.S. Department of Transportation, Federal Aviation Administration, "Engine Damage-Related Propulsion System Malfunctions," DOT/FAA/AR-08/24, 2008.

[2] T. Kurtoglu, K. Leone, M. Revely, and C. Sandifer, "A study on current and emerging technologies and future research requirements for integrated vehicle health management," Internal NASA Report, 2008.

[3] S. B. Lattime and B. M. Steinetz, "Turbine engine clearance control systems: current practices and future directions," NASA TM 2002-211794, AIAA-2002-3790, 2002.

[4] T. A. Holst, T. R. Kurfess, S. A. Billington, J. L. Geisheimer, and J. L. Littles, "Development of an optical-electromagnetic model of a microwave blade tip sensor," AIAA 2005-4377, 2005.

[5] J. L. Geisheimer, S. A. Billington, and D. W. Burgess, "A microwave blade tip clearance sensor for active clearance control applications," AIAA 2004-3720, 2004.

[6] T. A. Holst, *Analysis of spatial filtering in phase-based microwave measurements of turbine blade tips [M.S. thesis]*, Georgia Institute of Technology, Atlanta, Ga, USA, 2005.

[7] A. Abdul-Aziz, M. R. Woike, J. D. Lekki, and G. Y. Baaklini, "Health monitoring of a rotating disk using a combined analytical-experimental approach," NASA/TM 2009-215675, 2009.

[8] A. Abdul-Aziz, M. R. Woike, G. Abumeri, J. D. Lekki, and G. Y. Baakilini, "NDE using sensor based approach to propulsion health monitoring of a turbine engine disk," in *Health Monitoring of Structural and Biological Systems*, Proceedings of SPIE, pp. 9–12, San Diego, Calif, USA, March 2009.

[9] A. L. Gyekenyesi, J. T. Sawicki, and G. Y. Baaklini, "Vibration based crack detection in a rotating disk, part 1—an analytical study," NASA/TM 2003-212624, 2003.

[10] A. L. Gyekenyesi, J. T. Sawicki, R. E. Martin, W. C. Haase, and G. Y. Baaklini, "Vibration based crack detection in a rotating sisk, part 2—experimental results," NASA/TM 2005-212624/PART2, 2005.

[11] W. Haase and M. Drumm, "Detection, discrimination and real-time tracking of cracks in rotating disks," IEEE 0-7803-7321-X/01, 2002.

[12] D. L. Iverson, "Inductive system health monitoring," in *Proceedings of the International Conference on Artificial Intelligence, Proceedings of the International Conference on Machine Learning, Models, Technologies & Applications (MLMTA '04)*, vol. 2, June 2004.

[13] S. D. Bay and M. Schwabacher, "Mining distance-based outliers in near linear time with randomization and a simple pruning rule," in *Proceedings of the 9th ACM SIGKDD International Conference on Knowledge Discovery and Data Mining (KDD '03)*, pp. 29–38, Association for Computing Machinery, August 2003.

[14] D. M. J. Tax and R. P. W. Duin, "Support vector domain description," *Pattern Recognition Letters*, vol. 20, no. 11–13, pp. 1191–1199, 1999.

[15] B. Schölkopf, J. C. Platt, J. Shawe-Taylor, A. J. Smola, and R. C. Williamson, "Estimating the support of a high-dimensional distribution," *Neural Computation*, vol. 13, no. 7, pp. 1443–1471, 2001.

Hindawi Publishing Corporation
The Scientific World Journal
Volume 2013, Article ID 154984, 8 pages
http://dx.doi.org/10.1155/2013/154984

Research Article

Ultrasonic Characterization of the Fiber-Matrix Interfacial Bond in Aerospace Composites

D. G. Aggelis,[1,2] D. Kleitsa,[1] and T. E. Matikas[1]

[1] *Department of Mechanics of Materials and Constructions, Vrije Universiteit Brussel, Pleinlaan 2, 1050 Brussels, Belgium*
[2] *Department of Materials Science and Engineering, University of Ioannina, 45110 Ioannina, Greece*

Correspondence should be addressed to D. G. Aggelis; daggelis@cc.uoi.gr

Received 10 April 2013; Accepted 13 June 2013

Academic Editors: K.-M. Chung, E. E. Imrak, and A. F. B. A. Prado

The properties of advanced composites rely on the quality of the fiber-matrix bonding. Service-induced damage results in deterioration of bonding quality, seriously compromising the load-bearing capacity of the structure. While traditional methods to assess bonding are destructive, herein a nondestructive methodology based on shear wave reflection is numerically investigated. Reflection relies on the bonding quality and results in discernable changes in the received waveform. The key element is the "interphase" model material with varying stiffness. The study is an example of how computational methods enhance the understanding of delicate features concerning the nondestructive evaluation of materials used in advanced structures.

1. Introduction

Reinforcement of a bulk material with fibers is commonly applied in order to upgrade its properties in terms of stiffness, strength, and durability. Fiber composites are applicable in any type of material, like steel-fiber-reinforced concrete, polymer, or ceramic composites as well as metal matrix composite materials [1–3]. In most cases, the fibers exhibit higher mechanical properties than the matrix to improve its behavior. However, in order to take full advantage of the fiber potential, the bonding between fiber and matrix is of primary importance. Efficient stress transfer is desirable, and this is the reason that in certain cases chemical treatment of the fibers is applied in order to enhance bonding [4]. The chemical reaction between the matrix and fiber results in an "interphase" zone with properties different than the ones of the constituent phases (see Figure 1). This interphase zone may be very thin but it plays a crucial role in the mechanical performance of the medium. This is the zone through which stress is transferred, and therefore, all important mechanical properties of the composite like its strength and toughness heavily depend on the quality of the interphase [5, 6]. However, environmental and stress effects degrade the quality of the interphase compromising the structural capacity of the whole composite. It is understandable that the initial bonding conditions between fiber and matrix should be optimized in order to minimize the effect of service-induced deterioration. Assessing the quality of initial bonding is a task that can be conducted by certain mechanical tests like pull-out or push-in [7, 8]. However, these are destructive and focus on the strength, totally neglecting the elastic properties of the interphase. Therefore, a fast, nondestructive, and simple methodology of assessing the quality of the interphase is desirable. This should result in a quantifiable parameter related to the stiffness of the interphase and could be applied after manufacturing to assess the initial bonding condition in single fiber specimens or, under suitable circumstances, after service for assessment of bonding degradation. A reliable test will assist the design of the composite material by evaluating the stiffness of the interphase in terms of the different constituent materials' elastic and thermal properties, as well as regarding the suitable conditions to achieve optimal bonding, that is, temperature and pressure.

In the present paper, a numerical study of stress wave reflection is described in order to estimate the potential for characterization of the bonding and guide relevant experimental efforts [9]. The suitability of stress waves has been pointed out concerning characterization of surfaces and

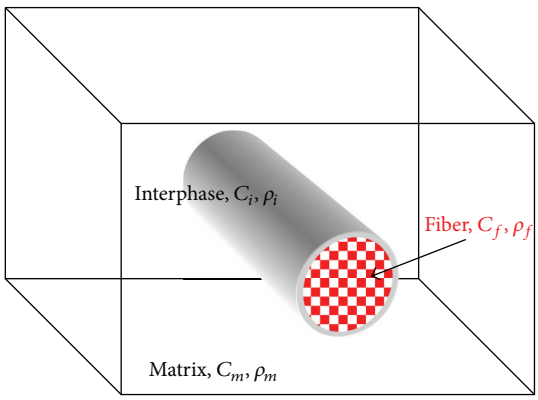

Figure 1: A typical part of the microstructure of the composite.

thin layers [10]. Stress waves employ infinitesimally small displacements and are influenced by the elastic properties of the materials. Therefore, their study reveals information on the stiffness of the materials and not directly their strength. Particularly, the immersion pulser-receiver technique is targeted. According to this technique, a pressure pulse is emitted inside a liquid (normally water). This pulse propagates with the sound velocity of water towards the material under test. When it meets an interface, it is partially transmitted and partially reflected through the medium. The number of reflections recorded by the sensor and their delay define the possible defects and their depth below the surface of the tested object. In the specific case described herein, the direction of the pulse relatively to the materials' surface is dictated by the shear critical angle so that only shear waves propagate in the medium, which are arguably more sensitive to the existence and quality of interphases [8, 11, 12]. The shear wave interacts with the embedded fiber and the reflection is eventually recorded by the receiver. Analysis of the recorded waveform sheds light into the condition of the interphase since the reflection depends on the relative mismatch of mechanical properties. When the bonding is inadequate due to incompatible materials or has worn out, there is essentially no contact between the materials. Therefore, a strong reflection is bound to occur since the fiber volume acts as a void in terms of wave propagation. In the case of a single scatterer, although dispersive effects are not expected, the analysis is based on the reflection on the scatterer in a pulser-receiver mode. On the other hand when two materials of similar stiffness are in good contact, the reflection will be minimized. The different possible conditions of bonding are simulated herein by an elastic "interphase" material with varying stiffness. This interphase should not be confused with the "interface" which is a boundary between the matrix and the fiber. This interphase is used to model the elastic properties of the interphasial zone between the matrix and fibers resulting from the chemical reaction between the two materials. Hence its behavior is governed by a user-defined varying elastic wave velocity to simulate different degrees of stiffness. This study includes the exact geometry of the fiber as an advancement of the analytical solution that was provided in [9] for the reflection on an inclined straight line instead of the circular cross-section of the fiber. The material system targeted herein is a metal matrix composite material [9]. Specifically, the matrix of the targeted material is Ti-6Al-4V reinforced with continuous SCS-6 fibers, a material widely used in aerospace. High strength titanium alloys, as well as fiber-reinforced metal matrix composite materials, are suitable for a number of highly demanding applications because of their improved mechanical properties in high temperature conditions. In applications where dynamic loading is expected and where life management is required, consideration must be given to the behavior of the material in the sensitive area of the interphase between the matrix and the fiber in order to verify the best possible performance of the material.

2. Numerical Simulations

2.1. Model. Numerical simulations are generally used to expand to cases that cannot be experimentally tested due to cost, geometry, or other limitations and also to increase the physical understanding in specific problems. Wave simulation studies enable also the recognition of wave modes and reflections inside a whole waveform. In the specific case, two-dimensional simulations were conducted on a cross-section of the geometry as is explained below.

The fundamental equation of two-dimensional propagation of elastic waves in an elastic medium neglecting viscosity is

$$\rho \frac{\partial^2 \underline{u}}{\partial t^2} = \mu \nabla^2 \underline{u} + (\lambda + \mu) \nabla \nabla \cdot \underline{u}, \tag{1}$$

where $\underline{u} = u(x, y, t)$ is the displacement vector as a function of time, t, ρ is the material density, and λ and μ are the first and second Lame constants, respectively. These parameters are related to the wave propagation velocities with the following equations:

$$C_L = \sqrt{\frac{\lambda + 2\mu}{\rho}}, \qquad C_S = \sqrt{\frac{\mu}{\rho}}, \tag{2}$$

where C_L is the longitudinal and C_S is the shear wave velocities respectively.

The simulations were conducted with commercially available software [13] that solves the above equation with respect to the boundary conditions of the object and the initial conditions [14]. The solution is in time domain with the finite difference method in the plane strain field. The excitation pulse has a defined displacement-time function and is applied at specified nodes of the geometry that simulate the "pulser." Continuity equations must be fulfilled at the interfaces between different entities. In the present analysis, individual materials are included in the geometry, and therefore propagation is solved in each distinct phase, while the continuity conditions for stresses and strains must be satisfied on the interfaces.

In the case described herein, the propagation of a stress wave after excitation in water is simulated. The geometry is

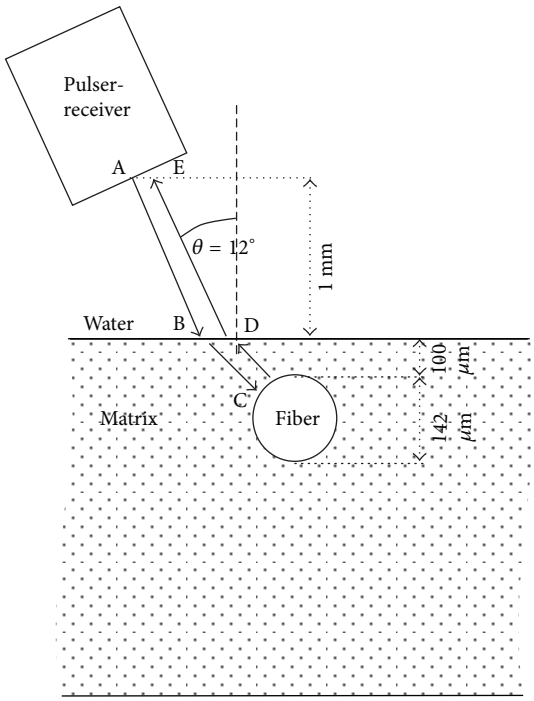

Figure 2: Geometry of the simulated test including wave directions.

shown in Figure 2 and the wave path of interest is indicated, while it is discussed in more detail in Section 3. The wave impinges on the matrix under the shear critical angle, thus allowing only shear waves to propagate into the matrix. The shear wave interacts with the fiber and a part is reflected back. After being refracted from the matrix/water interface, a longitudinal wave propagates through water back to the receiver (same as pulser, see Figure 2).

The "source" is placed at a specific angle, θ relatively to the vertical axis, equal to the critical shear angle of this horizontal liquid/solid interface. In the specific case, the angle is 12°, as calculated based on Snell's law and the mechanical properties of water and the titanium matrix [9]. The pulser introduces one cycle of different frequencies in the longitudinal mode. The applied frequencies were 1 MHz, 5 MHz, 10 MHz, 25 MHz, and 50 MHz.

The employed materials were considered elastic without viscosity. The basic properties of all the materials except the interphase are seen in Table 1. Both matrix and fiber materials are quite stiff with the fiber exhibiting approximately twice the longitudinal and shear wave velocities of the matrix. As already mentioned, the interphase obtained different values of stiffness expressed by the corresponding longitudinal wave velocities. This is a key parameter of the study and a practical way to simulate different contact levels between the matrix material and the fiber [11, 15]. Specifically, the lowest value was 300 m/s (case of loose interphase similar to air), and the maximum 11770 m/s which is the longitudinal wave velocity of the fiber. In between, the values were incremented by 1000 m/s, for example, 1000 m/s, 2000 m/s, 3000 m/s, and so forth. This includes the possible range of equivalent stiffness values that could be obtained by the interphase layer. The

Table 1: Basic properties for material modeling.

	Water	Matrix (Ti-6Al-4V)	Fiber (SCS-6)
λ (GPa)	2.25	25.9	61.9
μ (GPa)	10^{-4}	32.8	177.0
ρ (kg/m^3)	1000	2580	3000
C_L (m/s)	1500	5954	11774
C_S (m/s)	10	3566	7681

diameter of the fiber is 142 μm, and it is embedded 100 μm below the surface, (see Figure 2). Since there was no physical insight for the thickness of the actual interphase layer, it was set to 50 μm. In similar cases, it has been shown that the thickness of the interphase does not make critical difference in the results [11]. The vertical distance of the pulser was indicatively set to 1 mm above the surface of the specimen, while it can be adjusted to suit the relevant experimental geometry each time.

As in any simulation study, here also certain conditions must apply in order to ensure reliable and repeatable results. The mesh size is a crucial parameter since if it is defined to a relatively large value, the outcome will not be accurate but on the other hand there are computational power and time restrictions that prevent from applying an infinitesimally small value. Restrictions on the computational power do not always allow to use several elements per wavelength. In any case, since the study employs four materials (water, matrix, fiber, and interphase), there is no standard wavelength to adjust the element size accordingly. Therefore, another holistic approach was followed; different values of mesh sizes were tested; namely, from 0.4 mm down to 70 μm and the resulted waveforms were compared. Figure 3(a) shows the time window when the first part of the reflection (case of a loose interphase) is recorded for the frequency of 25 MHz for some indicative mesh sizes. Simulations with mesh sizes larger than 0.1 mm (specifically 0.3 and 0.4 mm in Figure 3(a)) result in quite different waveforms compared to the finer meshes and were not further considered. From the mesh size of 100 μm and finer, the waveforms converge in shape. In order to quantify the comparison of these cases, a threshold was chosen, namely, −0.012 units of amplitude (u.a.) in order to deterministically define the onset of the reflection (see Figure 3(a) and compare between different cases). As the mesh becomes finer, the calculated onset times changed and can be seen in Figure 3(b). The finer mesh tested (70 μm) resulted in an onset of 0.90067 μs but it was extremely time consuming. The simulations were conducted with the mesh of 80 μm which resulted in transit time of 0.89959 μs being 0.12% away from the result of the finest mesh applied. This was considered a suitable approximation due to the limited amount of error relatively to the specific available computational power. As an indication, a full simulation of a case in a computer with RAM of 3 GB and processor of 2.1 GHz lasted about 1 hr. Concerning the time step resolution, it resulted in 0.00034 μs, which even for the highest frequency (50 MHz with period of 0.02 μs) contains

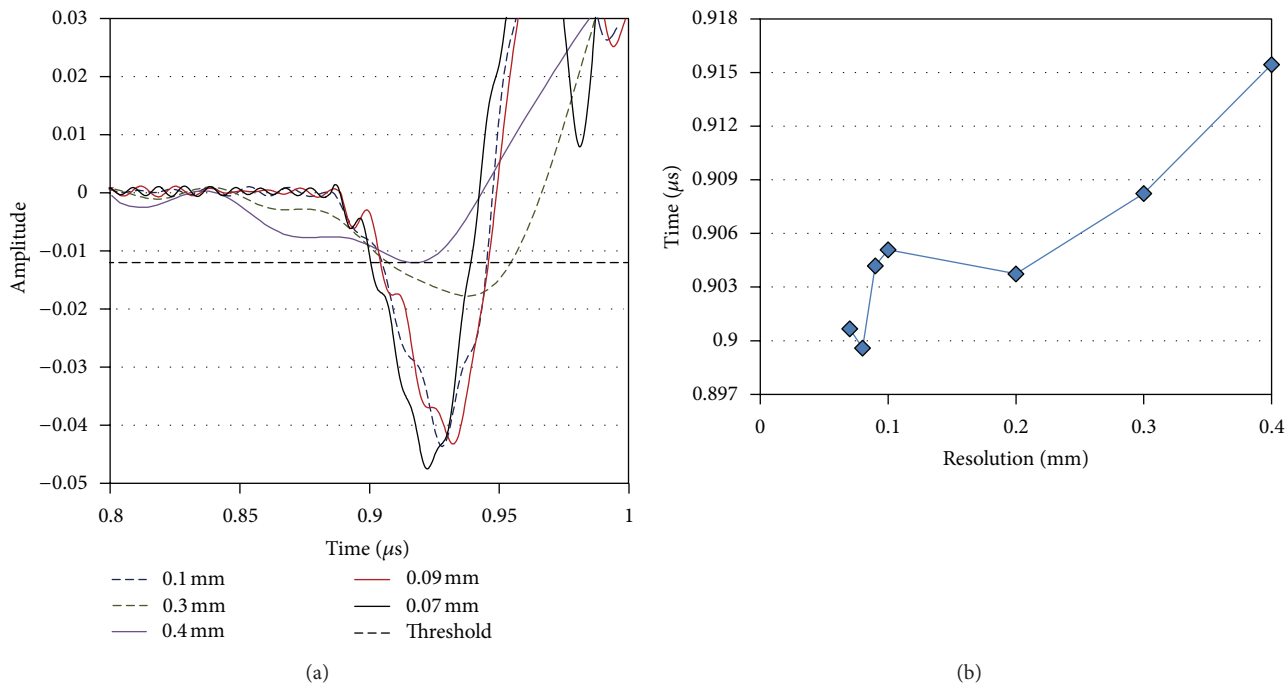

Figure 3: (a) Onset of the reflection in the received waveform for different resolutions. (b) Arrival time to the receiver for different resolutions (measured from the threshold crossing at 0.012 u.a.).

approximately 55–60 points in a cycle and is considered more than adequate sampling in similar cases [16].

3. Results

The longitudinal wave pulse is emitted by the pulser (point A in Figure 2). This pulse propagates initially through water and hits the water/matrix interface under the shear angle, θ, as has been discussed above (point B). The shear wave is transmitted through the matrix and reaches the fiber (C). Reasonably one part is reflected and another is transmitted past the fiber. The amount of energy reflected will depend on the shear wave impedance (product of shear velocity and density) mismatch of the two materials. The matrix impedance is of the level of 9 MRayl, while the fiber which is stiffer exhibits impedance of 23 MRayl. Therefore, in any case a reflection is expected when the materials are in perfect contact. If, on the contrary, the fiber is totally debonded from the matrix, the reflection will be stronger since the impedance of air is negligible compared to that of the matrix. It is reasonable that for any intermediate condition of bonding quality the reflection will be in between the above-mentioned extreme cases. This role (quality of bonding) is played by the "interphase" material, which in our analysis obtains variable values of stiffness, as expressed by the different longitudinal wave velocities. The wave reflected by the fiber, which now may again include longitudinal components after the reflection on the circular surface, propagates back to the surface of the matrix (D), and a part is refracted within water as longitudinal wave following the opposite direction of the initial incident pulse. This wave reaches the sensor as shown in Figure 2, point E. A typical

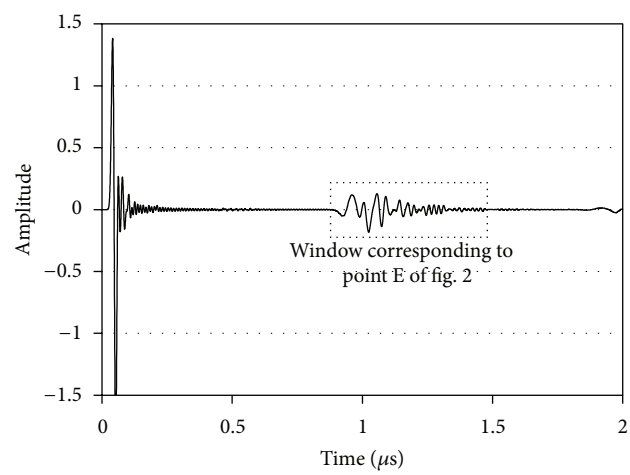

Figure 4: Typical waveform after excitation of 25 MHz.

waveform is seen in Figure 4 where the initial pulse and the reflection (window corresponding to point E of Figure 2) are shown, and in this part of the wave any analysis and evaluation should be focused to characterize the quality of the interphase.

Figure 5 shows some indicative views of the displacement field for the frequency of 25 MHz and for the stiff interphase with pulse velocity of 11770 m/s. In the first case (a), the wave is propagating through water, while in Figure 5(b) the shear wave starts to be refracted in the matrix traveling on a higher speed than the wave in water. In the last case of Figure 5(c), the clear reflection can be seen in water (see arrow) while

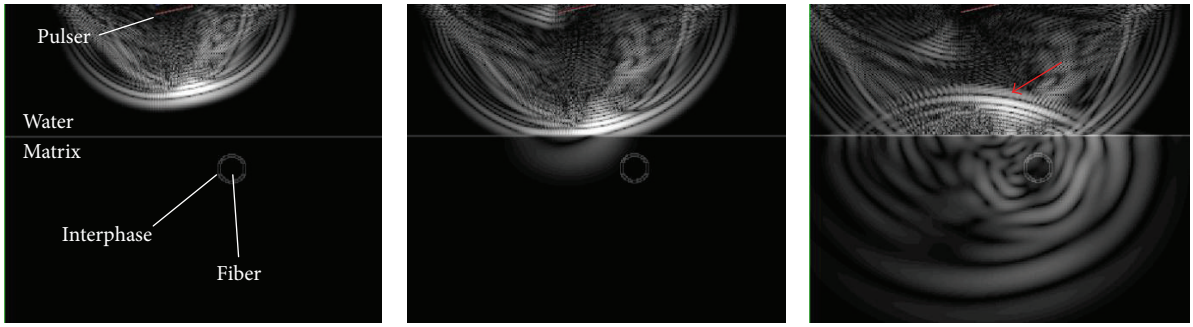

(a) (b) (c)

Figure 5: Consecutive snapshots of the displacement field for the case of stiff interphase.

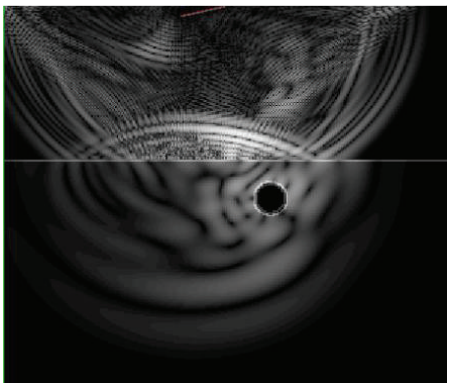

Figure 6: Snapshot of the displacement field for the case of loose interphase.

the refracted wave propagates deep in the matrix. Figure 6 shows the field at approximately the same time but with loose interphase. It is obvious that no wave is transmitted through the fiber, while the reflection traveling back to the receiver is similar to the previous case. However, it contains critical differences that make characterization of the different interphases possible, as discussed next.

Figure 7(a) shows the reflections (corresponding to window E of Figure 4) as recorded by the receiver for two extreme cases of interphase stiffness values, namely, equivalent to air (C_i = 330 m/s) and fiber (C_i = 11770 m/s). The waveforms are identical up to 1 μs, since the initial part of the waveform is due to the direct reflection on the water/solid interface which is not influenced by the fiber. The wave packet of the reflection between the matrix/fiber interphase arrives slightly later since the fiber is at a depth of 100 μm from the surface. Therefore, some discrepancies are visible after the time of 1 μs, with the waveform from the loose interphase exhibiting higher amplitude attributed more likely to the higher reflection coefficient. In order to focus on the differences between the two waveforms, they are subtracted and the resulted waveform is seen in Figure 7(b). Quite detectable discrepancies are noted after 1 μs. The result of the subtraction is a wave of similar amplitude mainly because the reflections from a less stiff second material are of opposite phase. The discrepancy can be quantified by the area of the signal envelope (measured area under the rectified signal envelope, see Figure 7(c)) denoted as "energy," which is a parameter widely used in waveforms analysis [17, 18]. The reflection from the stiff interphase was maintained as reference and the waveforms obtained for each other stiffness were subtracted by the reference in order to calculate the energy difference. The results are seen in Figure 8. For any of the applied frequencies, this energy indicator increases monotonically as the interphase stiffness decreases from its maximum value down to the value of loose interphase. This is because the reflection from the fiber with a loose interphase is maximum due to the extreme impedance mismatch, as has already been mentioned. Comparing the results derived for different frequencies, the maximum energy difference comes for the frequency of 5 MHz, where its value is more than 100 units, while its lowest for loose interphase comes at 1 MHz. Frequencies of 10, 25, and 50 MHz result in intermediate values of 40 to 55, while specifically 50 MHz exhibits a quite constant rate, being equally sensitive to changes of interphase velocity at any interphase velocity level. On the contrary, the 5 MHz curve is very sensitive to changes at the low level of interphase velocities but is not as sensitive to higher values close to good bonding (i.e., the initial signs of debonding in a real case). Therefore, in actual application the use of higher frequencies (25 MHz or 50 MHz) is suggested for assessment of even slight incompatibility or debonding trends, which corresponds to a drop of interphasial stiffness from 11770 m/s to 10000 m/s or 15%. In the same figure, the experimental values of the reflection coefficient for the two extreme cases (good bonding and simulated debonding) are also included, as measured in [9]. This reflection coefficient was obtained by comparing the FFT of the waveform corresponding to the actual geometry (e.g., with a hole) to the waveform of an angled surface which was considered a reference. This reflection coefficient, which again depends on the mismatch between the two sides of the interface, is much higher for the debonding than the case of regular bond between the fiber and the matrix. The qualitative similarity in the decreasing trend between the experimental and numerical energy-related features as the interphasial stiffness increases shows that the approach is in the right direction, and further study will enable accurate evaluations of the interphase quality.

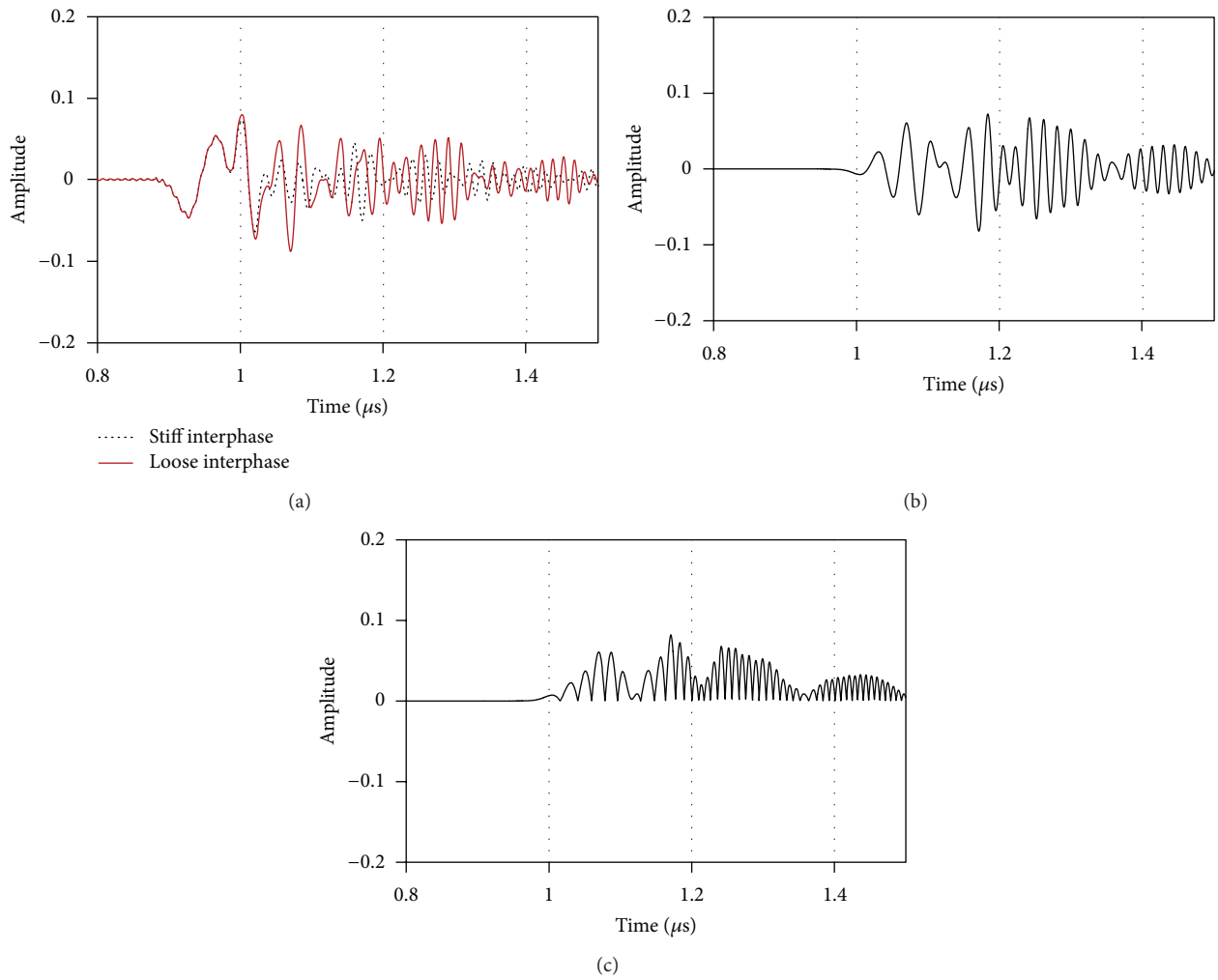

Figure 7: (a) Part of the waveform containing the reflection from the fiber for stiff (C_i = 11770 m/s) and loose (C_i = 300 m/s) interphase. (b) Subtraction of the two waveforms of (a). (c) Rectification of the waveform of (b).

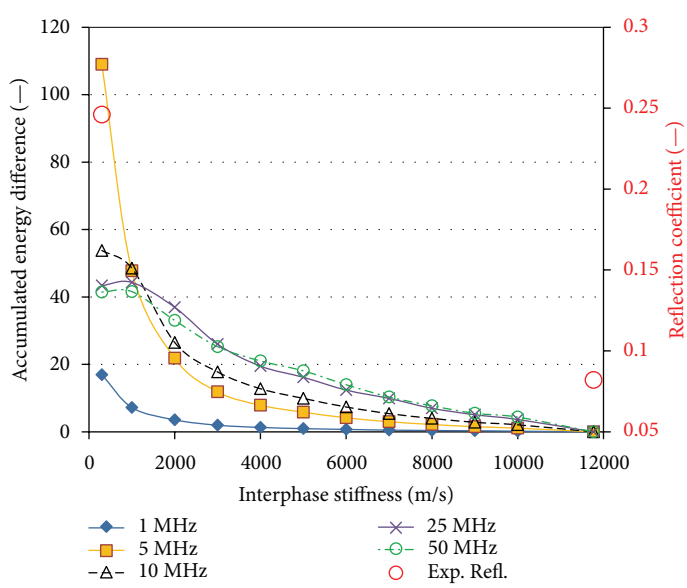

Figure 8: Reflection energy difference for several values of interphase stiffness (longitudinal velocities) and different frequencies.

4. Discussion

The results presented above show that ultrasonic reflection parameters exhibit a monotonic trend with respect to the interphase stiffness. This opens the possibilities not only to detect debonding or poor compatibility but to quantify the stiffness of the interphase. This property is handled by the equivalent wave velocity of the modeling material called "interphase" in this study in accordance to the actual layer between the matrix and fiber materials. The values of interphase stiffness are varied from the two extreme cases of similar to air (loose contact) and similar to fiber (strong bonding) including all the possible realistic values in between. Concerning some specific parameters that are encountered towards the experimental application, it should be mentioned that though the measurement is delicate, in a real experiment with the immersion technique, the quality of the acoustic coupling provided by water is constant and therefore, any difference due to even slight reflection changes will be detected. The sensor scans along the longitudinal axis of the fiber enabling characterization of the interphase bonding on its whole length. It should be kept in mind that this test is intended for material design purposes (compatibility of constituents) rather than deterioration assessment. Therefore, the targeted geometry is simple (e.g., single fiber specimen [9]), in order to avoid the interference with neighboring fibers that would occur in the actual material. The simple geometry will enable derivation of accurate information on the fiber-matrix interphase and will act as a guide for the material design process. This way the results from different systems can be compared in order to judge sort their interface compatibility. Additionally, the corresponding "stiffness" of the interphase can be correlated to the results of mechanical tests if they are also performed (i.e., pull-out or push-in). Concerning the fiber alignment, which is crucial for the aforementioned destructive tests, it is not crucial for the proposed ultrasonic reflection technique because the experimental wave beam cross-section is much larger than the fiber diameter.

5. Conclusion

Advanced metal matrix composites for aerospace applications require delicate methods to accurately assess their initial state as well as service-induced damage. This study concerns the nondestructive evaluation of the quality of bonding between fiber and matrix in such composites. The exact fiber geometry is simulated as an advancement of the previous analytic studies on a simplified geometry. The immersion ultrasonic technique is numerically simulated, while shear waves are targeted due to their sensitivity on bonding conditions. Different bonding is modeled by altering the stiffness of the "interphase" material which acquires properties from near-zero, simulating negligible contact up to stiffness similar to the fiber, simulating the stiffest possible bonding. The results indicate that despite the consecutive refractions between the water and matrix, the influence of the de-bonding is distinguishable compared to the case of stiff interphase. This is because the amount of energy reflected depends on the interphase elastic properties which cause small but discernible differences in the received waveform. The study shows how computational methods enhance our understanding and can give direction to the relevant experimental techniques with the aim of providing better characterization of crucial aspects of the material's condition in a nondestructive manner.

References

[1] P. Stähli and J. G. M. van Mier, "Manufacturing, fibre anisotropy and fracture of hybrid fibre concrete," *Engineering Fracture Mechanics*, vol. 74, no. 1-2, pp. 223–242, 2007.

[2] K. G. Dassios and C. Galiotis, "Direct measurement of fiber bridging in notched glass-ceramic-matrix composites," *Journal of Materials Research*, vol. 21, no. 5, pp. 1150–1160, 2006.

[3] U. Ramamurty, "Assessment of load transfer characteristics of a fiber-reinforced titanium-matrix composite," *Composites Science and Technology*, vol. 65, no. 11-12, pp. 1815–1825, 2005.

[4] D. G. Aggelis, D. V. Soulioti, N. M. Barkoula, A. S. Paipetis, and T. E. Matikas, "Influence of fiber chemical coating on the acoustic emission behavior of steel fiber reinforced concrete," *Cement and Concrete Composites*, vol. 34, no. 1, pp. 62–67, 2012.

[5] G. D. Zhang and R. Chen, "Effect of the interfacial bonding strength on the mechanical properties of metal matrix composites," *Composite Interfaces*, vol. 1, no. 4, pp. 337–355, 1993.

[6] H. An, Y. X. Li, M. Li, Y. Z. Gu, Y. N. Liu, and Z. G. Zhang, "Interfacial adhesion and micro-failure phenomena in multi-fiber micro-composites using fragmentation test," *Composite Interfaces*, vol. 19, no. 6, pp. 385–396, 2012.

[7] B. Hassoune-Rhabbour, L. Poussines, and V. Nassiet, "Development of an adhesion test for characterizing the interface fiber/polymer matrix," *Key Engineering Materials*, vol. 498, pp. 210–218, 2012.

[8] M. C. Waterbury, P. Karpur, T. E. Matikas, S. Krishnamurthy, and D. B. Miracle, "In situ observation of the single-fiber fragmentation process in metal-matrix composites by ultrasonic imaging," *Composites Science and Technology*, vol. 52, no. 2, pp. 261–266, 1994.

[9] P. Karpur, T. E. Matikas, and S. Krishnamurthy, "Ultrasonic characterization of the fiber-matrix interphase/interface for mechanics of continuous fiber reinforced metal matrix and ceramic matrix composites," *Composites Engineering*, vol. 5, no. 6, pp. 697–711, 1995.

[10] T. E. Matikas, "Assessment of interface deformation and fracture in metal matrix composites under transverse loading conditions," *Composite Interfaces*, vol. 15, no. 6, pp. 589–609, 2008.

[11] D. Kleitsa, K. Kawai, T. Shiotani, and D. G. Aggelis, "Assessment of metal strand wire pre-stress in anchor head by ultrasonics," *NDT and E International*, vol. 43, no. 7, pp. 547–554, 2010.

[12] P.-N. Tzounis, L. N. Gergidis, T. E. Matikas, and A. Charalambopoulos, "Mathematical investigation of interfacial property in fiber reinforced model composites," *Composites B*, vol. 43, no. 6, pp. 2605–2612, 2012.

[13] Wave2000, Cyber-Logic, New York, NY, USA, http://www.cyberlogic.org/.

[14] J. Kaufman, G. Luo, and R. Siffert, "Ultrasound simulation in bone," *IEEE Transactions on Ultrasonics, Ferroelectrics, and Frequency Control*, vol. 55, no. 6, pp. 1205–1218, 2008.

[15] C. Pecorari, "Scattering of a Rayleigh wave by a surface-breaking crack with faces in partial contact," *Wave Motion*, vol. 33, no. 3, pp. 259–270, 2001.

[16] F. Moser, L. J. Jacobs, and J. Qu, "Modeling elastic wave propagation in waveguides with the finite element method," *NDT and E International*, vol. 32, no. 4, pp. 225–234, 1999.

[17] D. G. Aggelis, "Classification of cracking mode in concrete by acoustic emission parameters," *Mechanics Research Communications*, vol. 38, no. 3, pp. 153–157, 2011.

[18] A. Anastasopoulos, D. Kourousis, S. Botten, and G. Wang, "Acoustic emission monitoring for detecting structural defects in vessels and offshore structures," *Ships and Offshore Structures*, vol. 4, no. 4, pp. 363–372, 2009.

Hindawi Publishing Corporation
The Scientific World Journal
Volume 2013, Article ID 413587, 8 pages
http://dx.doi.org/10.1155/2013/413587

Research Article

Turbine Rotor Disk Health Monitoring Assessment Based on Sensor Technology and Spin Tests Data

Ali Abdul-Aziz and Mark Woike

NASA Glenn Research Center, Cleveland, OH 44135, USA

Correspondence should be addressed to Ali Abdul-Aziz; ali.abdul-aziz-1@nasa.gov

Received 15 April 2013; Accepted 14 May 2013

Academic Editors: P.-C. Chen and M. Curioni

The paper focuses on presenting data obtained from spin test experiments of a turbine engine like rotor disk and assessing their correlation to the development of a structural health monitoring and fault detection system. The data were obtained under various operating conditions such as the rotor disk being artificially induced with and without a notch and rotated at a rotational speed of up to 10,000 rpm under balanced and imbalanced state. The data collected included blade tip clearance, blade tip timing measurements, and shaft displacements. Two different sensor technologies were employed in the testing: microwave and capacitive sensors, respectively. The experimental tests were conducted at the NASA Glenn Research Center's Rotordynamics Laboratory using a high precision spin system. Disk flaw observations and related assessments from the collected data for both sensors are reported and discussed.

1. Introduction

The strive to develop a robust health monitoring system to detect rotating engine component malfunctions is among the key areas of interest for engine companies and the associated aviation industry. Typically, health monitoring is performed using sensor systems and other similar means that are capable of functioning under harsh and severe environmental operating conditions. Such systems are to operate without interference with the overall operation of the engine. However, implementation of such technology is highly dependent on many factors and among them setting up specific types of experiments to simulate representative turbine engine conditions and frequent mishaps that the engine encounters during operation. Supportive studies like analytical verification and modeling are equally important in order to verify and complement the experimental findings. Testing under high temperature and wireless technology using durable and effective sensor technologies is also highly desirable.

Health monitoring is not only confined to sensor technology since there are many other ways of conducting such inspection which are mostly nondestructive evaluation-based approaches. These approaches are widely used in the aviation industry to track engine component performance and durability. They are further used to locate cracks and other anomalies before they become a risk factor that leads to catastrophic failure. Nevertheless, some if not most of these techniques can be both costly and impractical, in particular, when it comes to inspecting complex geometries and large structures [1]. Therefore, the urge for developing systematic, reliable and realistic diagnostic tools to detect damage and monitor the health of key components in the engine, such as rotor disks and turbine blades, is highly in need. It is greatly fundamental to maintaining engine safety, dependability, and life [2].

The NASA Aviation Safety Program under the Vehicle Systems Safety Technology (VSST) project is taking the lead in partnership with the Federal Aviation Administration, Aviation Industry and the Department of Defense [3], to promote the development of these technologies to improve and reduce the fatal aviation accidents and assist safety as a whole. This effort is being carried out at NASA Glenn Research Center through the Optical Instrumentation and NDE branch by conducting controlled spin experiments of turbine engine rotor like test articles to explore various sensing advancements for local and global detection of rotor damage. Comparison of test data for baseline disks without any damage with that of a disk with artificially induced

damage, a small crack or a notch, is performed to appraise the findings. Hence, this paper presents experimental results obtained from spin tests of a rotor disk and their association to the development of a structural health monitoring and fault detection system.

2. Technical Approach

The experimental work in this study considered a conceptual design of a disk with machined teeth to imitate compressor or turbine blades and provide a cost effective test article to simulate crack initiation and propagation; see Figure 1. The central region of the disk is counter-bored on both sides to create the rim, web, and bore regions of a typical turbine disk. The machined teeth on the rim simulate tip passing, but they trim down the blade mass loading on the web and bore usually experienced in most rotors. The goal is to induce changes in radial tip displacement without disk yielding in order to test the instrumentation and to then initiate and grow cracks by machining and/or increasing rotational speed. Two sensor types (capacitive and microwave) are employed to capture the blade tip clearance both for health monitoring and comparison purposes. An eddy current sensor is also included in the system to measure the shaft displacements.

Figure 1 illustrates a description of the disk specimen and the induced crack notch along with the tip clearance probes. The test specimen disk has an outside diameter of 23.495 cm (9.25 in), a bore and an outside rim thickness of 2.54 cm (1 in) and 3.175 cm (1.25 in), the thickness of the web is 0.254 cm (0.10 in), and the cross section and height of the blades are 3.175 cm × 0.330 cm (1.25 in × 0.13 in) and 0.838 cm (0.33 in), respectively. It has rotor-like blades, a total of 32, evenly spaced around the circumference. Eight holes, 0.508 cm (0.20 in) diameter each, were drilled through the disk halfway in the rim. The holes were spaced every 45°, and they were designed for future studies as possible mass add-on points or notch initiation sites. The disk specimen is made out of nickel base material alloy Haynes X-750 and it weighs approximately 4.88 Kg (10.75 Lb).

The notch had a width of 0.381 mm (0.015 in) as per wire thickness and burn area of the electric discharge machining (EDM) process. The notch region was intentionally selected to be in the web area since finite element analysis results revealed that this section encounters the highest stress level in the disk during the spin operation [1, 2]. Technical considerations were emphasized to preserve system consistency of all the operating parameters and other experimental conditions during the removal-reinstallation process of the disk specimen in both situations, baseline no-notch and notch states.

3. Sensor Technology

3.1. Capacitive Probe Sensor. For blade tip clearance measurements, a capacitive sensor system was installed; see Figure 1(a). These types of sensors are based on a direct current (DC) offset, an offsetting of a signal from zero where it refers to a direct current voltage, rather than a modulation technique which is a method used to digitally represent sampled analog signals. The capacitive sensors are designed to monitor the electrical property of "capacitance" to initiate and take measurements. The capacitance is a function of the physical dimensions (geometry) of the conductors and the permittivity of the dielectric. It is defined as a field that exists between two conductive surfaces within some rational proximity. Capacitance is directly proportional to the surface area of the conductor plates and inversely proportional to the separation distance between the plates. Variations in the distance between the surfaces lead to changes in the capacitance rate. This rate change is used by the sensors to indicate the difference in position of a target. High-performance displacement sensors use small sensing surfaces and as a result are positioned close to the targets (0.25–2 mm). The DC voltage, in conjunction with the motion of the rotor, allowed the current system to record three channels at a rate of 1 MHz each.

3.2. Microwave Sensor Background and Theory. The microwave tip clearance sensor system works on principles that are similar to a short-range radar system. The tip clearance probe is both a transmitting and receiving antenna [3–10]. The sensor emits a continuous microwave signal and measures the signal that is reflected off a passing blade. The motion of the blade modulates the reflected signal. The reflected signal is then compared to an internal reference signal and the phase difference directly corresponds to the distance to the blade. The system consists of two major components. The first component is the probe, (Figure 2(a)). The second component is the sensor electronics, (Figure 2(b)). The probe contains the transmitting and receiving antenna and is designed to be installed in the casing of the engine where it can measure the radial clearance between the face of the sensor and the turbine blade tips. The probes are made of high temperature material and are designed to operate in temperatures of 900°C uncooled, 1200°C with cooling air. Two generations of probes are in operation. The first-generation probes operate at 5.8 GHz and can measure clearance distances up to ~ 25 mm (i.e., one-half the radiating wavelength). The second-generation probes operate at 24 GHz and in theory can measure clearance distances up to ~6 mm. In regards to physical size, the first generation probes are approximately 14 mm in diameter and 26 mm long. The second-generation probes are approximately 9 mm in diameter and 19 mm long. This technology has an ultimate goal of obtaining clearance accuracies approaching 25 μm. Accuracies in this order were observed in the laboratory during testing [4]. A frequency response of up to 5 MHz is typical, with up to 25 MHz being possible with this technology.

The sensor electronics consist of the radio frequency (RF) generator, RF detector, and all of the associated hardware required to generate, measure, and convert the microwave signals into a displacement reading [4].

The sensor electronics are designed to be located off-board of the engine in an environmentally benign area. The probes are connected to the sensor electronics using a microwave rated coaxial cable. A rack-mounted PC is used to interface to the sensor electronics and run the data acquisition and display software. The data acquisition computer is connected to the sensor electronics through a network switch. The data acquisition computer is intended to be remotely

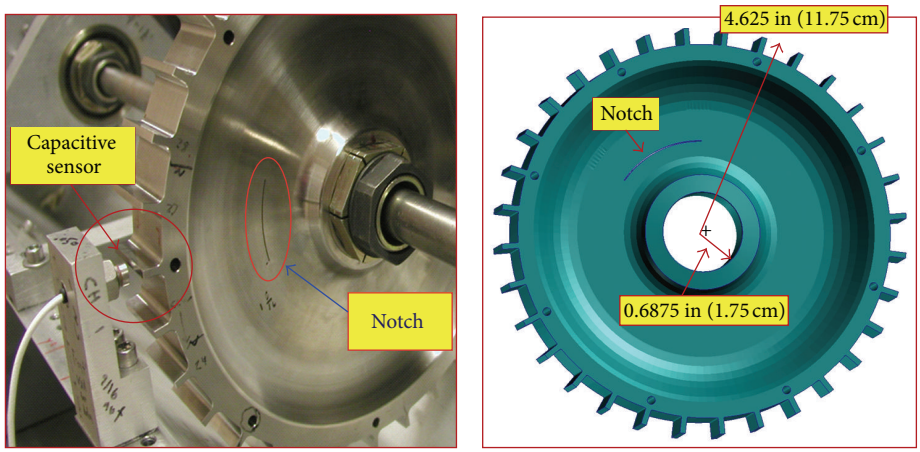

(a) Capacitive sensor probe (b) 3D model with the Notch

Figure 1: Test disk capacitive sensor assembly.

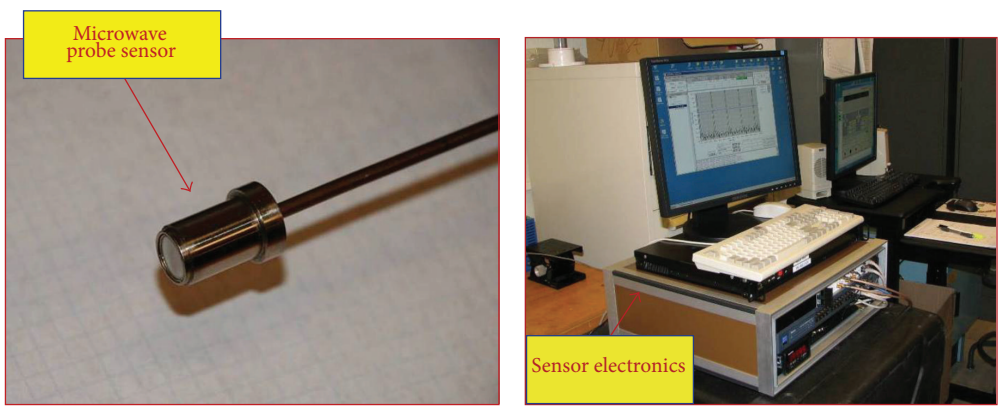

(a) Sensor probe (b) Sensor electronics

Figure 2: Microwave sensor probe and its electronics setup.

located away from the sensor electronics in an area such as a control room using a CAT5E connection.

3.3. Capacitive and Microwave Sensors Performance. Figure 3 demonstrates a comparison between the two primary blade tip clearance sensors, microwave and capacitive, attached to the data system. The data collected for both sensors compared relatively well. However, the similarity is not as uniform, the similarity is not as uniform as anticipated which implies that certain calibration is needed to fine-tune the sensor system further and bring the data closer. Perhaps, adding an additional filtering or average process for the microwave sensor may result in improving the agreement between the two measurements. Nevertheless, each sensor system is operating as expected. Their role in the experiment configuration is to serve the same functionality in a different fashion and to test their performance.

4. Experimental Results

Spin tests were performed on the rotor disk and covered baseline runs with both undamaged and damaged disks via the artificially induced notch, shown in Figure 1. The tests included spinning the rotor under various simulated engine mission profiles starting from a minimum rotational speed of 3000 up to a maximum of 10000 rpm. The controlled speed applied during the current testing was made with an acceleration-deceleration rate of 60 rpm/second. This insured passing the critical speed of 2,610 rpm and leading to post-critical state [11]. Figure 4 shows samples of two mission profiles that were used to test the rotors. These profiles were derived on the basis of revolutions per minute data obtained on different flights comprising different flight maneuvers [12].

Figure 4(a) is referred to as the constant engine power cycle profile; however the graph shown does not illustrate the constant behavior due to an input offset. The engine speed reaches 10,000 rpm in two steps, a take off with a brief hold up at 5000 rpm and 40 seconds hold at 10,000 rpm with a rapid decrease to 5000 rpm and a ramp up to 10,000 rpm for one repetitive cycle. Figure 4(b) shows another mission profile (engine cyclic power cycle) that allows the rotor disk to go through somewhat analogous series of events starting at a speed beyond the critical value [11] and up to 8500 rpm. These profiles are being used to imitate unusual engine conditions

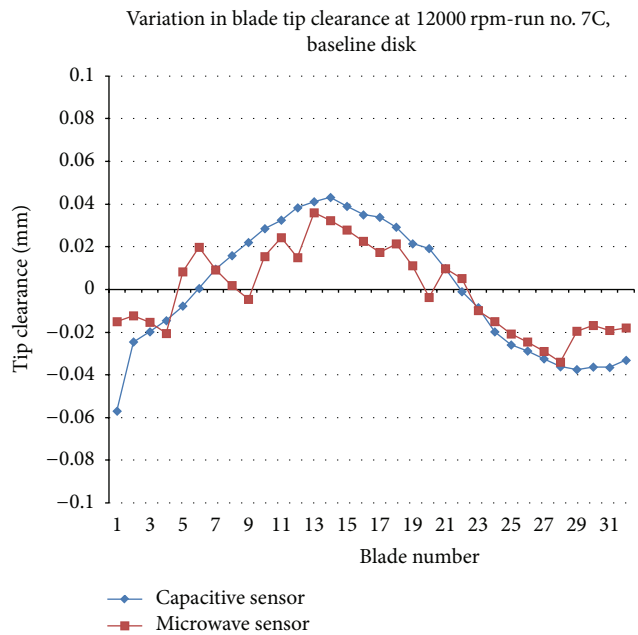

FIGURE 3: Sample of capacitive and microwave sensor data readings for a baseline disk at 12000 rpm.

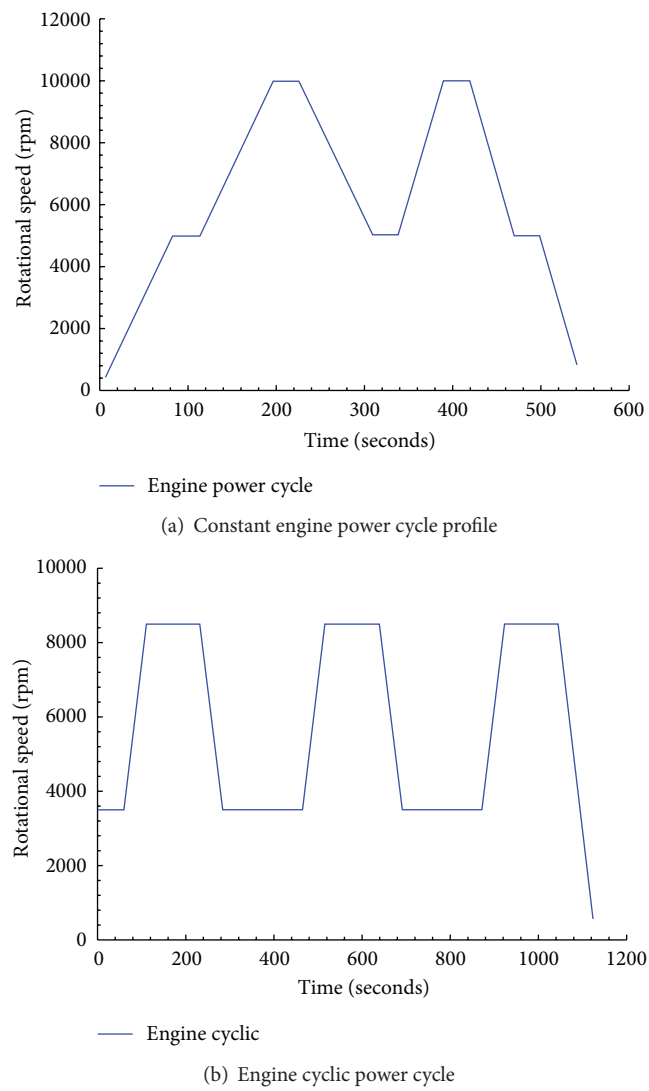

FIGURE 4: Simulated engine mission history test profiles.

and to help in evaluating the rotor performance under harsh and complex loading events in an attempt to fatigue the disk with the expectation that all the existing anomalies would appear in the test data. Additionally, under these conditions, these experiments supplied valuable assessments for both the crack detection scheme and the structural durability of the disk materials.

4.1. Spin Test Results. Experimental data under both mission profiles are represented in Figures 5 and 6. The data in Figure 5 are produced under the constant power cycle mission for both the baseline no-notch and the notched disks. The mission history is shown along with the trace vibration vector and Bode plots for the phase and amplitude response. Bode plots are a very useful way to represent the gain and phase of a system as a function of frequency. This is referred to as the frequency domain behavior of a system. The magnitude and phase plots determine the phasor representation of the transfer function at any frequency. It is typically used for transient analysis in both run-up and run-down tests. It can help identify the resonance speed of a rotor or examine the rotor dynamics on an order basis. The x-axis in a Bode plot is speed or frequency, which enables seeing the changes in magnitude and phase over speed or frequency.

A clear observation of data variation is noted in Figures 5 and 6 between the two plots. For instance, a circular loop representation for the trace of vibration vector (disk vibration response) is seen for the baseline disk, while a gap in the loop is present for the notched disk. This behavior hints that a difference in the vibration response for the two structures is present signifying the existence of some type of irregularity. Such observation has been reported in [13–17], where a crack in the rotor disk is documented via the presence of distorted trace of the vibration vector distribution and a rise in the phase and amplitude response upon surpassing the 1st critical speed; *see Figure 6 for additional clarifications and captions notation, axes labels and units.*

This conduct is certainly noticeable in Figure 5(a) for the notched disk. A rise in the phase magnitude response is noted. Also, it is noted that the peak is at a critical frequency (5000–9000 rpm), and then it begins to settle out at maximum speed close to critical frequency. So the damping ratio keeps the curve from flattening compared to no crack, (Figure 5(b)). Note how the magnitude phase graphs no longer represent a complete circle in the notched disk case, (Figure 7(a)).

This is a sign of a crack growing and is detected from the plot of a cycle worth of data. At the same time the magnitude graph (Figure 5(a)) has started a ω^2 (ω is the rotational speed) rise after settling past the critical frequency. A rise in amplitude and constant phase is typically an indication of the growth of a crack, assuming that some internal movement

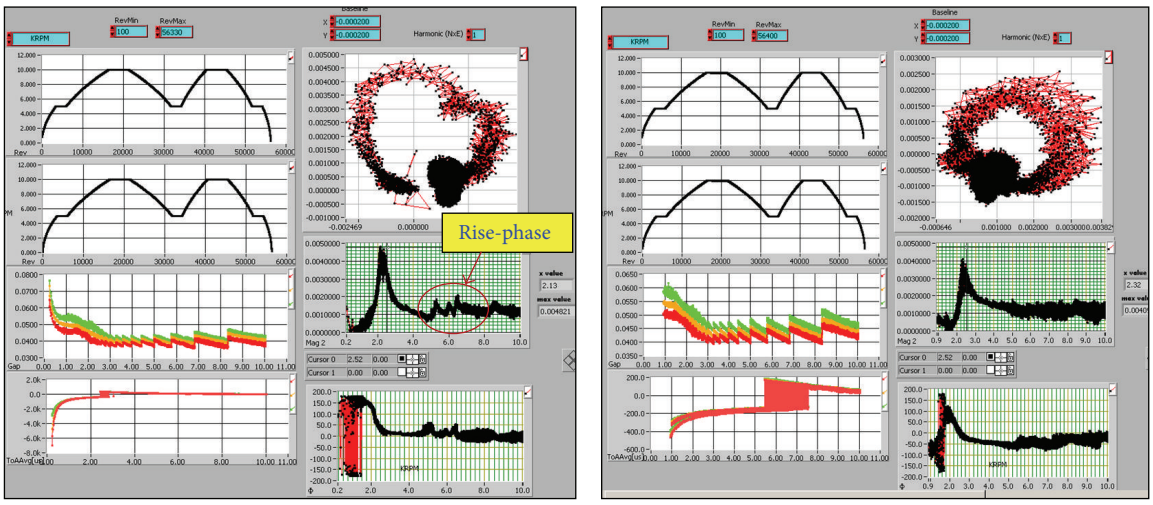

(a) Disk with notch

(b) Disk without notch

Figure 5: Bode Plots 9 minutes comparison test of the disk with and without notch, capacitive sensor data, Engine cyclic power profile at 5–10 Krpm rotational speed.

of the rotating structure does not cause the unbalance [13]. In this case the system is tracking a crack growing in the disk. Therefore, examination of the above data has verified that the detection scheme based on the blade tip clearance response allows identifying the presence of some sort of fault in the rotor disk. However, further confirmation is warranted throughconducting more tests for different rotors under similar operating conditions to authenticate that this type of behavior in the vibration response is accurately due to some existing structural defects in the rotor rather than a system-related unbalance [18–20].

Figure 6 shows the results obtained under the cyclic run time mission profile. The trace of vibrations vector in the Bode plot contains rather distorted data with an incomplete circular shape. Also, the amplitude shows a mild rise at the 5000–6000 rpm range which substantiates the theory of the presence of an unbalance condition or an anomaly state as noted in the data presented in Figure 5. However, the manifestation of such observations remains not as straightforward but it underlines or it confirms the presence of some type of defect. Still, further work to confirm this scrutiny is needed.

The data reported in Figure 7 shows the test output of the microwave sensor for a constant amplitude engine history profile. Only data for the takeoff portion of the profile up to the first 300 revolutions is shown, (Figure 7(a)). This is for a 1500 seconds long test at 100 rpm acceleration/deceleration rate for a notched disk. The response of the microwave sensor is very similar to that of the capacitive sensor; it has been introduced into the testing scheme to investigate its applicability and performance for engine health monitoring applications. And as mentioned earlier, the microwave tip clearance sensor system works on principles that are similar to a short-range radar system and are different than those for the capacitive sensor. The probe is both a transmitting and a receiving antenna; it emits a continuous microwave signal and measures the signal that is reflected off a rotating blade.

Figure 7(b) shows a magnified phase amplitude output produced by the data obtained from the microwave sensor for a spin test of a notched disk at 10,000 rpm rotational speed. It is obviously noted that a rise in the phase exhibiting a second-degree order (ω^2) is recognized at a speed range of 7000 to 10000 rpm. This supports the observations made earlier for the capacitive sensor data concerning the crack detection phenomena in the rotor and the similarity of the microwave sensor performance; see Figure 5.

4.2. Unbalance Test Results. An unbalance test was performed to institute a baseline database for the rotor at various operating conditions and to support investigating and evaluating the vibration response under nonordinary service environment such as imbalance situations. The test was conducted at 10,000 rpm at 100 seconds acceleration/deceleration rate and lasted 4.33 minutes long. The test covered a standard mission profile under transient ramp up, cruise, and ramp down conditions. Test conditions were kept the same as those applied during the non-unbalance state to enable precise assessments of the imbalance factors and their impact on the rotor vibrations response under consistent and refined test margins for the same rotor. Figure 8(a) shows a photo of the disk used for the unbalance tests with labels indicating the sites of the locations of the weight (0.5 gram) during the tests.

As noted, two cases were considered: one case with the extra weight being along the notch side (position A) and another one with weight being across from the notch (position B). Additionally, the purpose of the unbalance test is to check the capability of the sensors technology not only in crack detection, but also in predicting other major malfunctions in the rotor system such as unbalance provision. This further supports the theory which relates to rotor design; whereas the rotational velocity of any rotating object

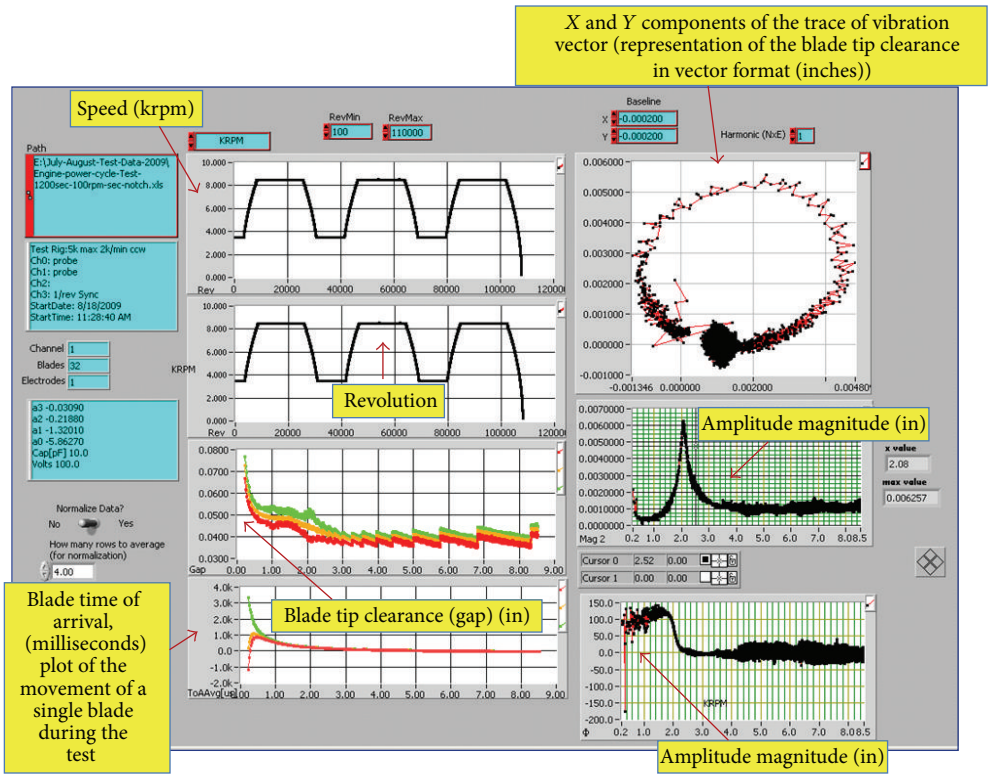

FIGURE 6: Engine constant power cycle test: capacitive sensor data at 8500 rpm, 1200 sec long at 100 rpm acceleration/deceleration rate for the Notched disk.

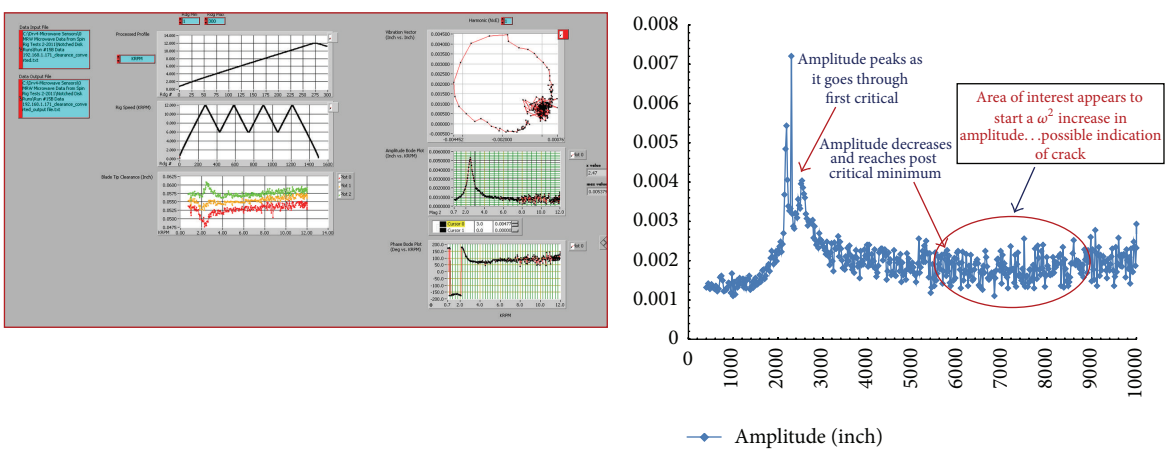

(a) Bode plot output

(b) Vibration amplitude as a function of rotational speed

FIGURE 7: Simulated engine mission history profile (constant amplitude) test, microwave sensor data.

increases, its level of vibration often passes through a maximum at what is called a critical speed [11]. This is commonly excited by unbalance of the rotating structure. If the amplitude of vibration at these critical speeds is excessive, catastrophic failure can occur. For this reason, it is typically recommended that in large rotors design the appropriate approach is to use physical prototypes and tests in order to ensure safe rotating machinery design and balance it well.

Figure 8(b) shows a test that runs for the notched rotor disk under unbalance test with the mass being at position B as indicated in Figure 8(a). Position B is on the opposite side of the notch. This location was intentionally chosen to investigate imbalance effects not only at positions within the region surrounding the notch, but also at areas outside the notch section and further out. Test results at "position A" are not shown due to space limitation and since similar results were observed as well.

It is also noted that the trace of vibration vector shown in Figure 8(b) shows a very irregular distribution signifying that the imbalance had eliminated the typical complete circular

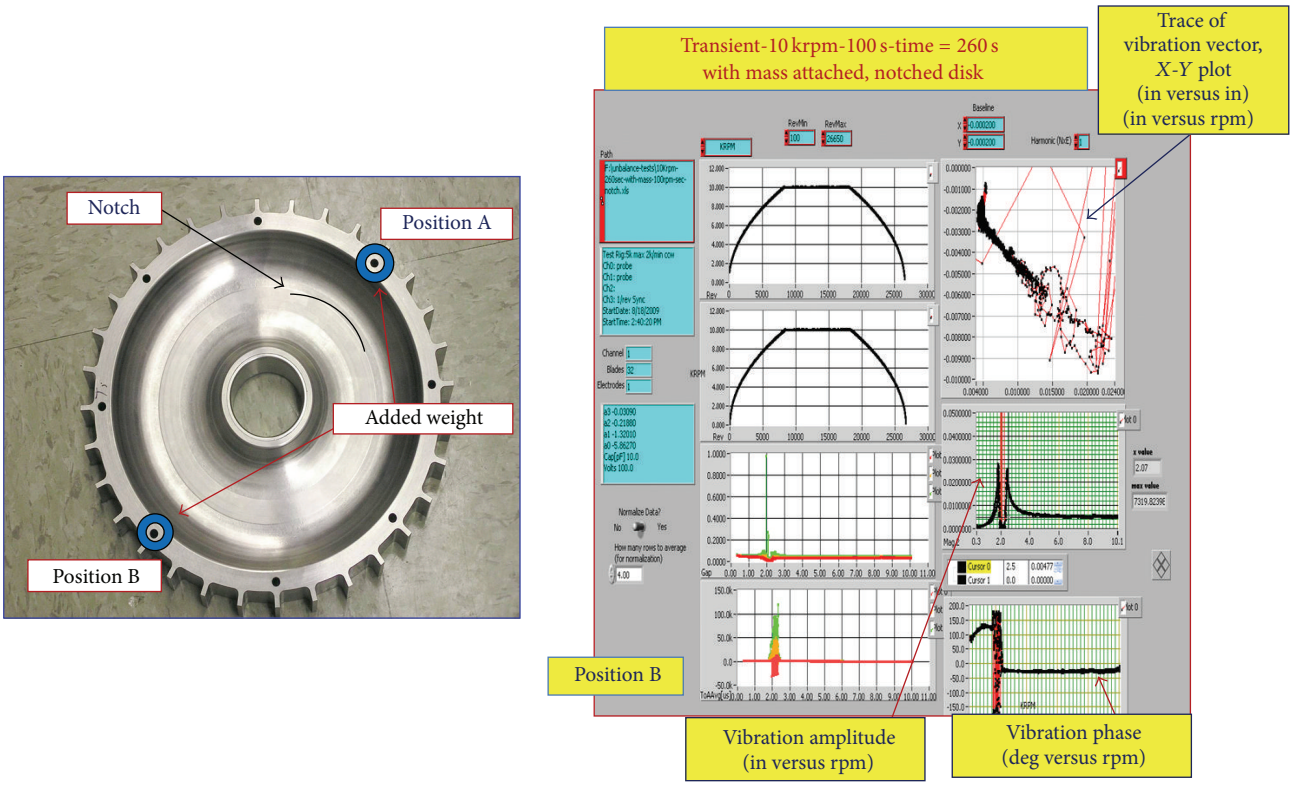

(a) Unbalance layout with added weight and locations

(b) Unbalance vibration response

Figure 8: Tip clearance variation with blade numbers and simulated rotor unbalance layout.

shape usually encountered when a clean baseline rotor disk without any balance weight or damage is in operation. This further designates that having an imbalance state whether it is due to the existence of a notch or other factors within the system will lead to nonordinary shape of the trace of the vibration vector curve. Additionally, these data confirm that upon altering the disk weight by adding or removing mass, the state of imbalance is imminent and the tip clearance magnitude will depend on the added mass size and location. Further, the findings of these results substantiated the purpose of these tests to help determine that the blade tip clearance sensors have recognized the significance of these critical parameters and their influence on the disk performance.

5. Conclusions

The work performed in this paper involved conducting spin experiments on the rotor disk with and without an artificially induced notch at different rotational speed levels. Bode plots of data from these tests provided indications of differences between the undamaged rotor with that of the damaged one. Crack growing signs have been detected where the amplitude magnitude in the Bode plot has started a ω^2 rise after settling past the critical frequency. This growth of the magnitude is a noteworthy indicator of a crack growth or another fault which confirms similar results cited by prior studies. Microwave and capacitive sensors delivered closely similar data for most of the blades except for some where the measurements were slightly dissimilar which can be attributed to factors such as equipment calibration and apparatus instrumentation fine tuning.

The trace of vibration vector which represents the imbalance mass showed very inconsistent distribution compared to data obtained from a balanced disk. This showed that the imbalance had eliminated the complete circular shape typically encountered when a clean baseline rotor disk without any damage is in operation. Additionally, this indicated that having an imbalance state whether it is due to the existence of a notch or other factors within the system, the trace of the vibration vector curve will have an asymmetrical non-circular and highly distorted shape. This leads to the conclusion that the data obtained from spin testing of the rotor to some extent showed that the detection scheme based on the blade tip clearance response is capable of identifying the presence of defects in the rotor.

Lastly, the experimental data enabled exploring the difference in the vibration response between a baseline and a damaged rotor suggesting when the existence of some type of anomaly is present. Also, the combined sensor technology, which included the capacitive, microwave and eddy current probes, supplemented the tests with ample evidence and allowed exploring the changes in the disk vibration response at different operating conditions. However, further work and more testing must be continued to develop, improve and link

this experimental investigation to put forward a more precise and accurate appraisal of monitoring the health of rotating components.

References

[1] A. Abdul-Aziz, M. R. Woike, J. D. Lekki, and G. Y. Baaklini, "Development of a flaw detection/health monitoring scheme for turbine engine rotating components," in *presented at the AIAA Infotech at Aerospace*, AIAA 2010-3329, Atlanta, Ga, USA, April 2010.

[2] A. Abdul-Aziz, M. R. Woike, G. Abumeri, J. D. Lekki, and G. Y. Baakilini, "NDE using sensor based approach to propulsion health monitoring of a turbine engine disk," in *Health Monitoring of Structural and Biological Systems*, vol. 7295 of *Proceeding SPIE*, San Diego, Calif, USA, March 2009.

[3] U. S. Department of Transportation and Federal Aviation Administration, *Engine Damage-Related Propulsion System Malfunctions*, DOT/FAA/AR-08/24, 2008.

[4] M. Woike, A. Abdul-Aziz, and T. Bencic, *A Microwave Blade Tip Clearance Sensor for Propulsion Health Monitoring*, NASA/TM-2010-216736, AIAA-2010-3308, 2010.

[5] M. Woike, J. Roeder, C. Hughes, and T. Bencic, *Testing of a Microwave Blade Tip Clearance Sensor at the NASA Glenn Research Center*, NASA/TM-2009-215589, AIAA-2009-1452, 2009.

[6] A. Abdul-Aziz, M. Woike, J. Lekki, and G. Y. Baaklini, *Health Monitoring of a Rotating Disk Using A Combined Analytical-Experimental Approach*, NASA Technical Memorandum, NASA/TM-2009-215675, 2009.

[7] T. A. Holst, T. R. Kurfess, S. A. Billington, J. L. Geisheimer, and J. L. Littles, *Development of an Optical-Electromagnetic Model of a Microwave Blade Tip Sensor*, AIAA-2005-4377, 2005.

[8] J. L. Geisheimer, S. A. Billington, T. Holst, and D. W. Burgess, *Performance Testing of a Microwave Tip Clearance Sensor*, AIAA-2005-3987, 2005.

[9] J. L. Geisheimer, S. A. Billington, and D. W. Burgess, *A Microwave Blade Tip Clearance Sensor for Active Clearance Control Applications*, AIAA-2004-3720, 2004.

[10] T. A. Holst, *Analysis of spatial filtering in phase-based microwave measurements of turbine blade tips [M.S. thesis]*, Georgia Institute of Technology, Atlanta, Ga, USA, 2005.

[11] A. L. Gyekenyesi, J. T. Sawicki, and W. C. Haase, "Modeling disk cracks in rotors by utilizing speed dependent eccentricity," *Journal of Materials Engineering and Performance*, vol. 19, no. 2, pp. 207–212, 2010.

[12] U. S. Department of Transportation, Federal Aviation Administration, and Office of Aviation Research, *Turbine Engine Fan Disk Crack Detection Test*, DOT/FAA-AIAR-04/28, Washington, DC, USA, 2004.

[13] W. C. Hass and M. J. Drumm, "Detection, discrimination and real-time tracking of cracks in rotating disks," in *IEEE Aerospace Conference*, Big sky, March 2002.

[14] M. Drumm and C. W. Haase, *High Performance Rotor Health Monitoring*, Exsell Instruments, Acton, Mass, USA, 2000.

[15] W. C. Hasse, "High performance rotor health monitoring," in *Proceedings the SAE Conference on Engine Condition Monitoring*, Montreal, Canada, October 1999.

[16] W. C. Hasse and M. J. Drumm, "Detection, discrimination and real-time tracking of cracks in rotating disks," in *Proceedings of the 9th International Symposium on Transport Phenomena and Dynamics of Rotating Machinery (ISROMAC-9 '02)*, Honolulu, Hawaii, USA, February 2002.

[17] A. S. Sekhar and B. S. Prabhu, "Condition monitoring of cracked rotors through transient response," *Mechanism and Machine Theory*, vol. 33, no. 8, pp. 1167–1175, 1998.

[18] D. E. Bentlty, "Detecting cracked shafts at earlier levels," *Orbit Magazine, Bently Nevada*, vol. 3, no. 2, 1982.

[19] J. Wauer, "On the dynamics of cracked rotors: a literature survey," *Applied Mechanics Review*, vol. 43, no. 1, pp. 13–17, 1990.

[20] A. K. Koul and R. V. Dainty, "Fatigue fracture of aircraft engine compressor disks," in *Rotating Equipment, Handbook of Case Histories in Failure Analysis*, vol. 1, pp. 241–250, 2002.